Université de Liège

Faculté des Sciences

Centre Spatial de Liège

Towards Operational Use of Combined Split-Band Interferometry and Multidimensional Small Baseline Subset

Application to geohazard monitoring in the Kivu region

Ludivine Libert

Academic year 2018-2019

This thesis is presented in fulfillment of the requirements for the degree of Doctor in Sciences.

Supervisor:	Dr. Christian Barbier
President of the Jury:	Prof. Serge Habraken
Members of the Jury:	Dr. Dominique Derauw Dr. Nicolas d'Oreye Prof. Ramon Hanssen Prof. Jérôme Loicq Dr. Alberto Refice

October 2018

Abstract

The vulnerable region of Kivu is strongly affected by geohazards such as volcanism and landslides. An essential ingredient for modelling the geophysical processes from which these geohazards originate is the measure of the Earth's surface displacements. In this complex region, monitoring these ground deformations can be efficiently performed by using Synthetic Aperture Radar Interferometry (InSAR). Nevertheless, geophysical modelling requires accurate measurements of the displacements over time, which are not always manageable with conventional InSAR due to area-related limitations such as geometric distortions. Consequently, we consider advanced processing techniques such as Split-Band Interferometry (SBInSAR), which potentially allows to calculate the absolute interferometric phase, and Multidimensional Small Baseline Subset (MSBAS), which reconstructs the history of deformations along the horizontal and vertical directions. The aims of this thesis are the investigation of the SBInSAR and MSBAS techniques for improving the ground deformation measurements, the development of these techniques in order to achieve an operational tool of monitoring, and eventually to combine the information provided by both methods. Regarding the Split-Band Interferometry, we consider its theoretical applicability, determine optimum processing parameters and propose a method that corrects phase ambiguities by using SBInSAR as a complement to classical phase unwrapping, which we call SBInSAR-assisted phase unwrapping. We establish that the best criterion for the detection of spectrally stable pixels is the slope standard deviation. We also study the temporal behaviour of spectrally stable pixels and show that few of them persist over time. We analyze the behaviour of artificial reflectors with respect to SBInSAR and provide strong evidences that there exists a correlation between the signal-to-clutter ratio of a target and its detectability as a spectrally stable pixel. Regarding the Multidimensional Small Baseline Subset, we present the InSAR mass processing chain developed in collaboration with the European Center for Geodynamics and Seismicity for MSBAS preprocessing, and we propose to optimize the spatial coverage of MSBAS measurements by using interpolation or global masking. An MSBAS analysis is carried out over the city of Bukavu for the period from January 2016 to September 2017. We also study temporal decorrelation over the Virunga Volcanic Province and we model it using a decreasing exponential function. As a complement, we implement the Range Split-Spectrum technique in the CIS software for the ionospheric phase compensation in low frequency interferograms. We finally discuss the options for merging SBInSAR and MSBAS together.

Résumé

Le Kivu est une région vulnérable menacée par de nombreuses catastrophes naturelles telles que le volcanisme et les glissements de terrain. Afin de modéliser les processus géophysiques qui sont à l'origine de ces phénomènes, il est nécessaire d'estimer les déformations qu'ils induisent à la surface terrestre. Dans cette région complexe, celles-ci peuvent être estimées efficacement grâce l'interférométrie radar par synthèse d'ouverture. Néanmoins, la modélisation géophysique nécessite une connaissance précise de ces déformations au cours du temps, ce qu'il n'est pas toujours possible d'obtenir avec l'interfémotrie conventionnelle à cause de certaines limitations telles que les distortions géométriques liées à la région étudiée. Nous considérons donc des méthodes de traitement avancé, comme l'interférométrie Split-Band, qui permet potentiellement de calculer la phase absolue, et la technique du Multidimensional Small Baseline Subset (MSBAS), qui reconstruit les déformations de terrain au cours du temps et les décompose selon les directions horizontale et verticale. Cette thèse a pour objectif d'étudier ces deux techniques et leur capacité à améliorer les mesures de déformation de terrain, de développer ces techniques afin d'obtenir des outils de traitement opérationels pour le monitoring, et enfin de combiner les informations dispensées par les deux méthodes. En ce qui concerne l'interférométrie Split-Band, nous étudions sa faisabilité théorique, nous déterminons les paramètres optimaux pour le traitement et nous proposons une méthode qui corrige les ambiguïtés de phase en utilisant l'interférometrie Split-Band en complément du déroulage de phase classique. Nous appelons cette méthode le déroulage de phase assisté par interférométrie Split-Band. Nous établissons que le critère le plus efficace pour la détection de pixels spectralement stables est l'écart-type sur la pente. Nous nous intéressons également au comportement de ces pixels spectralement stables et nous montrons que peu d'entre eux persistent au cours du temps. Nous analysons le comportement des réflecteurs artificiels vis-à-vis de l'interférométrie Split-Band et nous donnons des indications tangibles de l'existence d'une corrélation entre le rapport signal-sur-bruit d'un réflecteur et sa détectabilité en tant que pixel spectralement stable. D'autre part, en ce qui concerne le MSBAS, nous présentons la chaine de traitement interférométrique automatisé qui a été développée en collaboration avec l'European Center for Geodynamis and Seismicity pour le pré-traitement du MSBAS. Nous proposons d'optimiser la couverture spatiale des mesures MSBAS en utilisant une interpolation ou un masque global. Nous réalisons ensuite une analyse MSBAS sur la ville de Bukavu, étudiant la période allant de janvier 2016 à septembre 2017. Nous étudions également la décorrélation temporelle sur la région du Virunga et nous modélisons celle-ci empiriquement comme ayant un comportement d'exponentielle décroissante. En complément, nous intégrons également la technique du Range Split-Spectrum au logiciel de traitement intéférométrique CIS, afin de corriger les effets ionosphériques dans les interférogrammes à basse fréquence. Enfin, nous discutons les options qui permettraient de combiner l'interférométrie Split-Band et le MSBAS.

Acknowledgements

After having written almost 200 pages, inspiration deserted me before I could find some poetic sentence to express that a thesis work is a long journey, but fortunately not a lonely one. I would like to express my gratitude to the people who contributed to make this work a success.

First, I would like to express my sincere gratitude to my supervisor, Dr. Christian Barbier. For its time and guidance, but also for sharing its incredible knowledge of physics and its endless passion for music, I would like to thank him. I hope this experience was as successful for him as it was for me.

I am also grateful to Prof. Ramon Hanssen, Prof. Serge Habraken, Prof. Jérôme Loicq, Dr. Alberto Refice, Dr. Nicolas d'Oreye and Dr. Dominique Derauw, who kindly accepted to be part of my jury. I wish them a pleasant reading of this dissertation.

I would also like to thank all the members of the RESIST consortium. Beyond the pleasure of working with them, I will also remember the games of cards and the informal evenings we spent during some conferences.

I owe a special thank to Dominique and Nicolas. I am grateful for your help, your time, your advice and your proofreading, often given with a touch of humour. It was truly a pleasure to work with you.

For the good times, for the bad times, for all the giggles and the drinks, it want to warmly thank the members of the CSL signal processing laboratory. Some left and some have been there for a shorter time than others, but you are all part of the beautiful memories that I will keep of these four years. I add a special mention to my careful proofreaders, Katerina, Quentin and Denis.

Because they always supported me (despite not always understanding the purpose of my work), I owe a thank to my family. I would also like to thank my friends for keeping me sane, by means of food, ski holidays, friday night training and other parties.

Most of all, I would like to thank Antoine. You always believed in me, even when I suffered from the *fraud* syndrom. You had more faith in me than I ever did myself, and this means the world to me. Let me just tell you that *you have always been my inspiration.*

I would eventually like to thank the Belgian Science Policy for funding this thesis research in the scope of the STEREO III program (contract SR/00/305). Many thanks as well to Hans van der Marel and Ramon Hanssen from TU Delft for sharing information about their experiment in Wassenaar, and to the team of the Earth and Planetary Sciences Department of Hokkaido University for sharing ALOS-2 data.

Abbreviations

BELSPO	*Belgian Science Policy*
BIRA-IASB	*Belgian Institute for Space Aeronomy*
CDR	*Correlated-to-Decorrelated Ratio*
CIS	*CSL InSAR Suite*
CR	*Corner Reflector*
CSL	*Centre Spatial de Liège*
DEM	*Digital Elevation Model*
DInSAR	*Differential Synthetic Aperture Radar Interferometry*
DRC	*Democratic Republic of Congo*
DGPS	*Differential Global Positioning System*
DLR	*Deutsches zentrum für Luft- und Raumfhart (German Space Agency)*
EAR	*East African Rift*
ECGS	*European Centre for Geodynamics and Seismology*
ECR	*Electronic Corner Reflector*
FFT	*Fast Fourier Transform*
FNR	*Fond National de la Recherche (National Fund for Research)*
GNSS	*Global Navigation Satellite System*
GPS	*Global Positioning System*
InSAR	*Synthetic Aperture Radar Interferometry*
IW	*Interferometric Wide*
LOS	*Line-of-sight*
MCA	*Multichromatic Analysis*
MSBAS	*Multidimensional Small Baseline Subset*
NMNH	*Natural Museum of Natural History*

PS	*Permanent/Persistent Scatterer*
$\mathbf{PS_f}$	*Pixel Stable in the frequency domain (Spectrally stable pixel)*
PSI	*Permanent Scatterers Interferometry*
RCS	*Radar Cross Section*
RESIST	*REmote Sensing and In Situ detection and Tracking of geohazards*
RMCA	*Royal Museum for Central Africa*
SAR	*Synthetic Aperture Radar*
SBAS	*Small BAseline Subset*
SBInSAR	*Split-Band Interferometry*
SCR	*Signal-to-Clutter Ratio*
SLC	*Single Look Complex*
SNAPHU	*Statistical-cost, Network-flow Algorithm for Phase Unwrapping*
SNR	*Signal-to-Noise Ratio*
SRTM	*Shuttle Radar Topography Mission*
StaMPS	*Stanford Method for Persistent Scatterers*
SVD	*Singular Value Decomposition*
TEC	*Total Electron Content*
TECU	*Total Electron Content Unit*
VVP	*Virunga Volcanic Province*

Contents

Context

This thesis is part of the *REmote Sensing and In Situ detection and Tracking of geohazards* (RESIST) project. Funded by the Belgian Science Policy (BELSPO) in the framework of the STEREO III program and the Luxembourg National Research Fund (FNR), RESIST is dedicated to improving the understanding of the mechanisms driving volcanic activity and landslides in the Kivu Region. This project is an international collaboration involving partners experts in various research fields: the Royal Museum for Central Africa (RMCA, Belgium), the National Museum of Natural History/European Center for Geodynamics and Seismology (NMNH/ECGS, Luxembourg), Centre Spatial de Liège (CSL, Belgium), the Belgian Institute for Space Aeronomy (BIRA-IASB, Belgium), and NASA (USA). It also involves local partners, like the Goma Volcano Observatory and the Université Officielle de Bukavu.

The region of interest is centered on lake *Kivu*, which is located at the border between Democratic Republic of Congo (DRC), Rwanda, Burundi and Uganda (see map in Figure 1). On the north shore of the lake, we find the city of *Goma* and the *Virunga Volcanic Province* (VVP). This highly vegetated region owes its name to the presence of numerous volcanic edifices. The RESIST project is particularly interested in the study of the active *Nyamuragira* and *Nyiragongo* volcanoes, located north of Goma. These volcanoes have been the scene of spectacular events in the past, causing casualties and destruction in the region.

The Nyamuragira, or *Nyamulagira*, is a shield volcano culminating at 3058 m. Its caldera extends on a diameter of about 2 km and its intense activity has created more than 100 adventive cones. Since the 19th century, 42 eruptions have been recorded for this volcano, with an increasing frequency during the past 30 years. Its eruptions have created lava flows of several tens of kilometers. A map of the lava field is provided in Figure 2. The most recent eruptions occurred in 2000, 2001, 2002, 2004, 2006, 2010 and 2011-2012 (not shown on the map).

On the other hand, the Nyiragongo is a stratovolcano reaching 3470 m of altitude. Its 1.3 km wide main crater hosts a permanent lava lake since 2008, whose level varied in the past years depending on the activity of the volcano. The crater is characterized by platforms located on its inner flanks, corresponding to lava lake level before the last eruptions, that occurred in 1977 and 2002. These eruptions have created long lava flows starting from eruptive fissures on the flanks of the volcano (see Figure 2). Some of these flows reached inhabited areas, causing casualties and destruction of urban structures.

Even though volcanism constitutes an actual risk, this is not the only hazard threatening the area. Landslides are also common in this tropical region of dissected landscapes and heavy rainfalls, and the whole area around the lake is prone to ground movements. Landslides can occur in remote and unpopulated regions, but also in urban areas like the densely populated city of *Bukavu*, located on the south shore of the lake. In particular, a large landslide measuring approximately 1.5 km^2 is affecting the neighbourhood of *Funu*, where thousands of people are settled (see Figure 3). The human activity contributes to the slow motion of this landslide and exposes the inhabitants to probable damage.

In addition to volcanism and landslides, the region is also characterized by tectonic and seis-

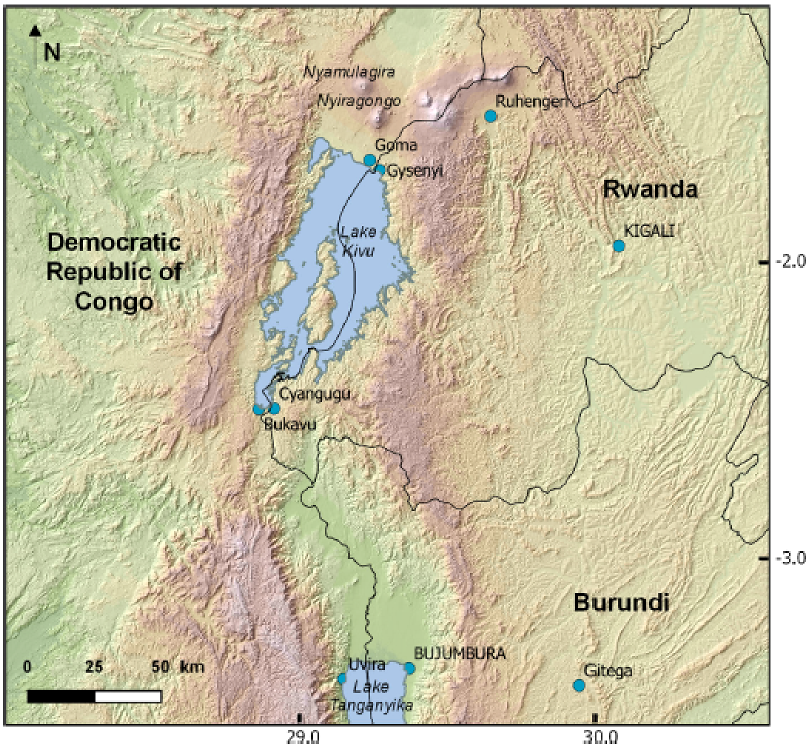

Figure 1: Map of the Kivu Region, from Reference [1]. Axes units correspond to the latitude and longitude coordinates, in decimal degrees.

mic activity, with the presence of geological faults caused by earthquakes. The combination of seismic, volcanic and landslides hazards with the dense population of the area makes it prone to natural disasters, leading to important material and physical damage, and sometimes fatalities. The vulnerability of the area brings out the importance of understanding the geophysical processes that are at work in the region.

In this context, RESIST aims at improving the understanding the physical processes underlying the volcanic activity and the activation of landslides in the Kivu region. For this purpose, it proposes to combine ground-based measurements and remote sensing techniques, and it investigates various parameters. Regarding the volcanoes, the investigated parameters are the ground deformations, the seismicity and the SO_2 gas flux, while for the landslides, the parameters of interest are the ground deformations, the rainfall levels, the spatio-temporal distribution of landslides throughout the region and their types. For the needs of the project, ground-based measurements capabilities have been improved by installing seismic stations and a dense GNSS network (KivuGNet), and by carrying out measurements campaigns with a SO_2 camera on the volcanoes, as well as DGPS campaigns over the Bukavu city. These ground-based measurements have been complemented by satellite data from TRMM, Sentinel 5-P and various spaceborne *Synthetic Aperture Radar* (SAR) sensors, thus achieving an unprecedented data set over this region.

In the scope of RESIST, this thesis was dedicated to the specific topics of ground deformation measurements with *Synthetic Aperture Radar Interferometry* (InSAR), the associated multitemporal approaches and the way to improve these deformation measurements. Because the spatio-temporal distribution of ground deformations is a relevant element to the study of volcanic activity and landslides dynamics, the quality of these measurements is thus of prime importance to correctly model the underlying processes. Besides, a consequent amount of SAR acquisitions

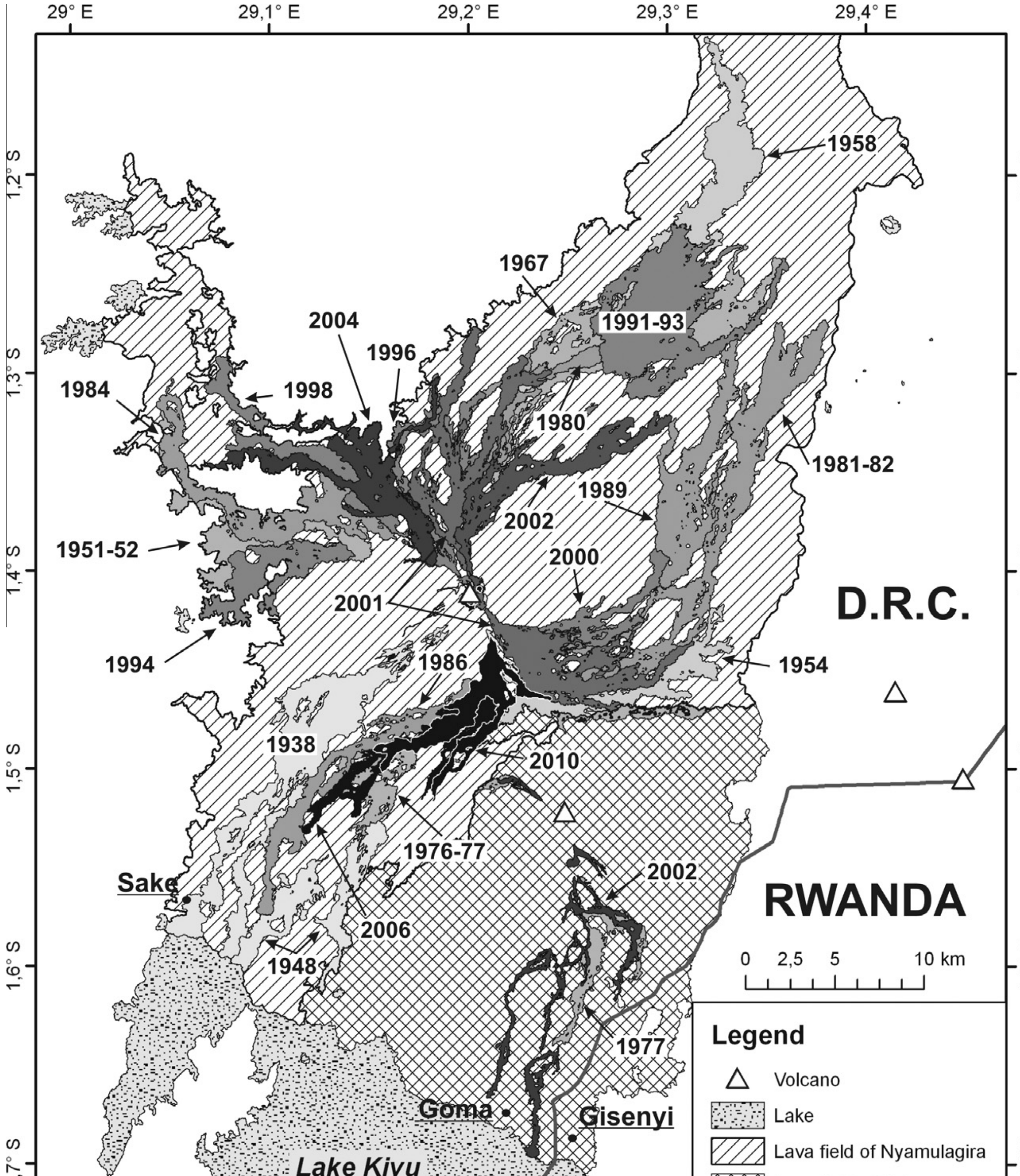

Figure 2: Map of the Nyamuragira lava flows (1938-2010), from Reference [2] with permission. Darker flows are the most recent ones. Nyiragongo lava field is also shown, with its two eruptions that occured in 1977 and 2002.

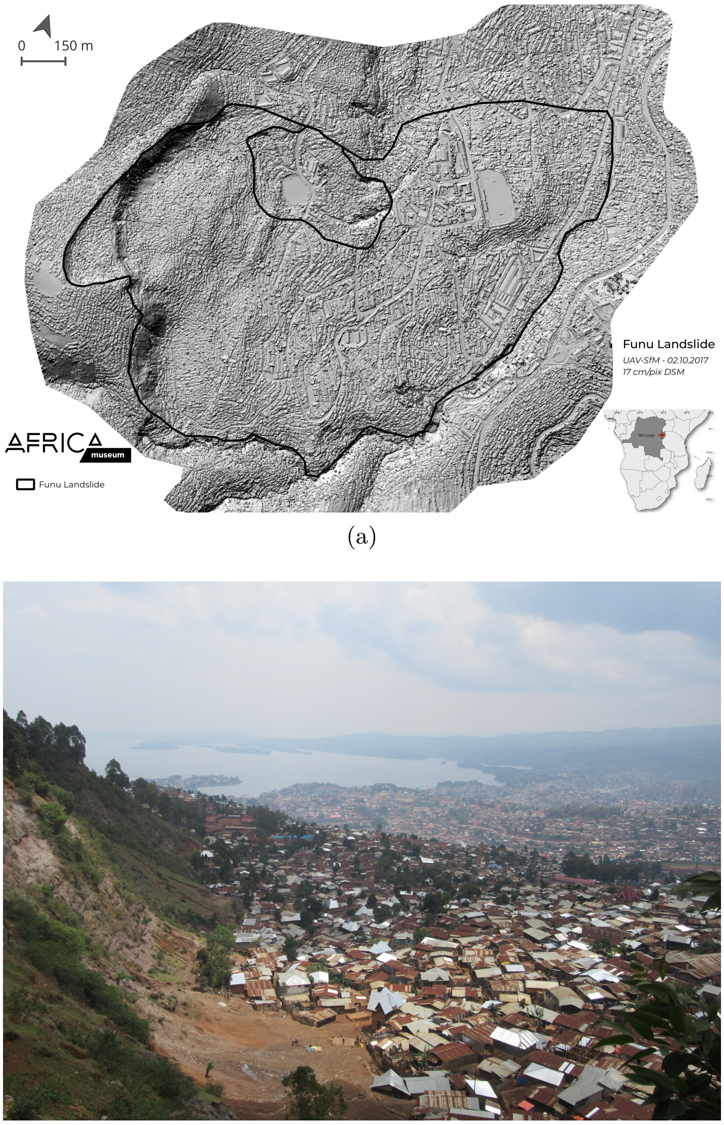

(a)

(b)

Figure 3: Funu landslide. (a) Digital elevation model of the Funu landslide. The black line indicates the extent of the landslide. (b) Picture of the scarp of Funu landslide. Images are courtesy of the Royal Museum for Central Africa.

has been collected by the RESIST consortium over the years. Multitemporal approaches such as the *Small Baseline Subset* (SBAS) and *Multidimensional Small Baseline Subset* (MSBAS) allow to exploit this huge amount of data in order to reconstruct the history of deformations over the region. Correlated with time series of other parameters like seismicity, the history of deformations should enable detection of pre-eruptive signals, characterizing the volcanoes and the landslides, inferring transitions in volcanic activity behaviour and monitoring specific areas known for their vulnerability.

In addition to the temporal aspects of the deformation measurements, this thesis also focuses on the spectral diversity of SAR acquisitions in order to add a new channel of information to the interferometric measurements. Let us note that this work is not particularly interested in the interpretation of the geophysical processes as it constitutes the expertise of other partners of the RESIST project, but rather in the processing aspects and the technical developments.

Introduction

Kivu is a region prone to geohazards such as volcanism, seismicity or landslides. As those are threats to the local population, the need for a regular monitoring and an improved understanding of the underlying geophysical mechanisms has become essential. However, modelling these processes requires a precise knowledge on where and when they induce deformations of the Earth's surface, as well as the magnitude of these deformations. *Synthetic Aperture Radar Interferometry* (InSAR) has the ability to estimate such displacements of the ground. Indeed, by using the phase difference between two SAR images, interferometry can map the *topography* of a region [3–5] or measure *displacements* of the surface [6, 7]. The use of SAR interferometry offers many advantages, such as all weather imaging capabilities, day and night acquisitions, and a global coverage of the observed area. Thanks to these specific attributes, it is possible for InSAR to overcome the difficulties inherent to the study of the Kivu region, such as the almost permanent cloud cover that limits the use of optical images, the lack of information in remote and hardly accessible areas, or the regular maintenance needed for electronic devices such as GPS, that can be struck by the frequent lightning.

Despite its a priori benefit for estimating ground displacements, there also exist factors limiting the use of InSAR over our region of interest. For instance, the area is densely covered by vegetation, where the phase information is not reliable. Besides, strong variations of the atmosphere water content can occur in this tropical region, and this causes radar signals to lose coherence over time. Furthermore, the steep topography induces geometric distortions in the radar images. Because of these constraints, the phase cannot be measured continuously all over the region: for instance, in the Virunga Volcanic Province, coherence can only be maintained over the lava flows. As the lava fields of Nyiragongo and Nyamuragira volcanoes are separated by vegetation, the phase is reconstructed independently for both fields. Likewise, the phase inside the Nyiragongo crater cannot be connected to the phase over the rim because of the sharp walls of the crater, which create a spatial discontinuity. Unfortunately, due to phase unwrapping, conventional SAR interferometry only provides relative measurements, making impossible to compare the phases of disconnected regions. Indeed, it cannot calculate the absolute interferometric phase needed to circumvent the issue of disconnected measurements. More advanced techniques, like *Split-Band Interferometry* (SBInSAR) must be used to obtained the absolute phase we are looking for [8,9].

The last generations of SAR sensors (TerraSAR-X, Cosmo-SkyMed, Radarsat-2) have benefited from a radical increase of their range bandwidth compared to their predecessors, giving access to a new information channel: the *spectral diversity.* Indeed, by splitting the range spectrum of a SAR image into subbands, it is possible to generate several images of a single scene at coarser resolution and different frequencies. Starting from the spectral decomposition of an interferometric couple, Split-Band Interferometry, also known as *Multichromatic analysis* (MCA), performs interferometry on the subbands of the master and slave images, and yields a frequency-varying stack of interferograms. For *spectrally stable targets*, also called *frequency-stable pixels* or *frequency-persistent scatterers* ($\mathrm{PS_f}$), the phase varies linearly with the frequency through the stack, and the slope of the linear regression is proportional to the absolute phase. Consequently, the absolute interferometric phase can be calculated for targets with a stable spectral behaviour. In practice, the use of SBInSAR has turned out to be challenging: the adequate targets must be properly detected, their presence must be secured in the studied area and the pointwise phase is not necessarily known at the expected location. Despite these difficulties, there exists a true potential for Split-Band Interferometry to enhance ground deformation estimates.

As another limitation, classical SAR interferometry only measures the deformation along the sensor line-of-sight between two given dates, while the temporal dimension of the ground deformations is a crucial aspect of the Earth surface monitoring and the displacements history is essential for geophysical modelling. Dealing with the temporal dimension of InSAR measurements has been the focus of many studies in the past years and, today, a number of multi-temporal approaches based on SAR interferometry are available. Let us mention the Persistent Scatterers Interferometry (PSI), the Small Baseline Subset (SBAS), the Stanford Method for Persistent scatterers (StaMPS), or the Squee-SAR Interferometry [10–13]. In particular, the *Multidimensional Small Baseline Subset* (MSBAS) reconstructs time series of two-dimensional displacements, along the east-west and vertical directions, by integration of SAR data from different satellites acquired with various viewing geometries [14]. Because it is dedicated to the analysis of distributed targets, MSBAS is particularly well suited to poorly urbanized areas such as Kivu.

On the one hand, Split-Band Interferometry takes advantage of the spectral channel of SAR data to recover an estimate of the absolute phase, while, on the other hand, MSBAS focuses on the temporal dimension of InSAR measurements and computes the history of ground deformations. Therefore, both methods have potential to solve the problems encountered when applying SAR interferometry over the Kivu region. The purpose of this work is to study Split-Band Interferometry and MSBAS, analyze the efficiency of these methods and determine how they can contribute to improve InSAR measurements. We also aim at developing operational tools for both methods, destined to be used by the RESIST consortium for monitoring the Kivu region. Furthermore, we eventually look for combining the information coming from SBInSAR with the measurements performed by MSBAS, if possible.

In Chapter 1, we introduce basic concepts of synthetic aperture radar imaging and synthetic aperture radar interferometry. We explain the formation of a SAR image, how it is possible to measure topography and ground deformations by combining the phase information of two SAR images, and the conditions for the feasibility of an interferometric measurement.

In Chapter 2, we consider the Split-Band Interferometry and its potential to retrieve the absolute interferometric phase. We first investigate its feasibility from the theoretical point of view and establish the limiting factors of the processing. We then investigate the problem of phase ambiguities and propose a method using SBInSAR as an assistance to phase unwrapping for correcting phase ambiguities. We determine the best criterion for the detection of spectrally stable pixels and we also check for the optimum processing parameters in practice. We attempt to characterize the temporal behaviour of spectrally stable targets and their physical nature. At last, we test the method proposed for correcting phase ambiguities on several SAR satellites and modes.

In Chapter 3, we consider the problem of the Multidimensional Small Baseline Subset and its implementation. We present the InSAR mass processing chain developed in collaboration with the ECGS for the MSBAS preprocessing. Then, we propose to improve this preprocessing by optimizing the spatial coverage with interpolation and masking, and we perform an MSBAS study on the Bukavu city. In the last part of the chapter, we consider the temporal decorrelation and we model it empirically.

In Chapter 4, we study artificial reflectors and their behaviour regarding Split-Band Interferometry. We consider their potential for being used as SBInSAR reference points and investigate the conditions under which this assumption is valid.

In Chapter 5, we present the Range Split-Spectrum method for correcting the ionospheric effects in SAR interferograms. As it is an extra application of Split-Band Interferometry, this method is developed, even though ionosphere has little influence over the Kivu region. We present our advances regarding the development of this method, as well as our first results.

In Chapter 6, the perspectives of this work are discussed. Approaches for combining SBInSAR and MSBAS are also suggested.

Finally, in the end of the manuscript, summary and conclusions of the work are presented. Let us note that the reader is provided with a list of symbols at the end of each chapter.

Chapter 1

Basic Notions of SAR Interferometry

Because of its ability to observe the Earth's surface day and night, and under any weather conditions, synthetic aperture radar imaging has become a unique instrument for Earth observation. Another benefit of SAR images is that they can achieve a high resolution, whatever the sensor altitude or wavelength. SAR images contain information about the backscattering properties of the Earth surface and they are intrinsically different from optical images in their geometry and in the properties they map. They can be used for a number of applications such as flood detection [15], agriculture monitoring [16] or soil moisture retrieval [17].

On the basis of SAR technology, several advanced post-processing techniques have been developed for assessing some geophysical parameters. Among them, the well known synthetic aperture radar interferometry has become increasingly popular in the last decades, as it allows to map topography and, most importantly, to measure ground deformations with an precision better than a centimeter. Precision is not the only reason for the popularity of SAR interferometry: with InSAR, ground deformations are mapped as an image, thus providing an extended spatial information. Compared to GPS pointwise measurements, the spatial coverage of InSAR represents an added-value for geophysical modelling. SAR interferometry has been successfully used to study many geophysical phenomena, such as earthquakes [18], volcanic eruptions [19], ice motion [20] or land subsidence [21].

This chapter is a brief introduction to SAR imaging and SAR interferometry. It is meant to provide the uninitiated reader with the concepts necessary to understand this work. Theoretical considerations are provided without extensive descriptions and developments, as we only mean to introduce the basics of the theory. The content of this chapter is based on References [22, 23] for SAR imaging and Reference [24] for SAR interferometry, that can be consulted by the reader interested in further explanations.

In the first section, we introduce the principle of synthetic aperture radar imaging. We describe the method of acquisition and we explain the formation of an image. We also highlight how a satisfactory resolution is obtained with SAR, in both range and azimuth dimensions. In the second section, we present the rationale of synthetic aperture radar interferometry. We first focus on its use for topographic measurements, and then explain its interest for ground deformations. We introduce the concept of coherence, characterizing the feasibility of an interferometric measurement. We describe the main contributions that can lead to a coherence loss. Finally, we shortly describe a conventional interferometric processing.

1.1 Synthetic Aperture Radar

Radio Detection and Ranging (radar) systems use electromagnetic pulses to determine the distance of the sensor to an object. By emitting an electromagnetic pulse and receiving its reflected

Band	**Frequency [GHz]**	**Wavelength [cm]**	**Past or current missions**
P	0.230 - 1	130 - 30	Biomass, UAVSAR-P
L	1 - 2	30 - 15	JERS-1, ALOS-1/2, UAVSAR-L
S	2 - 4	15 - 7.5	Magellan, Cosmos-1870, ALMAZ-1
C	4 - 8	7.5 - 3.75	ERS-1/2, Envisat, Radarsat-1/2, Sentinel-1
X	8 - 12.5	3.75 - 2.40	TerraSAR-X, TanDEM-X, Cosmo-SkyMed
Ka	26.5 - 40	1.13 - 0.75	UAVSAR-Ka

Table 1.1: Frequency bands of radar systems, from Reference [25]. Examples of SAR missions are also provided for each frequency band.

echo, a radar can measure the distance to an object based on the two-way travel time of the pulse. The intensity of the backscattered signal can also be used to infer information about the size, the material and the roughness of the object.

Synthetic aperture radar systems belong to the class of *imaging* radars. Imaging sensors are used to observe the Earth, its surface and its atmosphere, and they contribute greatly to improve our knowledge of geophysical processes. Imaging sensors can either be *passive* or *active*: passive sensors use the radiation naturally emitted by the Sun or the Earth surface, while active sensors get free of this natural source of radiation by emitting their own radiation and sensing the backscattered signal. SAR systems are active sensors and are thus able to acquire images during day and night. Compared to optical imaging sensors, they also present all-weather acquisition capabilities because they operate in the radio and microwave regions of the electromagnetic spectrum, for which the atmosphere is transparent. These wavelengths can thus penetrate through clouds and rain before being reflected on the Earth surface. The typical frequency bands of SAR operations are listed in Table 1.1.

Synthetic aperture radars are usually *airborne* or *spaceborne* systems. In particular, they are *side-looking radars*: such systems have their antenna pointing laterally with respect to the flight direction of their carrying platform. This sideways looking geometry enables an unambiguous knowledge of the direction of the backscattered echo and therefore an imaging capability. However, for *real aperture radars* using side looking geometries, the along-track azimuth resolution is proportional to the antenna size, meaning that obly poor resolution can be obtained with antennas of reasonable size. The use of the *synthetic aperture* principle, which consists in synthesizing a long antenna by taking advantage of the motion of the antenna along the flight path, improves the resolution, as explained in the following. Compared to real aperture radar, SAR systems present the advantage of a high achievable resolution without using physically long and unpractical antennas. Moreover, they are coherent radars, meaning that they provide a phase information in addition to the backscatter intensity and the two-way travel time.

1.1.1 Imaging geometry

Let us consider a SAR system mounted on a platform, e.g. a spacecraft moving along the azimuth direction, as illustrated in Figure 1.1. The sensor is equipped with an antenna directed sideways with respect to the spacecraft orbit and pointing towards the ground. As it moves along its flight path, the SAR satellite emits radar pulses of duration τ, at a rate called *pulse repetition frequency*. The dimensions of the antenna determine the size of the footprint of the radar echo on the ground and therefore the imaged area, and the scene is scanned as the antenna sweeps across the ground due to the satellite motion.

The natural coordinates matching the acquisition geometry of a SAR image are the *slant range*

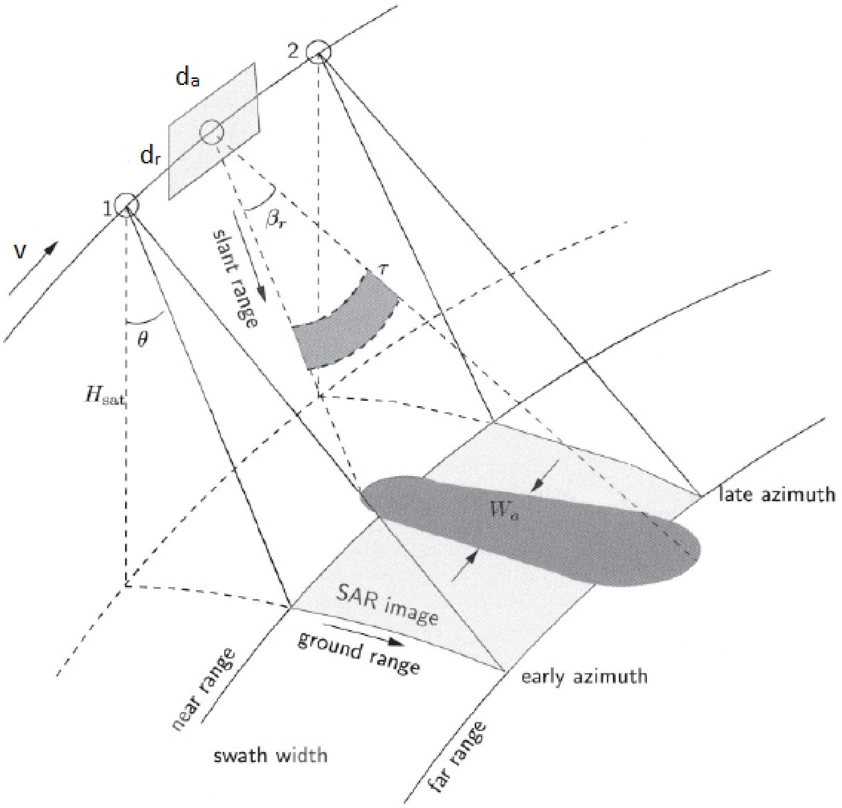

Figure 1.1: Imaging geometry of a SAR acquisition, modified from Reference [24]. As the SAR sensor moves along the azimuth direction at a velocity v, the antenna of dimensions $d_r \times d_a$ emits pulses of duration τ in the slant range direction. The illuminated swath is parallel to the flight direction and the area imaged by a single pulse is indicated by the shaded area. The area imaged by the SAR acquisition is defined by the early and late azimuth coordinates, determined by the acquisition timing for which the satellite moves from orbital position 1 to orbital position 2. In the range direction, the borders of the SAR image are given by the near range and the far range, determined by the antenna beamwidth.

and *azimuth* coordinates. The azimuth coordinate corresponds to the distance travelled by the satellite along its flight path. The slant range coordinate, often simply referred to as the *range*, is the distance between the SAR sensor and a target on the ground. The slant range distance can be projected on the ground in order to obtain the *ground range* coordinate, if the local incidence angle is known. The SAR image is built up from the azimuth and range coordinates, as well as the strength of the backscattered echo.

The azimuth and range distances are inferred from time delays: on the one hand, the azimuth position corresponding to a given radar echo is defined by its emission time, which is characterized by the pulse repetition frequency; on the other hand, the range is calculated from the time delay spent between the transmitted and the received signals. Both scanning mechanisms have different time scales, and the azimuth and range coordinates can therefore be considered independently for SAR processing.

Geometric distortions

Due to the slant viewing geometry and the use of the range distance, terrain elevation is mapped with geometrical distortions in SAR images. As shown in Figure 1.2, these distortions can either be the effects of *foreshortening*, *layover* or *shadow*. The foreshortening corresponds to a dilation

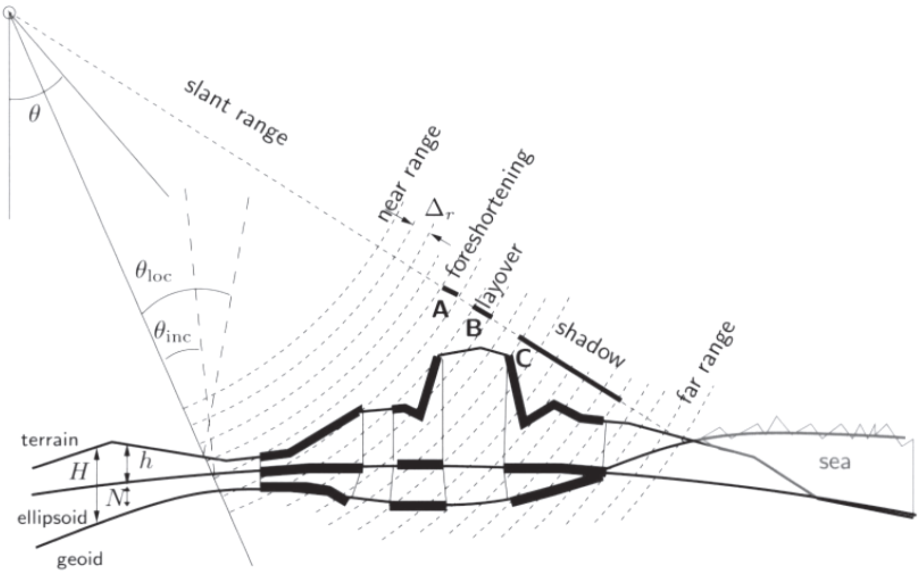

Figure 1.2: Geometric distortions in side-looking radar images, from Reference [24]. The concentric dotted lines indicate the near and the far ranges of the emitted radar pulses. The spacing Δ_r between these concentric lines represents the size of a resolution cell in the range direction. **A** indicates the foreshortening effect: a long strip of land is imaged into a single resolution cell, reducing its aspect in the image. **B** indicates the layover effect: higher topography is imaged at a smaller range, leading to an upside-down aspect of the slope in the image. **C** indicates the shadow effect: the area is masked from the radar signal and appears as a dark area with no backscattered intensity in the image.

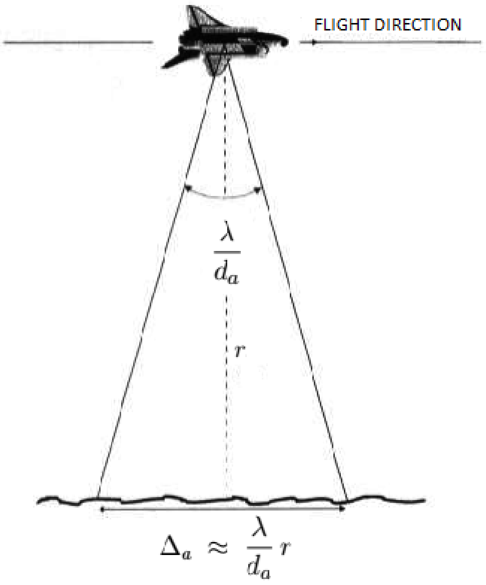

Figure 1.3: Azimuth resolution of real aperture radar, modified from Reference [23].

or a compression of the resolution cell with respect to the distance that would be mapped in the absence of topography. Layover happens when the topography is so steep that the summit of a slope is imaged before its foot. In this case, the imaged geometry is inverted with respect to the true topography. Shadow occurs when the topography hides a part of the ground from the radar signal, preventing the signal from being backscattered at this place. The area in the shadow appears dark in the image.

Let us note that the imaged distortions are strongly dependent on the acquisition geometry, i.e. the looking angle and the orientation of the satellite with respect to the scene. It is in particular impacted by the position of the satellite along its orbit: given that the antenna has a fixed orientation with respect to the sensor velocity, e.g. right-handed, the scene is scanned from a different side if the satellite travels on the *ascending* (south to north) or the *descending* (north to south) part of its orbit. A scene observed from an ascending orbit presents geometric distortions different from those obtained when the same scene is observed from a descending orbit, especially in the presence of a steep topography.

1.1.2 Range resolution

The *range resolution* of a radar system is defined as the shortest range distance between two objects that can be distinguished from each other by this system. Let us consider a radar system emitting electromagnetic pulses of duration τ at frequency ν_0. The emitted pulses are described by the waveform

$$S(t) \;=\; g(t)\, e^{i2\pi\nu_0 t} \quad \text{for} \quad -\frac{\tau}{2} < t < \frac{\tau}{2}, \tag{1.1}$$

where $g(t)$ is the amplitude factor. For such a radar system, the range resolution Δ_r depends on the pulse length:

$$\Delta_r \;=\; \frac{c\tau}{2}. \tag{1.2}$$

Here c is the speed of light and the factor 2 accounts for the two-way travel of the pulse. Based on this equation, one way to improve the range resolution is a priori to reduce the pulse length. Doing so, a resolution of a few meters can be reached for pulse durations of about 10^{-8} s. However, this also means that less energy is emitted in the pulse, leading to a weak signal-to-noise ratio of the radar image and poor detection capabilities. We are thus facing a conflict between resolution and detection when using simple radar pulses.

This issue of short pulses can be overcome by the use of modulated pulses of long duration. A linearly modulated *chirp* pulse of duration τ is described by the waveform

$$S(t) \;=\; g(t)\, e^{i2\pi\left(\nu_0 t + \beta t^2\right)} \quad \text{for} \quad -\frac{\tau}{2} < t < \frac{\tau}{2}, \tag{1.3}$$

where β is the rate of frequency change. Consequently, the signal is centered on the carrier frequency ν_0 and has a certain *bandwidth*, given by $B = \beta\tau$, within which the frequency varies linearly. By means of a chirp compression, also known as matched filtering, the resolution improves to

$$\Delta_r \;=\; \frac{c}{2B}. \tag{1.4}$$

Actually, the chirp compression consists in a correlation of the received signal by a replica of the transmitted chirp, and it generates the spread function of the image target. This spread function is a cardinal sine and the range resolution given by Equation (1.4) corresponds to the distance between the -3 dB points of this cardinal sine response [23].

Let us consider the example of Cosmo-SkyMed acquisitions in HIMAGE Stripmap mode. For such acquisitions, $\tau = 35$ µs. In the case of a simple pulse, it would lead to a range resolution of 5.25 km, or approximately 9 km in ground range. However, using a frequency modulated chirp with 100 MHz of bandwidth, the range resolution drastically improves to reach 1.5 m.

1.1.3 Azimuth resolution

For real aperture radar systems, two targets at a given range can be resolved along the azimuth direction if they are not within the antenna footprint at same time. The *azimuth resolution* is thus defined as the extent of the antenna footprint on the ground in the azimuth direction and is directly related to the size of the antenna, the wavelength of the signal and the altitude of the spacecraft. Let us consider an antenna of range-azimuth dimensions $d_r \times d_a$. If the signal emitted by the antenna has a wavelength λ, then its beamwidth along the azimuth direction is given by $\frac{\lambda}{d_a}$. As illustrated in Figure 1.3, for a side-looking radar at a range distance r from the observed area, the extent of the antenna footprint, i.e. the azimuth resolution, is given by the approximate relation

$$\Delta_a \approx \frac{\lambda}{d_a} r. \tag{1.5}$$

Let us now consider the Cosmo-SkyMed example for the azimuth resolution: we have $d_a = 5.7$ m and $\lambda = 3.1$ cm. If the satellite is at a typical range distance of 700 km from the ground, then the azimuth resolution is approximately 3.8 km, and this coarse resolution is unacceptable for most applications. Given Equation (1.5), the azimuth resolution can be improved by either changing the wavelength, increasing the size of the antenna, or changing the altitude and thus the range distance of the sensor. Nevertheless, none of these solutions can be used in practice: indeed, the wavelength is an intrinsic parameter of the system, the altitude is constrained by the satellite orbit and increasing the size of the antenna is not realistic either, as it would require an unpractically long antenna in order to achieve a satisfactory resolution.

However, a very long antenna can be simulated by moving a physically small antenna along a given path: this is the synthetic aperture principle. The movement of the spacecraft with respect to a given target on the ground causes the target to be included within the azimuth beamwidth for a number of consecutive backscattered echoes. The synthesis is carried out by coherently combining the received echoes. Considering the simplified approach presented in Reference [23], the azimuth resolution achieved by applying the aperture synthesis is approximately given by

$$\Delta_a = \frac{d_a}{2}. \tag{1.6}$$

Applying the synthetic aperture principle, the azimuth resolution becomes independent of the altitude and the wavelength. It only depends on the antenna size: the smaller the antenna, the better the resolution. Referring once again to the Cosmo-SkyMed example, the achievable resolution improves to about $d_a = 2.85$ m. However, the aperture synthesis requires to apply numerical processing on the image such as range migration and azimuth focusing. Therefore, the resolution improvement is obtained at the cost of an expensive computing effort: each pixel of the image must be focused numerically and this represents hundreds of mathematical operations. Though not presented here, the developments relative to aperture synthesis, range migration and azimuth focusing can be found in Reference [22].

1.2 Synthetic Aperture Radar Interferometry

Despite the knowledge of the range and azimuth distances of each resolution cell in a SAR image, an ambiguity remains on the corresponding position on the ground: indeed, for a given

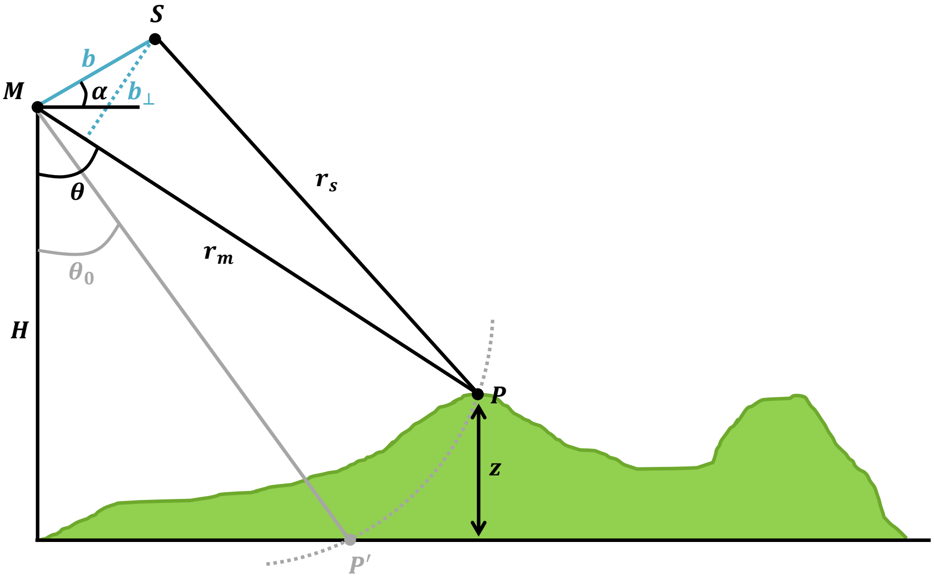

Figure 1.4: Interferometric SAR configuration. All possible positions of a point P with a range coordinate r_m in the master image are given by an arc of circle (dotted grey line). In SAR interferometry, the combination of two images acquired with slightly different viewing angles enables to retrieve the position of this point and its height z. The master image is taken from the orbital position M while the slave image is taken from orbital position S. The distance between the orbital positions is the spatial baseline b. The green surface represents the topographic profile.

azimuth position, two targets with the same range coordinate cannot be distinguished from each other in a single SAR acquisition, because their heights are not known (see Figure 1.4). This ambiguity on the position can be solved by looking at the target from two slightly different points of view: the difference of path travelled by the signal for each geometry corresponds to only one possible position of the target. This difference of range distances could be inferred from the two-way travel time. However, this measurement has a precision limited by the range resolution and is not accurate enough to clear the ambiguity on the target position. Fortunately, the phase information of SAR images is related to the geometric path travelled by the SAR signal and it provides a useful information for determining the difference in the range distances. This determination of path difference based on the phase constitutes the basic problem of SAR interferometry.

Let us consider a first image taken from the orbital position M, which is the reference image called *master* image, and a second image acquired from the orbital position S, referred to as *slave* image. The situation is schematically illustrated in Figure 1.4. These images can be acquired either simultaneously, in which case we perform *single-pass* interferometry, or they can be acquired at different moments, during the revisit of the satellite. In this second case, we talk about *repeat-pass* interferometry and the time delay between the two acquisitions is called the *temporal baseline*. The distance separating the orbital positions M and S is called the *spatial baseline* and is denoted by b. It can be decomposed into its perpendicular and parallel components $b_\perp$ and $b_\parallel$ respectively, the perpendicular and parallel directions being defined with respect to the master line-of-sight. As explained in the following, this decomposition of the baseline is fundamental to characterize the sensitivity of InSAR measurements to the topography.

SAR images are built as regular grids of complex values, meaning that each pixel of the image possesses an amplitude and a phase. A pixel corresponding to a given area on the ground is respectively described in the master and slave images by

$$S_m = |S_m|\, e^{i\psi_m}, \tag{1.7}$$

$$S_s = |S_s|\, e^{i\psi_s}, \tag{1.8}$$

The interferometric term associated to this pixel is calculated as the coherent cross-multiplication of the two signals, expressed as

$$S_m S_s^* = |S_m|\,|S_s|\, e^{i(\psi_m - \psi_s)}, \tag{1.9}$$

where the symbol $*$ denotes the complex conjugation operation. The phases ψ_m and ψ_s of the considered pixel are dependent on two contributions: the first is the optical path travelled by the radar signal, that can be associated to a geometric distance; the second, called *scattering phase*, is linked to the multiple reflections undergone by the signal within the resolution cell. These phases are expressed as

$$\psi_m = -2\,\frac{2\pi}{\lambda}\, r_m + \psi_{\text{scat},m}, \tag{1.10}$$

$$\psi_s = -2\,\frac{2\pi}{\lambda}\, r_s + \psi_{\text{scat},s}, \tag{1.11}$$

where λ is the wavelength of the radar signal, r_m and r_s are the range distances, and $\psi_{\text{scat},m}$, $\psi_{\text{scat},s}$ are the scattering phases of the master and slave images, respectively. The factor 2 accounts for the two-way travel of the signal and is valid for a monostatic pair of images. In the bistatic case, this factor reduces to 1. Assuming that the scene characteristics remain unchanged from one acquisition to the other, the scattering phases can be considered as equal and they cancel each other. The interferometric phase calculated in the interferogram is then given by

$$\Delta\phi = \frac{4\pi}{\lambda}\left(r_s - r_m\right). \tag{1.12}$$

Therefore, under the assumption of unchanged conditions in the observed scene, the phase is only linked to the range difference of the two viewing geometries. Using simple trigonometry, the interferometric phase of the considered pixel can be related to the height z of the corresponding target above a reference surface:

$$\Delta\phi = -\frac{4\pi}{\lambda} b \sin(\theta_0 - \alpha) - \frac{4\pi}{\lambda}\frac{b_\perp}{r_m \sin\theta} z, \tag{1.13}$$

where θ is the look angle of the master line-of-sight, θ_0 is the look angle corresponding to a flat reference surface and α is the tilt angle of the baseline vector with respect to the horizontal plane. Though not presented here, the developments leading to this expression can be found in Reference [26]. Let us analyze the right-hand side of Equation (1.13): the first term is called *flat earth phase*. It corresponds to the phase contribution due to a flat ground surface and can be modelled easily. The second term is the *topographic phase*. It is proportional to the height of the point target through the value of the baseline. As a consequence, if the flat earth contribution is subtracted from the interferometric phase, the height of the point target can be isolated and a map of topography can be reconstructed from this information. SAR interferometry can thus be used for Digital Elevation Model (DEM) generation.

Obviously, the height precision σ_z of topographic measurements is directly dependent on the phase precision σ_ϕ, as expressed by

$$\sigma_z = \frac{\lambda}{4\pi}\frac{r \sin\theta}{b_\perp}\sigma_\phi. \tag{1.14}$$

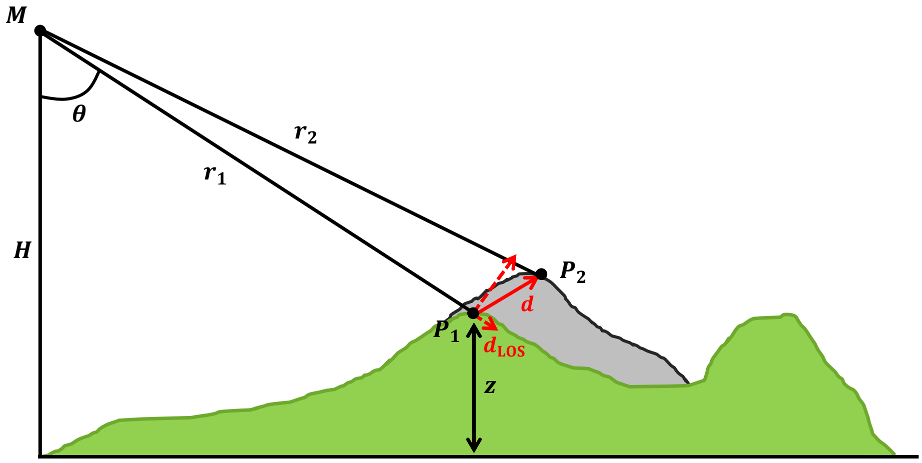

Figure 1.5: Geometry of differential SAR interferometry. The green surface represents the topographic profile in the first acquisitions. P_1 is the position of the considered target in the first acquisition. The grey surface represents the change of topographic profile in the second acquisition. P_2 is the position the considered target in this second acquisition. Differential interferometry measures the displacement vector $\mathbf{d}$ projected onto the line-of-sight direction, i.e. d_{LOS}.

From this equation, we observe that the height accuracy can be improved by increasing the perpendicular baseline. However, as it is explained in Section 1.2.2, an increase of the baseline also corresponds to a coherence loss and limits the feasibility of an interferometric measurement. In practice, the choice of the baseline is a trade-off between the height accuracy and the noise level in the interferogram. Interferometric performance for the height estimates can also be assessed from the *height ambiguity*, which is defined as the change in height accounting for a one-cycle variation of the phase. The height ambiguity $z_{2\pi}$ is expressed by

$$z_{2\pi} = \left| \frac{\lambda r_m \sin\theta}{2b_\perp} \right|. \tag{1.15}$$

Small height ambiguities result in high fringe rates in the wrapped interferogram and therefore an increased sensitivity to the topography.

1.2.1 Differential interferometry

As explained in the previous section, SAR interferometry can be used for topographic measurements and therefore for the generation of DEM. However, it is also especially popular for its ability to map ground displacements. Indeed, we made the assumption in the previous section that the scene remains unchanged from one acquisition to the other. Even though this can be assumed to be valid for single-pass interferometry, this is not necessarily true when dealing with repeat-pass interferometry: when images are not acquired simultaneously, the scene can change between the acquisitions. These changes can modify the optical path and give rise to an additional phase contribution $\Delta\phi_{\mathrm{diff}}$, called *differential phase*. Consequently, Equation (1.13) becomes

$$\Delta\phi = -\frac{4\pi}{\lambda} b \sin(\theta_0 - \alpha) - \frac{4\pi}{\lambda} \frac{b_\perp}{r_m \sin\theta} z + \Delta\phi_{\mathrm{diff}}, \tag{1.16}$$

where the differential phase term accounts for all possible changes in the scene. The analysis of this differential phase is the object of *differential* SAR interferometry.

In particular, variations in the scene can correspond to a displacement of the observed target. If no other change contribution must be taken into account, then the interferometric phase can be expressed as

$$\Delta\phi \;=\; -\frac{4\pi}{\lambda} b \sin(\theta_0 - \alpha) \;-\; \frac{4\pi}{\lambda}\frac{b_\perp}{r_m \sin\theta} z \;+\; \frac{4\pi}{\lambda} d_{\mathrm{LOS}}, \tag{1.17}$$

where d_{LOS} is the displacement of the target projected on the line-of-sight direction and a positive displacement corresponds to a movement away from the satellite (see Figure 1.5). The right-hand side of Equation (1.17) represents the whole phase information contained in the interferometric term. In practice, the flat earth phase and topographic phase must be subtracted from the interferogram in order to obtained a differential interferogram that contains the information relative to ground displacements only. The flat earth phase is easily calculated and the topographic phase is usually simulated from an external DEM of the studied region.

From Equation (1.17), we see that the phase term arising from ground displacements is independent from the baseline and that a one-cycle phase variation corresponds to a displacement of $\lambda/2$. Given the few centimeters wavelength of SAR acquisitions, a precision better than a centimeter can be achieved for ground deformations measured with InSAR. Nevertheless, errors can be introduced by the removal of topographic phase, due to the limited precision of the DEM. In order to estimate the ground deformations, we made here the assumption that the differential phase was entirely generated ground displacements. However, there exist undesirable contributions that can also be the source of a differential phase. For instance, in differential interferometry, the atmosphere and the ionosphere can be affected by a variation of their refractive index, leading to an optical path change for the radar signal and thus creating an unwanted phase contribution.

1.2.2 Feasibility of interferometric measurements

The feasibility of an interferometric measurement is intrinsically linked to the ability of the two signals to interfere with each other. This is estimated by the interferometric *coherence* and it also constitutes a measure of the phase quality. The coherence γ is the normalized cross-correlation of the master signal S_m and the slave signal S_s. It is mathematically defined by

$$\gamma \;=\; \frac{E\left(S_m S_s^*\right)}{\sqrt{E(|S_m|^2)}\,\sqrt{E(|S_s|^2)}}, \tag{1.18}$$

where the operator $E(\,\cdot\,)$ denotes the statistical expectation and the target coordinates have been omitted. The coherence ranges between 0 and 1: when equal to 1, the signals are perfectly correlated and we have a high quality phase measurement; when equal to 0, the signals are completely uncorrelated and the phase information is not reliable.

A loss of coherence, also called *decorrelation*, may originate from a number of mechanisms and the contribution of each mechanism to the global coherence is quantified by a correlation term. The effect of each correlation term being multiplicative, the coherence level is expressed as:

$$\gamma \;=\; \gamma_{\mathrm{s}} \times \gamma_{\mathrm{t}} \times \gamma_{\mathrm{other}}, \tag{1.19}$$

where γ_{s} is the geometrical or spatial correlation, γ_{t} is the temporal correlation and γ_{other} accounts for other contributions, like processing-induced coherence losses, volume scattering or thermal noise. Let us focus on the two major contributions to coherence loss: the geometrical decorrelation and the temporal decorrelation.

Geometrical or spatial decorrelation is induced by the difference in viewing geometry for the two acquisitions. It results from their difference in incidence angle at the earth surface and the correlation term relative to this effect can be modelled as [5, 27]

$$\begin{aligned}\gamma_s &= 1 - \frac{2\Delta_r |b_\perp|}{r\lambda \tan\theta} \\ &= 1 - \frac{c|b_\perp|}{rB\lambda \tan\theta},\end{aligned} \tag{1.20}$$

where $b_\perp$ is the perpendicular baseline, θ is the looking angle, r is the range distance of the target, λ is the wavelength, Δ_r is the range resolution, B is the range bandwidth and c is the speed of light. We see from this equation that, in addition to the dependency on the incidence angle, the spatial decorrelation is also related to the length of the spatial baseline. The coherence reduces as the spatial baseline increases, and for a given value called the *critical baseline*, the coherence becomes null.

On the other hand, temporal decorrelation accounts for the changes occuring in the observed scene between two acquisitions and therefore occurs for repeat-pass interferometry only. These changes can consist in scatterers appearing or disappearing within the resolution cell, in a modification of their positions, or a variation of the electrical properties of the ground. As it is strongly dependent on the observed scene and the acquisition timing, modelling of this effect consists essentially in a case by case study.

1.2.3 Interferometric SAR processing

Although the theory relative to SAR interferometry has been presented hereinabove, the computation of an interferogram is not a straightforward process. We present here a brief overview of interferometric SAR processing and we focus on the specific step of phase unwrapping, as it will be further investigated in this work.

An interferometric processing starts from properly focused SAR images, known as Single-Look Complex (SLC) images. These are focused SAR images provided in slant range-azimuth coordinates with full resolution. The master and slave SLC must be acquired over the same area and from similar orbits. However, since they are not acquired in the exact same geometry, the master and slave images cannot not directly be superimposed on each other: due to the existing path difference for a given scatterer in the two images, its location in one image is different from its location in the other. The path difference can only be extracted if the two images are correctly *coregistered*. Coregistration consists in determining the proper transformation between the slave and master coordinates, and then in resampling the slave image so as it matches the master geometry.

Once the slave image is resampled onto the master image geometry, the interferometric phase can be computed. The flat earth phase is usually removed at this stage. If dealing with differential interferometry, the topographic phase is also subtracted. In general, the topographic contribution is provided by a DEM. The DEM is mapped in geographical coordinates, and it must be resampled to match the range-azimuth geometry of the master image. The height must be converted into phase measurements before subtracting the topographic phase from the global interferometric phase. At the same time, the coherence image can also be generated. In addition, the phase noise present in the interferogram can be mitigated by applying a phase filtering.

At this stage, we face a major issue in the processing: since the phase values of a complex SAR images are only known within the interval $]-\pi, \pi]$ radians, this is consequently also the case for the interferometric phase of the generated interferogram. The phase is said to be *wrapped*: the interferogram is made of fringes with values between $-\pi$ and π that follow either the topography,

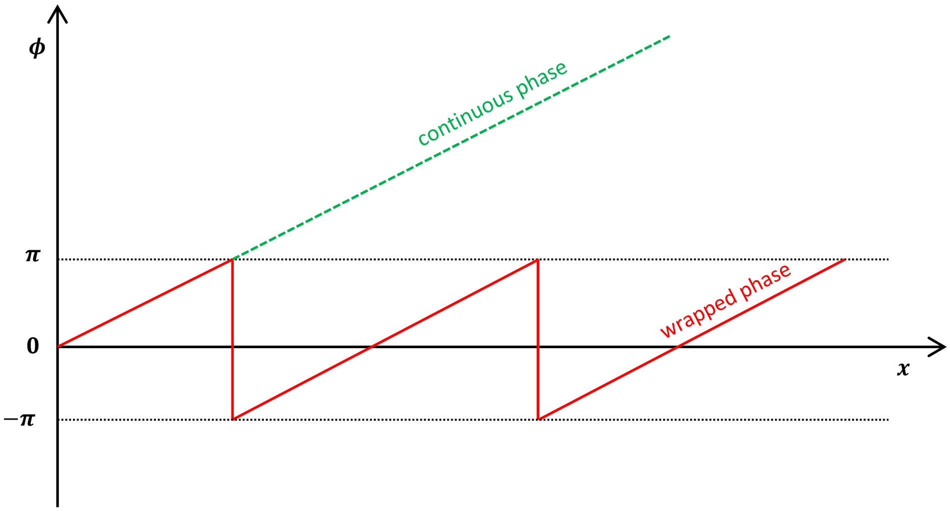

Figure 1.6: Schematic representation of the phase unwrapping problem in one dimension. Phase unwrapping consists in retrieving the continuous phase profile (green) from the wrapped phase (red).

if performing single-pass interferometry, or the ground displacements, if performing differential interferometry. A *phase unwrapping* must be performed in order to retrieve a continuous phase profile. The problem of phase unwrapping is detailed hereafter.

Once the phase is unwrapped, it can be converted into either height measurements or line-of-sight deformations. However, at this stage, height or deformation images are generated in the range-azimuth geometry. This geometry does not allow to geolocate the image points while this in necessary for most applications. Therefore, a final geocoding step can be performed to project the measurements onto a universal cartographic grid.

The phase unwrapping problem

As mentioned earlier, the phase obtained during the interferogram generation is wrapped: only its principal part is known, while the associated number of cycles is missing. Phase unwrapping consists in retrieving this unknown number of cycles, so that a continuous phase can be reconstructed (see Figure 1.6). Indeed, the physical information related to the path difference is contained in the unwrapped phase, not in the wrapped phase.

Given the wrapped phase $\Delta\phi_{\mathrm{w}}$ and the unknown number of cycles n, the unwrapped phase $\Delta\phi_{\mathrm{unw}}$ can be written

$$\Delta\phi_{\mathrm{unw}} = \Delta\phi_{\mathrm{w}} + 2\pi n. \tag{1.21}$$

Despite its simple formulation, phase unwrapping is a complex problem. In order to solve this problem, many methods have been proposed, like path following methods or minimum cost flow algorithms that are reviewed in Reference [28]. Let us focus on the first class of methods.

For path following methods, the unwrapped phase is computed by integrating the wrapped phase along a given path. This path can for instance be defined by looking for residues and connecting them [29]. These methods are based on the assumption that the phase cannot exhibit phase jumps larger than half a cycle along the integration path, in order to avoid aliasing. Therefore, following the integration path, the continuous phase profile is basically retrieved by estimating the phase difference between the considered pixel and the previous one, and keeping the phase value of the pixel unchanged when the phase difference included between $-\pi$ and π; adding 2π to the pixel phase value when the phase difference is lower than $-\pi$; subtracting 2π from the pixel phase value when the phase difference is larger than π.

This method allows to reconstruct a continuous phase profile, as the phase value of a pixel is known with respect to the phase value of its neighbours. However, the true number of cycles cannot usually be determined by the usual phase unwrapping methods. Though this phase is indeed unwrapped, there exists a phase ambiguity and the absolute phase remains unknown. This makes InSAR phase an intrinsically relative measurement.

The phase unwrapping step is one of the most significant sources of error of SAR interferometric processing: in practice, unwrapping large phase gradients is a very sensitive problem as such regions can suffer from aliasing and therefore violate the basic assumptions. Therefore, large deformations or steep topography, as well as layover or shadow areas are prone to phase unwrapping errors.

Furthermore, let us note that path following methods preserve the property of *congruence*, i.e. the unwrapped and wrapped phases can only differ by an integer number of cycles [30]. Consequently, the unknown phase ambiguity, that corresponds the phase shift between the absolute and the unwrapped phase, is also an integer number of cycles. This property is exploited in Chapter 2, when correcting the phase ambiguities.

List of symbols for Chapter 1

α	Tilt angle of the baseline vector
b	Spatial baseline
$b_{\parallel}$	Parallel baseline
$b_{\perp}$	Perpendicular baseline
B	Range bandwidth
β	Rate of frequency modulation
d_a	Antenna dimension along the azimuth direction
d_r	Antenna dimension along the range direction
d_{LOS}	Line-of-sight deformation
Δ_a	Azimuth resolution
Δ_r	Range resolution
$\Delta\phi$	Interferometric phase
$\Delta\phi_{\text{diff}}$	Differential phase
$\Delta\phi_{\text{unw}}$	Unwrapped phase
$\Delta\phi_{\text{w}}$	Wrapped phase
γ	Coherence
γ_{s}	Spatial coherence
γ_{t}	Temporal coherence
λ	Wavelength
ν_0	Radar carrier frequency
ψ_m	Phase of a point target in the master image
ψ_s	Phase of a point target in the slave image
$\psi_{\text{scat},m}$	Scattering phase in the master image
$\psi_{\text{scat},s}$	Scattering phase in the slave image
r	Range distance
r_m	Range distance in the master image
r_s	Range distance in the slave image
S_m	Point target response in the master image
S_s	Point target response in the slave image

σ_z	Height accuracy
σ_ϕ	Phase accuracy
τ	Radar pulse duration
θ	Look angle
θ_0	Look angle corresponding to a flat reference surface
z	Height
$z_{2\pi}$	Height ambiguity

Chapter 2

Split-Band Interferometry to Assist Phase Unwrapping

It is well known that resolution of SAR images is ruled by the synthetic aperture principle along the azimuth direction and the frequency band of the chirp signal along the range direction. While Envisat achieved about 30 m of cross-track resolution with a frequency band up to 15 MHz, recent sensors like TerraSAR-X or Cosmo-SkyMed, in Spotlight mode, can reach the metric range resolution thanks to their much larger band signal (i.e. some hundreds of megahertz). In addition to improving range resolution, wideband signals opened a new domain of applications to the SAR community by giving access to a new channel of information: the range spectral diversity.

Split-Band Interferometry is one way to exploit the spectral content of SAR images: the principle is to split the range spectrum of an interferometric pair of acquisitions in order to produce frequency-shifted subband scenes of range resolution coarser than the original master and slave acquisitions. Interferometric products are then generated from the subband images to yield a stack of frequency-varying interferograms, called in this context *partial interferograms.* For pixels with a stable behaviour through these partial interferograms, known as *frequency-persistent scatterers* or *frequency-stable pixels* ($\mathrm{PS_f}$), the pointwise phase evolves linearly with the frequency through the stack of interferograms. The slope of the linear regression being proportional to the range difference between the master and the slave acquisitions, it is then possible to compute the absolute phase of an interferogram. This process is equivalent to an absolute and spatially independent phase unwrapping, as long as it is performed on spectrally stable targets.

Veneziani et al. discussed the rationale and the applicability of the technique in Reference [8]. They showed that the SBInSAR phase accuracy depends an appropriate balance between preserving a sufficient resolution of the subband images and splitting the spectrum into a large amount of subbands. As a condition for performing SBInSAR, an essential ingredient is the availability of frequency-stable targets: phase can only be considered as absolute at these points and their detection is therefore fundamental. Previous works on SBInSAR, e.g. References [31, 32], have considered the multifrequency phase error for the selection of frequency-persistent scatterers. The scattering properties of these targets have been further investigated and compared to permanent scatterers (PS), and it was shown that temporal the PS stability condition does not imply frequency stability within the whole bandwidth [33].

A direct application of SBInSAR is the topographic mapping, given the absolute nature of the SBInSAR phase. The practical feasibility of topographic measurements has been assessed for TerraSAR-X and Cosmo-SkyMed Spotlight data over the arid site of Uluru monolith, Australia [9, 34]. Another study by Derauw et al. demonstrated the potential of SBInSAR for height retrieval using TanDEM-X acquisitions in Stripmap mode over the Nyiragongo volcano, DRC [35]. Among other potential applications of Split-Band Interferometry, let us cite ground deformation monitoring, estimation of high-gradient surface displacements such as earthquake ruptures [36], phase unwrapping [37] or even ionospheric corrections [38–40]. The spectral information of a SAR image can also be exploited for cover classification, ship detection [33, 41] or coregistration [42].

Nevertheless, despite the amount work already accomplished on this subject, Split-Band Interferometry is hardly an operational tool. So far, it has been essentially used in the context of methodological developments and applied on ideal test cases. For example, demonstrations on Uluru monolith are based on data with a very large bandwidth, which are not standard, and over an arid environment characterized by low temporal decorrelation, thus perfect for SAR interferometry [9, 34]. A study by Bovenga et al. also concluded that Multichromatic Analysis requires Spotlight acquisitions to obtain reliable results, which restricts noticeably its usefulness [32].

In this work, we are concerned with extending the applicability of this technique and making it available for a more common use. Fundamental questions are to be addressed: under which conditions can we use Split-Band Interferometry? With which sensors, which modes? What are the sensitive parameters to take into account? Could we imagine to run SBInSAR on Stripmap data instead of Spotlight, and how? These are the questions we attempt to answer in this chapter.

In a first step, we review the formalism and the feasibility of Split-Band Interferometry from a slightly new point of view. We determine the processing parameters that should be preferred, both in theory and in practice, and handle the detection problem of frequency-stable targets. In addition, we propose to relax the precision requirements on the SBInSAR phase in order to simply get the phase ambiguity, rather than the exact absolute phase, and we use SBInSAR as an help to phase unwrapping. Moreover, we show that frequency-stable scatterers are a key element of Split-Band Interferometry and that it is crucial to get a deeper understanding of their interactions with the radar signal. Finally, we propose to extend the developed approach to acquisitions from different sensors, more or less adequate to SBInSAR processing, in order to test the limits of the phase unwrapping assistance. Except for one study case, we stick to our region of interest and perform tests over the Virunga Volcanic Province. We demonstrate that Split-Band Interferometry can be managed on this quite challenging area of vegetation and volcanic rocks.

2.1 Rationale

Split-Band Interferometry is a three-step process that takes advantage of the large range bandwidth of modern SAR sensors (e.g. TerraSAR-X, Cosmo-SkyMed or Radarsat-2) to retrieve the absolute interferometric phase. As depicted in Figure 2.1, the process starts from a pair of already coregistered master and slave SLC images. During the first step of the process, the same spectral decomposition is applied to both images. In the second step, interferometry is performed on each pair of master and slave subimages. This yields a set of lower resolution interferograms, in which the pointwise phase is assumed to behave linearly with the varying frequency. This assumption is verified only for pixels with a stable behaviour across the spectral domain. During the last step of the process, called *multichromatic analysis*, a pixel-by-pixel linear regression is carried out on the subband phase. If the phase behaviour is indeed linear, then the slope of the linear regression is proportional to the absolute optical path and absolute phase measurements can be recovered at points considered as frequency-stable targets.

In the following section, we present a formal mathematical description of Split-Band Interferometry that is valid for a monostatic pair of acquisitions, as well as a short description of the Split-Band and Split-Band Interferometry processors. Further details about the implementation

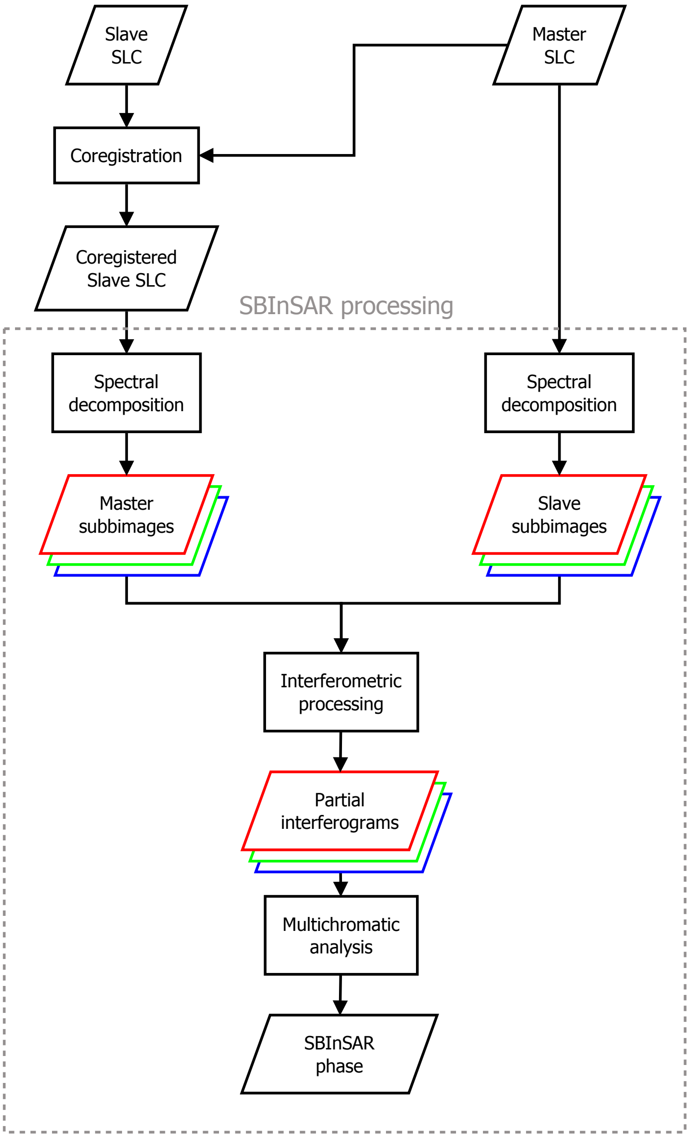

Figure 2.1: Flow chart of SBInSAR processing.

of the processors can be found in Reference [43].

2.1.1 Mathematical description

Let us consider a transmitted radar pulse of carrier frequency ν_0. In order to ease the calculation, we consider the signal along the range dimension only, and the simplified case of a square band-pass spectrum. We also neglect the multiplying factors that are of no interest in the formalism of Split-Band Interferometry (e.g. gain, diagram of antenna, etc.). Given these considerations, in the monostatic case, the generic response of a point scatterer located at a distance r_m away from the sensor has a cardinal sine shape and can be written under its integral form as

$$\begin{aligned} S(r) &\propto e^{-2\pi i \nu_0 \frac{2}{c} r_m} \operatorname{sinc}\left(\pi B \frac{2}{c} (r - r_m)\right) \\ &\propto e^{-2\pi i \nu_0 \frac{2}{c} r_m} \int_{-\frac{B}{2}}^{\frac{B}{2}} e^{2\pi i \nu \frac{2}{c}(r - r_m)} \, d\nu, \end{aligned} \tag{2.1}$$

where B is the original range bandwidth of the signal, c is the speed of light and the cardinal sine function is defined as $\operatorname{sinc}(x) = \frac{\sin(x)}{x}$.

Spectral decomposition

In a first step, as shown in Figure 2.2, the master acquisition is spectrally decomposed into N subbands of partial bandwidth B_s. N is assumed to be odd to ensure a symmetrical split with respect to the initial carrier frequency. Each subband is centered on a slightly different frequency ν_i ($i = 1, 2, \ldots, N$) and the frequency shift from one subband to the next is defined by $\Delta\nu = \frac{B - B_s}{N - 1}$. Let us note that subbands can overlap, if the frequency shift is smaller than the partial bandwidth (Figure 2.2c). Once the master acquisition is split into subbands, the point scatterer signal in the i-th master chromatic view is described by

$$\begin{aligned} S_i^m(r) &\propto e^{-2\pi i \nu_0 \frac{2}{c} r_m} \int_{\nu_i - \nu_0 - \frac{B_s}{2}}^{\nu_i - \nu_0 + \frac{B_s}{2}} e^{2\pi i \nu \frac{2}{c}(r - r_m)} \, d\nu \\ &\propto e^{-2\pi i \nu_0 \frac{2}{c} r_m} e^{2\pi i (\nu_i - \nu_0) \frac{2}{c}(r - r_m)} \operatorname{sinc}\left(\pi B_s \frac{2}{c} (r - r_m)\right). \end{aligned} \tag{2.2}$$

As expected, given that $B_s < B$, Equation (2.2) shows that the response of a point scatterer after band split is a cardinal sine of lower resolution than the sinc response of the initial acquisition. Phase contributions appear in the arguments of the complex exponential terms. The first phase term is related to the sensor-target distance in the master image r_m, as for the conventional signal described by Equation (2.1), while the second phase term, that depends on the spectral shift $(\nu_i - \nu_0)$, arises from spectral decomposition.

Let us stress that, in Expression (2.2), demodulation has been applied with respect to the initial carrier frequency. As we will explain in Chapter 5, this is not the case when spectral decomposition is used to estimate the ionospheric phase contribution: for this purpose, demodulation must be performed with respect to the subband frequency.

Interferometric process

A similar spectral decomposition is applied to the slave acquisition. At this stage, the slave image has been coregistered and resampled onto the master acquisition, which has implications on the signal in the split slave image. Similarly to the master signal, the first phase term depends on the distance r_s between the sensor and the target in the slave image. As for the second phase term, it relies on the position of the phase center. In the ideal case of exact coregistration, corresponding pixels of the slave and master images overlap perfectly and the phase center position of a pixel in the resampled slave image is the pixel location r_m. In this case, the second phase term is the same for the master and the slave, and it cancels out during the interferometric process, leaving an interferogram identical to the classical one except for the coarser resolution.

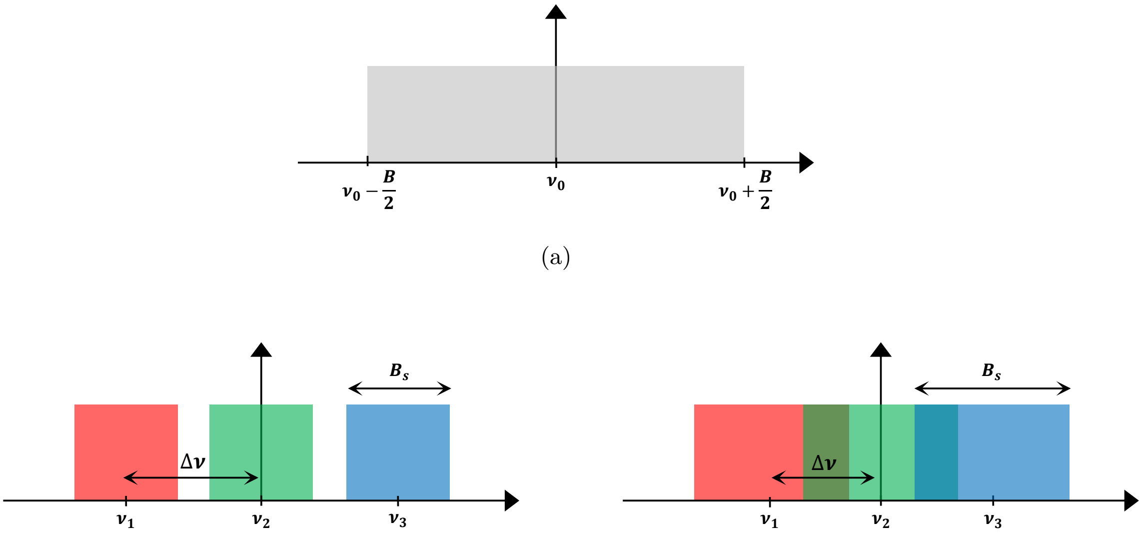

(a)

(b)

(c)

Figure 2.2: Range spectrum before and after spectral decomposition. (a) Original square band-pass spectrum, with bandwidth B and centered on frequency ν_0. (b) Spectrum of subband images. In the non overlapping case, the subband shift $\Delta\nu$ is larger then or equal to the partial bandwidth B_s. (c) On the contrary, when the subband shift $\Delta\nu$ is smaller than the partial bandwidth B_s, then subbands overlap.

However, coregistration is always approximated and the phase contribution due to coregistration errors is dispersive. This is the basis of Split-Band Interferometry for absolute ranging. As a reminder, coregistration is the resampling of the slave image onto the master geometry, in order to obtain the same pixel location in both images for a given target on the ground. The transformation applied to a given pixel in range dimension can be expressed by

$$r_s = r_m + \Delta r + e_c, \tag{2.3}$$

where Δr is the estimated offset between the slave and master range coordinates, and e_c is the range coregistration error. As coregistration is tainted by an error, the phase center in the interpolated image is therefore not located in r_m, but rather in $r_m + e_c$. Taking this into account, the point scatterer response in the resampled and split slave image is given by

$$S_i^s(r) \propto \; e^{-2\pi i \nu_0 \frac{2}{c} r_s} \, e^{2\pi i (\nu_i - \nu_0) \frac{2}{c} (r - r_m - e_c)} \; \mathrm{sinc}\left(\pi B_s \frac{2}{c} \left(r - r_m - e_c\right)\right). \tag{2.4}$$

The coregistration error appears in the second phase term and introduces a disruption of the interferometric phase proportional to the frequency shift. Indeed, the interferometric phase in the i-th partial interferogram is derived as

$$\begin{aligned} \phi_i \; &= \; \frac{4\pi}{c} \left(r_s - r_m\right) \nu_0 \; + \; \frac{4\pi}{c} e_c \left(\nu_i - \nu_0\right) \\ &= \; \frac{4\pi}{c} \left(r_s - r_m - e_c\right) \nu_0 \; + \; \frac{4\pi}{c} e_c \nu_i. \end{aligned} \tag{2.5}$$

We note that the subband phase has a linear behaviour with a misregistration-dependent slope.

Multichromatic analysis

With conventional radar interferometry, one wishes to retrieve the optical path difference between the slave and master views. However, it is usually not possible to obtain absolute phase

measurements using classical methods because phase ambiguities remain unknown, even after phase unwrapping. With SBInSAR, this limitation can be potentially overcome.
Based on the Expression (2.3), we see that the optical path difference is equal to the sum of the coregistration offset and the error of coregistration: $r_s - r_m = \Delta r + e_c$. The SBInSAR phase $\Delta\varphi$ is then computed as the contribution of a registration phase $\Delta\phi_{reg}$ and a misregistration phase $\Delta\phi_{e_c}$:

$$\begin{aligned}\Delta\varphi &= \frac{4\pi}{c}\nu_0\left(r_s - r_m\right) \\ &= \underbrace{\frac{4\pi}{c}\nu_0\Delta r}_{\Delta\phi_{reg}} + \underbrace{\frac{4\pi}{c}\nu_0 e_c}_{\Delta\phi_{e_c}}.\end{aligned} \tag{2.6}$$

On the one hand, the registration phase is directly obtained and exactly known from the applied range coregistration offset Δr. On the other hand, the misregistration contribution is estimated with a multichromatic analysis, i.e. an analysis of the phase from the frequency point of view. Indeed, the phase behaviour in the partial interferograms, given by Equation (2.5), has a linear behaviour with respect to the subband frequency and the slope of this straight line is proportional to the local misregistration:

$$\frac{\partial\phi_i}{\partial\nu_i} = \frac{4\pi}{c}e_c. \tag{2.7}$$

This slope is estimated for each pixel separately by fitting a linear function $p\left(\nu_i\right) = s\nu_i + u$ to the phase values through the partial interferograms, s and u being respectively the slope and intercept parameters of the fit. The obtained value of the slope is then introduced in Equation (2.6) to compute the SBInSAR phase. This phase is a measure of the absolute optical path difference on a pointwise basis and it is not wrapped. For pixels with sufficient precision of the slope estimate, the SBInSAR phase is considered as an absolute phase measurement.

Remarks

In order to estimate the order of magnitude of the slope, let us convert the coregistration error into pixel units. If the SAR image is not oversampled, then the sampling frequency is equal to signal bandwidth, and the pixel size Δx is equal to the range dimension of the resolution cell:

$$\Delta x = \frac{c}{2B}. \tag{2.8}$$

The coregistration error in terms of pixel units, denoted by e_p, is then expressed as

$$e_p = \frac{e_c}{\Delta x} = \frac{2B}{c}e_c. \tag{2.9}$$

Rewriting Equation (2.7) as a function of e_p instead of e_c, we obtain

$$\frac{\partial\phi_i}{\partial\nu_i} = \frac{2\pi}{B}e_p. \tag{2.10}$$

If we consider a misregistration of half a pixel and a bandwidth of 100 MHz, the order of magnitude of the measured slope is about 10^{-8} rad/GHz. InSAR usually requires coregistration with an accuracy better than 1/10th of a pixel, leading to slope rather of the order of 10^{-9} rad/GHz. Such a low value makes the slope very sensitive to the noise in the phase samples: for an equal level of noise, the relative error will be larger for a low slope than for a steep one. It can also be shown that phase variations larger than π do not occur within the available bandwidth, preventing the phase from aliasing [44].

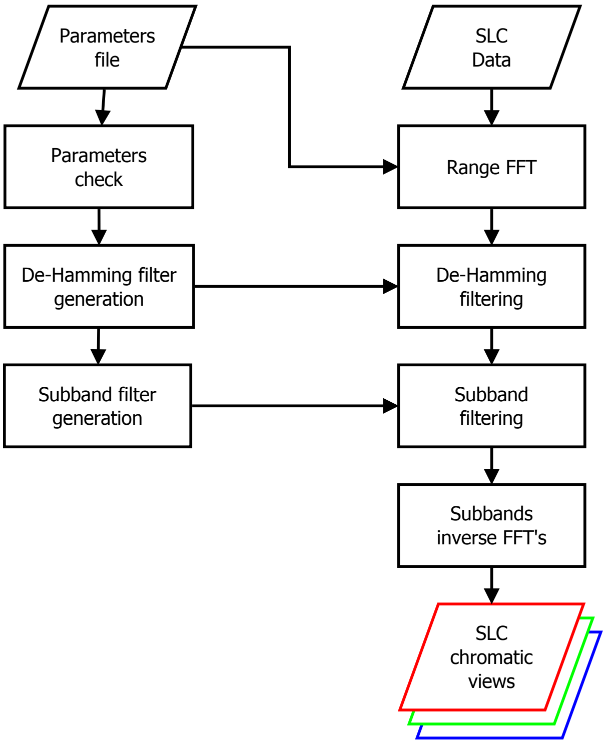

Figure 2.3: Flow chart of the spectral decomposition module, which is part of the SBInSAR processing flow presented in Figure 2.1.

2.1.2 SBInSAR processor

The mathematical formalism described in Section 2.1.1 has been implemented in an SBInSAR processor integrated to the CSL InSAR Suite (CIS) software, coded in C language. Although this implementation was not part of the present study, it is worth describing some steps in detail. The overall working flow of the SBInSAR processor is given in Figure 2.1. Let us focus on the spectral decomposition module in particular: as presented in Figure 2.3, starting from focused SLC images, we move to the spectral domain by applying a Fourier transform to the data along the range direction. For each subband, an equal portion of the spectrum is then selected by a band pass filtering centered on the adequate frequency, and an inverse Fourier transform is performed to move back into the image domain and obtain a chromatic view of the scene. Both direct and inverse Fourier transforms make use of the Fast Fourier Transform algorithm (FFT). However, in practice, the initial SLC data are filtered to reduce sidelobes and this has to be compensated for before subband filtering. The sidelobe mitigation is done by filtering focused data with an apodization filter, described by the function

$$f(\nu) = \alpha - (1-\alpha)\cos\left(2\pi\left(\nu-\nu_0\right)\right) \tag{2.11}$$

with α the apodization coefficient which is sensor-dependent. Therefore, data must be filtered with the inverse apodization filter in order to recover the original full band spectrum, before splitting it into subbands, i.e. before band pass filtering.

Regarding the multichromatic analysis module, it essentially consists in a point-by-point linear regression of the subband phase. As a prerequisite, it is necessary to ensure phase continuity by unwrapping it along the subbands. As noted in the previous section, the low slope values

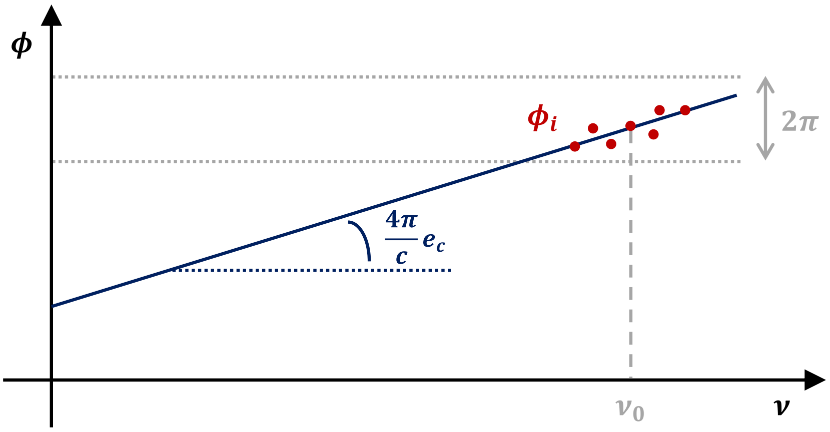

Figure 2.4: Schematic representation of the linear regression applied for the multichromatic analysis. Phase samples are unaliased and the slope of the line gives the misregistration phase.

prevent phase aliasing and thus phase jumps larger than π between subbands do not happen. Phase integration along the subbands frequencies results then in the actual phase values [28,45]. The situation at this stage is represented schematically in Figure 2.4. Given the low value of the slope, it can be viewed in good approximation as the angle of the linear regression with respect to the horizontal.

Linear regression is then managed by a chi-square fit of the unwrapped phase samples. The chi-square merit function to minimize is given by

$$\chi^2(s,u) = \sum_{i=1}^{N} \frac{(\phi_i - s\nu_i - u)^2}{\sigma^2_{\phi_i}}, \tag{2.12}$$

where s and u are the slope and intercept parameters of the linear regression, and the merit function can be weighted or not by the phase variance of the partial interferograms, according to the user's will. In addition to the SBInSAR phase image, the SBInSAR processor also provides images of the registration phase, of the intercepts values, of the standard deviation of the intercepts estimates σ_{int}, of the multifrequency phase error σ_ν, of the SBInSAR coherence γ_ν and of the linear correlation coefficient R^2.

In the framework of this study, additional modules have been integrated to the already existing processor in order to estimate the phase variance stability and generate standard deviation on the slope σ_s and the goodness-of-fit estimators χ^2_ν and Q. These estimators are defined in more details in Section 2.3.1.

2.2 Feasibility study

In order to manage absolute ranging or to remove phase ambiguities using Split-Band Interferometry, requirements on the SBInSAR phase precision are extremely stringent. This is the reason why it is important to analyze the influence of spectral decomposition parameters and determine the limits of the technique before addressing practical cases. In this section, we study the performance of Split-Band Interferometry as a function of the processing parameters and we describe the limiting factors. Finally, we prescribe adequate values for the processing parameters.

2.2.1 Parameters analysis

As established by Equation (2.6), inacurracies of the SBInSAR phase mainly arise from errors on the slope estimate. Actually, the registration phase is known exactly since it originates from a defined coordinate transformation and the misregistration is taken into account in the second term. The estimated linear regression coefficients are thus the major source of error and the standard deviation of the SBInSAR phase is expressed as

$$\sigma_{\Delta\varphi} = \nu_0 \sigma_s. \tag{2.13}$$

A lack of precision on the slope estimates directly propagates to the phase estimates. The slope standard deviation is multiplied by a frequency of some gigahertz, making the SBInSAR phase very sensitive to inaccuracies.

From the chi-square fitting formalism [46], the expression of the slope standard deviation σ_s can be derived. Let $\sigma^2_{\phi_i}$ be the phase variance of the i-th partial interferogram and x_i the subband number for a numbering that is symmetrical with respect to the central subband : $x_i = -\frac{N-1}{2}, \ldots, \frac{N-1}{2}$. For independent data samples, i.e. non overlapping subbands, the slope standard deviation is computed as

$$\sigma_s = \frac{1}{\Delta\nu} \sqrt{\frac{\sum\limits_{i=1}^{N} \frac{1}{\sigma^2_{\phi_i}}}{\sum\limits_{i=1}^{N} \frac{1}{\sigma^2_{\phi_i}} \sum\limits_{i=1}^{N} \frac{x_i^2}{\sigma^2_{\phi_i}} - \left(\sum\limits_{i=1}^{N} \frac{x_i}{\sigma^2_{\phi_i}} \right)^2}}. \tag{2.14}$$

In the case of an unweighted linear regression of the phase samples, $\sigma^2_{\phi_i}$ is replaced by unitary weights for all values of i, and σ_s must be multiplied by a factor $\sqrt{\chi^2/(N-2)}$. Rigorously, in the case of overlapping subbands, correlation terms should be taken into account. However, the number of correlation terms increases quadratically with the number of subbands, and they are thus computationally expensive and memory consuming to estimate, for a negligible gain of knowledge. In the following, we ignore the correlation terms and assume that the expression of the slope standard deviation is the same in the overlapping and non overlapping cases. This is validated in practice in Section 2.5.

Given Equation (2.14) and the definition of the frequency shift, we transform Equation (2.13) to make it explicit:

$$\sigma_{\Delta\varphi} = \nu_0 \frac{N-1}{B-B_s} \sqrt{\frac{\sum\limits_{i=1}^{N} \frac{1}{\sigma^2_{\phi_i}}}{\sum\limits_{i=1}^{N} \frac{1}{\sigma^2_{\phi_i}} \sum\limits_{i=1}^{N} \frac{x_i^2}{\sigma^2_{\phi_i}} - \left(\sum\limits_{i=1}^{N} \frac{x_i}{\sigma^2_{\phi_i}} \right)^2}}. \tag{2.15}$$

Regarding the dependency of this expression on the parameters, we have that the SBInSAR standard deviation follows $\sigma_{\Delta\varphi} = \sigma_{\Delta\varphi}(\nu_0, N, B, B_s, \sigma_{\phi_i})$. In Figure 2.5, we simulate the value of the split-band standard deviation for typical X-band and C-band cases. Each time, we consider the case of an unweighted linear regression and a linear regression weighted with a constant phase standard deviation of 0.3 rad. We observe that a one-cycle accuracy, indicated by the dashed line, is hardly obtained. Even with a standard deviation of the partial phase better than 1/20th of a cycle, such a precision is only reached by the simulation for the case of a TerraSAR-X Spotlight pair of images, with a weighted linear regression. However, we expect better results in the case of a non constant weighting. We also note that the larger the initial bandwidth, the less dispersion we have in the simulated values. This shows that the influence of spectral decomposition becomes less important when the bandwidth is large. Let us now review the influence of the parameters one by one.

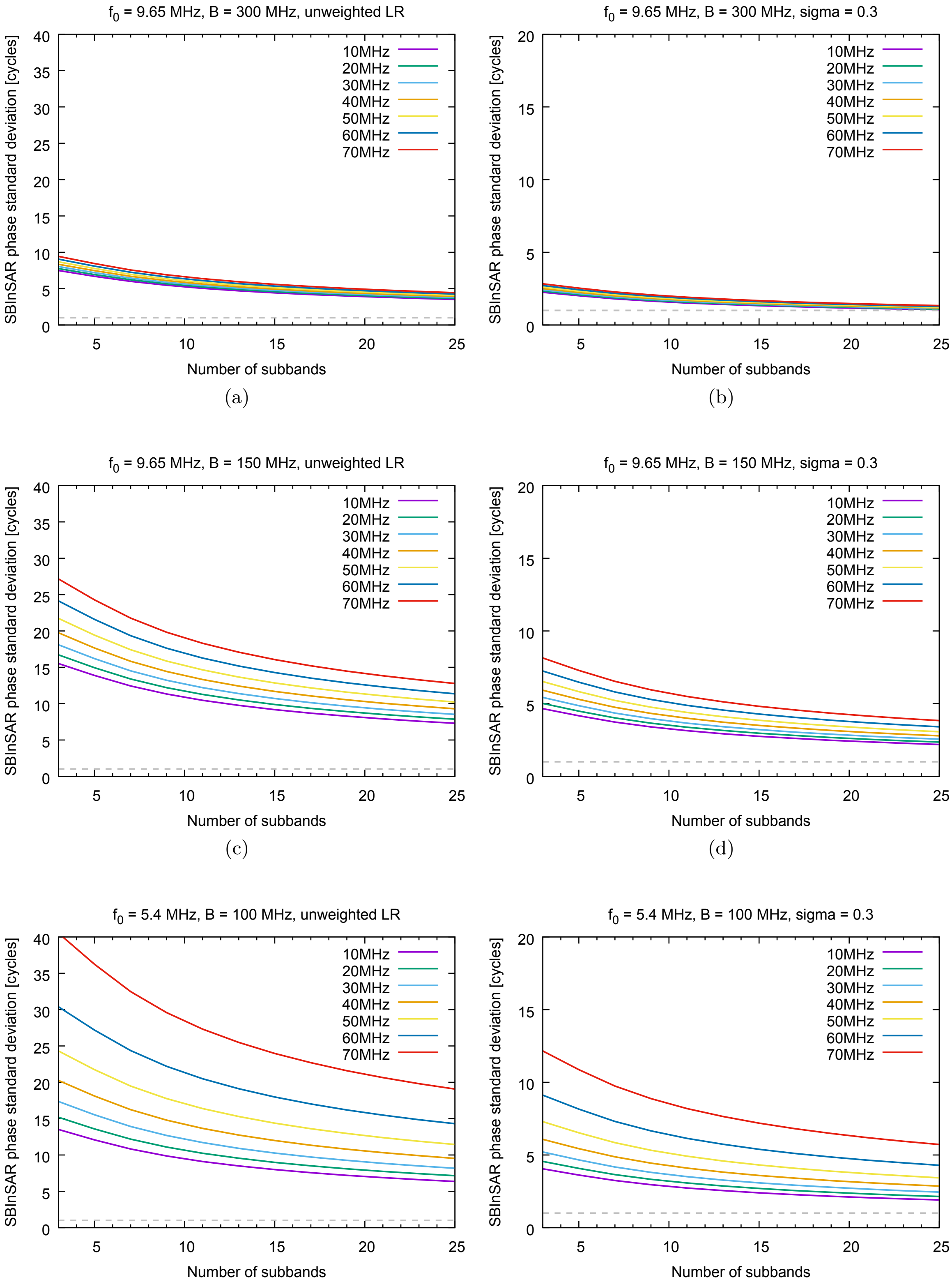

(a) (b)

(c) (d)

(e) (f)

Figure 2.5: Simulations of the SBInSAR phase standard deviation for various spectral decomposition schemes. We considered parameter values typical of (a)-(b) TerraSAR-X Spotlight mode, (c)-(d) TerraSAR-X Stripmap mode and (e)-(f) Radarsat-2 Ultra-Fine mode. The left column is the case of an unweighted linear regression. The right column is the case of a linear regression weighted with a constant value of $\sigma_{\phi_i} = 0.3$ rad. The horizontal dashed line indicates a one-cycle accuracy.

Initial carrier frequency ν_0 A direct implication of Equation (2.15) is that the SBInSAR phase error decreases with the original carrier frequency. It means that a C-band sensor is a priori more suited than an X-band sensor for absolute ranging. Unfortunately, C-band sensors usually have a smaller bandwidth than X-band sensors. For example, TerraSAR-X has a bandwidth of 150 MHz in Stripmap mode and 300 MHz in Spotlight mode, while Radarsat-2 reaches at best 100 MHz in Ultra-Fine mode, and only 30 MHz in Fine mode.

Original bandwidth B The initial bandwidth of the images should be as large as possible. This enables the exploration of a larger range of frequencies and a split into a larger number of subbands for a given partial bandwidth. As discussed previously, it also makes the results less sensitive to the choice of the other parameters. The magnitude order of the SBInSAR phase standard deviation is proportional to the ratio $\frac{\nu_0}{B}$, which should be as small as possible to get a satisfactory precision on the SBInSAR phase. This ratio also characterizes the spectral diversity of a SAR image. Examples of ratio values for different types of sensors and modes are given in Table 2.1.

Partial bandwidth B_s A priori, based on the mathematical expression, the partial bandwidth should be small to mitigate the SBInSAR phase error, as it can be observed in Figure 2.5. However, a decrease of the bandwidth means a lower resolution and an intensified influence of the decorrelation noise.

Number of subbands N Even though we could expect at first sight the error to decrease with the number of subbands, the accuracy of the fit usually improves with the number of data samples. In the next paragraph, it is shown that, under some assumptions, the SBInSAR phase behaves as the inverse of the square root of the number of subbands. A large number of subbands should then be preferred.

Partial phase variance $\sigma^2_{\phi_i}$ Phase variance in partial interferograms is not a parameter we can control. It represents the noise in the phase samples. When weighting is applied for the linear regression, the partial phase variance enables mitigating the influence of outliers and thus reducing the effect of the noise.

The influence of the partial phase variance on the SBInSAR phase can be studied by expressing it as a function of the coherence and the number of looks used for phase estimation, as done in Reference [8]. Nevertheless, this approach still introduces new parameters and makes the problem even more complex. By means of two assumptions, we develop another approach to estimate the phase variance effect. Let us assume the two following statements:

- The spectral decomposition into subbands is symmetrical with respect to ν_0.
- The phase variance $\sigma^2_{\phi_i}$ does not vary much from one subband to another.

The first assumption is always verified due to the way spectral decomposition is applied by the SBInSAR processor. The second one is assumed to be true when neglecting the squared sum in Equation (2.15) induces a variation of less than 5% of the computed quantity. In this case, the squared sum can be neglected and we can introduce an upper bound $\sigma^2_{\phi,max}$ on the partial

Sensor	**Mode**	ν_0	B	$\frac{\nu_0}{B}$
TerraSAR-X	Stripmap	9.65 GHz	150 MHz	64.33
TerraSAR-X	Spotlight	9.65 GHz	300 MHz	32.16
Cosmo-SkyMed	HIMAGE *	9.60 GHz	96 MHz	100.00
Cosmo-SkyMed	HIMAGE *	9.60 GHz	129 MHz	74.42
Radarsat-2	Fine	5.40 GHz	30 MHz	180.00
Radarsat-2	Ultra-Fine	5.40 GHz	100 MHz	54.00
Sentinel-1	Interferometric Wide	5.40 GHz	56 MHz	96.43

Table 2.1: Typical values of carrier frequency ν_0, range bandwidth B and associated quality ratio $\frac{\nu_0}{B}$ for sensor and modes used in this study.
*Cosmo-SkyMed images acquired in HIMAGE mode have a bandwidth accomodated along the range to have constant ground range resolution across the image. The bandwidth depends therefore on the incidence angle. We give here parameters for two cases with different incidence angles of approximately 35.5° and 26.6°.

phase variance:

$$\begin{aligned}\sigma_{\Delta\varphi} &= \nu_0 \, \frac{N-1}{B-B_s} \sqrt{\frac{1}{\sum\limits_{i=1}^{N} \frac{x_i^2}{\sigma_{\phi_i}^2}}} \\ &\leqslant \nu_0 \, \frac{N-1}{B-B_s} \, \sigma_{\phi,max} \sqrt{\frac{1}{\sum\limits_{i=1}^{N} x_i^2}}.\end{aligned} \tag{2.16}$$

Given the symmetry of the x_i values, the remaining sum in Equation (2.16) can be developed as the double sum of the $\frac{N-1}{2}$ first integers and we obtain

$$\sigma_{\Delta\varphi} \leqslant \nu_0 \, \frac{N-1}{B-B_s} \, \sigma_{\phi,max} \sqrt{\frac{12}{N(N+1)(N-1)}}. \tag{2.17}$$

As a consequence, the SBInSAR phase error is be limited by the subband with the largest value of partial phase variance. Moreover, as it can be expected, the smaller the upper bound of the phase variance, the better the SBInSAR phase precision. From this expression, we can also note that the SBInSAR phase standard deviation follows a law $\sim \frac{1}{\sqrt{N}}$. Let us mention that, in practice, the standard deviation of the subband interferograms is computed by the SBInSAR processor and this upper bound can be found easily.

2.2.2 Limiting factors

Performances of SBInSAR happen to be limited mainly by two antagonistic factors: the first one is the SBInSAR phase accuracy, which has been extensively analyzed in the previous section; the second one is the resolution loss induced by spectral decomposition. The latter effect is less obvious in the presented mathematical formalism, but is very intuitive for any SAR user. In fact, the range resolution of the partial interferometric products is degraded due to the reduced bandwidth considered during SBInSAR processing. If this resolution loss becomes too important, the signal could be overcome by geometrical decorrelation. In this case, one would measure noise instead of signal, even though the SBInSAR phase satisfies the precision requirements.
These limiting factors are not easy to reconcile, since it would require a large partial bandwidth to mitigate the resolution loss, but a small partial bandwidth to get a precise SBInSAR phase.

The user then has the difficult task to manage a trade-off between both aspects. This can be eased by quantifying them: as already stated, a dimensionless number characteristic of the SBInSAR phase precision is the ratio $\frac{\nu_0}{B}$. The resolution loss effect can be estimated by the *correlated-to-decorrelated ratio* (CDR), defined in the next section.

Correlated-to-Decorrelated Ratio (CDR)

We propose to quantify the resolution loss effect on the SBInSAR products via a ratio between the correlated and decorrelated parts of the signal, which is large when signal information is preserved and small when phase decorrelation becomes important. In Reference [27], Zebker and Villasenor derived an expression of the coherence that depends on the signal-to-noise ratio (SNR). Based on a similar calculation, neglecting the noise component and the temporal decorrelation, it is possible to link the coherence γ to the ratio $\frac{|C|^2}{|D|^2}$ of the correlated part $|C|^2$ and the decorrelated part $|D|^2$ of the signal:

$$\gamma = \frac{1}{1+\frac{|C|^2}{|D|^2}} = \frac{1}{1+\frac{1}{\mathrm{CDR}}}. \tag{2.18}$$

This equation can be related to the spatial decorrelation expression given by Equation (1.20) in Chapter 1. If we consider the partial bandwidth instead of the original bandwidth in this expression, the CDR can finally be approximated by

$$\mathrm{CDR} = \frac{\lambda B_s r_m \tan\theta}{c|b_\perp|} - 1, \tag{2.19}$$

where λ is the wavelength, r_m the range distance, θ the incidence angle, c the speed of light, $b_\perp$ the perpendicular baseline and B_s the subband range bandwidth. The optimum CDR is obtained for low incidence, large wavelength, large range distance and large partial bandwidth. These are sensor- and geometry-related parameters. However, the CDR also depends on the perpendicular baseline that is not an intrinsic parameter of the SAR images. Despite a data set with fixed sensor, a fixed mode and a fixed viewing geometry, the CDR varies from an interferometric pair to another according to the perpendicular baseline value.

This dimensionless quantity is completely equivalent to the spatial coherence γ_s, but it underlines the need for a balance between the signal and the loss of correlation. In Table 2.2, we list values of the CDR and the spatial coherence for a constant perpendicular baseline of 100 m and for various sensors and modes used in this work. These values show that the CDR has more contrasted values, which makes it more readable regarding the effect of the resolution loss. For example, less favorable study cases can have spatial coherence as high as 0.8, but then the CDR will be lower than 10.

2.2.3 Prescribed parameters

It becomes clear that defining optimum parameters for SBInSAR processing is not an easy task. Several aspects must be taken into account. Performances are impacted by data parameters, as well as processing parameters. We consider three types of parameters, each of importance: spectral decomposition parameters, acquisition parameters and interferometric parameters. Even if it might be impossible to cope with all aspects of these recommendations, the user should meet them at best to reach a satisfactory precision.

Regarding spectral decomposition parameters, one should prefer a large original range bandwidth. For non overlapping subbands, a trade-off must be found between a large number of subbands and a reasonable partial bandwidth. In practice, we observe good results for TerraSAR-X

Sensor	**Mode**	λ	θ	r_m	B_s	CDR	γ_s
TerraSAR-X	Stripmap	3.1 cm	26.4°	564 km	30.0 MHz	7.68	0.88
TerraSAR-X	Spotlight	3.1 cm	33.3°	615 km	60.0 MHz	24.05	0.96
Cosmo-SkyMed	HIMAGE	3.1 cm	35.5°	753 km	19.2 MHz	9.66	0.91
Cosmo-SkyMed	HIMAGE	3.1 cm	26.6°	693 km	25.8 MHz	8.25	0.89
Radarsat-2	Fine	5.5 cm	35.5°	949 km	6.0 MHz	6.44	0.87
Radarsat-2	Ultra-Fine	5.5 cm	36.9°	964 km	20.0 MHz	25.15	0.96
Sentinel-1	Interferometric Wide	5.5 cm	33.4°	825 km	11.2 MHz	10.17	0.91

Table 2.2: List of the wavelength λ, the median incidence angle θ and the median range distance r_m for different sensors and modes. The associated values of the CDR and the spatial coherence γ_s are also provided, for the case of a spectral decomposition into five non overlapping subbands of $B_s = B/5$ and a perpendicular baseline of 100 m.

images with a 150 MHz bandwidth split into 5 non overlapping subbands of 30 MHz. In the overlapping case, the number of subbands should be significantly increased, with a restriction depending on the memory allocated to the process. A weighted linear regression usually gives better results.

Sensor parameters intervene in the choice of the sensor and the mode of the SAR images. Of course, when one wants to study a particular region at a given time, data availability can be limited. However, if the choice is possible, the user should select data having the smallest ratio $\frac{\nu_0}{B}$. Regarding the geometry of acquisition, large incidence angles are preferable to moderate the exacerbated decorrelation caused by the reduced resolution.

Finally, the interferometric pair should have a small perpendicular baseline, typically under 100 m. The smaller the baseline, the less decorrelation. Besides, we also recommend to apply spatial averaging for a further mitigation of the decorrelation.

2.3 Frequency-stable targets

The linearity of the phase assumed in Equation (2.5) holds only for targets with a stable behaviour across the spectral domain, called frequency-persistent scatterers [47]. The stable nature of a frequency-persistent scatterer ensures the precision of the SBInSAR phase measurement and it is therefore fundamental to correctly detect $\mathrm{PS_f}$. These targets serve as seed points for correcting phase ambiguities. In the following, we review all estimators tested in this work for $\mathrm{PS_f}$ detection, and we propose a first approach to evaluate their efficiency.

Let us note that although the name frequency-persistent scatterer has been extensively used in past studies [31, 32], it is shown in Section 2.7 that it is inadequate and confusing. For this reason, we rather use the naming *frequency-stable pixels* or *spectrally stable targets* in this work. We keep on using the abbreviation $\mathrm{PS_f}$ for the sake of consistency, but from now on it stands for *Pixel Stable in the frequency domain.*

2.3.1 Detection criteria

In practice, we do not know which physical features are responsible for a spectrally stable behaviour, nor which pixel is a $\mathrm{PS_f}$ and which one is not. We have to find indications about the nature of $\mathrm{PS_f}$ and criteria that secure the stability of the selected targets.

So far, most studies have exploited the multifrequency phase error to detect frequency-stable targets [9,32,33]. In Reference [37], we presented two new detection criteria: the *slope standard* *deviation* and the *phase variance stability.* In this thesis, we consider additional estimators. Investigated criteria can be arranged in three categories: the phase quality estimators, the goodness-of-fit estimators and the phase variance stability.

Phase quality estimators

A first way to determine whether scatterers are spectrally stable is to assess the quality of the phase signal from the SBInSAR phase accuracy. If the uncertainty on the SBInSAR phase is large, we do not expect to face a target that behaves linearly from the spectral point of view. The multifrequency phase error, the slope standard deviation and the SBInSAR coherence are three different ways to estimate the phase quality. These quantities are defined hereafter.

Multifrequency phase error σ_ν The multifrequency phase error is basically the a posteriori uncertainty of the phase value in partial interferograms. Considering the fitting function $p(\nu_i)$ of the phase through partial interferograms, the multifrequency phase error is mathematically defined as

$$\sigma_\nu = \sqrt{\frac{1}{N-2}\sum_{i=1}^{N}\left(\phi_i - p(\nu_i)\right)^2}. \tag{2.20}$$

Slope standard deviation σ_s In the framework of the phase ambiguities retrieval, the SBInSAR phase must be measured with a precision better than a cycle, and we use this one-cycle precision to characterize frequency-stable pixels. Setting a threshold of 2π in Equation (2.13) leads us to a criterion of detection based on the standard deviation of the slope of the linear regression:

$$\sigma_s < \frac{2\pi}{\nu_0}. \tag{2.21}$$

This threshold only depends on the initial carrier frequency. In X-band, the upper limit of the phase slope standard deviation has a typical value of 0.65 rad/GHz, while in C-band this value is around 1.16 rad/GHz.

SBInSAR coherence γ_ν Given the signals S_m^i and S_s^i of a point target in the master and slave partial images, respectively, the SBInSAR coherence is estimated as

$$\gamma_\nu = \frac{\left|\sum_{i=1}^{N} \left|S_m^i\right| \left|S_s^i\right| \, e^{\,i(\phi_i - p(\nu_i))}\right|}{\sqrt{\sum_{i=1}^{N} \left|S_m^i\right|^2}\sqrt{\sum_{i=1}^{N} \left|S_s^i\right|^2}}. \tag{2.22}$$

This estimator evaluates the deviation of the phase samples ϕ_i from the modelled phase $p(\nu_i)$. It is computed in a similar way as the conventional coherence, though by frequency average rather than a space average. It ranges from 0 for a completely spectrally incoherent signal to 1 for a perfectly coherent signal.

Goodness-of-fit estimators

For this category of detection criteria, the quality of the SBInSAR phase signal is assessed from the quality of the linear regression instead of the quality of the signal. The considered criteria are the linear correlation, the reduced chi-square and the plausibility of the fit.

Linear correlation coefficient r^2 The linear correlation coefficient measures the degree of linear correlation between the subband index x_i and the partial phase ϕ_i. It is given by

$$r^2 = \frac{\sigma_{x\phi}^2}{\sigma_x^2\,\sigma_\phi^2} \tag{2.23}$$

with σ_x and σ_ϕ the standard deviations of the subband index and partial phase respectively, and $\sigma_{x\phi}$ the covariance of these variables. Here, the coefficient is raised to the power of 2, so that its value ranges from 0 if no linear correlation exists between the x_i's and ϕ_i's, to 1 if both quantities are completely correlated. Given the linear behaviour of $\mathrm{PS_f}$, their linear correlation coefficient is expected to be close to 1.

Reduced chi-square χ_ν^2 The reduced chi-square is a ratio that compares the a posteriori variance estimate to the parent variance of the data. It is given by the chi-square value per degree of freedom:

$$\chi_\nu^2 = \frac{\chi^2}{N_{DOF}}. \tag{2.24}$$

Here, χ^2 is the merit function of the fit and N_{DOF} is the number of degrees of freedom of the fit, equal to $N-2$ in the case of a linear regression on N phase samples. If the fit is representative of the true behaviour of the data, the a posteriori variance should agree well with the parent variance and the reduced chi-square should be close to 1. If χ_ν^2 is larger than 1, it means that the estimated deviations are large and the fitting function is probably inappropriate. A χ_ν^2 that is significantly smaller than 1 is typical of an overestimation of the uncertainties [48].

Goodness-of-fit probability Q The probability Q measures the plausibility of the fit. It gives the probability that a set of data samples would yield a value of χ^2 equal to or greater than the computed value. In other words, it is the probability that a value of the χ^2 as low as the one found for our merit function should occur by chance [46, 48]. It is computed from the chi-square cumulative distribution and is expressed as

$$Q\left(\frac{N_{DOF}}{2}, \frac{\chi^2}{2}\right) = 1 - \frac{\gamma\left(\frac{N_{DOF}}{2}, \frac{\chi^2}{2}\right)}{\Gamma\left(\frac{N_{DOF}}{2}\right)}, \tag{2.25}$$

where χ^2 is the computed value of our merit function, N_{DOF} is the number of degrees of freedom of the fit, Γ is the gamma function and γ is the lower incomplete gamma function. The fit is generally considered as believable if Q is larger than 0.1 and acceptable if larger than 0.001. On the contrary, if Q is very close to unity, the value is considered to be too good to be true and is probably due to an overestimation of the measurement errors.

Phase variance stability

This last criterion is also based on the quality of the phase signal, but the approach is slightly different than for the other criteria. Let us get back to the influence of the subband phase variance. In Section 2.2.1, we showed that SBInSAR phase error is restricted by the value of the partial phase variance upper bound when the assumptions of symmetry and weak variations of the variance are valid. Considering that a $\mathrm{PS_f}$ is a target with a phase precision better than a fringe, as done for the slope standard deviation, its partial phase variance satisfies the bound

$$\sigma_{\phi,max}^2 \leqslant \left(\frac{2\pi}{\nu_0}\,\frac{B-B_s}{N-1}\right)^2 \frac{N(N+1)(N-1)}{12}. \tag{2.26}$$

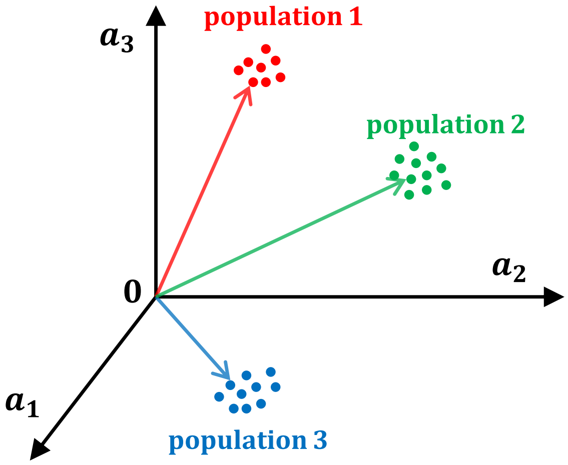

Figure 2.6: Schematic representation of the space of observations. Parameters a_1, a_2 and a_3 are used to define the observations points. Distinct populations are characterized by typical values of the parameters. Identification of the populations is performed by dividing the space into the corresponding number of regions. Each region is associated to a particular range of values of each parameter.

Frequency-stable pixels are then selected if they fulfill two conditions: first, the assumption of the negligible variations of the partial phase variance from a subband to the other must be verified. Second, the partial phase variance must observe the upper bound limit in all subbands:

$$\sigma^2_{\phi_i} \leqslant \left(\frac{2\pi}{\nu_0} \frac{B - B_s}{N-1} \right)^2 \frac{N(N+1)(N-1)}{12} \qquad \forall i = 1, 2, \ldots, N. \tag{2.27}$$

In the typical case of TerraSAR-X stripmap mode, when images are split into five non overlapping subbands, this limit reaches approximately 0.2 rad^2.

2.3.2 First insights about PS$_\mathrm{f}$ detection

The detection of frequency-stable targets is a classical binary decision process. We have the choice between two terms of an alternative: is the target a frequency-stable pixel, or is it not? Usually, such a decision process is handled by a classification based on the observation of one or several parameters. In our case, the quality estimators, defined in Section 2.3.1, are the reliable parameters to discriminate between PS$_\mathrm{f}$ and non-PS$_\mathrm{f}$, even though the relevant criteria are still to be determined. In ideal cases, an identification problem can easily be handled by plotting the values of the parameters for each observation, each parameter corresponding to an axis. Populations can then be distinguished, as represented schematically in Figure 2.6, and they are identified by partitioning the space into the corresponding number of regions. The problem consists mainly in finding the adequate thresholds that minimize the number of false detections [49].

We adopt this approach for the PS$_\mathrm{f}$ identification we apply it to a pair of acquisitions over the Virunga region, which extensively studied in the following sections. However, we observe that populations of PS$_\mathrm{f}$ and non-PS$_\mathrm{f}$ are not that easy to identify. We hence impose arbitrary thresholds for certain estimators. We have a first estimate of the efficiency of each criterion to detect PS$_\mathrm{f}$ and we show that, in the context of the phase ambiguity correction, this approach is efficient to remove outliers.

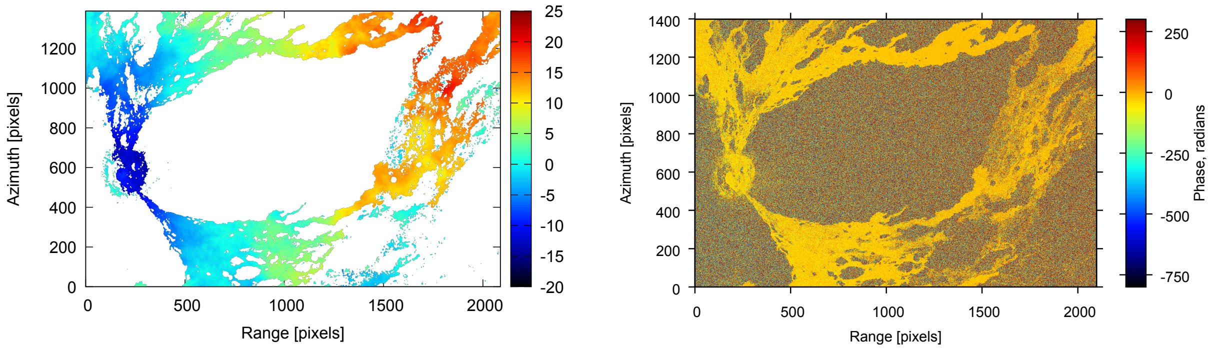

(a) (b)

Figure 2.7: TerraSAR-X pair of June 22nd and July 3rd, 2008 centered on Nyamuragira volcano and its lava field. (a) Conventional unwrapped phase. (b) SBInSAR phase.

Data set and processing

We consider a pair of TerraSAR-X Stripmap images acquired over the Virunga Volcanic Province (DRC) on June 22nd and July 3rd, 2008. These data have an original bandwidth of 150 MHz, an horizontal co-polarization (HH) and a look angle ranging from approximately 24.7° to 28.0°. The acquisitions form a perpendicular baseline of about 13 m associated to an altitude of ambiguity of 300 m.

On the one hand, we apply the conventional InSAR processing, focusing on Nyamuragira volcano and its lava field. The interferometric products are averaged over a 5×5 pixels box, without DEM subtraction, and the interferogram is unwrapped using a coherence guided branch-cut algorithm. We set a coherence threshold of 0.7 below which pixels are dismissed for phase unwrapping. This leaves a main coherent and continuously unwrapped region made of the Nyamuragira's crater and lava field. On the other hand, we apply SBInSAR processing on these images using a spectral decomposition into 5 non overlapping subbands and a weighted linear regression. The unwrapped phase and the SBInSAR phase are given in Figure 2.7.

Observations

For all pixels located in the main coherent area, i.e. the lava field, we record the values of the various detection criteria and make correlative plots of the observations for one criterion against another. A lot of criteria combinations are possible and we present therefore only the most relevant ones in Figure 2.8. Of course, phase variance stability is not taken into account in this correlative study since we cannot simply apply a threshold for this criterion. We first note that there is no gap in the values of the observations: all parameters show a continuously populated range of values and no distinct border exists between populations. However, in some cases, we can observe a relationship between the different parameters.

We have a clear correlation between the multifrequency phase error and the SBInSAR coherence (Figure 2.8a). It was to be expected, since both parameters measures the same quantity in different ways. The slope standard deviation also shows some correlation with the multifrequency phase error and the SBInSAR coherence, but the dispersion is more important in this case (Figures 2.8b and 2.8c). However, goodness-of-fit estimators do not seem to be correlated somehow with phase quality estimators. The dispersion of the linear correlation coefficient is important for low values of the multifrequency phase error (Figure 2.8d). As for the probability Q, its values fill uniformly the space of observations, without giving a clue on what could be the best values of this estimator (Figure 2.8e). Regarding the reduced chi-square, values around

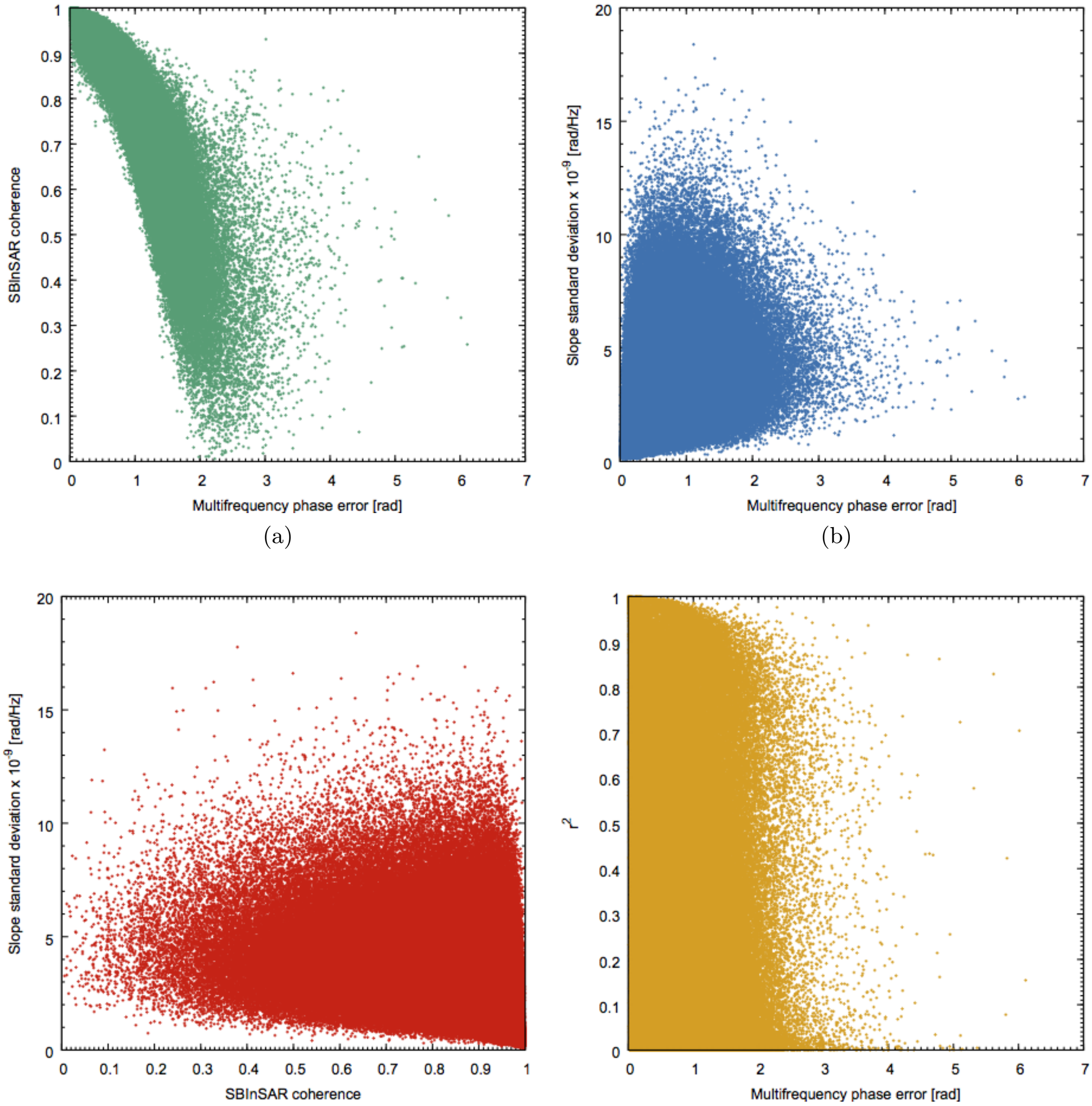

(a) (b)

(c) (d)

Figure 2.8: TerraSAR-X pair of June 22nd and July 3rd, 2008 centered on Nyamuragira volcano and its lava field. Correlative plots of the detection criteria. Each point of the plot represent a pixel of the Nyamuragira's lava field.

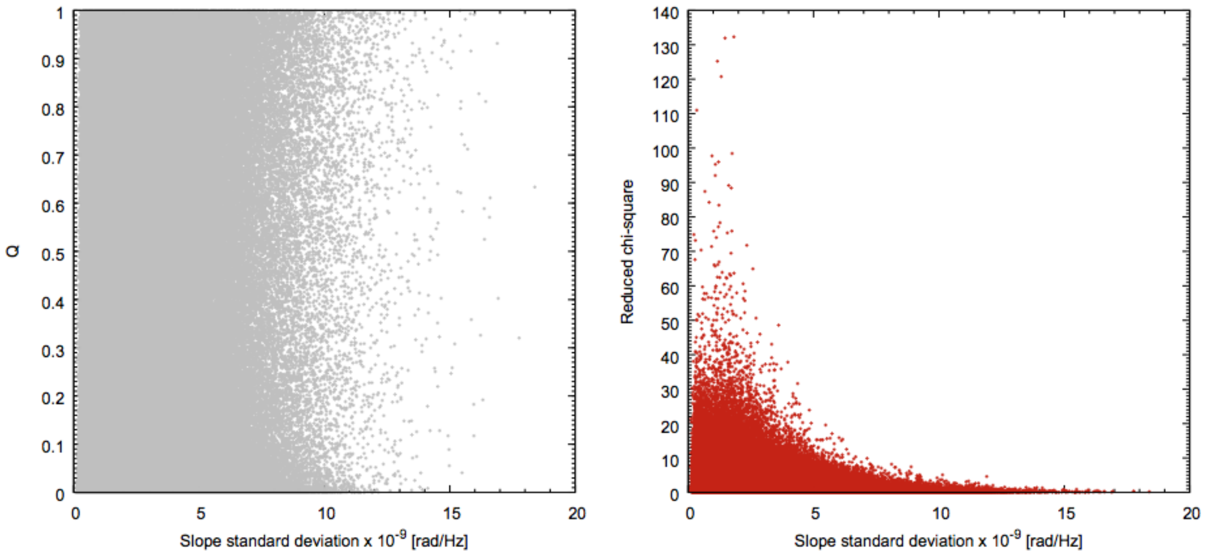

(e) (f)

Figure 2.8: Continued.

Detection criterion	Thresholds
Multifrequency phase error	$0 < \sigma_\nu < 0.5$
Slope standard deviation (X-band)	$0 < \sigma_s < 0.65 \times 10^{-9}$
Spectral coherence	$0.9 < \gamma_\nu < 1.00$
Squared linear correlation coefficient	$0.9 < r^2 < 1.0$
Reduced chi-square	$0.8 < \chi^2_\nu < 1.2$
Plausibility of the fit	$0.05 < Q < 0.75$

Table 2.3: Thresholds set on the estimators for identifying frequency-stable pixels.

unity can correspond to any range of slope standard deviation (Figure 2.8f).

Partition of the space of observations

Let us now determine the partition of the space of observations. The threshold on the slope standard deviation is set by the required precision on the SBInSAR phase and depends on the sensor frequency. Here, it is set to 0.65 rad/GHz. Given the definitions of the reduced chi-square and the probability Q, their ranges of values could not be chosen randomly. We had to choose thresholds in line with the interpretations of these probabilities: a good fit is defined by a reduced chi-square with a value around 1 and a probability Q neither too close to 0, nor 1. Finally, for the other estimators, thresholds have been chosen rather arbitrarily. We know that the SBInSAR coherence should be close to 1, as does the squared linear correlation coefficient. The multifrequency phase error should not be large as it is the a posteriori error on the phase. We set its threshold to 0.5 rad. The applied thresholds are listed in Table 2.3.

Phase ambiguity distribution

In order to evaluate the efficiency of the criteria for discriminating $\mathrm{PS_f}$ from non-$\mathrm{PS_f}$, we have to introduce the concept of phase ambiguities. The procedure for correcting phase ambiguities using SBInSAR is detailed in Section 2.4.

A phase ambiguity is an entire number of cycles that can appear between two regions of an interferogram that are unwrapped independently. In this case, the phase cannot be compared between both regions, due to the unknown constant offset value necessary to level the phase. Given the unwrapped phase $\Delta\phi$ obtained with classical SAR interferometry and the SBInSAR phase $\Delta\varphi$ of the same scene, the phase ambiguity n is estimated for each pixel with coordinate (k, l) from a continuous region as

$$n(k,l) \;=\; \left\lfloor \frac{\Delta\varphi(k,l) \;-\; \Delta\phi(k,l)}{2\pi} \right\rceil,$$

where $\lfloor \cdot \rceil$ is the nearest integer rounding operator. If no error occurs during the phase unwrapping process, the phase ambiguity is supposed to be constant through a given continuous region. We would therefore expect all $\mathrm{PS_f}$ to provide a correct and uniform value of the phase ambiguity, while non-$\mathrm{PS_f}$ would be a source of erroneous estimates. We test the different detection criteria with the previously defined thresholds and select a population of pixels for each criterion. We compute the distribution of phase ambiguity estimates for the selected populations over the lava field. Let us take a look at the normalized distribution of the phase ambiguity estimates (Figure 2.9): when no pixel discrimination is applied, the distribution spreads over a large range of values with a very low probability associated to the mode (Figure 2.9a, grey curve). Obviously, the observations in the wings of the distribution are outliers and must be removed when a detection criterion is applied. The best discrimination is characterized by the narrowest distribution and the highest probability.

For the phase quality estimators (Figures 2.9a and 2.9b), when we take a look at the graph in logarithmic scale, we see that all the criteria remove the unwanted values from the distribution wings. We observe well-peaked distributions for the phase variance stability and the slope standard deviation. This suggests that these criteria are the most efficient ones.

For the goodness-of-fit estimators (Figures 2.9c and 2.9d), we clearly note an unexpected and undesirable shape of the distribution for the linear correlation coefficient. In addition to provide a mode different from the other distributions, this distribution is multimodal and has a lower maximum. Regarding the reduced chi-square and the plausibility Q of the fit, they do not improve much the shape of the distribution. Indeed, they remove some outlier values but the reduction of the function spread is not pronounced and the probability of the mode is not noticeably increased. Given these observations, we conclude that goodness-of-fit estimators are not the most adequate criteria to identify $\mathrm{PS_f}$.

Finally, we also tested a combination of thresholds on several criteria (Figures 2.9e and 2.9f). With the combined thresholds of the multifrequency phase error, the SBInSAR coherence and the slope standard deviation, we do not observe much improvement with respect to the slope standard deviation alone. Actually, only 1% of the targets selected by the slope standard deviation are removed from the distribution by the other two criteria. Therefore, this combined use of criteria does not improve efficiently the $\mathrm{PS_f}$ identification with respect to the slope standard deviation. It performs even less efficiently than the phase variance stability criterion.

Summary

Based on these observations, we get as a first conclusion that goodness-of-fit estimators are not suited to detect frequency-stable targets: neither the reduced chi-square nor the probability Q

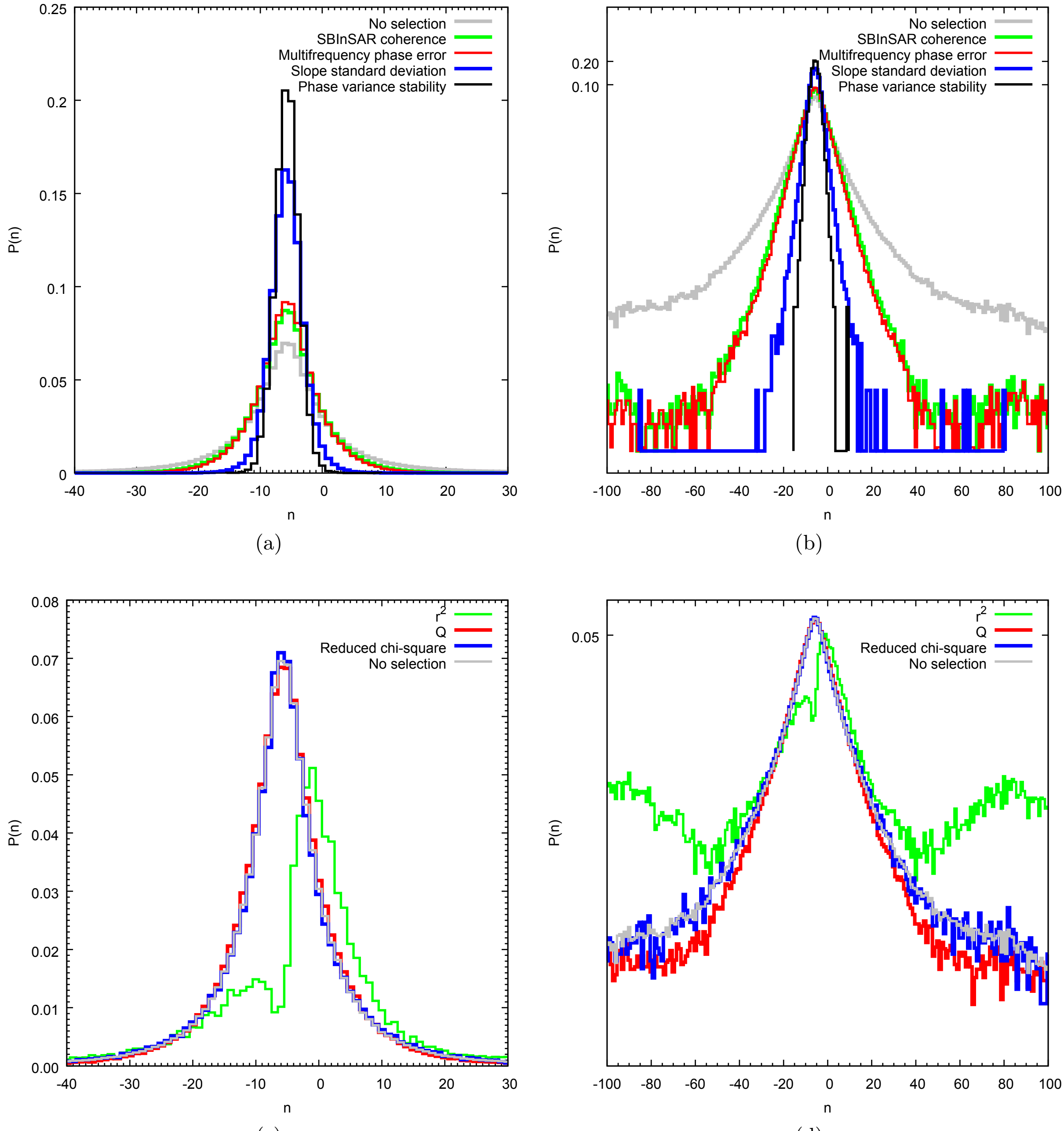

(a)

(b)

(c)

(d)

Figure 2.9: TerraSAR-X pair of June 22nd and July 3rd, 2008 centered on Nyamuragira volcano and its lava field. Normalized distributions of the phase ambiguity estimates over the lava field for different PS_f detection criteria. The y-axis is in logarithmic scale for the right column. (a)-(b) Discrimination with phase quality estimators. (c)-(d) Discrimination with goodness-of-fit estimators.

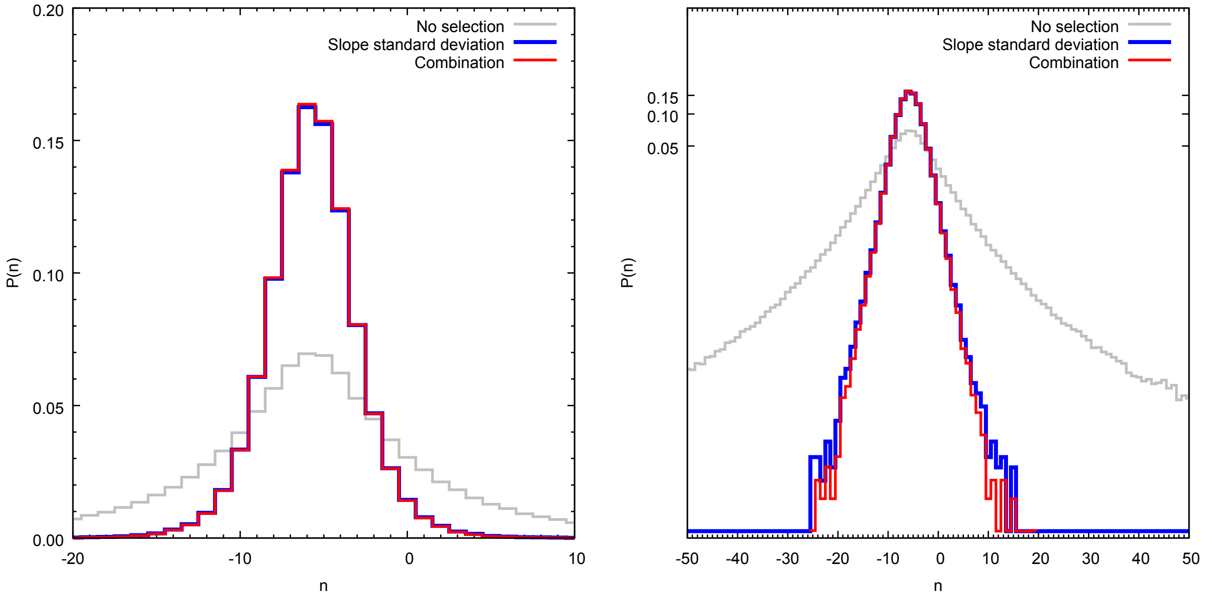

(e) (f)

Figure 2.9: Continued. (e)-(f) Discrimination with the slope standard deviation and a combination of multifrequency phase error, SBInSAR coherence and slope standard deviation.

improve the aspect of the phase ambiguity distribution, and the linear correlation does not even show a regular shape for this distribution.

Regarding the phase quality estimators and given the imposed thresholds, the slope standard deviation performs the best and provides a well-peaked curve for the phase ambiguity distribution. However, it is outperformed by the phase variance stability in this case. Moreover, using a combination of thresholds on several estimators does not seem to improve the detection performance noticeably compared to the slope standard deviation.

2.4 SBInSAR-assisted phase unwrapping

It is well known that phase unwrapping algorithms usually provide relative measurements of the phase. It means that, if no additional information is available, the phase of a pixel is only known with respect to the phase of its neighbours. This causes problems in practice because isolated coherent patches separated by non coherent regions must be unwrapped independently (decorrelation can be due to geometrical distortions such as layover or shadowing, volume scattering or modifications of the ground cover). An unknown phase shift might therefore exist, as represented in Figure 2.10. This prevents from comparing the phases of the two regions. As a practical example, let us cite Nyiragongo volcano: as shown by Figure 2.11, due to the steep topography and the depth of the crater, a discontinuity appears at the border between the rim of the volcano and the bottom of the crater. Both parts are disconnected and it is not possible to directly estimate the level of the lava lake with respect to the rim. The method of the shadows on the lava lake has been developed to monitor the lake level [50, 51], but Split-Band Interferometry could also be a way to overcome this issue.

In this section, we propose an approach based on SBInSAR to complement the InSAR phase unwrapping in order to estimate and correct phase ambiguities [37]. The SBInSAR-assisted phase unwrapping is tested and validated for a pair of TerraSAR-X Spotlight images over the Copahue volcano. We first describe the method, then we present the test site. An indirect

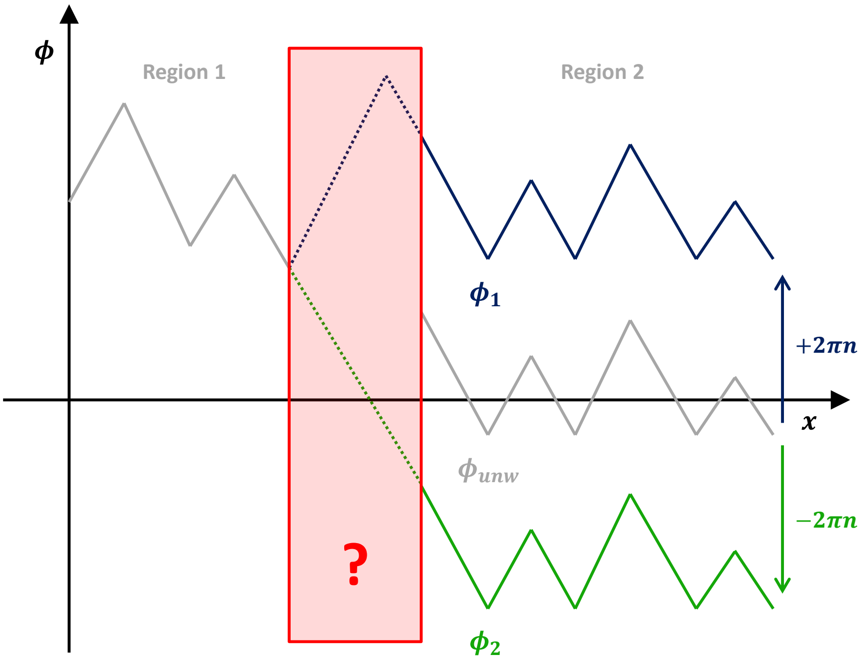

Figure 2.10: Schematic 1D representation of the phase ambiguities. The phases of region 1 and region 2 are disconnected by a decorrelated patch, with no information on the phase behaviour. An unknown shift is introduced between the regions, making them impossible to compare. Here, we show that the unknwon phase behaviour in the decorrelated patch could lead to noticeably different phase shifts.

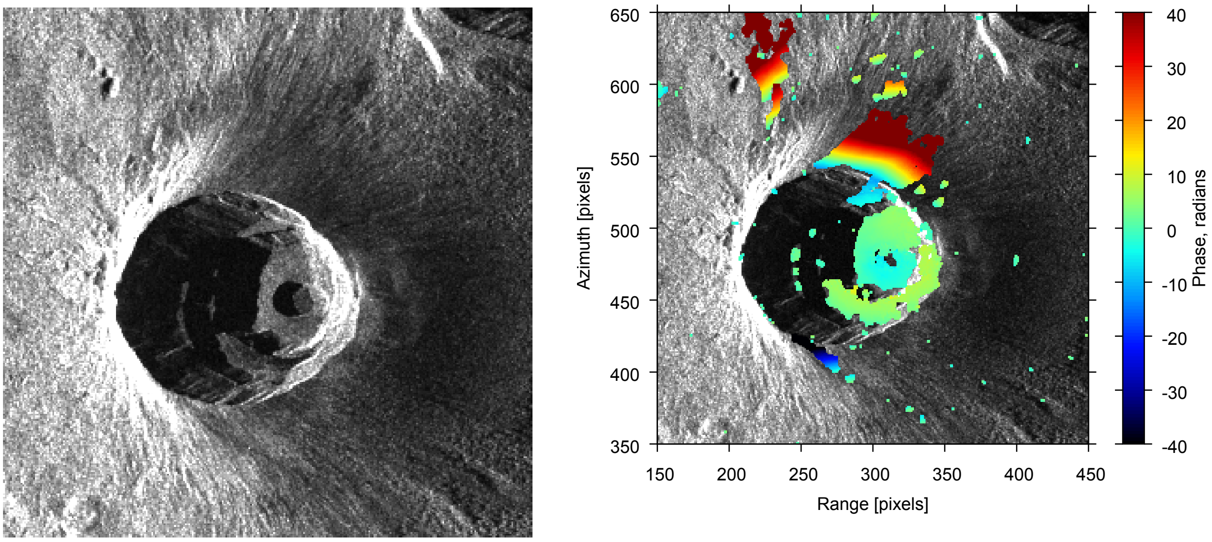

(a) (b)

Figure 2.11: (a) Amplitude image of the Nyiragongo's crater from a Cosmo-SkyMed ascending acquisition on July 11th, 2015. The left part of the internal platforms and the lava lake are shadowed, while the right part of the rim is subject to layover effect. (b) Unwrapped topographic phase over the crater for acquisitions on July 11th and 15th, 2015 overlaid on the amplitude image. The phase on the rim is disconnected from the inside of the crater. A coherence threshold of 0.5 is applied for phase unwrapping.

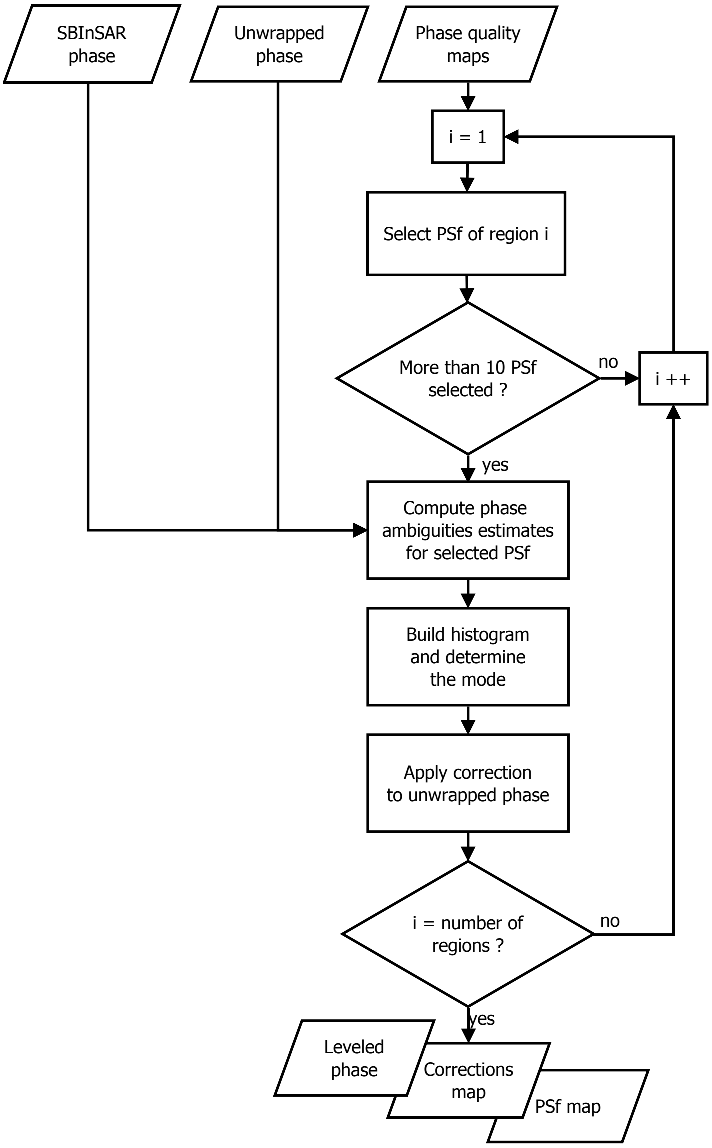

Figure 2.12: Flow chart of SBInSAR-assisted phase unwrapping.

validation procedure is also proposed, along with an indicator of the precision of the results. Finally, we demonstrate the validity of the approach. The results presented in this section were published in Reference [37].

2.4.1 Method

The method presented here estimates and corrects the phase ambiguities of regions separately unwrapped. In this context, we define the phase ambiguity as the phase shift between the unwrapped phase and the absolute phase. We consider the general case where the phase ambiguity is an entire number of cycles $2\pi n$, with n being a positive or negative integer. Assuming that the phase is correctly unwrapped, the phase ambiguity is constant through a region of continuously unwrapped phase. For the sake of clarity, let us stress that the phase ambiguity, or phase-offset, denotes the $2\pi n$-discrepancy but we will largely use these terms to refer to the number of cycles

n alone.

In theory, the knowledge of the absolute phase of a single point should suffice to solve the phase ambiguity, and therefore the presence of a single stable target per region might be enough to estimate it. However, in practice, we have to deal with phase noise, phase unwrapping errors, uncertainties and false detections. This is why we adopt a statistical analysis of the $\mathrm{PS_f}$ to derive the phase ambiguity.

Let us write $\Delta\phi$ the unwrapped phase obtained with the classical phase unwrapping process and $\Delta\varphi$ the SBInSAR phase. For a given $\mathrm{PS_f}$ with coordinates (k, l) in the image, neglecting the noise and the phase unwrapping errors, the unknown number of cycles can be computed as

$$n(k,l) \;=\; \left\lfloor \frac{\Delta\varphi(k,l) \;-\; \Delta\phi(k,l)}{2\pi} \right\rceil, \tag{2.28}$$

where $\lfloor \cdot \rceil$ is the nearest integer rounding operator. The SBInSAR-assisted phase unwrapping considers one region of the phase unwrapping at the time. For each region, it selects $\mathrm{PS_f}$ based on one or several of the criteria presented in Section 2.3.1. Phase ambiguities are then estimated for each selected pixel using Equation (2.28). The rounded value with the largest number of occurrences across the region, i.e. the mode of the distribution, is assumed to be the phase ambiguity we are looking for. Finally, the phase of the considered region is shifted by this amount of cycles in order to correct the phase ambiguity. When the distribution of the estimated phase ambiguities has multiple modes, then no correction can be applied. We do not correct regions with less than 10 $\mathrm{PS_f}$, because they are not statistically meaningful and they frequently show multiple modes.

Algorithm steps are outlined in Figure 2.12. In practice, the described routine provides an image of the levelled unwrapped phase, showing the shifted areas only. A map of the corrected regions is also provided, as well as a mask of the selected $\mathrm{PS_f}$. Since the correction is applied to the conventional unwrapped phase, the original resolution is preserved despite the use of SBInSAR products.

Let us also stress that the SBInSAR-assisted phase unwrapping can be run either in *topographic mode* or in *deformation mode*. In the second case, the residual phase is the unwrapped phase and the DEM is also subtracted from the SBInSAR phase. As an identical topographic phase component is removed from both the unwrapped and SBInSAR phases, we do not expect other changes in the phase ambiguities computation than those due to the improvement of the phase unwrapping.

2.4.2 Validation procedure

For the validation of the SBInSAR-assisted phase unwrapping, we had a limited amount of data at our disposal and no additional information, such as GPS measurements, at suitable locations. Moreover, in order to challenge the method and test its limits, it is necessary to apply it to a large data set. However, it is not possible to have complementary measurements for all the test sites at given dates. Therefore, we designed another way to validate the performance of our approach.

We imagined an indirect validation strategy, that is valid when a branch-cut algorithm [29] is used to unwrap the phase. It consists in artificially disconnecting some patches from a coherent area before the phase unwrapping process. Knowing the unwrapped phase $\Delta\phi_c$ of the *"fully connected"* version of the interferogram and the unwrapped phase $\Delta\phi_d$ of the *"artificially disconnected"* version, and knowing that their values only differ by an entire number of cycles $2\pi m$ with m integer, one can obviously state that

$$m(k,l) \;=\; \frac{\Delta\phi_c(k,l) \;-\; \Delta\phi_d(k,l)}{2\pi}. \tag{2.29}$$

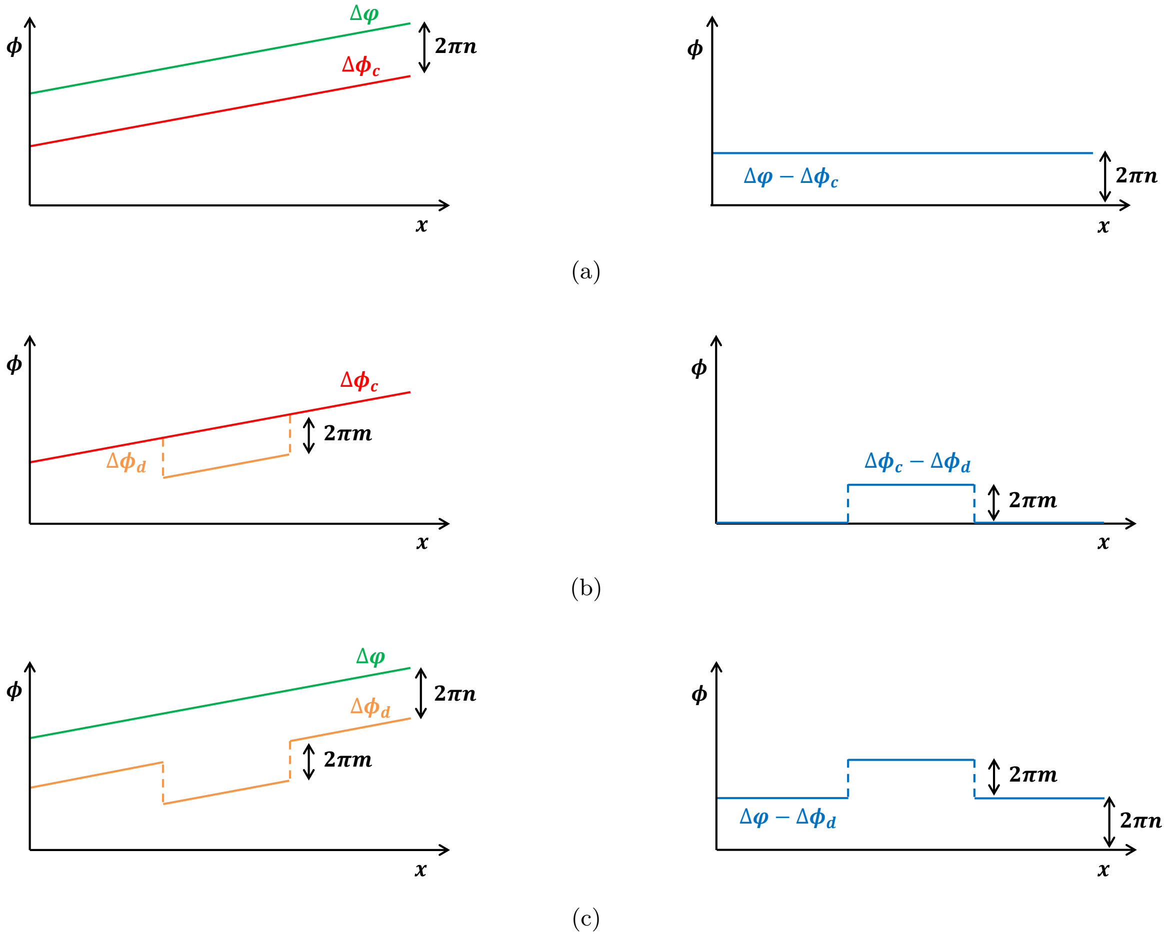

(a)

(b)

(c)

Figure 2.13: Diagrams of the validation procedure for a simplified one-dimensional interferogram. (a) If the connected InSAR phase $\Delta\phi_c$ is subtracted from the SBInSAR phase $\Delta\varphi$, the difference gives an offset $2\pi n$. (b) If a region of the one-dimensional interferogram is disconnected, an offset $2\pi m$ is introduced between the connected InSAR phase $\Delta\phi_c$ and the disconnected InSAR phase $\Delta\phi_d$. (c) If the disconnected InSAR phase is subtracted from the SBInSAR phase, the relative offset $2\pi m$ between the disconnected regions remains the same as in case (b).

This phase-offset will not necessarily be the same as the correction n computed with the SBInSAR-assisted phase unwrapping, but the phase-offset difference between two pixels of coordinates (k_1, l_1) and (k_2, l_2) should be the same for both m and n:

$$n(k_1, l_1) - n(k_2, l_2) = m(k_1, l_1) - m(k_2, l_2). \tag{2.30}$$

If we focus on pixels in two separate regions, then the relative offset values can be used to validate the results, as illustrated in Figure 2.13. Of course, increasing the quantity of disconnected regions improves the reliability of the validation strategy.

2.4.3 Indicator of quality

In the proposed approach for the SBInSAR-assisted phase unwrapping, the phase ambiguity is chosen as the mode of the phase-offset distribution. In order to have confidence in this correction, two requirements are necessary: first, the probability associated to the mode value must be high; second, the dispersion of the distribution must be low. These two conditions are summarized by a low W/H ratio, W and H being respectively the width and the height of the normalized

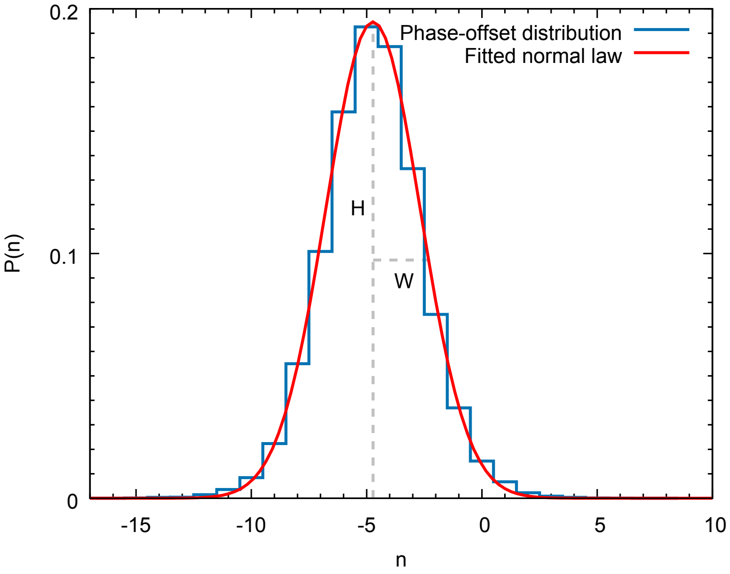

Figure 2.14: Example of phase-offset distribution fitted by a normal law. The height H is given by the maximum of the normal law and the width W by the half width at half maximum.

distribution. The normalized distribution of the rounded phase-offsets n can be fitted by a normal law expressed as

$$f(n) = \frac{1}{\sigma\sqrt{2\pi}} \exp\left(-\frac{1}{2}\left(\frac{n-\mu}{\sigma}\right)^2\right), \tag{2.31}$$

with the expectation value μ and the standard deviation σ being the parameters of the fit. The height of the distribution is defined as the maximum of the fitted normal law and the width is quantified by the half width at half maximum, as represented for the example in Figure 2.14. The ratio is then given by

$$\frac{W}{H} = \frac{\sigma\sqrt{2\ln(2)}}{f(\mu)}. \tag{2.32}$$

The aspect ratio of the distribution is an indication regarding the precision of the measurement, not its accuracy. It will therefore allow to compare the precision of two different estimations, but it will not assess whether the calculated phase ambiguity is correct or not.

2.4.4 Validation case: Copahue volcano

At this stage, we presented the rationale of a method to assist phase unwrapping, we proposed a indirect way to check the phase ambiguity corrections and we defined an indicator of the quality of the result. It is now time to apply these developments to a practical case in order to validate our approach. This time, we choose to focus on Copahue volcano, for which we have Spotlight images that are particularly adequate for SBInSAR processing, instead of Kivu region for which we do not have such acquisitions at our disposal.

Test site

Copahue is an active stratovolcano located at the border between Argentina and Chile, in the northwest of the Argentinean province of Neuquén in the Andes (Figure 2.15a). This volcano

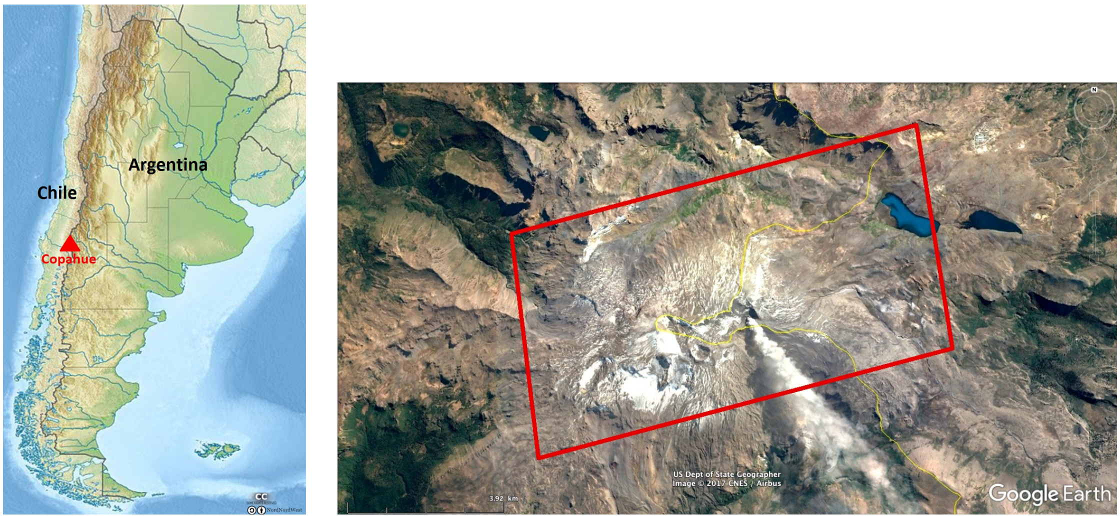

(a) (b)

Figure 2.15: (a) Location of Copahue volcano (red triangle) on the border between Chile and Argentina. (b) Google Earth$^{\mathrm{TM}}$ image of Copahue volcano in 2017. The footprint of the InSAR pair is drawn in red.

has an elliptical shape of about 22 km × 8 km and is oriented along the SW-NE direction. Its summit peaks at almost 3000 m and its nine craters are clustered along the N60°E direction. Only the eastern-most one is active, with its 300 meters of depth containing an acid lake created by the abundant precipitations and the ice melt [52]. The most recent eruptions of Copahue have been reported in 2000, 2012 and 2014 [53]. Deformations observed using InSAR over Copahue volcano are discussed in References [54, 55].

A Google Earth$^{\mathrm{TM}}$ optical view of the area is given in Figure 2.15b. It shows steep topography, little vegetation and a snow cover that can vary over the year. Change in the snow cover and in the liquid water content of the snow can cause local coherence losses in InSAR products. The variety in topography and slope orientations, the important geometrical distortions that can be observed in amplitude images of the volcano (Figure 2.16a), and the presence of natural scatterers make Copahue volcano an interesting site to apply SBInSAR-assisted phase unwrapping.

Data set

The data set consists in two TerraSAR-X Spotlight images acquired on ascending orbits on December 15th and 26th, 2014. Each image is the master image of a pair acquired in Pursuit Monostatic mode, and the ensemble of both constitutes therefore a standard Spotlight interferometric pair. They are acquired in VV-polarization with a look angle ranging from approximately 32.8° to 33.8° and a range bandwidth of 300 MHz. Such a bandwidth makes this example particularly suitable to test SBInSAR-assisted phase unwrapping. The interferometric pair has a perpendicular baseline of about 32 m which corresponds to a height of ambiguity of 163 m, and a temporal baseline of 11 days, which minimizes the effect of temporal decorrelation. SBInSAR phase precision is characterized by a $\frac{\nu_0}{B}$ ratio of 32.17, while the CDR value is of 76.38.

Processing

A spatial averaging of 5×5 pixels is applied to the images and a coherence threshold of 0.5 is set, below which the phase is dismissed for unwrapping. The phase is unwrapped using a coherence-guided branch-cut algorithm [41], rather than the popular SNAPHU software [56–58] because it guarantees a phase ambiguity that is an integer number of cycles, as explained in Chapter 1. The

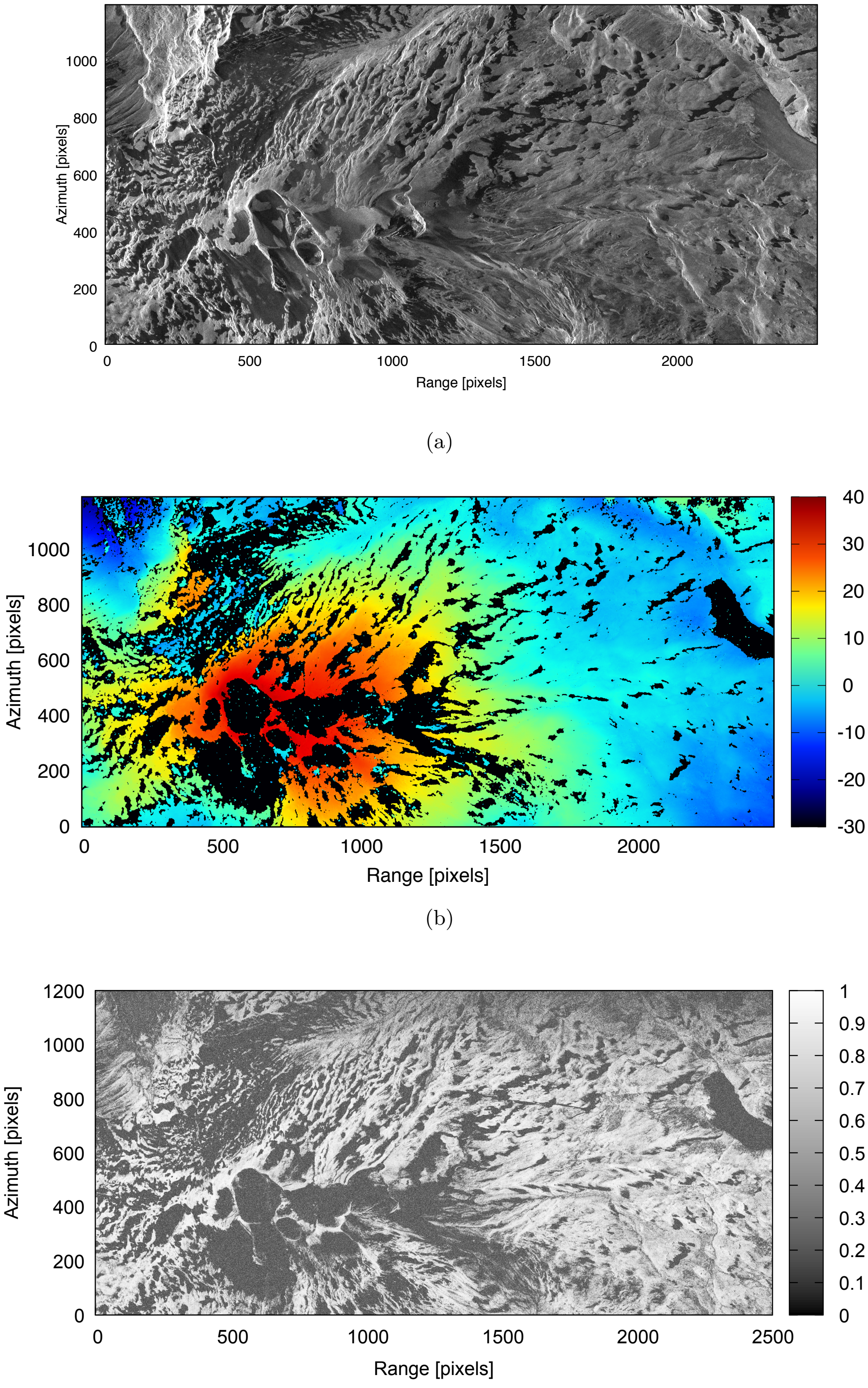

(a)

(b)

(c)

Figure 2.16: Copahue test case, December 15th - 26th, 2014. (a) Non-calibrated amplitude image of the area on December 15th, 2014. (b) Connected version of the unwrapped phase. Colour chart values are given in radians. (c) Coherence map.

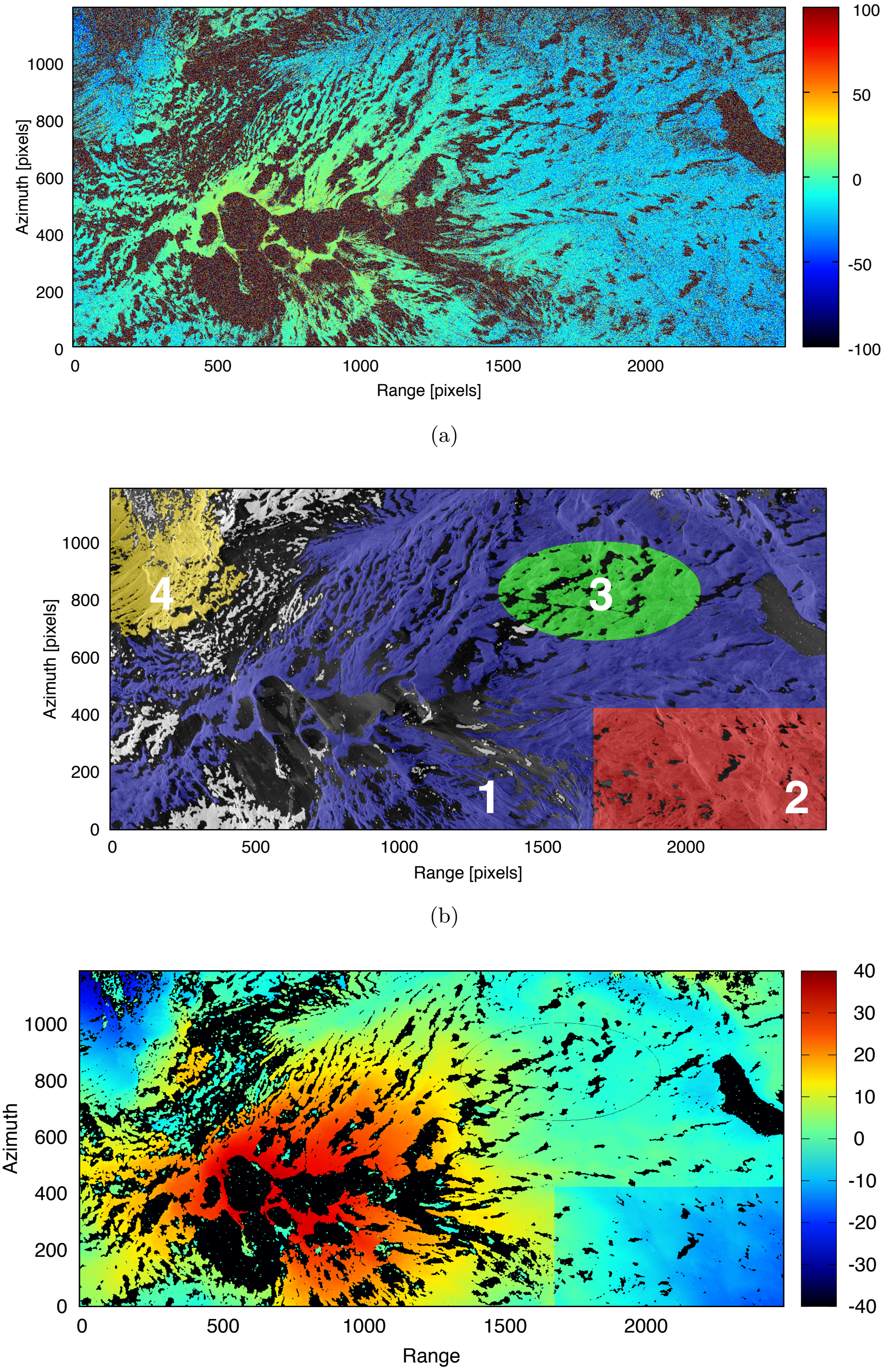

(a)

(b)

(c)

Figure 2.17: Copahue test case, December 15th - 26th, 2014. (a) SBInSAR phase. The colour scale has been tightened for better contrast. (b) Map of the artificially disconnected regions. The blue region, the red rectangle, the green ellipse and the yellow area are respectively referred to as region 1, 2, 3 and 4. White areas represent the naturally disconnected region while black areas are the regions masked by the coherence threshold. (c) Disconnected version of the unwrapped phase. Colour chart values are given in radians.

Relative phase-offset	**Cycles**
$m_1 - m_2$	-1
$m_1 - m_3$	0
$m_1 - m_4$	-1
$m_2 - m_3$	1
$m_2 - m_4$	0
$m_3 - m_4$	-1

(a)

Phase-offset	**Cycles**
n_1	-3
n_2	-2
n_3	-3
n_4	-2

(b)

Table 2.4: Phase-offset of artificially disconnected regions of the Copahue test case, December 15th - 26th, 2014. (a) Relative phase-offset values. (b) Computed phase-offset corrections. Indices in subscript refer to the number of the phase unwrapping region.

coherence map and the corresponding unwrapped InSAR phase are presented in Figure 2.16. In the coherence map shown in Figure 2.16c, large decorrelated patches are present in regions corresponding mainly to the snow cover. In Figure 2.16b, we observe a smooth phase gradient on the main part of the interferogram and a number of smaller regions that are phase-shifted with respect to the main area.

In order to apply our validation scheme, we artificially cut off three patches of different shapes from the main region. The map of the disconnected regions is shown in Figure 2.17b and the corresponding unwrapped phase is found in Figure 2.17c. Comparing it with the connected version of the unwrapped phase, it is obvious that a phase shift has been introduced in region 2. The relative phase-offsets computed following Equation (2.29) are given in Table 2.4a.

Regarding the SBInSAR processing, images are split into 5 subbands of 60 MHz and a weighted linear regression is applied. Given the 300 MHz of original bandwidth, the subbands do not overlap and this large bandwidth ensures the quality of the phase measurements. The SBInSAR phase (Figure 2.17a) features large areas of noisy phase corresponding in general to noncoherent areas of the InSAR phase. The high dispersion of SBInSAR phase values clearly illustrates the spectral instability of most scatterers and highlights the need for a selection of adequate pixels.

Let us stress that studying deformations over Copahue volcano is outside the scope of the present study, as we wish to make a methodological demonstration only. Therefore, no DEM is used to remove topographic information of the phase during the InSAR processing. Hence the analyzed signal contains the topography but also possible deformations or artifacts from atmospheric origin.

Results and discussion

The SBInSAR-assisted phase unwrapping is carried out on the four artificially disconnected regions and different PS_f detection criteria are tested. In this study case, we only test the multifrequency phase error, the slope standard deviation and the phase variance stability criteria, because the first one was the most used in previous studies and the two others are suspected to be the most efficient, as shown in Section 2.3.2. Thresholds of 0.5 rad and 0.65×10^{-9} rad/s are used for the multifrequency phase error and the slope standard deviation, respectively. The number of selected PS_f per region and per detection criterion is featured in Figure 2.18a. The first region is noticeably larger than the other three and it shows therefore a larger amount of PS_f for any criterion. The multifrequency phase error is the criterion that selects the largest amount of targets. However, all criteria define curves that follow the same trend. The phase variance stability selects approximately 2-3% of the initial population as stable targets, while the proportion is about ten times larger for the slope standard deviation.

$\mathrm{PS_f}$ Selector	Region 1 W/H	Region 2 W/H	Region 3 W/H	Region 4 W/H
None	54	43	43	85
σ_ν	25	26	25	30
σ_s	12	14	12	13
$\sigma^2_{\phi_i}$	8	9	8	9

Table 2.5: Aspect ratio W/H of the phase-offset distributions for the Copahue test case, December 15th - 26th, 2014.

With and without $\mathrm{PS_f}$ selection, the estimated phase ambiguities are the same for all artificially disconnected regions. These corrections are given in Table 2.4b and their relative values are consistent with the expected offsets of Table 2.4a. Even though the four situations lead to similar estimations, precision of the results is not quite the same. With the normalized histogram of the phase ambiguities in region 3 shown in Figure 2.18, we visualize the variable dispersion of the distributions, even if the mode remains the same for all criteria. As explained in Section 2.4.3, the quality of the distribution can be quantified by the aspect ratio W/H, whose values are given in Table 2.5. When no detection criterion is applied, the distribution spreads over a large range of values and the probability of the mode is quite low. Distributions for the other regions in the absence of $\mathrm{PS_f}$ selection have similar behaviour and they all exhibit a W/H value of about $45 - 55$, except for region 4, which has a noticeably larger value of 85. This is probably due to the large portion of noisy phase in this zone, which may contain false detections. When the multifrequency phase error selection is applied, the aspect ratio is lowered and the contrast in W/H is significantly reduced. The aspect ratio is still improved by a factor 2 with the standard deviation of the slope, but the best aspect ratio is reached by the phase variance stability.

The W/H ratio seems to be correlated with the size of the $\mathrm{PS_f}$ population: the smaller the amount of selected targets, the lower the aspect ratio. Actually, when targets are discriminated on a more stringent basis, the number of outliers is decreased. Based on this aspect ratio, the phase variance stability seems to lead to the most precise results. However, when applied to less favorable cases (e.g. smaller bandwidth and/or larger baseline) the criterion could be too restrictive and select a population too small for a statistically meaningful approach. The standard deviation of the slope is a satisfactory alternative in such cases.

Now that our approach has been validated regarding the phase ambiguities, we perform SBInSAR-assisted phase unwrapping on both artificially and naturally disconnected phase unwrapping regions. Let us remind that a region is corrected if it has more than 10 $\mathrm{PS_f}$ detected and if the distribution mode is unique. Without assessing the exactness of the corrections, we observe that the multifrequency phase error allows the correction of 33 regions out of 1796 while the slope standard deviation corrects 74. This difference is mainly due to the numerous multiple modes observed for the multifrequency phase error. For naturally disconnected regions, we observed once again that the phase variance stability detects fewer targets than the other two criteria, but we also note that the majority of the pixels identified by the phase variance stability are also detected by the slope standard deviation. Less than 1% of the population is selected by the phase variance only.

For regions with a size larger than 30 $\mathrm{PS_f}$, we observe in Figure 2.19a that stable proportions of about 20-30% and 25-35% of the targets, respectively selected by the slope standard deviation and the phase variance stability, contribute to the mode of the phase-offset distribution. Even though this proportion can be larger for regions containing less $\mathrm{PS_f}$, then it becomes more variable. This let us think that the phase ambiguity estimated for regions with less than 30 $\mathrm{PS_f}$ is not reliable because the $\mathrm{PS_f}$ population is not large enough to be statistically meaningful.

Since the availability of a population of stable targets the key point of the SBInSAR-assisted phase unwrapping, it is necessary to guarantee the presence of PS$_{\mathrm{f}}$ in a given region, for example with the existence of a relationship between the number of selected PS$_{\mathrm{f}}$ and the size of a region. This would allow to determine the minimum size of a corrigible region and make the results of the method more predictable. Having a look at Figure 2.19b, it might seem at first sight that a relationship exists between the size of a patch and the PS$_{\mathrm{f}}$ population. Nevertheless, it is important to stress that the axes are in logarithmic scale and that no such obvious behaviour is observed for a linear scale. The stable nature of a target is probably related to its intrinsic characteristics and/or the geometry of observation, which would cause an heterogeneous distribution of stable targets across the scene. Physical features of PS$_{\mathrm{f}}$ will be investigated in more details in Section 2.7. Nonetheless, we observe that when the standard deviation of the slope is considered, the largest region with no PS$_{\mathrm{f}}$ at all is made of less than 400 pixels. For the phase variance stability criterion, the largest region has a size of 3665 pixels, but most of them contain less than 500 pixels. Very small regions are not corrected in general, as they often do not contain stable scatterers.

Summary

Let us review shortly the results of this section. First, we demonstrated that the proposed method for correcting phase ambiguities is valid in the case of TerraSAR-X Spotlight acquisitions. The expected corrections were retrieved whatever the detection criterion, but the best aspect ratio was achieved by the phase variance stability. However, this criterion is very restrictive. A better compromise between the accuracy and the number of corrected regions is obtained for the slope standard deviation.

We also noted that a minimum population (> 30 PS$_{\mathrm{f}}$) seems to be required to have a reliable distribution of the phase-offset. Unfortunately, we observed that no relationship exists between the size of a region and the number of PS$_{\mathrm{f}}$ it contains. Therefore, we have no certainty to find stable targets at a given location, even in large regions.

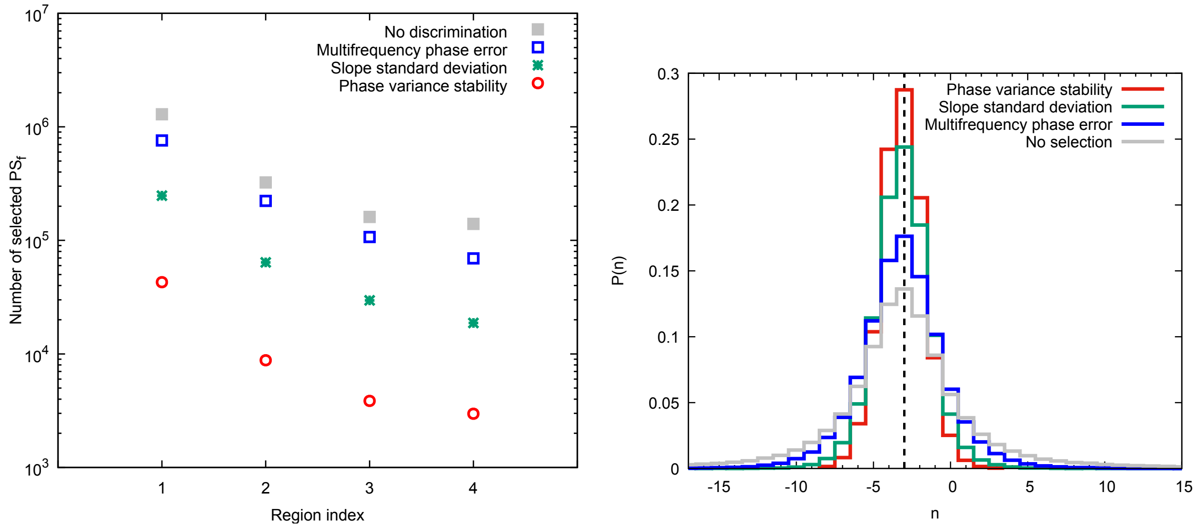

(a) (b)

Figure 2.18: Copahue test case, December 15th - 26th, 2014. (a) Amount of selected PS$_{\mathrm{f}}$ for regions 1 to 4, with different detection criteria. The y-axis is in logarithmic scale. (b) Normalized histograms of the phase-offset values for region 3. The gray line represents the case for which no selection of PS$_{\mathrm{f}}$ is applied. Other curves represent different PS$_{\mathrm{f}}$ detection criteria. The vertical dashed line indicates the expected phase ambiguity. Similar figures are obtained for the other regions.

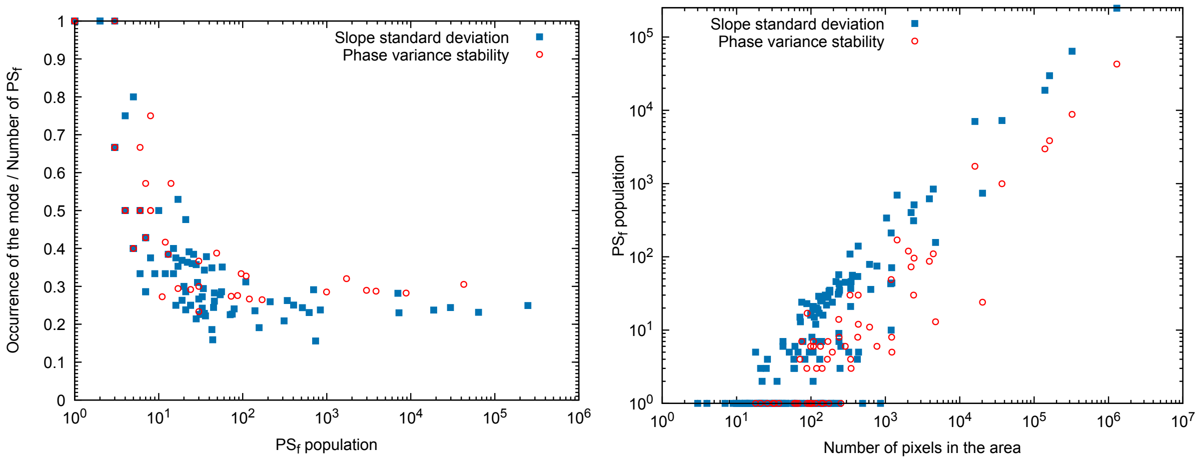

(a) (b)

Figure 2.19: Copahue test case, December 15th - 26th, 2014. (a) Probability of the phase-offset distribution mode as a function of the amount of detected PS$_f$ in a given region, for both artificially and naturally disconnected areas. Regions with multiple modes are not represented. The x-axis is in logarithmic scale. (b) PS$_f$ population as function of the size of the phase unwrapping region, for both artificially and naturally disconnected areas. Regions with no PS$_f$ are not represented. Axes are in logarithmic scale.

Relative phase-offset	**Cycles**
$m_1 - m_2$	-1
$m_1 - m_3$	2
$m_1 - m_4$	-1
$m_2 - m_3$	3
$m_2 - m_4$	0
$m_3 - m_4$	-3

Table 2.6: Nyamuragira test case, June 22nd - July 3rd, 2008. Relative phase-offsets of artificially disconnected regions. Indices in subscript refer to the number of the phase unwrapping region.

2.5 Optimum split-band parameters

In Section 2.2, we set the theoretical basis of the SBInSAR phase behaviour regarding the processing and acquisition parameters. Here, we consider a practical example to determine the optimum split parameters and find an agreement with the theoretical behaviour of the parameters.

Data set

We use the same pair of TerraSAR-X Stripmap acquisitions as the one studied in Section 2.3.2. These images were acquired over the Virunga Volcanic Province (DRC) on June 22nd and July 3rd, 2008 with a bandwidth of 150 MHz, an horizontal co-polarization (HH) and a look angle at mid-range of approximately 26°. The acquisitions form a perpendicular baseline of about 13 m corresponding to an altitude of ambiguity of 300 m.
Because the area cover consists mostly in volcanic rocks and dense vegetation, and due to the smaller bandwidth of the images, retrieving the phase-offsets turns out to be more challenging in this case than for the Copahue test case. It is therefore a good example to test the performances of SBInSAR with respect to different parameters combinations.

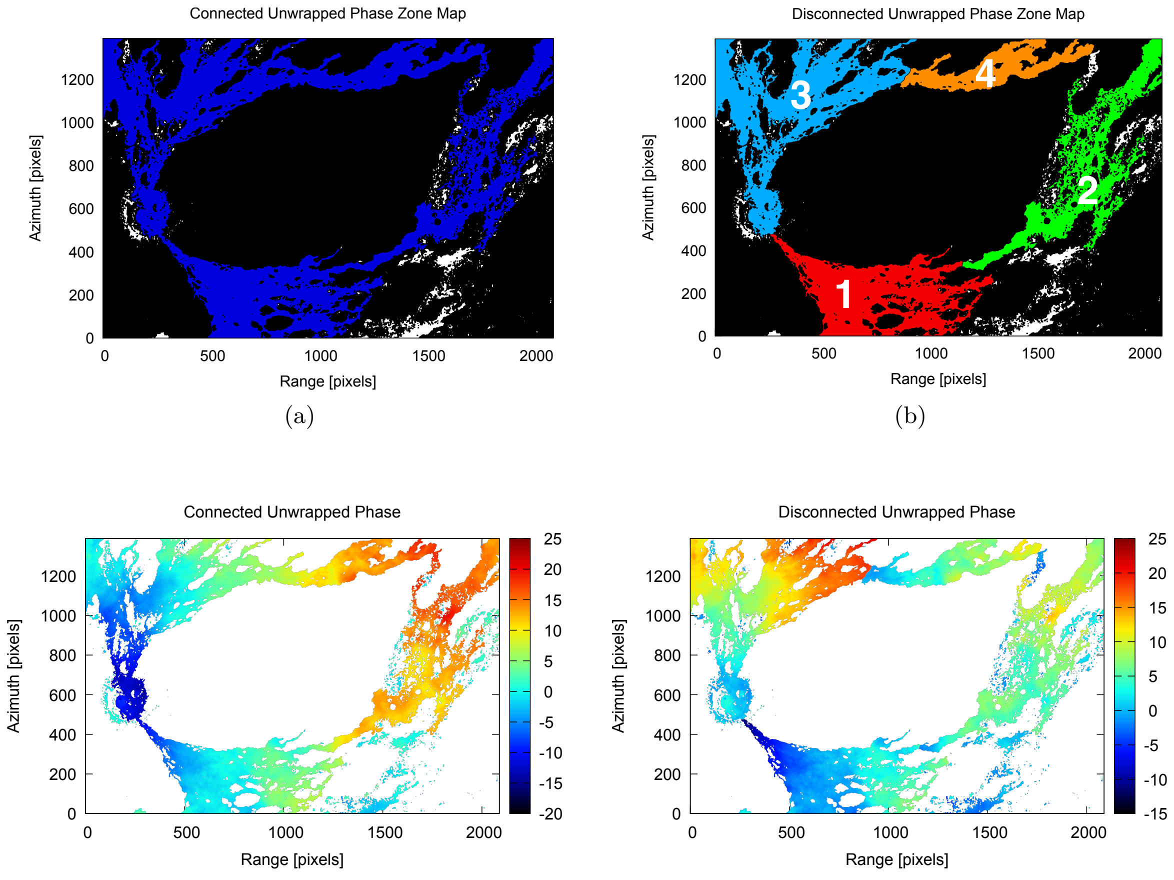

(a) (b)

(c) (d)

Figure 2.20: TerraSAR-X pair of June 22nd and July 3rd, 2008 centered around Nyamuragira volcano. (a) Map of the main phase unwrapping region for the connected case. (b) Map of the artificially disconnected regions. Red, green, blue and orange areas are respectively referred to as zone 1, 2, 3 and 4. (c) Unwrapped phase of the connected case. (d) Unwrapped phase of the artificially disconnected case.

Processing

In a first step, we apply the conventional InSAR processing, focusing on the Nyamuragira volcano and its lava field. The interferometric products are averaged over a box of 5×5 pixels, without DEM subtraction, and the interferogram is unwrapped using the same branch-cut algorithm as for the Copahue example, with a coherence threshold of 0.7. This leaves a main coherent and continuously unwrapped region made of the Nyamuragira's crater and lava flows. The unwrapped area and the associated unwrapped phase are shown in Figures 2.20a and 2.20c.

In a second time, following the same strategy as for the Copahue example, we separate the main coherent area into four regions by introducing artificial branch-cuts and we perform phase unwrapping once again (Figures 2.20b and 2.20d). The relative phase ambiguities for the validation are given in Table 2.6.

Finally, the SBInSAR-assisted phase unwrapping is applied to the study case for several spectral decompositions. We vary the amount of subbands ($N = 5, 9, 15$) as well as the partial bandwidth ($B_s = 30, 50$ MHz). For each combination of split parameters, we also consider a linear regression of the phase that can be weighted or not. All combinations of parameters correspond to overlapping subbands, except those with 5 subbands of 30 MHz. In Figure 2.22a, the SBInSAR phase is provided for a such spectral decomposition with a weighted linear regression of the phase. The SBInSAR phase is noisier outside the lava field, on vegetated areas where coherence is lost. We apply the slope standard deviation as $\mathrm{PS_f}$ detection criterion, with an upper threshold of 0.5 rad/GHz. Given the aspect of the SBInSAR phase, we expect stable targets to be located preferentially on the lava flows.

Parameters analysis

The phase ambiguities estimated for the different combinations of parameters are given by the histogram of Figure 2.21. Comparing it with the values given in Table 2.6, we observe that the relative phase-offsets are satisfied by the non overlapping weighted case only, with 5 subbands of 30 MHz. The other parameters give rise to errors of one cycle for at least one region, sometimes more. Therefore, we deduce that the correct phase ambiguities are those estimated by the weighted non overlapping case and that this is the best combination of parameters. Let us note that a one-cycle error represents a variation of 300 m in the topography estimate.

In Figure 2.22b, the detected $\mathrm{PS_f}$ population of the non overlapping weighted case is mapped over an amplitude image, with colours associated to the different unwrapping zones. We observe that the portion of stable targets is much higher in zone 4 than in the other three. Actually, the presence of $\mathrm{PS_f}$ seems to be linked to the coherence and therefore the age of the lavaflows: referring to the Nyamuragira lava field map (see Figure 2, p.3), we observe that the amount of detected $\mathrm{PS_f}$ is the largest at the location of the 2002 lava flow, the most recent and the most coherent flow within the frame at the time of acquisition; the amount of detection decreases a bit for the flow of the 2001 eruption and becomes sparse for older flows. A priori, regions with a high density of $\mathrm{PS_f}$ are less subject to the split-parameters effect: despite the missed detections, the selected population is still be significant whatever the split parameters and the parameters do not influence much the phase ambiguity estimation.

We now focus on region 4, but the following conclusions can also be drawn for the other regions,

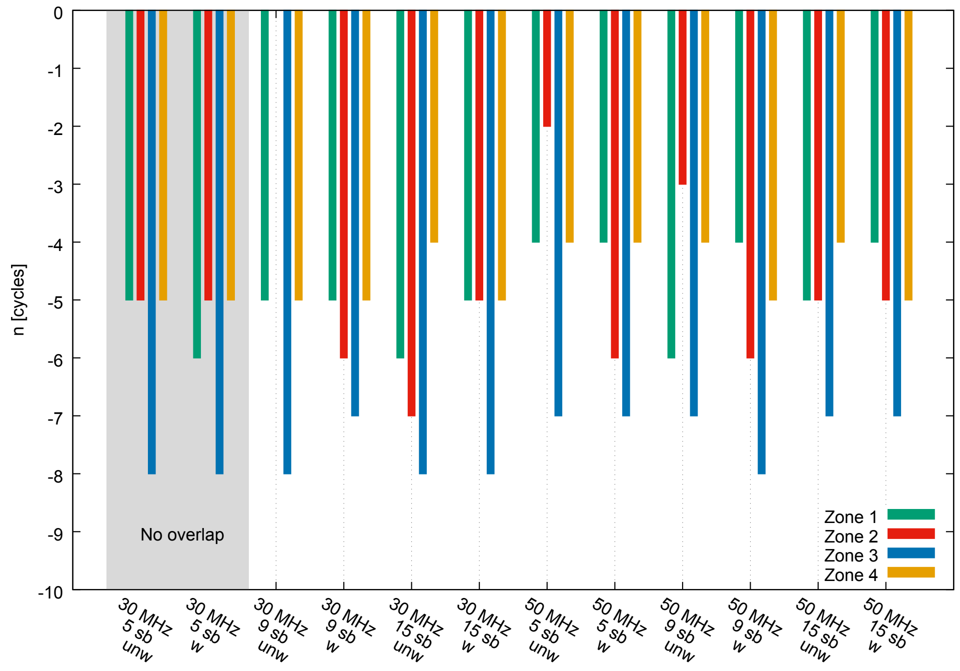

Figure 2.21: Nyamuragira test case, June 22nd - July 3rd, 2008. Histogram of the phase-offsets computed for different combinations of parameters in the artificially disconnected case. The expected relative offsets are only retrieved for the case of 5 subbands of 30 MHz and a weighted linear regression.

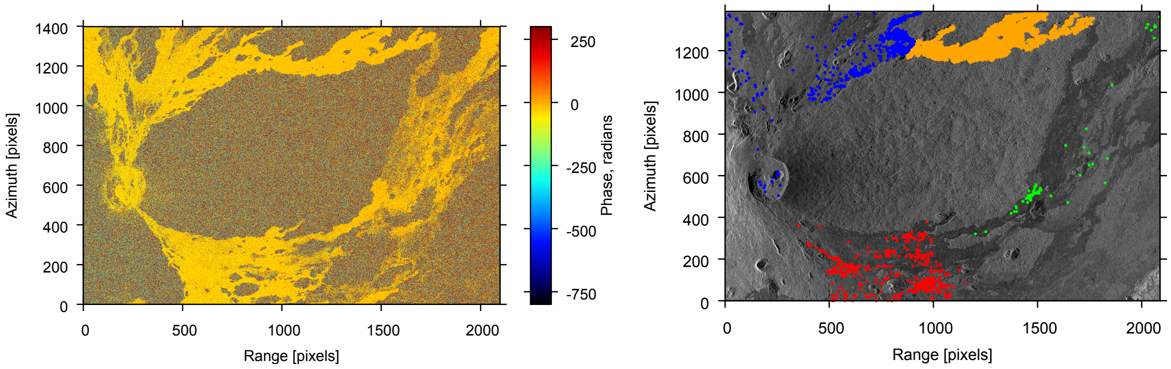

(a) (b)

Figure 2.22: Nyamuragira test case, June 22nd - July 3rd, 2008. (a) SBInSAR phase of June 22nd and July 3rd, 2008 acquisitions. The SBInSAR phase is calculated for a spectral decomposition into 5 subbands of 30 MHz, with a weighted linear regression. (b) Map of the $\mathrm{PS_f}$ detected with the slope standard deviation overlaid on an amplitude image of the area. Red, green, blue and orange colours correspond to $\mathrm{PS_f}$ detected in zones 1, 2, 3 and 4 respectively.

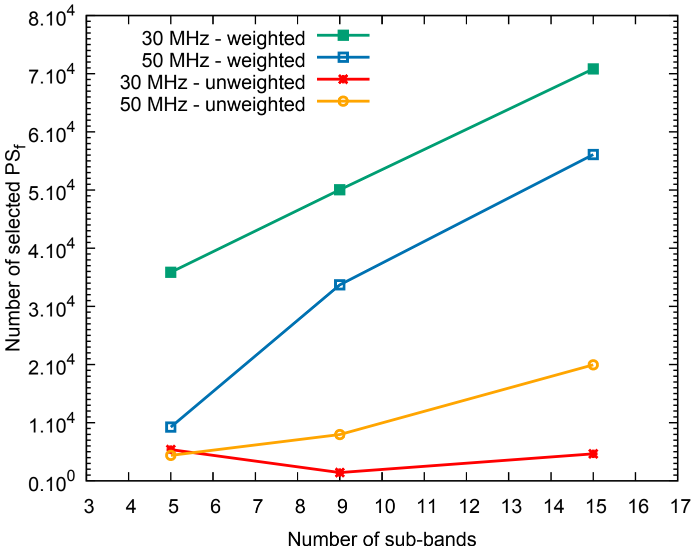

Figure 2.23: Nyamuragira test case, June 22nd - July 3rd, 2008. Increase of the selected $\mathrm{PS_f}$ population with the number of subbands, in the case of zone 4.

even though the results are not presented here. In Section 2.2, we noted that the SBInSAR phase error follows in theory a $\sim \frac{1}{\sqrt{N}}$ law. Hence, we expect a more precise phase estimate and more $\mathrm{PS_f}$ detected when the number of subbands N is large. Indeed, Figure 2.23 shows the $\mathrm{PS_f}$ population increasing with the number of subbands for two values of the partial bandwidth, in the weighted and unweighted cases. An anomaly is spotted for the data point corresponding to the non overlapping unweighted case, where the curve does not have a monotonic increase. We also observe more targets selected in the case of a weighted linear regression. Looking at the phase-offset distributions of Figure 2.24a, we see that despite a larger dispersion, the weighted case tends to compute the correct offset more often than the unweighted case.

The theory also tells us that the smaller the partial bandwidth, the better the precision of the SBInSAR phase, even though a trade-off must be found regarding the resolution loss. In Figure 2.24b, distributions in the case of a 50 MHz partial bandwidth show larger dispersion than those in the case of a 30 MHz partial bandwidth, as expected from theoretical considerations.

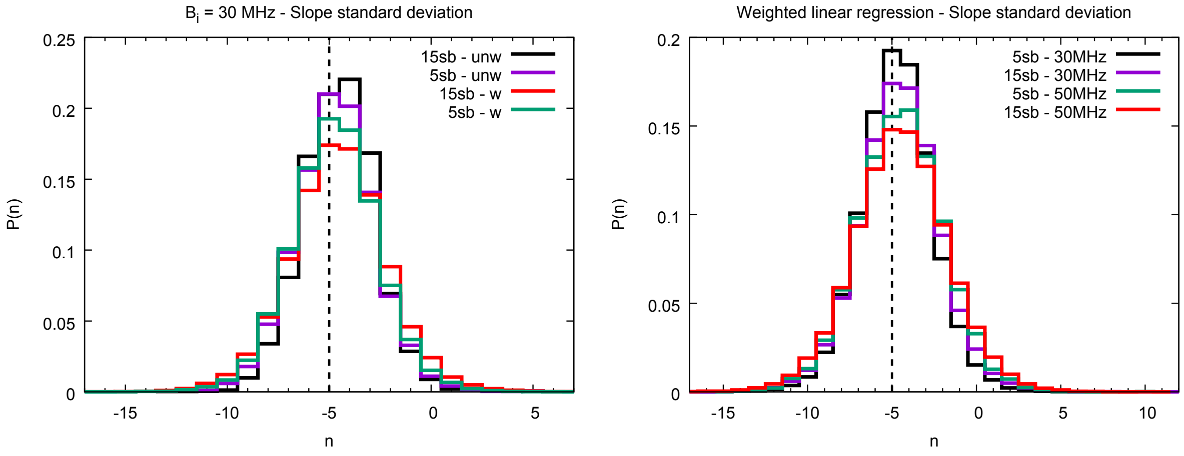

(a) (b)

Figure 2.24: Nyamuragira test case, June 22nd - July 3rd, 2008. Normalized phase-offset distributions across zone 4. (a) Comparison of the phase-offset distributions in the weighted/unweighted cases, for subbands of 30 MHz. (b) Comparison of the phase-offset distributions in the cases of a partial bandwidth of 30 MHz/50 MHz, for a weighted linear regression. The vertical dashed line indicates the expected phase ambiguity.

Moreover, the combination of $N = 5$ and $B_s = 50$ MHz shows a mode with a one-cycle error with respect to the expected phase ambiguity. Considering values of the CDR, $B_s = 30$ MHz is associated to a CDR of 64 while $B_s = 50$ MHz corresponds to a better value of 107. It points out that, in this particular case, the precision of the SBInSAR phase prevails over the loss of resolution.

Summary

Let us sum up briefly the observations made in this section: first, the best spectral decomposition corresponds to a split into 5 non overlapping subbands, with an additional weighted linear regression. If the user prefers overlapping subbands, then he should favor a large number of those. Second, we observe that the density of frequency-stable pixels is higher on recent, thus coherent, lava flows. Moreover, the phase behaviour expected from the theory is conclusive with an increase of the number of $\mathrm{PS_f}$ with the number of subbands. Finally, weighted linear regression appears more efficient to retrieve the phase ambiguity.

2.6 The frequency-stable targets detection problem

So far, Split-Band Interferometry has been considered to estimate the phase ambiguities introduced in the phase by the phase unwrapping. Based on a detection criterion, a $\mathrm{PS_f}$ population is selected for each independent area and statistics helps us to define the phase ambiguity of the region. However, it is interesting to go the other way around and reverse the approach in order to determine which detection criterion operates the best. Indeed, in Section 2.3.2, we got a first insight on the behaviour of the detection criteria regarding spectrally stable targets, but we did not evaluate quantitatively their detection efficiency. In this section, we formulate the detection of frequency-stable targets as a probabilistic decision process, we evaluate the detection, non detection and false alarm rates and we compare the results obtained for different detection criteria.

Here is the general idea: instead of selecting a population of stable targets to determine the phase ambiguity, we start from an estimate of this phase ambiguity and look for the pixels that can be associated to this supposedly correct offset or to a really close value. Besides, we select $\mathrm{PS_f}$ using different criteria, and we compare the population with the correct mode to the populations selected by the detection criteria. At this stage, we have two types of populations to help us decide on the nature of the scatterers and define the probabilities.

Data set and processing

We use the same data set as for the definition of the optimum split-band parameters, whose parameters are described in detail in Section 2.5. It is a TerraSAR-X pair of Stripmap images acquired on June 22nd and July 3rd, 2008 over the Nyamuragira area. The InSAR processing parameters are the same as before, except for the area of interest on the Nyamuragira which is slightly larger. We apply a spatial averaging of 5×5 pixels. This time, we do not introduce artificial cuts and we consider the whole lava field. Since it has been demonstrated in the previous example that this combination leads to the best results, we apply a spectral decomposition into 5 subbands of 30 MHz without overlap and a weighted linear regression.

Phase ambiguity population

In a first step, we must estimate the phase ambiguity associated to the main unwrapped region and determine the population of pixels leading to the corresponding ambiguity, or a value close to it. These pixels constitute the so called *phase ambiguity population.*

In practice, the phase ambiguity $n(k,l)$ is estimated for each pixel with coordinates (k,l) belonging to the studied region using Equation (2.28). The value with the largest occurrence is considered as the *true* phase ambiguity n_{true}. By comparing the results with the previous test case validated for the same data set, we are confident that we obtain the correct offset. Once the phase ambiguity is determined, pixels with the correct estimation of the ambiguity or an acceptable error of one cycle are selected. Formally, a pixel with coordinates (k,l) is part of the phase ambiguity population if

$$n_{\text{true}} - 1 \;\leqslant\; n(k,l) \;\leqslant\; n_{\text{true}} + 1. \tag{2.33}$$

In order to formulate the problem, it is necessary to define the two possible states of a target: s_0 for a non-$\mathrm{PS_f}$ and s_1 for a $\mathrm{PS_f}$. In the context of this study, the main interest of selecting $\mathrm{PS_f}$ is to determine the phase ambiguity. Therefore, since we have not established a definition yet, we can define a frequency-stable pixel as a target that produces the expected ambiguity. Based on this assumption, it is possible to define the probability $p_1 = p(s_1)$ of a pixel to be a $\mathrm{PS_f}$ located in the considered region as the proportion of pixels with the correct phase-offset.

Detection criterion	**Thresholds**
Multifrequency phase error	$0 < \sigma_\nu < 0.05$
Slope standard deviation (X-band)	$0 < \sigma_s < 0.65 \times 10^{-9}$
Spectral coherence	$0.95 < \gamma_\nu < 1.00$
Squared linear correlation coefficient	$0.9 < r^2 < 1.0$
Reduced chi-square	$0.8 < \chi^2_\nu < 1.2$
Plausibility of the fit	$0.05 < Q < 0.75$
Phase variance stability	$\sigma_{\phi_i} < \sigma_{\phi,max}$

Table 2.7: Frequency-stable targets detection problem. Thresholds set on the detection criteria.

The a priori probability $p_0 = p(s_0)$ for a pixel not to be a $\mathrm{PS_f}$ is simply the proportion of pixels with an incorrect phase-offset in the region:

$$p_1 = \frac{\text{phase ambiguity population}}{\text{total population}}; \tag{2.34}$$

$$p_0 = \frac{\text{total population} - \text{phase ambiguity population}}{\text{total population}} = 1 - p_1. \tag{2.35}$$

$\mathrm{PS_f}$ candidates population

In general, we do not know the correct value of the phase ambiguity we are looking for. We then have to rely on the detection of the $\mathrm{PS_f}$ to provide us with a reliable and precise estimate. As explained in Section 2.3.2, $\mathrm{PS_f}$ are detected by creating a partition of the space of observations, i.e. by setting an upper and a lower threshold on one or several quality estimators.

In parallel to the phase ambiguity population, we select potential frequency-stable pixels based on several detection criteria. Let us refer to the population of pixels selected by a detection criterion as *PS_f candidates population*. Since we test the 7 criteria presented in Section 2.3.1, we have 7 distinct $\mathrm{PS_f}$ candidates populations. The applied thresholds are listed in Table 2.7.

Definition of the problem

As already stated, this detection problem is a classical binary decision. We can therefore formulate two mutually exclusive hypotheses:

- H_0: the target is not a true $\mathrm{PS_f}$
- H_1: the target is a true $\mathrm{PS_f}$

Let us consider a single detection criterion at the time. The hypothesis H_1 is accepted when the target satisfies the thresholds of the detection criterion, and H_0 is accepted otherwise. A choice between those hypotheses leads to four configurations, with their associated joint probabilities:

1 - Select the target while it is indeed a $\mathrm{PS_f}$	$p\,(H_1, s_1)$
2 - Reject the target while it is indeed not a $\mathrm{PS_f}$	$p\,(H_0, s_0)$
3 - Select the target while it not a $\mathrm{PS_f}$	$p\,(H_1, s_0)$
4 - Reject the target while it is a $\mathrm{PS_f}$	$p\,(H_0, s_1)$

The last two situations obviously lead to an erroneous decision. The total probability of error p_ϵ is the sum of the probabilities associated to these two situations. Given that for conditional probabilities we have $p\,(H_i \,|\, s_j) = \frac{p(H_i, s_j)}{p(s_j)}$ with $i, j = 0, 1$, we obtain

$$p_\epsilon = p\,(H_1, s_0) + p\,(H_0, s_1) = p_0\, p\,(H_1 \,|\, s_0) + p_1\, p\,(H_0 \,|\, s_1)\,. \tag{2.36}$$

When we defined the phase ambiguity population, we made the assumption that the *"true"* frequency-stable pixels are the targets associated to a phase-offset really close to the correct value. Consequently, the joint probabilities are computed as

$$p\,(H_0, s_1) = \frac{\text{non } \mathrm{PS_f} \text{ candidates population } \cap \text{ phase ambiguity population}}{\text{total population}}, \tag{2.37}$$

$$p\,(H_1, s_0) = \frac{\mathrm{PS_f} \text{ candidates population } \cap \text{ wrong phase ambiguity population}}{\text{total population}}, \tag{2.38}$$

where the symbol $\cap$ indicates the intersection of the populations, i.e. a logical AND. These definitions of the joint probabilities are used in the following to estimate the total probability of error for each detection criteria. On the other hand, in the usual terminology, the conditional probabilities are the probability of detection, the probability of false alarm and the probability of non detection, and they are computed as follows:

Probability of detection $p_d \;=\; p\,(H_1\,|\,s_1) \;=\; \frac{\mathrm{PS_f\ candidates\ pop.\ \cap\ phase\ ambiguity\ pop.}}{\mathrm{phase\ ambiguity\ pop.}}$

Probability of false alarm $p_f \;=\; p\,(H_1\,|\,s_0) \;=\; \frac{\mathrm{PS_f\ candidates\ pop.\ \cap\ wrong\ phase\ ambiguity\ pop.}}{\mathrm{wrong\ phase\ ambiguity\ pop.}}$

Probability of non detection $p_n \;=\; p\,(H_0\,|\,s_1) \;=\; \frac{\mathrm{non\ PS_f\ candidates\ pop.\ \cap\ phase\ ambiguity\ pop.}}{\mathrm{phase\ ambiguity\ pop.}}$

The total probability of error is then : $p_\epsilon \;=\; p_0\,p_f \;+\; p_1\,p_n$.

Discussion

In Figure 2.25a, we present the joint probabilities associated to the true detection, the erroneous detection and the missed detection scenarii for the various detection criteria and the total probability of error. We first note that the total probability of error is always larger for goodness-of-fit estimators than for the phase quality estimators. This is mainly due to a larger probability $p\,(H_1, s_0)$ in the case of the goodness-of-fit estimators. It was expected from our previous results for the goodness-of-fit to perform less successfully than the phase quality estimators. We therefore leave them aside. As for the phase quality estimators, they all exhibit similar probabilities of error (~ 0.17). Let us investigate their behaviour in more details.

In Figure 2.25b, probabilities of detection, false alarm and non detection are shown. First, we note that the detection and false alarm probabilities for the phase variance stability are so low that we were not able to make them visible on the plot. Even though the $\mathrm{PS_f}$ candidates selected with this criterion are reliable, the rate of missed detection is too high for a statistical estimation of the phase ambiguity. Besides, it is obvious that the probability of non detection is important (> 0.9) whatever the criterion. However, the probability of false alarm is of much more importance than the probability of non detection for the phase ambiguity problem because it can lead to wrong estimates. This probability is the lowest for the slope standard deviation and the multifrequency phase error. The detection probability is larger for the slope standard deviation, which gives a better aspect ratio to the phase-offset distribution of this criterion. Indeed, the number of mode occurrences is larger in this case, making the height of the distribution larger as well.

Let us now focus on the map of detections obtained with the slope standard deviation (Figure 2.26): targets corresponding to non detections, false alarms and detections are respectively plotted in blue, red and green. We observe that the density of detections is the highest on the lava flows of 2002 and 2004, the most recent parts of the unwrapped lava field. Actually, the density of false alarms is also important, but it is compensated by the presence of true $\mathrm{PS_f}$. The presence of detections can be noted over the 2001 and 1991-1993 lava flows, but they are balanced with an important proportion of false alarms. In other places, the presence of $\mathrm{PS_f}$ is tenuous: five false alarms are found in the crater, for only 3 detections. Apparently, false alarms and detections appear both with similar density and preferentially in areas of high coherence. These observations are of course similar to those stated for Figure 2.22b since we work with the same criterion on the same data, but with a slightly larger frame and a discrimination between true and false detections.

As the detectability of frequency-stable targets depends on the resolution loss and is hence variable for one pair to another, probabilities computed in this particular context cannot be extended to another example. However, it gives a pretty good idea of the efficiency of a detection

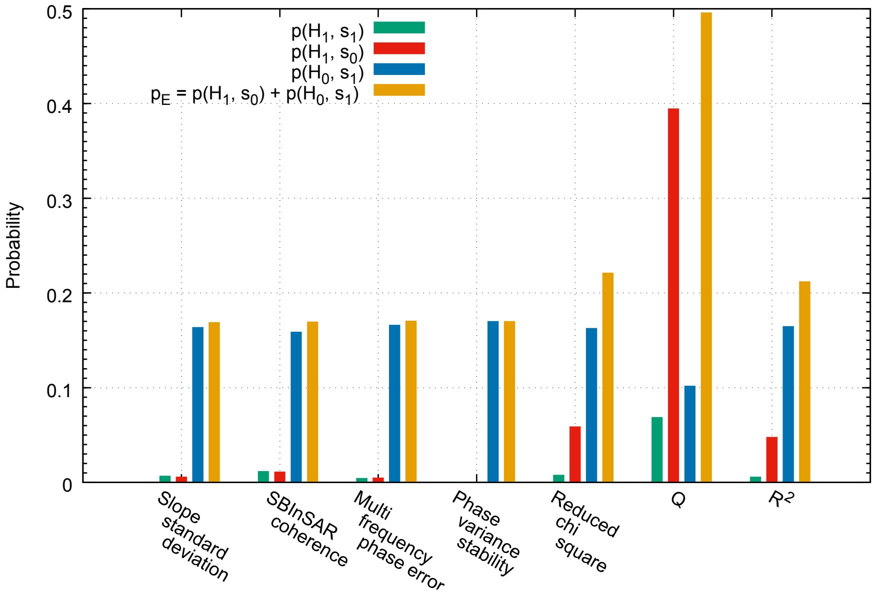

(a)

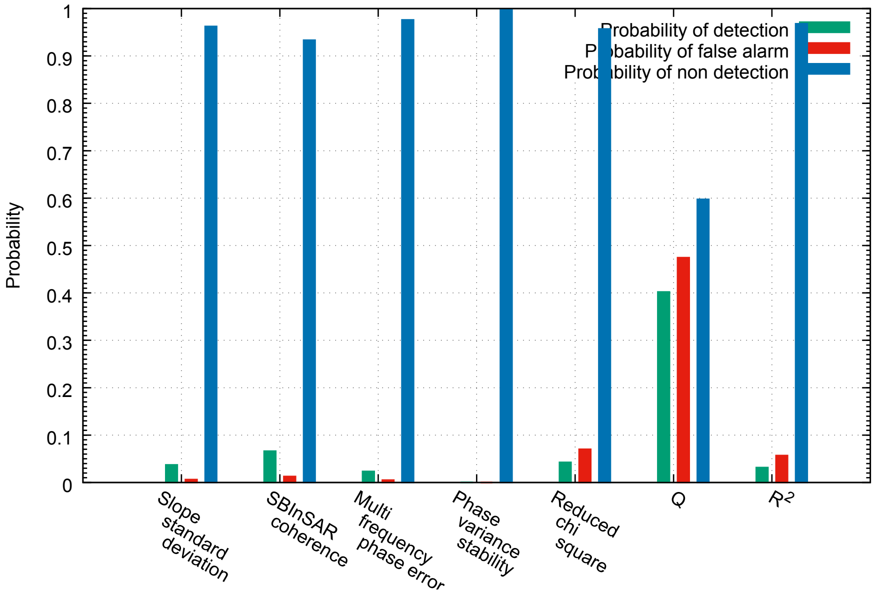

(b)

Figure 2.25: Frequency-stable targets detection problem. (a) Joint probabilities estimated for different detection criteria. (b) Corresponding probabilities of detection, false alarm and non detection. For both figures, some probabilities relative to the phase variance stability are not visible because they are too low compared to the values of the other criteria.

criterion with respect to another. This relative efficiency can reasonably be assumed similar for other examples.

Summary

In agreement with the first clues about the frequency-stable targets detection, we observe that goodness-of-fit estimators perform less efficiently than the other criteria. Their rate of false alarm is much larger. Even though the probability of non detection matters less than the probability

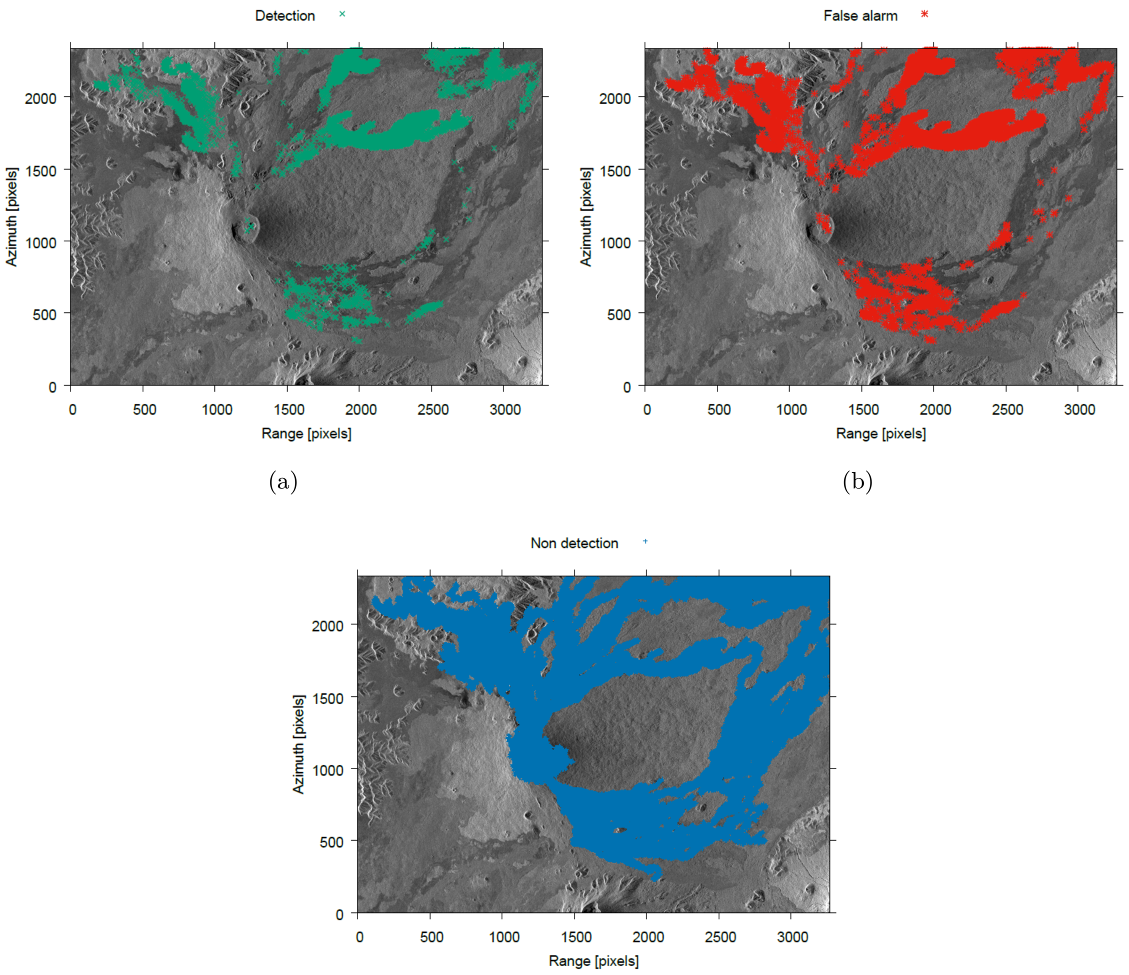

(a)

(b)

(c)

Figure 2.26: Frequency-stable targets detection problem. Maps of the targets corresponding to (a) detections in green, (b) false alarms in red, and (c) non detections in blue. The targets were selected on the basis of the standard deviation criterion and their locations are overlaid on an amplitude image of Nyamuragira.

of false alarm, it becomes so important in the case of the phase variance stability that the criterion becomes useless. Actually, as concluded before, the slope standard deviation proposes a reasonable probability of detection for a low rate of false alarms. Regarding the location, false alarms can in general be found in the same places as true detections. Their density is a bit larger on less coherent areas.

2.7 Characterization of frequency-stable targets in Split-Band Interferometry

The major limitation for SBInSAR to turn operational is the need for reliable frequency-stable targets within the studied scene, while we do not know exactly what a PS_f is. So far, the only indication we have about where to find PS_f is that they are usually located in highly coherent areas. For example, the density of detection is more important over the recent Nyamuragira lava flows than over the older ones. We have not studied urban areas yet, but given the coherence and the stability of such places, we expect to easily detect frequency-stable scatterers over cities.

For operational use, it would be ideal to have PS_f that are stable in time because a target detected in many images would allow a continuous monitoring. However, we do not know if this scenario is believable. What is the physical nature of a PS_f? Is a PS_f stable in the time domain the same way it is in the spectral domain? The observations we made did not answer any of those questions so far. In this section, we offer some clues to physically characterize a frequency-stable target. In a first step, we undertake a temporal analysis of the frequency-stable pixels over the VVP in order to determine if they are persistent in time, i.e. if they are permanent scatterers (PS) [10], or if spectral stability is at least a stationary characteristic. We will also attempt to associate the stable targets to Google Earth$^{\text{TM}}$ optical views and we investigate their scattering mechanisms by analyzing the intensity and the spectral properties of these targets.

2.7.1 Definition of a frequency-stable target

Before characterizing it, it is important to have an agreement on what we call a frequency-stable target. Initially, a frequency-stable target was defined as a target exhibiting a stable radar echo [59] or a stable phase [32,34] behaviour across the frequency domain. In our understanding, such targets are the ones exhibiting a precise measurement of the SBInSAR phase and we are going a step further by defining frequency-stable targets as targets with an error on the SBInSAR phase smaller than a cycle. This is equivalent to say that a PS_f is a target that allows to measure the exact phase ambiguity, up to one cycle.

2.7.2 Data set and processing

We use five TerraSAR-X Stripmap scenes acquired over the VVP between April and July, 2008. These images were all acquired along an ascending orbit, with an incidence angle of about 26°, an horizontal co-polarization (HH) and a bandwidth of 150 MHz. From these five acquisitions, we form four interferometric pairs with the image of July 3rd as common master. This image is chosen as the global master because it minimizes the perpendicular baselines with the other images. Having a common master ensures that all interferograms are coregistered on the same grid and that we do not have to work on a geoprojected frame. Moreover, it gives a temporal reference: the master contribution is fixed and only the slave contributions vary from one pair to another. Pairs of acquisitions are listed in Table 2.8, with their associated perpendicular baselines and CDR. The common footprint of all five images includes the Nyiragongo volcano, a part of the Nyamuragira lava field and the urban area of Goma. The test site is therefore a mixture of vegetation, volcanic rocks and buildings.

A spectral decomposition into 5 non overlapping subbands of 30 MHz is applied to all pairs. For each pair, we select the population of PS_f using the slope standard deviation criterion with a threshold of 0.65 rad/GHz. At this stage, we have four populations of PS_f at our disposal, one for each pair. Since the master component is the same for all the pairs, variations in the detected PS_f from one pair to the other must be due to the slave signal onlyy. This provides a good basis to operate a temporal analysis.

2.7.3 Temporal analysis

In order to determine if targets that are stable in the frequency domain are also stable in the time domain, we cross check PS_f populations and look for redundancies. A map of the PS_f is given in Figure 2.27, where targets are classified by colour according to the number of populations they belong to. If a target is selected in the four populations of PS_f, which corresponds to the red dots, we consider it as a *persistent* PS_f, i.e. a PS_f with a stable signal over the considered time period. In Figure 2.28a, we see that most of the PS_f are selected in a single pair. Only 2% of

Master Date	**Slave Date**	$\lvert b_\perp \rvert$	CDR
July 3rd, 2008	April 4th, 2008	81 m	9.55
July 3rd, 2008	May 9th, 2008	56 m	14.25
July 3rd, 2008	June 22nd, 2008	13 m	64.71
July 3rd, 2008	July 25th, 2008	50 m	16.09

Table 2.8: Pairs of acquisitions used for the temporal analysis over the Virunga Volcanic Province, with their associated perpendicular baseline and CDR values.

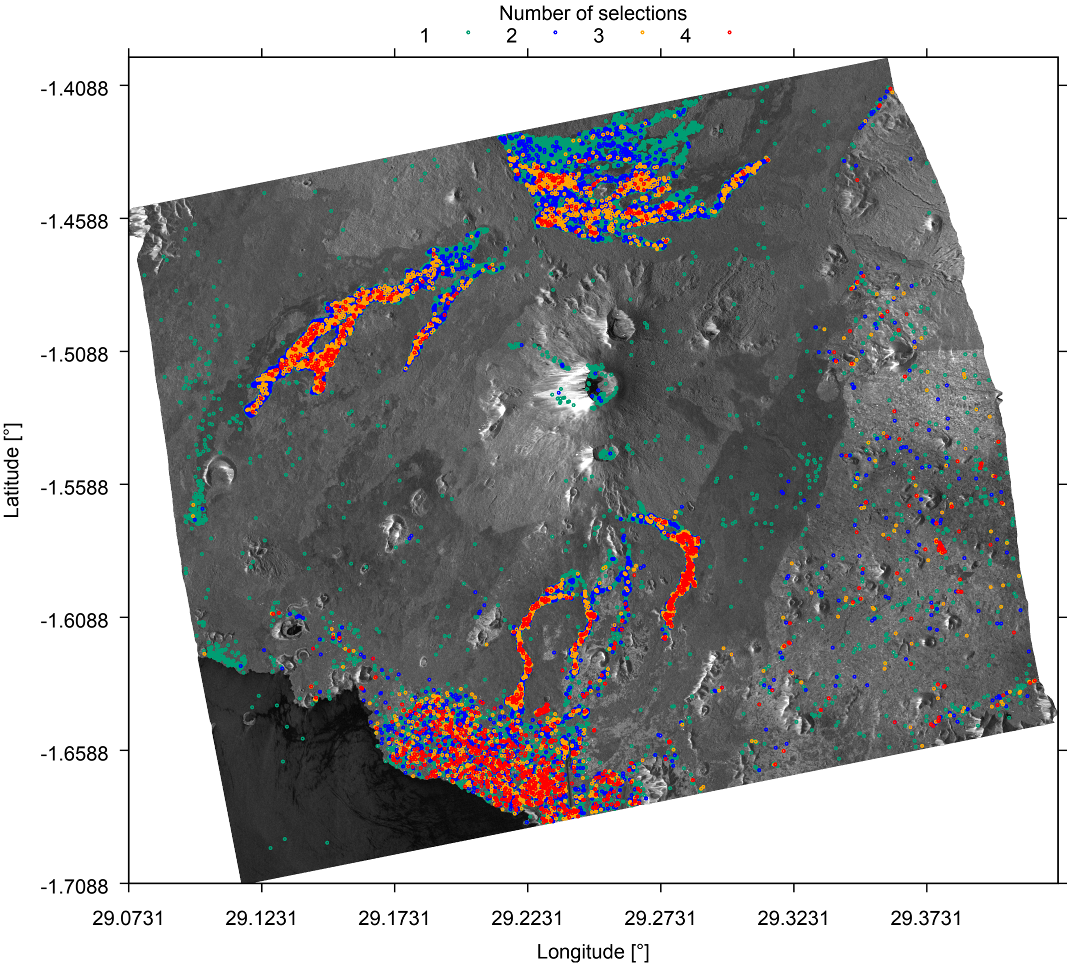

Figure 2.27: Temporal analysis of the frequency-stable targets over the Virunga Volcanic Province. Map of the PS_f classified by colour according to their number of detections. Green, blue, orange and red dots correspond respectively to PS_f selected in 1, 2, 3 or 4 pairs.

the PS_f are selected in all populations and it seems therefore that only a minority of PS_f persists over time. Looking at the location of persistent PS_f, we note that they are not associated to a particular area: as we suspected, the density of selected targets is important over the city area, but multiple detections are also present over lava flows of Nyiragongo and Nyamuragira volcanoes. In general, urban areas are associated to double bounce scattering while we have diffuse scattering over the rough lava flows. This first approach suggest that PS_f may arise from different scattering mechanisms. As expected, few detections occur in the vegetated areas that are non coherent due to volume scattering.

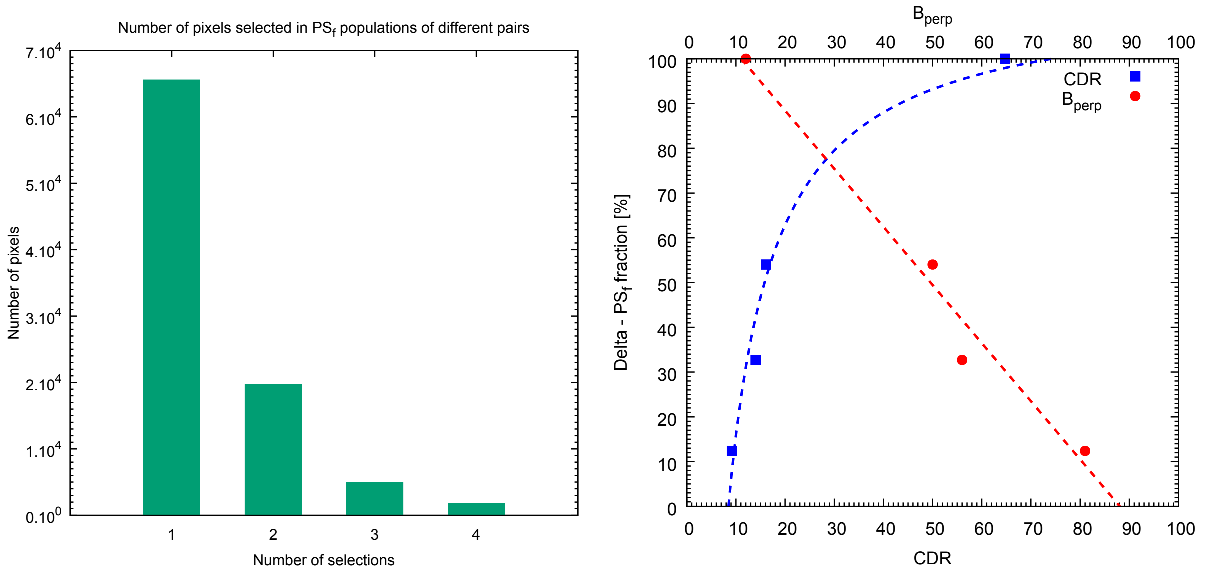

(a)

(b)

Figure 2.28: Temporal analysis of the frequency-stable targets over the Virunga Volcanic Province. (a) Histogram of the $\mathrm{PS_f}$ selections, in 1, 2, 3 or 4 pairs. (b) Percentage of the selected $\mathrm{PS_f}$ as a function of the perpendicular baseline (red) and the CDR (blue).

Effect of the resolution loss and permanent scatterers

When we analyze the temporal stability of $\mathrm{PS_f}$, it is important to take into account the effect of the resolution loss. As explained in Section 2.2.2, the SBInSAR performance is limited by the intensified geometrical decorrelation due to the bandwidth degradation. This effect is a function of the bandwidth, the incidence angle, the wavelength and the perpendicular baseline, and it can be quantified by the value of the CDR. When decorrelation is too important, the signal of $\mathrm{PS_f}$ can be drowned into decorrelation noise and become undetectable.

This consideration gives us clues to answer a first question: does a $\mathrm{PS_f}$ have a persistent behaviour in the sense of Permanent Scatterers Interferometry [10]? A permanent scatterer is a point-like target that exhibits a stable signal over a long period of time. The very interest of this kind of targets is that they are not much sensitive to geometrical decorrelation. For example, they remain coherent even in the case of very large baselines. If frequency-stable targets were PS, they would not be affected by the loss of resolution and would remain stable over time anyway. Therefore, as the population of persistent $\mathrm{PS_f}$ constitutes a small fraction of the detected $\mathrm{PS_f}$, we conclude that a $\mathrm{PS_f}$ is not necessarily a PS. Moreover, PS are point scatterers while frequency-stable scatterers can correspond to point targets like buildings, but also to distributions of scatterers, as we will show in the next sections. The distinction between $\mathrm{PS_f}$ and PS might seem anecdotal, but the fact that $\mathrm{PS_f}$ could be found in natural places where PS are usually not present opens a perspective for the monitoring of rural areas, for example.

Limit of detection

As explained above, an increase of geometrical decorrelation can lead to undetectable targets. As a consequence, for a given level of decorrelation, a limit of detection must be reached, beyond which no $\mathrm{PS_f}$ can be detected anymore. Let us focus on this limit of detection and characterize it empirically in terms of CDR.

Let us take Equation (2.19): the wavelength, the incidence angle and the bandwidth are here fixed parameters of the CDR function. The perpendicular baseline is the only variable parameter, which defines the dependency of the CDR function. Let us consider the number of detected $\mathrm{PS_f}$ in each pair normalized by the largest $\mathrm{PS_f}$ population, which gives the fraction δ of detected $\mathrm{PS_f}$. This quantity seems to behave linearly with the perpendicular baseline (Figure 2.28b). Let us assume such a linear relationship and fit it to the data points:

$$\delta \;=\; a\,|b_\perp| \;+\; b. \tag{2.39}$$

Here, a is the slope and b the intercept of the linear regression. Given the relationship between $b_\perp$ and the CDR, it comes that

$$\delta \;=\; a\,\frac{1}{1+\mathrm{CDR}}\,\frac{\lambda B_s r_m \tan\theta}{c|b_\perp|} \;+\; b. \tag{2.40}$$

This function is also fitted to the data, as represented in blue in Figure 2.28b. If the CDR decreases and the perpendicular baseline increases, then we observe that the fraction of $\mathrm{PS_f}$ decreases. Given this phenomenological behaviour, it follows that the fraction of detected $\mathrm{PS_f}$ should fall to zero for a perpendicular baseline of 88 m, or equivalently for a critical CDR of 8.65. Even if it is not an absolute threshold, the critical value of the CDR gives a typical value of the limit of detection for the studied region. If we had to change the sensor or the mode of the data over the region, this CDR threshold would give an indication on the parameters to use.

Stationarity

Even though $\mathrm{PS_f}$ are not necessarily PS, spectral stability could be a stationary feature of a $\mathrm{PS_f}$. Let us now try to determine if the small fraction of persistent $\mathrm{PS_f}$ is due to the degradation of the resolution, or to a transient feature of the targets.

The loss of resolution can only partly explain the small part of persistent $\mathrm{PS_f}$: indeed, we have shown that the smaller the CDR, the smaller the detected population. For poor CDR, we obviously miss detections in multiple pairs. Nevertheless, if frequency-stable targets were stationary, we would expect to have a base population of *strong* $\mathrm{PS_f}$ that are not affected by the decorrelation noise and that is common to all pairs. Similarly, we would expect to face a population of *weak* $\mathrm{PS_f}$, that are more easily impacted by the spatial decorrelation effect. When the decorrelation decreases (i.e. the CDR increases), more and more weak $\mathrm{PS_f}$ should then be detected. In this scenario, weak $\mathrm{PS_f}$ should not be detected in the worst case of decorrelation, leaving only the common population of strong $\mathrm{PS_f}$.

However, we observe that new targets are identified for the pair with the largest decorrelation noise. These targets were not detected in the other case and this contradicts the considered scenario. It translates into less than 5000 triple-detections and less than 1800 quadruple-detections, while the smallest $\mathrm{PS_f}$ population is about 7886 targets. More than 6000 targets that do not cross-check others populations are hard to reconcile with a scenario of strong and weak $\mathrm{PS_f}$, or a potential stationary feature.

In conclusion, we are confident that the spectral stability of the targets is in general a transient feature of a scatterer. For this reason, the name *frequency-persistent scatterers* seems ill-advised, as "persistent" may be interpreted as a reference to the temporal stability. We would recommend to talk about *frequency-stable* or *spectrally stable scatterers* instead. Nevertheless, a population of persistent $\mathrm{PS_f}$ exists. This population is of interest for operational purposes and we will study it in more details in the following sections.

2.7.4 Targets identification

In order to get some clues about the physical nature of a frequency-stable scatterer, we have identified the detected $\mathrm{PS_f}$ in optical views from Google Earth$^{\mathrm{TM}}$. With the "archive" option of

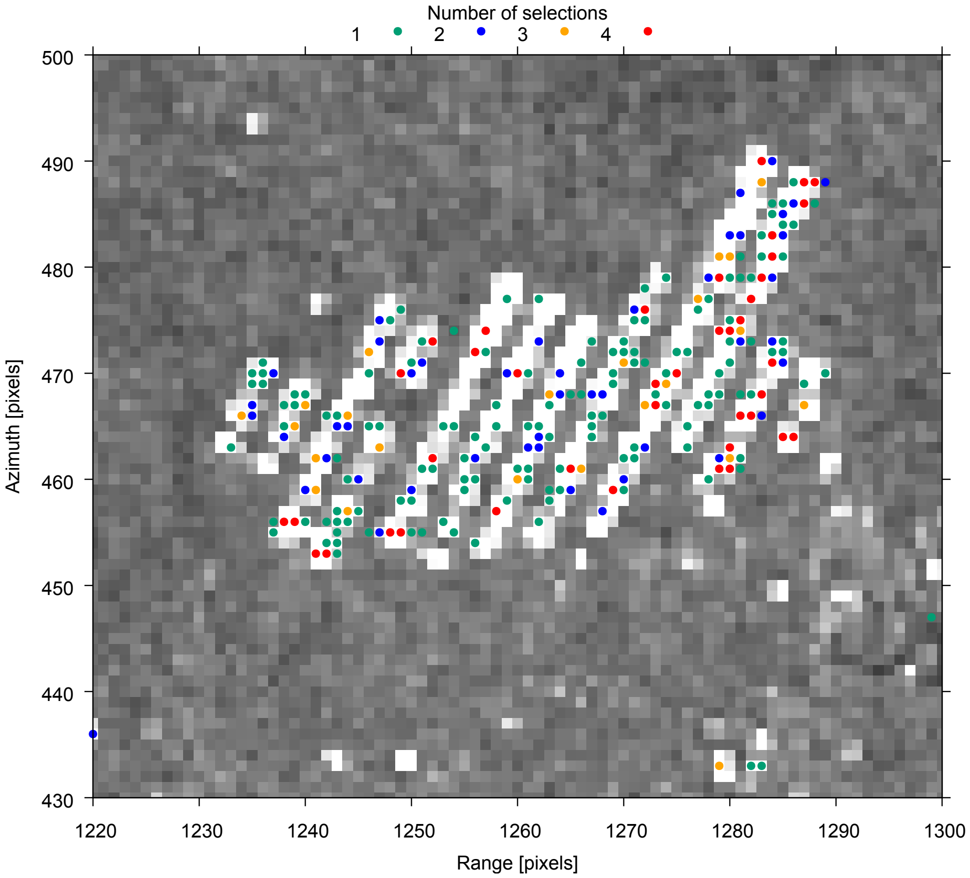

(a)

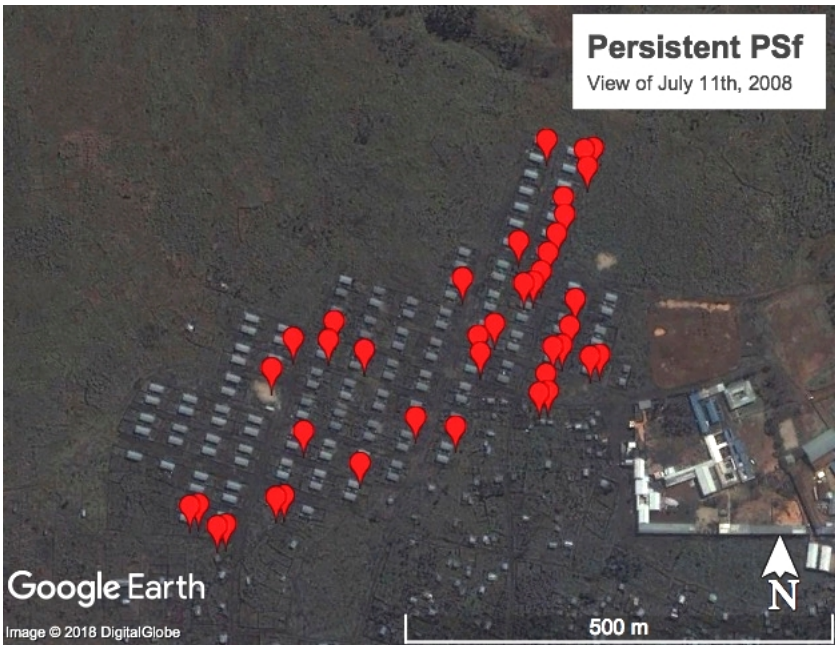

(b)

Figure 2.29: Temporal analysis of the frequency-stable targets over the Virunga Volcanic Province. (a) Sigma-nought image of July 3rd, 2008 focused on the refugees tents with the frequency-stable targets overlaid and classified by colour according to their number of selections. (b) Google Earth view$^{\text{TM}}$ of the corresponding area on July 11th, 2008.

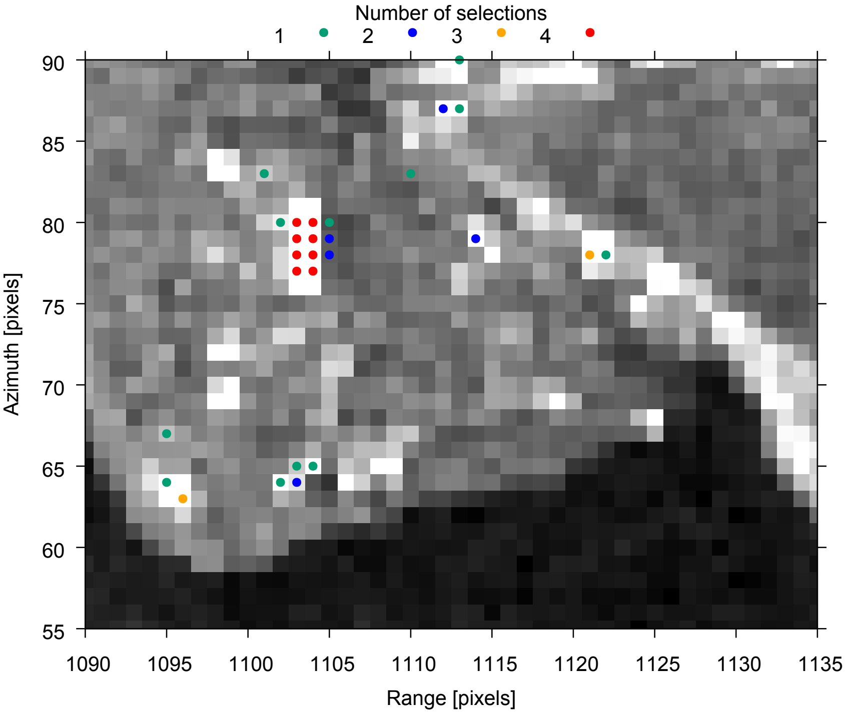

(a)

(b)

Figure 2.30: Temporal analysis of the frequency-stable targets over the Virunga Volcanic Province. (a) Sigma-nought image of July 3rd, 2008 focused on a residential neighbourhood of Goma with the frequency-stable targets overlaid and classified by colour according to their number of selections. (b) Google Earth$^{\mathrm{TM}}$ view of the corresponding area on July 11th, 2008.

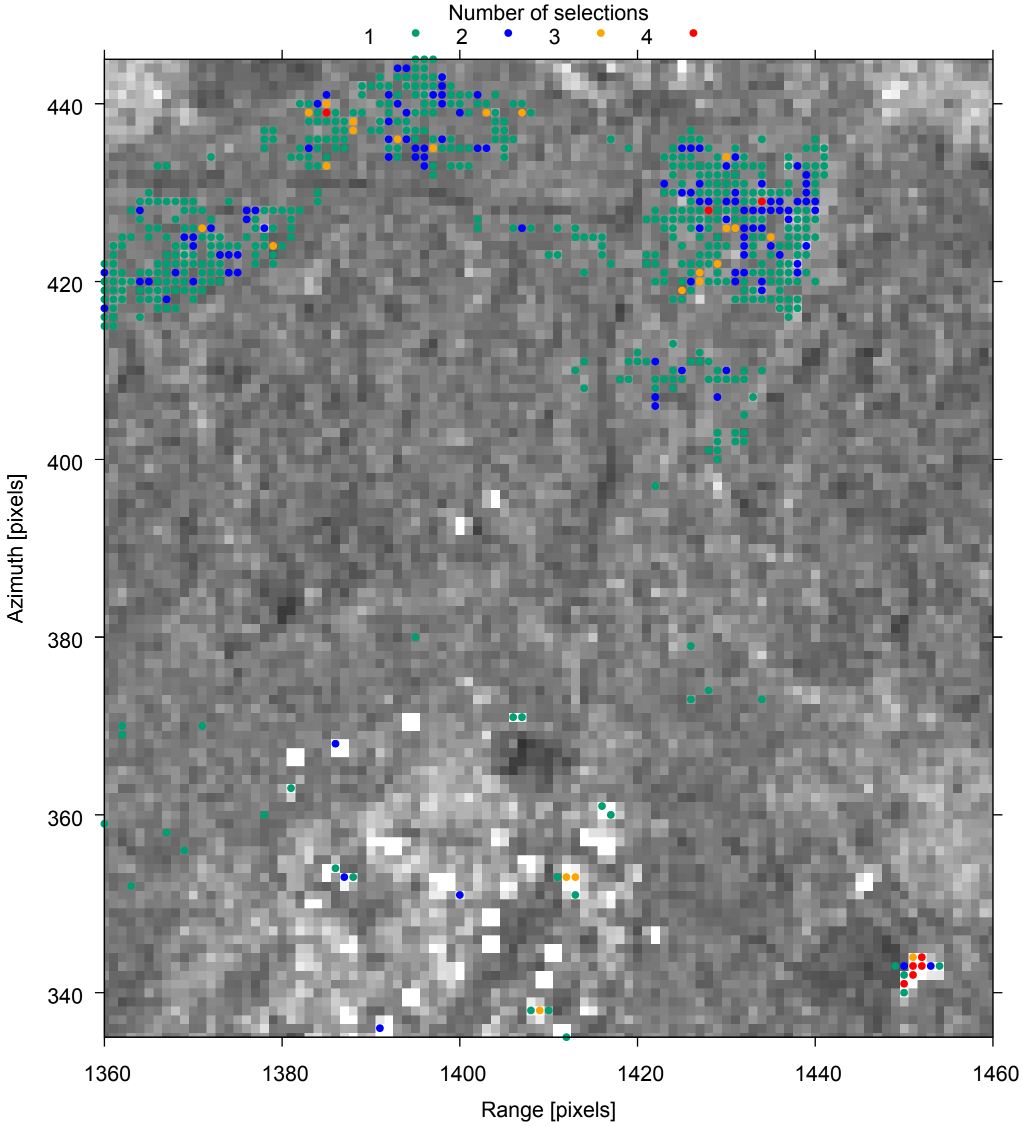

Figure 2.31: Temporal analysis of the frequency-stable targets over the Virunga Volcanic Province. Sigma-nought image of July 3rd, 2008 focused on the north-east area of Goma and the surrounding lava flow. Frequency-stable targets are overlaid and classified by colour according to their number of selections.

Google Earth$^{\text{TM}}$, it was possible to work on an image from July 11th, 2008 that corresponds perfectly to the time frame of our temporal analysis. We compare the amplitude image, overlaid with the multiple detections, to the corresponding area in the optical view for three different areas around Goma. Given the very large number of targets, we focus on persistent PS_f in the Google Earth$^{\text{TM}}$ views to keep them as clear as possible.

Besides, it is worth considering the resolution of the images when we attempt to associate frequency-stable pixels to recognizable structures. With a spatial averaging of 5×5 pixels and a bandwidth degraded down to 30 MHz, SBInSAR products have a range resolution of about 25 m and an azimuth resolution of 10 m. Given an incidence angle of 26°, it corresponds to a ground range resolution of approximately 50 m. Given these large values, we expect PS_f to correspond either to isolated single point targets with a strong signal, or to distributions of scatterers organized in a particular pattern.

In the first view (Figure 2.29), we see a high concentration of persistent PS_f over a refugee

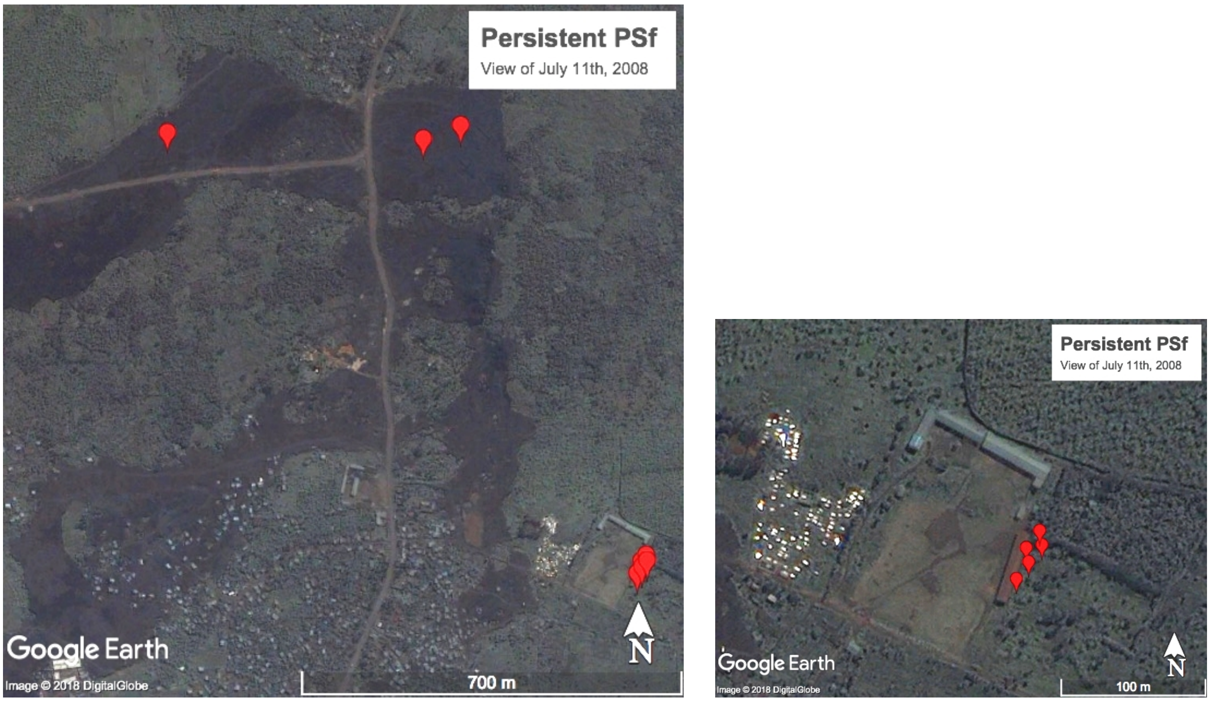

(a) (b)

Figure 2.32: (a) Google Earth$^{\text{TM}}$ view acquired on July 11th, 2008 over the area corresponding to the sigma-nought image of Figure 2.31 .(b) Zoom on the lower right corner of (a).

camp, made of aligned tents. The number of detected PS_f is important on the tents that show a bright signal. The temporary nature of this kind of camp might explain the temporal instability of PS_f over this particular area: the camp may grow fast, with new tents added between dates of our acquisitions. However, when comparing the intensity images for all dates, we do not observe bright pixels appearing or disappearing over the camp from one acquisition to the other. In the second view (Figure 2.30), we observe that persistent PS_f correspond to a large building, likely a warehouse or a factory. We note that there is a slight offset with respect to Google Earth$^{\text{TM}}$ georeferencing, but the shape drawn by the red pins is clearly associated to the building. Here again, the building has a bright echo in the amplitude image (red dots in Figure 2.30a). In the last view (Figure 2.32), we observe that persistent PS_f can be found over buildings, but over bare lava flows as well. We see from the amplitude image (Figure 2.31) that PS_f detections are dense over the lava flow, though with only a few multiple detections over time. They do not correspond to a particularly bright signal. The resolution of the optical image does not allow to observe particular details of the lava flow structure that would explain the presence of a PS_f at these particular locations.

Even though we do not show the corresponding images here, we did a similar analysis with single detections and we observe that they could be associated to various type of objects: houses, bare soils, trees, the Nyamuragira crater and old lava flows. Unfortunately, no particular pattern emerges from these observations.

2.7.5 Backscattering mechanisms analysis

As explained above, even though most frequency-stable targets do not persist in time, there exist a persistent population. These targets are the most useful for monitoring purposes, and this section aims at studying their backscattering characteristics.

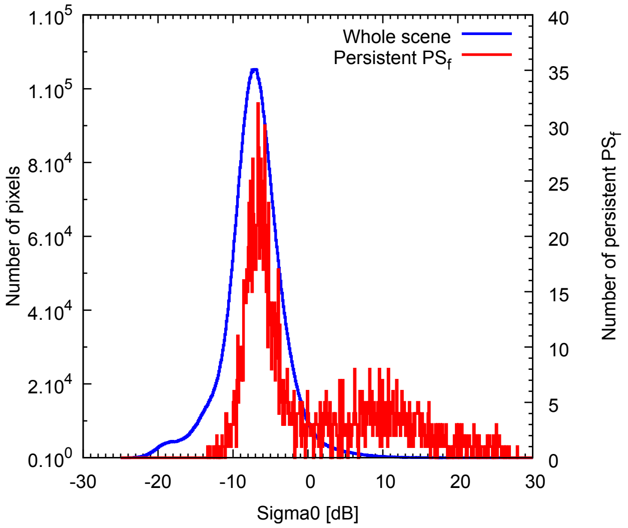

Figure 2.33: Temporal analysis of the frequency-stable targets over the Virunga Volcanic Province. Histogram of sigma-nought values for the July 3rd, 2008 scene. Blue: whole scene, associated to the left y-axis. Red: persistent PS$_f$ only, associated to the right y-axis.

Reflectivity

Information about PS$_f$ can be obtained from their reflectivity, measured via the sigma-nought that is an estimate of the backscattering coefficient [60]. For this purpose, the image of July 3rd is radiometrically calibrated and geocoded to obtain the geoprojected sigma-nought coefficient σ^0. The distribution of σ^0 is determined for the whole scene and for persistent PS$_f$ (Figure 2.33). For the whole image, the σ^0 distribution peaks around -7 dB. For the persistent PS$_f$, we observe a similar peak slightly shifted towards higher values, and a smaller and more spread one around 10 dB. Both peaks are separated by a drop around zero: we use this value to make a distinction between both populations. Pixels of the calibrated sigma-nought image with a value larger than 0 dB are shown in red in Figure 2.34. We see that places of steep topography show geometrical artifacts (fortshortening, layover, errors in geoprojection) that give erroneous bright reflectivity estimates. We are not interested in those artifacts, since no PS$_f$ is usually found over there. In contrast, lava flows do not show backscattering as bright as 0 dB or more. Comparing red pixels to the map of persistent PS$_f$ in Figure 2.27, we observe that they mostly correspond to the area of Goma and they are therefore most probably associated to double bounce backscattering over houses and buildings.

Inversely, the lower reflectivity peak of persistent PS$_f$ corresponds to targets located over lava flows. These places are characterized by distributions of scatterers rather than single point targets, associated diffuse scattering mechanisms that lead to a lower reflectivity than over the Goma area.

Spectral coherence

In this work, we have been interested in Split-Band Interferometry that exploits the spectral information of two images. However, it is also possible to gain information from the spectral decomposition of a single image through *spectral coherence*. Knowing that, it is of interest to check if frequency-stable pixels are also frequency-coherent scatterers, i.e. targets with a high spectral coherence.

Spectral coherence, sometimes called *interband coherence*, is an estimator of the coherence between the subimages of a given spectral decomposition. It is similar to the conventional co-

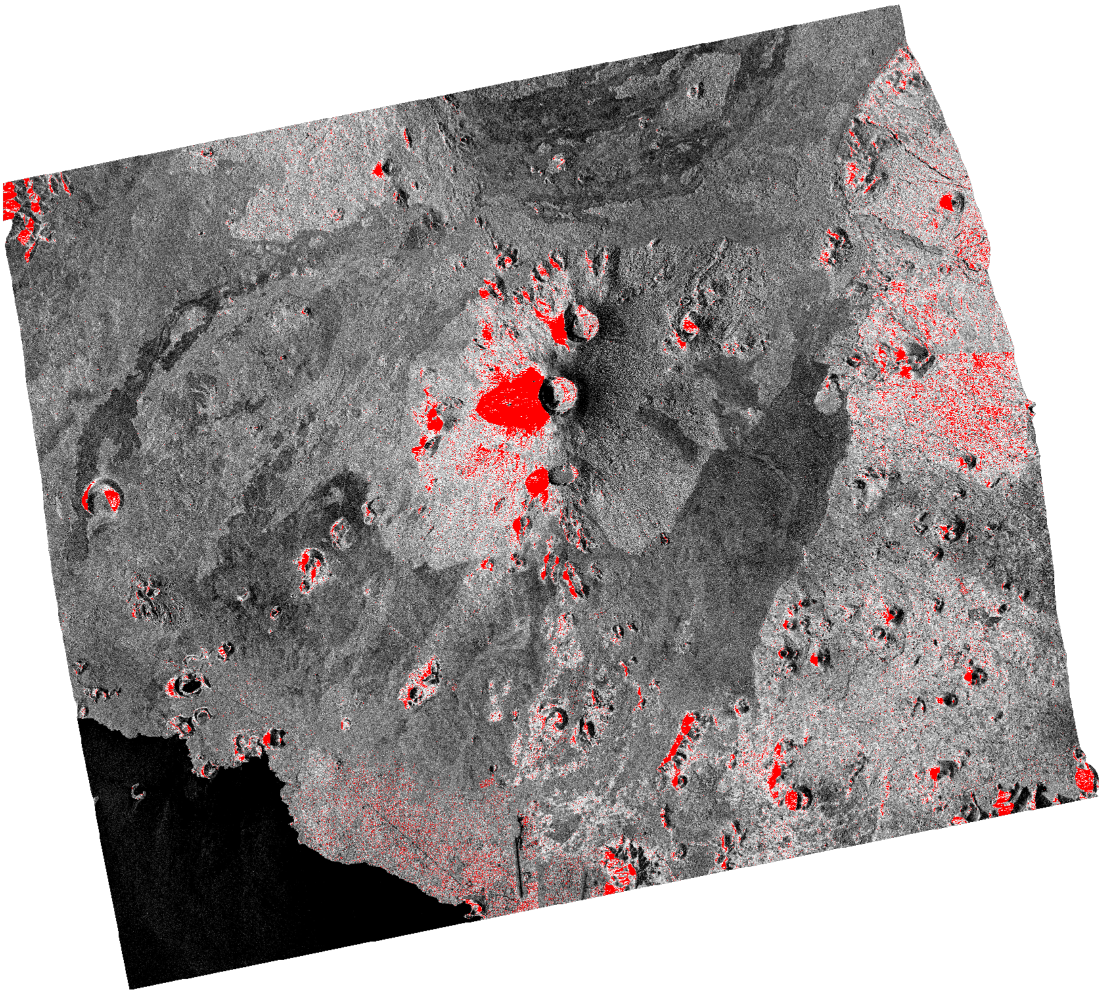

Figure 2.34: Temporal analysis of the frequency-stable targets over the Virunga Volcanic Province. Calibrated image of July 3rd, 2008. Pixels with a sigma-nought value larger than 0 dB are outlined in red.

herence, but applied to subband images of a given scene rather than master and slave original acquisitions. The spectral coherence model developed by Derauw et al. in Reference [61] shows that a uniform and uncorrelated distribution of surface scatterers has a spectral coherence depending on the subband overlap:

$$\gamma_s^{ij} = 1 - \frac{(\nu_i - \nu_j)}{B_s}. \tag{2.41}$$

Here, $(\nu_i - \nu_j)$ is the frequency shift between the subbands i and j, and B_s is the partial bandwidth. For the assumed distribution, spectral coherence should equal 1 for completely overlapping subbands and it should decrease linearly with the overlap, until it finally reaches zero for null-overlap. If scatterers depart from the assumed distribution (e.g. volume scattering, dihedral scattering, etc.), spectral coherence may be preserved even for non overlapping subbands, depending on the degree of divergence from a distribution of random surface scatterers. Spectral coherence is a tool of scene classification and we can hence infer information about the type of scatterers. For example, spectral coherence analysis can be applied to ship detection: water surface agrees well with the random surface scatterers assumption and its spectral coherence drops for non overlapping subbands, while ships behave very differently and are prone to be spectrally coherent [33].

In practice, spectral coherence is calculated for all possible subband combinations of the spectral decomposition. As for the conventional coherence, it is estimated rather than measured. For a given point, the estimate is obtained by averaging the subband interferometric signals over a window of $L \times K$ pixels centered on the considered point, taking its amplitude and normalizing it:

$$\gamma_s^{ij} = \frac{\left| \sum_{l=1}^{L} \sum_{k=1}^{K} S^i(x_l, z_k)\, S^{j\,*}(x_l, z_k) \right|}{\sqrt{\sum_{l=1}^{L} \sum_{k=1}^{K} |S^i(x_l, z_k)|^2} \sqrt{\sum_{l=1}^{L} \sum_{k=1}^{K} |S^j(x_l, z_k)|^2}}. \tag{2.42}$$

Here, S^i and S^j are the point signals in the subbands i and j respectively, i and j are the subband indices, and (x, z) are the range-azimuth coordinates of the pixels included within the considered window.

Let us consider the pair July 3rd - June 22nd from our temporal analysis, which is the pair with the best CDR. We calculate spectral coherence for these two images, with a spectral decomposition into 9 non overlapping subbands of 16.66 MHz. These parameters give better contrast of the spectral coherence than the previous split into 5 subbands. With this constant null-overlap, we expect to have values close to zero if the targets are a distribution of random surface scatterers and higher values otherwise. We average spectral coherence over all subband combinations and get rid of the subbands dependency. As for the intensity, we compute distributions of the mean spectral coherence $\langle \gamma_s \rangle$ for the whole scene and for persistent $\mathrm{PS_f}$ (Figure 2.35). Distributions for the two dates have similar shapes shifted by approximately 0.05. Distributions of the whole scenes exhibit peaks at low values of coherence (around 0.28 and 0.33), associated to the expected bias in low coherence estimates. Therefore, this peak is linked to random surface scattering that is the main scattering mechanism in the studied scene. In a fashion similar to the intensity, a second peak appears for the persistent $\mathrm{PS_f}$ population, at a higher value of the spectral coherence. The population of this peak must be somehow of a different nature.

Let us focus on two different areas: a lava flow of Nyiragongo and the surroundings of the Goma airport and its landing strip. The spectral coherence images of these two zones are given

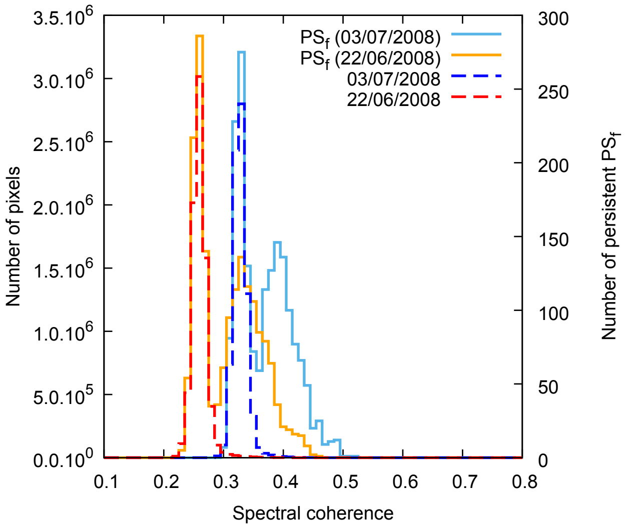

Figure 2.35: Histogram comparison for the average spectral coherence of July 3rd and June 22nd scenes. Dashed and plain lines give respectively the distributions for the whole scenes (associated to the left y-axis) and for persistent $\mathrm{PS_f}$ only (associated to the right y-axis).

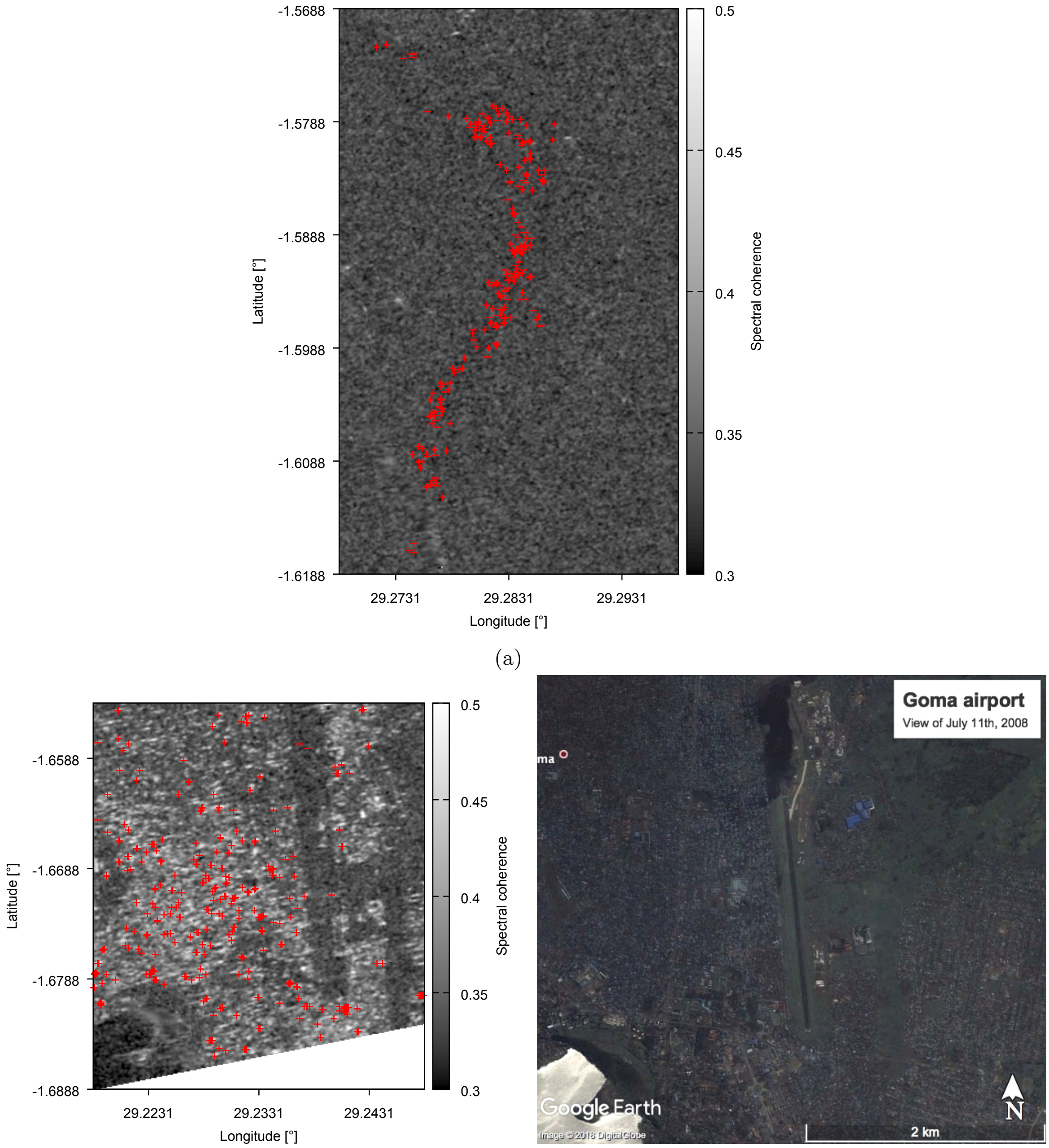

(a)

(b) (c)

Figure 2.36: Spectral coherence for July 3rd. Focus on (a) lava flow of the Nyiragongo volcano - (b) Goma airport and its neighbourhood. Red crosses represent persistent $\mathrm{PS_f}$. (c) Google Earth$^{\mathrm{TM}}$ view of the Goma airport on July 11th, 2008.

respectively in Figures 2.36a and 2.36b. A Google Earth$^{\mathrm{TM}}$ image of the Goma airport area is also given in Figure 2.36c. Over the Nyiragongo's lava flow, we observe a dense population of persistent $\mathrm{PS_f}$ with a low spectral coherence. This population corresponds to the lower peak. On the urban area around the airport, we observe persistent $\mathrm{PS_f}$ with higher spectral coherence corresponding to buildings. However, on the landing strip, where the soil is bare and flat, we do not have much $\mathrm{PS_f}$ and spectral coherence is low.

The observations made with spectral coherence comforts our previous results. Here again, we observe two types of scattering populations: the main one corresponding to distribution of

Sensor	**Mode**	**Master date**	**Slave date**	B	$\frac{\nu_0}{B}$	CDR
TerraSAR-X	Stripmap	June 22nd, 2008	July 3rd, 2008	150 MHz	64.33	64.71
TerraSAR-X	Stripmap	September 1st, 2014	September 12th, 2014	150 MHz	64.33	10.79
Radarsat-2	Ultra-Fine	May 4th, 2014	May 28th, 2014	100 MHz	54.00	331.95
Radarsat-2	Ultra-Fine	March 12th, 2015	April 5th, 2015	100 MHz	54.00	52.27
Cosmo-SkyMed	HIMAGE	February 10th, 2016	February 18th, 2016	129 MHz	74.42	26.87
Cosmo-SkyMed	HIMAGE	February 26th, 2016	March 5th, 2016	129 MHz	74.42	8.39

Table 2.9: Sample cases of SBInSAR-assisted phase unwrapping generalization.

surface scatterers and the other, more scarce, corresponding to single point targets like buildings and houses.

Identified scattering mechanisms

Based on a reflectivity and spectral coherence analysis, we demonstrated that frequency-stable scatterers in the region of the Virunga can arise from two types of populations: on the one hand, from distributions of surface scatterers over the lava flows; on the other hand, from single points scatterers like buildings and houses mainly located in the city. Surface scatterers have low reflectivity and low spectral coherence values, while single point scatterers are brighter and are spectrally coherent. Consequently, $\mathrm{PS_f}$ are not related to a particular type of scattering mechanism: these targets can show dihedral backscattering or diffuse scattering over rough surfaces. Although further insights about the backscattering mechanisms could be obtained with a polarimetric study, we unfortunatly do not have access to wideband data with full or dual-polarization.

Besides, after showing that $\mathrm{PS_f}$ are not necessarily persistent over time, we have demonstrated that they are not inevitably single point scatterers. Since they can also correspond to distributions of scatterers, it is indicated to talk about spectrally stable *pixels* rather than *scatterers*.

2.8 Generalization

After studying extensively the TerraSAR-X test case over the Virunga Volcanic Province, determining the optimum split parameters, establishing the performance of the $\mathrm{PS_f}$ detection criteria and attempting to better characterize frequency-stable pixels, it is now time to go one step further and extend the SBInSAR-assisted phase unwrapping to new sample cases.

In this section, SBInSAR-assisted phase unwrapping is still applied on couples of images acquired over the VVP, but with different sensors. The analyzed pairs are listed in Table 2.9 with their sensor, their acquisition mode and their characteristic parameters of SBInSAR performance. In our data set, we have X-band acquisitions from TerraSAR-X and Cosmo-SkyMed, and C-band acquisitions from Radarsat-2. For each sensor, we choose to work with the best mode at our disposal, i.e. the one with the largest bandwidth, and to vary the baseline to test the limits. A recurrent processing is applied to all study cases: regarding SBInSAR processing, all images are split into 5 non overlapping subbands of one-fifth of the original bandwidth and we opt for the weighted linear regression. Regarding the InSAR processing, a spatial averaging on a window of 5 × 5 5 pixels is performed and the coherence-guided branch-cut algorithm [41] is used for phase unwrapping, with a variable coherence threshold. In order to assess the success of the method, we will adopt an approach similar to the one applied to the Copahue test case for each studied pair: in a first step, we run SBInSAR-assisted phase unwrapping on artificially disconnected regions for an indirect validation of the phase ambiguity corrections. In each case, the slope standard deviation is considered for the $\mathrm{PS_f}$ selection because it reaches better results than the multifrequency phase error and the phase variance stability in global. We then locate the selected $\mathrm{PS_f}$ in the image and highlight the $\mathrm{PS_f}$ with the expected phase ambiguity. Finally, we look at the occurrence rate of the phase ambiguity correction with respect to the $\mathrm{PS_f}$ content of the corrected region, in order to define the minimum size of a statistically significant $\mathrm{PS_f}$ population.

2.8.1 TerraSAR-X

June 22nd, 2008 - July 3rd, 2008

This example has already been studied in detail with different approaches. In Section 2.5, it was demonstrated that phase ambiguities over the Nyamuragira lava field could be corrected when we take the adequate split parameters. This time, we keep the entire spatial coverage of the interferogram and we choose a challenging disconnection pattern to go one step further with this example: we split the interferogram into five regions for the southern half of the image and five other regions for the northern half (Figure 2.37a). The southern half includes Goma, the surroundings of the city and the Nyiragongo lava field; the northern half consists essentially in the Nyamuragira lava field. The north and south regions are initially disconnected from each other. If we manage to correct the phase ambiguities, we could then level the phase of both halves.

Phase-offset	Cycles
n_1	0
n_2	0
n_3	NC
n_4	-1
n_5	0
n_6	2
n_7	NC
n_8	2
n_9	2
n_{10}	1

(a)

Relative phase-offset	Cycles
$m_1 - m_2$	0
$m_1 - m_3$	0
$m_1 - m_4$	1
$m_1 - m_5$	0
$m_2 - m_3$	0
$m_2 - m_4$	1
$m_2 - m_5$	0
$m_3 - m_4$	1
$m_3 - m_5$	0
$m_4 - m_5$	-1

(b)

Relative phase-offset	Cycles
$m_6 - m_7$	0
$m_6 - m_8$	0
$m_6 - m_9$	0
$m_6 - m_{10}$	1
$m_7 - m_8$	0
$m_7 - m_9$	0
$m_7 - m_{10}$	1
$m_8 - m_9$	0
$m_8 - m_{10}$	1
$m_9 - m_{10}$	1

(c)

Table 2.10: TerraSAR-X, June 22nd, 2008 - July 3rd, 2008. (a) Computed phase-offset corrections. NC stands for "not corrected". Regions 1 to 5 are independent from regions 6 to 10. (b) Relative phase-offsets for regions 1 to 5. (c) Relative phase-offsets for regions 6 to 10. Indices in subscript refer to the number of phase unwrapping region.

In Table 2.10, phase ambiguities of the artificially disconnected regions are given along with the relative phase-offsets of the southern and northern regions. First, we observe that for both parts, a region is not corrected. Actually these regions correspond to the Nyamuragira crater (yellow) and a Nyiragongo lava flow (light blue), which are small regions with few detected $\mathrm{PS_f}$ and hence multimodal distributions of the phase ambiguity estimates. Despite the two non corrected regions, other phase ambiguity values fulfill the expected relative offsets.

In Figure 2.37b, we depict the corrected regions and their levelled phase. We see that extra regions have been corrected, even though we observe obvious errors for at least one of them. In addition, we have located $\mathrm{PS_f}$ with the expected phase-offsets.

Finally, Figure 2.38 gives the probability for a $\mathrm{PS_f}$ to correspond to the mode of the distribution as a function of the $\mathrm{PS_f}$ population of the corrected region. The plot considers different detection criteria: the multifrequency phase error, the slope standard deviation and the phase variance stability. We observe a stabilization of the probability for regions larger than 20 pixels.

September 1st, 2014 - September 12th, 2014

This second TerraSAR-X case has a slightly higher incidence with an angle of about 21° instead of 26° for the first one. It has also a larger perpendicular baseline of 55 m instead of 13 m. The consequence is a six times lower value of the CDR. We expect therefore this case to be harder to correct than the previous one.

Phase-offset	**Cycles**	**Error**
n_1	27	
n_2	33	
n_3	53	-1 cycle

(a)

Relative phase-offset	**Cycles**
$m_1 - m_2$	-6
$m_1 - m_3$	-25
$m_2 - m_3$	-19

(b)

Table 2.11: TerraSAR-X, September 1st, 2014 - September 12th, 2014. (a) Computed phase-offset corrections. The error column gives the number of cycles to add in order to obtain the correct phase ambiguity, inferred from the cross-checking with relative phase-offsets. (b) Relative phase-offsets.

We divide the interferogram into three regions (Figure 2.39a). Let us note that in this case the images were acquired along a descending orbit six years after the first study case. The view is therefore a bit different and new flows have emerged in the lava field.

The calculated phase ambiguity corrections and the relative phase-offsets are given in Table 2.11. Given the expected relative phase-offsets, we conclude that region 3 (blue) is corrected with a one-cycle error. In Figure 2.39b, the levelled phase is represented with the selected $\mathrm{PS_f}$ location. We observe that most of the $\mathrm{PS_f}$ with the correct offset are found over the newest lava flows (2001, 2002, 2004, 2006, 2010).

Finally, regarding the phase-offset distribution (Figure 2.40), a stabilization of the mode occurence probability appears for regions containing more than 30 $\mathrm{PS_f}$. However, this limit could be smaller, as there is a gap for populations around 10 $\mathrm{PS_f}$. Moreover, we note that, for the slope standard deviation, the algorithm enables the correction of only 4 regions with more than 10 $\mathrm{PS_f}$.

2.8.2 Radarsat-2

We now extend our sample group to C-band Radarsat-2 data. In this section, we consider two examples of Radarsat-2 Ultra-Fine acquisitions spanning May, 2014 and the period from March to April, 2015. Ultra-Fine images are a priori less suited to SBInSAR processing than TerraSAR-X Stripmap images because they are acquired with a 100 MHz bandwidth and a minimum revisit time of 24 days. On the other hand, we have shown with the feasibility study that a better accuracy is expected for acquisitions with a larger wavelength. Thus, we should obtain concluding results with Radarsat-2 examples, even for smaller bandwidth. Nevertheless, we should keep in mind that another wavelength means that different interactions with the ground cover can come into play and change the performance of Split-Band Interferometry.

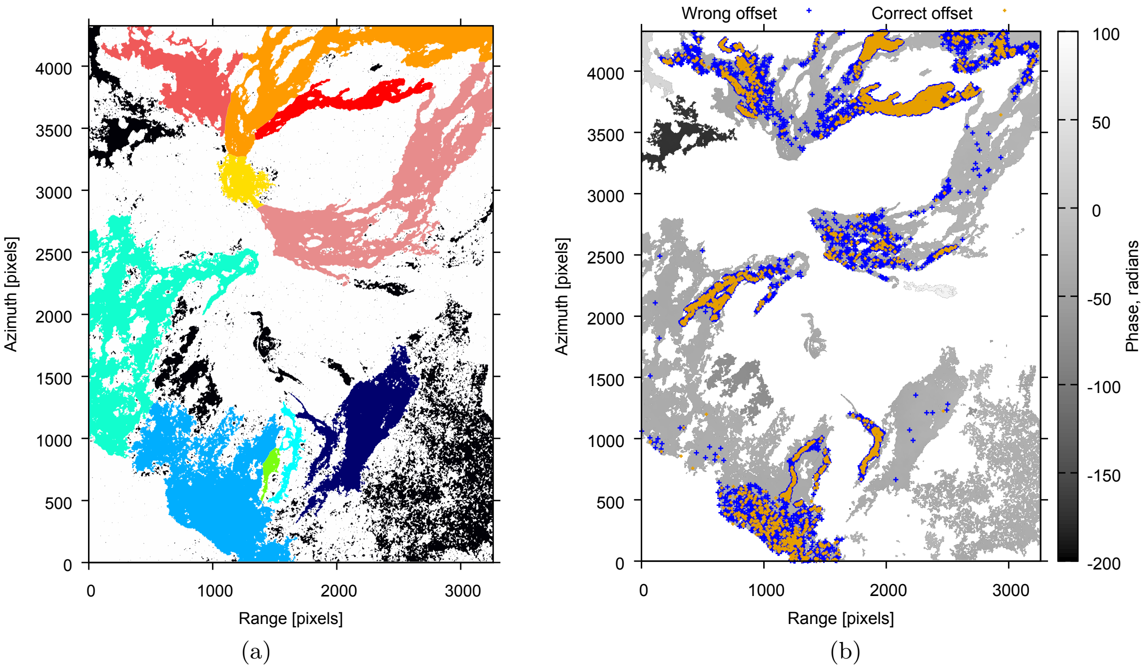

(a) (b)

Figure 2.37: TerraSAR-X, June 22nd, 2008 - July 3rd, 2008. (a) Map of the artificially disconnected regions. The lower half, in blue and green tones, corresponds to the city of Goma, the surroundings and the Nyiragongo lava field (zones 1 to 5). the upper half, in orange and pink tones, corresponds to the northern region of the Nyamuragira lava field (zones 6 to 10). The southern and northern regions are initially disconnected from each other. Regions in black are the naturally disconnected areas, not considered for indirect validation. (b) Frequency-stable targets located over an image of the levelled phase after phase ambiguity correction. An erroneous correction has obviously been introduced for the 1994 flow. PS_f with the expected phase-offset are highlighted in orange, while the others are represented in blue.

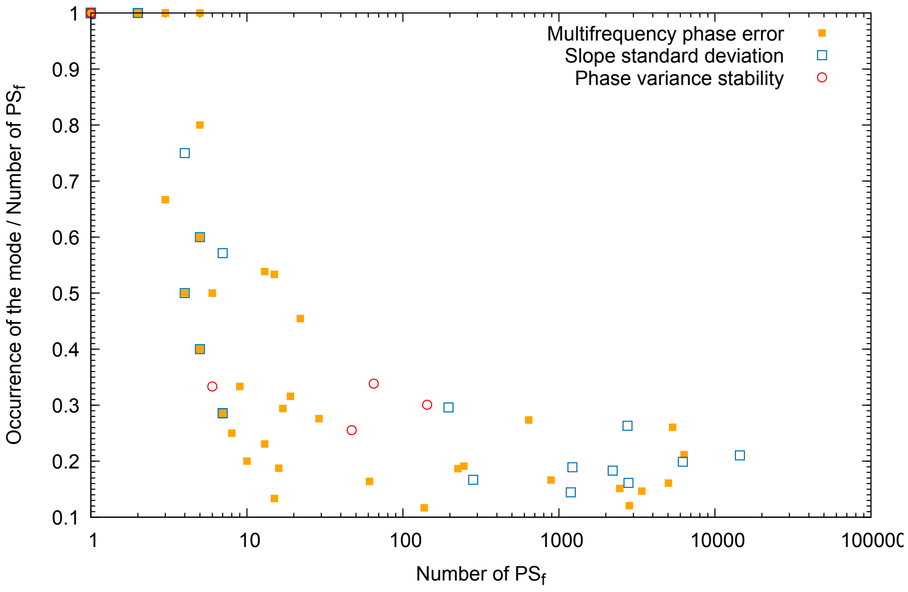

Figure 2.38: TerraSAR-X, June 22nd, 2008 - July 3rd, 2008. Probability for a PS_f to correspond to the mode of the phase-offset distribution as a function of the PS_f population in a corrected region.

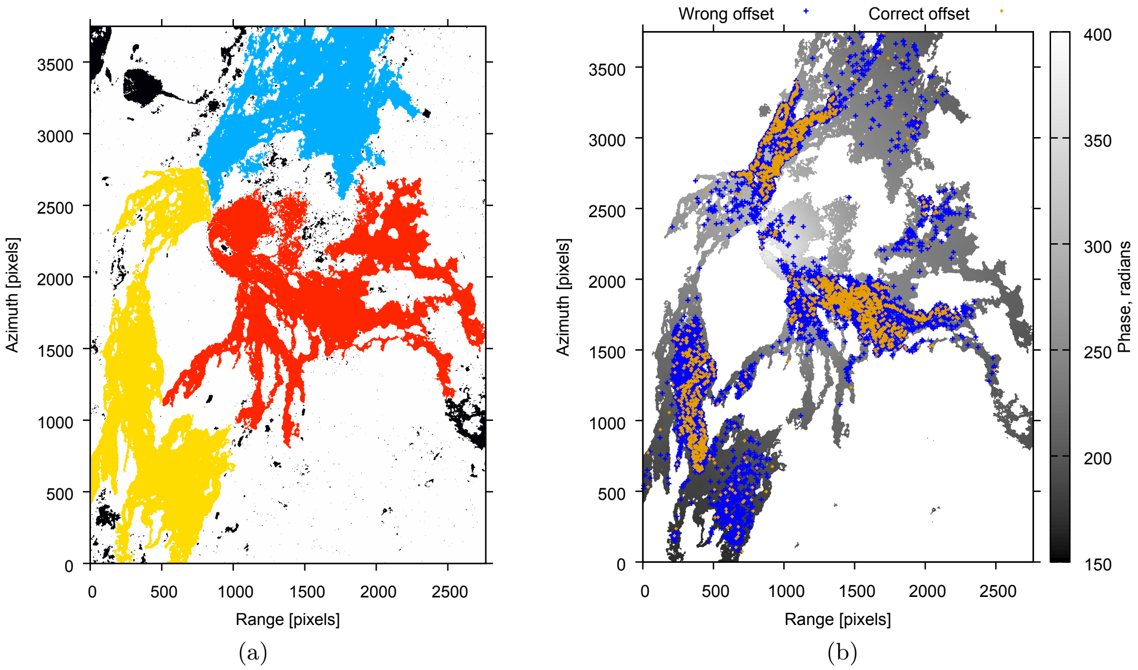

(a) (b)

Figure 2.39: TerraSAR-X, September 1st, 2014 - September 12th, 2014. (a) Map of the artificially disconnected regions. The yellow, red and blue regions are respectively regions 1, 2 and 3. Regions in black are the naturally disconnected areas, not considered for indirect validation. (b) Frequency-stable targets located over an image of the levelled phase after phase ambiguity correction. PS_f with the expected phase-offset are highlighted in orange, while the others are represented in blue.

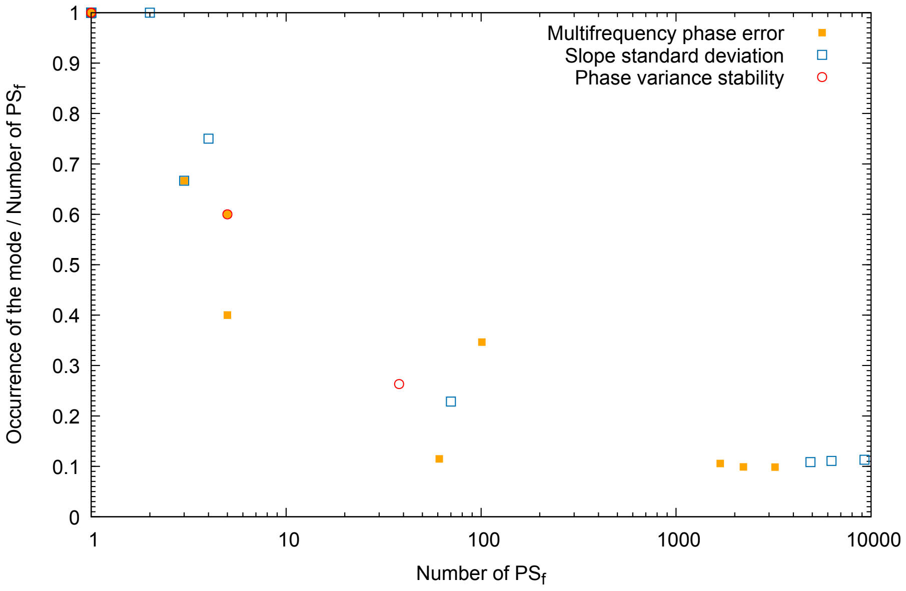

Figure 2.40: TerraSAR-X, September 1st, 2014 - September 12th, 2014. Probability for a PS_f to correspond to the mode of the phase-offset distribution as a function of the PS_f population in a corrected region.

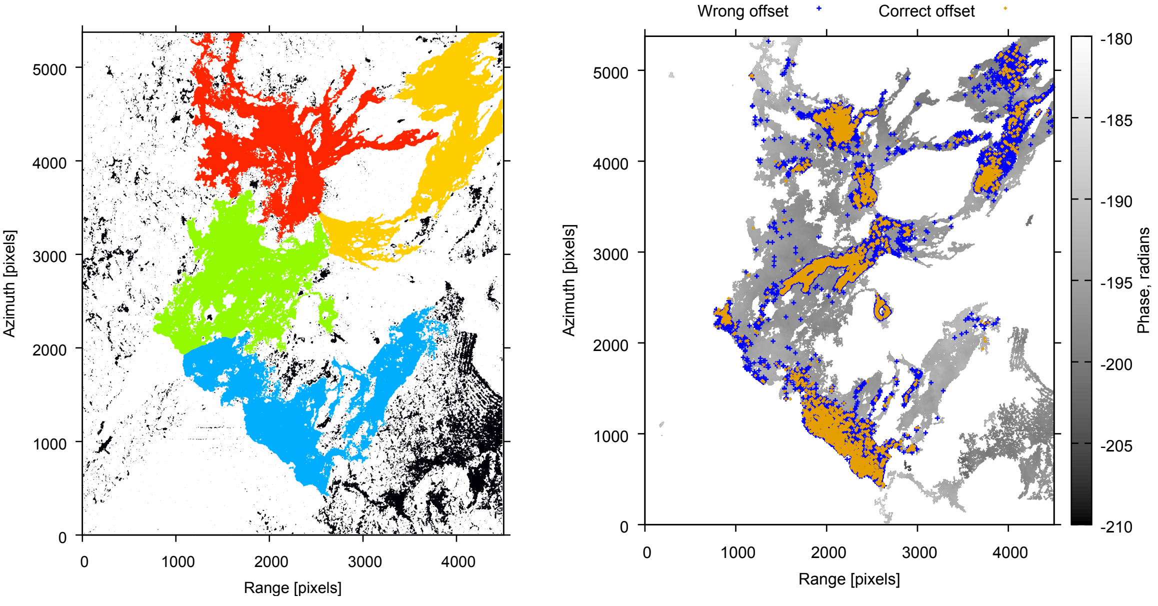

(a) (b)

Figure 2.41: Radarsat-2, May 4th, 2014 - May 28th, 2014. Map of the artificially disconnected regions. The blue, green, yellow and red regions are respectively regions 1, 2, 3 and 4. Regions in black are the naturally disconnected areas, not considered for indirect validation. (b) Frequency-stable targets located over an image of the levelled phase after phase ambiguity correction. PS_f with the expected phase-offset are highlighted in orange, while the others are represented in blue.

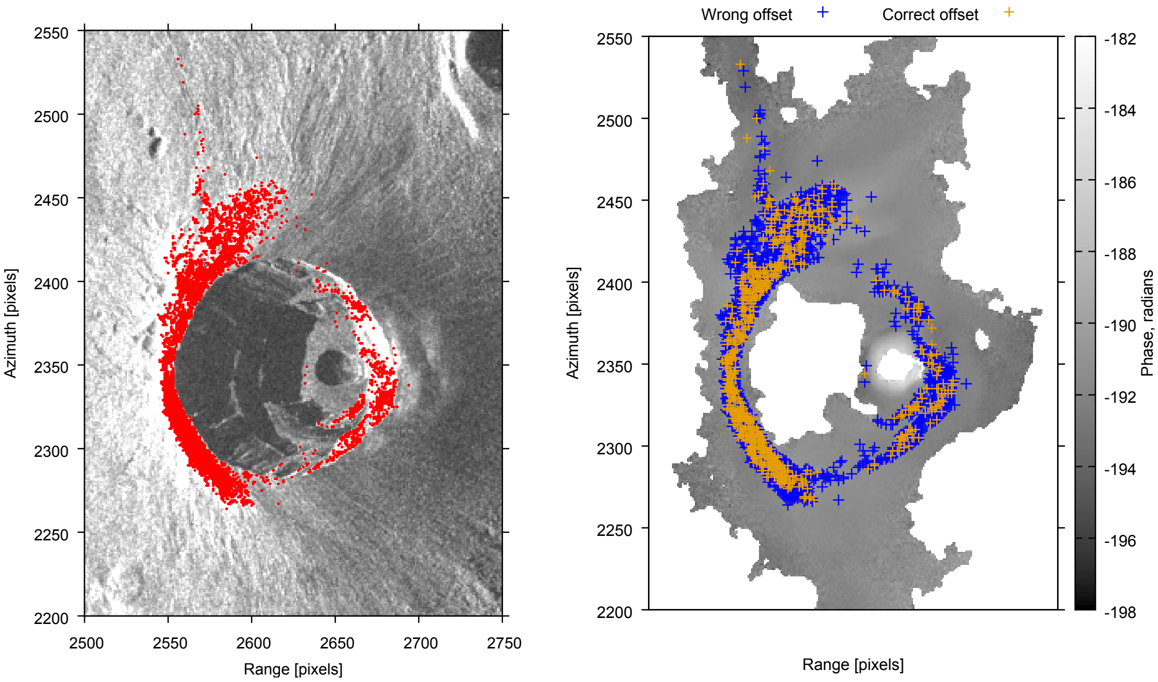

(a) (b)

Figure 2.42: Radarsat-2, May 4th, 2014 - May 28th, 2014. (a) Zoom on the Nyiragongo's crater overlaid with PS_f location. (b) Corresponding levelled unwrapped phase. PS_f with the expected phase ambiguity correction are highlighted in orange.

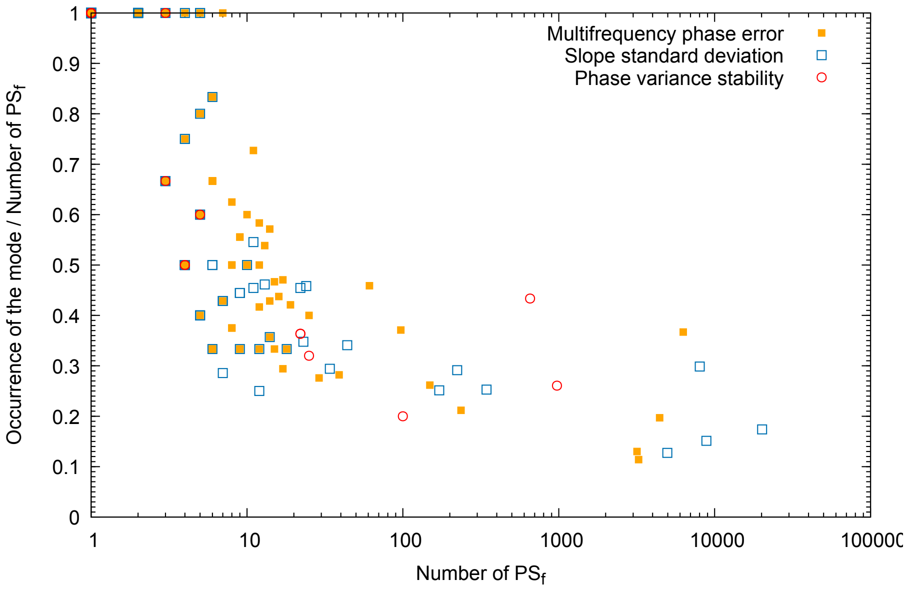

Figure 2.43: Radarsat-2, May 4th, 2014 - May 28th, 2014. Probability for a PS$_f$ to correspond to the mode of the phase-offset distribution as a function of the PS$_f$ population in a corrected region.

May 4th, 2014 - May 28th, 2014

The first Radarsat-2 example is a pair of Ultra-Fine images acquired on May 4th and May 28th, 2014 with an incidence angle at median range of 36°. The pair spans a time period of 24 days, which is the minimum with this sensor, but temporal decorrelation could still have an important influence. The perpendicular baseline is about 8 m and we apply a spectral decomposition into 5 subbands of 20 MHz that gives a very high CDR value of 331.95. As we work with C-band data, the threshold on the slope standard deviation is now set to 1.16 rad/GHz.

Phase-offset	Cycles
n_1	-31
n_2	-32
n_3	-31
n_4	-32

(a)

Relative phase-offset	Cycles
$m_1 - m_2$	1
$m_1 - m_3$	0
$m_1 - m_4$	1
$m_2 - m_3$	-1
$m_2 - m_4$	0
$m_3 - m_4$	1

(b)

Table 2.12: Radarsat-2, May 4th, 2014 - May 28th, 2014. (a) Computed phase-offset corrections. (b) Relative phase-offsets.

The main continuously unwrapped region is split into four regions, as depicted by the coloured regions in Figure 2.41a. The corresponding relative phase-offsets are listed in Table 2.12, along with the calculated corrections of the phase ambiguities. We observe that the relative values of the phase-ambiguities are obeyed for all combinations of the four regions. The corrections are therefore valid for this example.

In Figure 2.41b, we indicate the frequency-stable targets and highlight the ones with the correct phase ambiguity correction. Unlike the previous example, we observe a high density of selected targets on the Nyiragongo's rim. Let us zoom on this particular area (Figure 2.42). The density

of PS_f with the expected correction is larger on the left side of the crater. However, inside the crater, we detect some targets on each platform. If other examples were found with such density of detected targets, it could be used for monitoring the relative level of the platforms.
Finally, we take a look at the probability of the mode occurrence (Figure 2.43). Once again, we observe a stabilization of the probability for regions with more than 20-30 PS_f. However, we have larger dispersion in the values of the probability.

March 12th, 2015 - April 5th, 2015

The second Radarsat-2 example is a pair of Ultra-Fine acquisitions on March 12th and April 5th, 2015. The time span is again 24 days, and the perpendicular baseline is about 50 m. The CDR has a value of 52.27, which is lower than the previous example but still quite good.

Phase-offset	Cycles	Error
n_1	8	
n_2	7	
n_3	6	-1 cycle
n_4	8	

(a)

Relative phase-offset	Cycles
$m_1 - m_2$	1
$m_1 - m_3$	1
$m_1 - m_4$	0
$m_2 - m_3$	0
$m_2 - m_4$	-1
$m_3 - m_4$	-1

(b)

Table 2.13: Radarsat-2, March 12th, 2015 - April 5th, 2015. (a) Computed phase-offset corrections. The error column gives the error inferred from the cross-checking with relative phase-offsets. (b) Relative phase-offsets.

The applied disconnection pattern into four regions is very similar to the previous example (Figure 2.44a). Regarding the phase ambiguity corrections and the relative phase-offsets given in Table 2.13, it results that most regions are correctly levelled, except for region 3 (yellow) that shows a one-cycle error. As it can be observed in Figure 2.44b, although it does not provide the expected correction, region 3 shows a higher density of PS_f than region 4 (red). Actually, the observed error is within the expected range precision set by the slope standard deviation criterion and we should not worry about this result. We also observe that the region of the Nyiragongo's crater is corrected: there are targets detected in this region once again.
Finally, in compliance with the previous examples, we note a stabilization of the mode occurrence probability around 20-30 PS_f per region, even though the dispersion of the probability is important.

2.8.3 Cosmo-SkyMed

Our sample group is finally extended to Cosmo-SkyMed data. These are X-band data, like TerraSAR-X, and we have at our disposal acquisitions in HIMAGE mode with a range bandwidth of 129 MHz. The applied spectral decomposition is made of 5 subbands of 25.8 MHz. The main issue with Cosmo-SkyMed acquisitions is their overall large perpendicular baselines that induce important spatial decorrelation. Nevertheless, we manage to find pairs of acquisitions with baselines smaller than 100 m, in addition to a minimum revisit time of 8 days.

February 10th, 2016 - February 18th, 2016

The first Cosmo-SkyMed test case is made of images acquired on February 10th and 18th, 2016. Images form a perpendicular of about 33 m and have an approximate incidence angle of 26.5°. These parameters correspond to a CDR of 26.87.

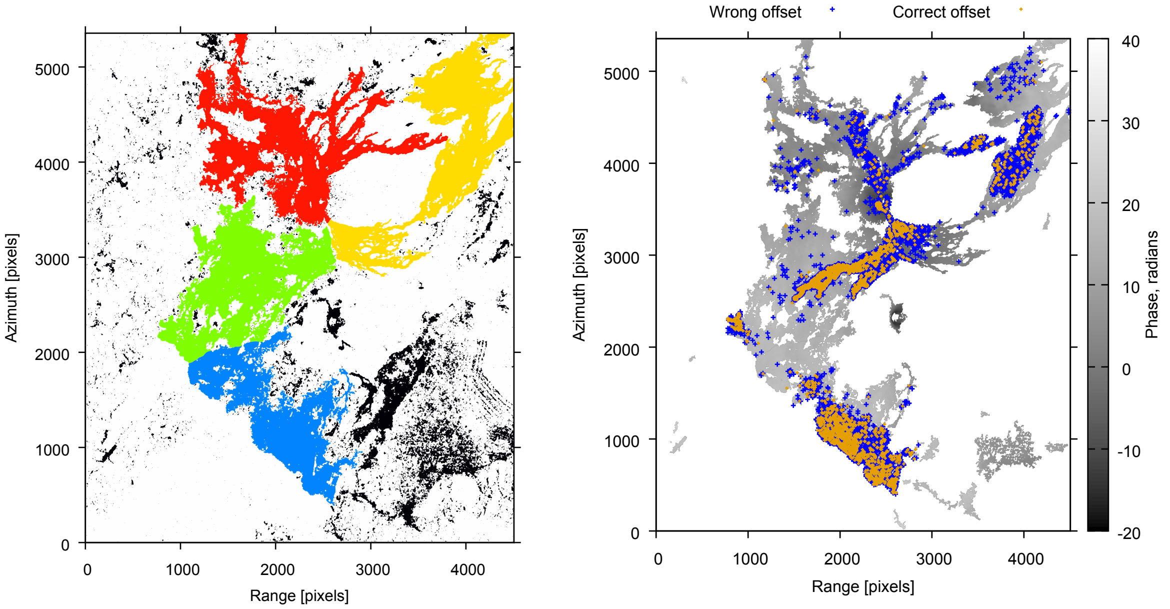

(a) (b)

Figure 2.44: Radarsat-2, March 12th, 2015 - April 5th, 2015. Map of the artificially disconnected regions. The blue, green, yellow and red regions are respectively regions 1, 2, 3 and 4. Regions in black are the naturally disconnected areas, not considered for indirect validation. (b) Frequency-stable targets located over an image of the levelled phase after phase ambiguity correction. $\mathrm{PS_f}$ with the expected phase-offset are highlighted in orange, while the others are represented in blue.

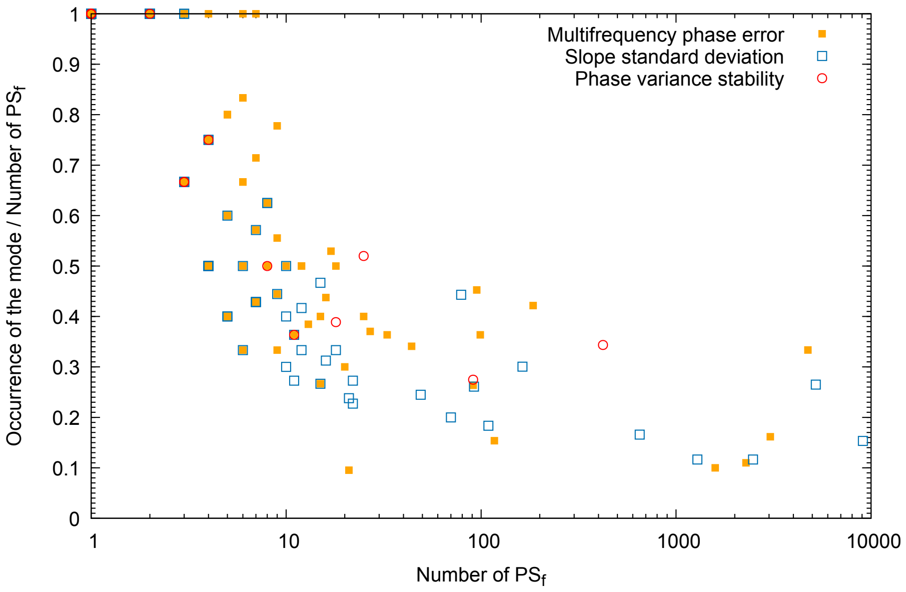

Figure 2.45: Radarsat-2, May 4th, 2014 - May 28th, 2014. Probability for a $\mathrm{PS_f}$ to correspond to the mode of the phase-offset distribution as a function of the $\mathrm{PS_f}$ population in a corrected region.

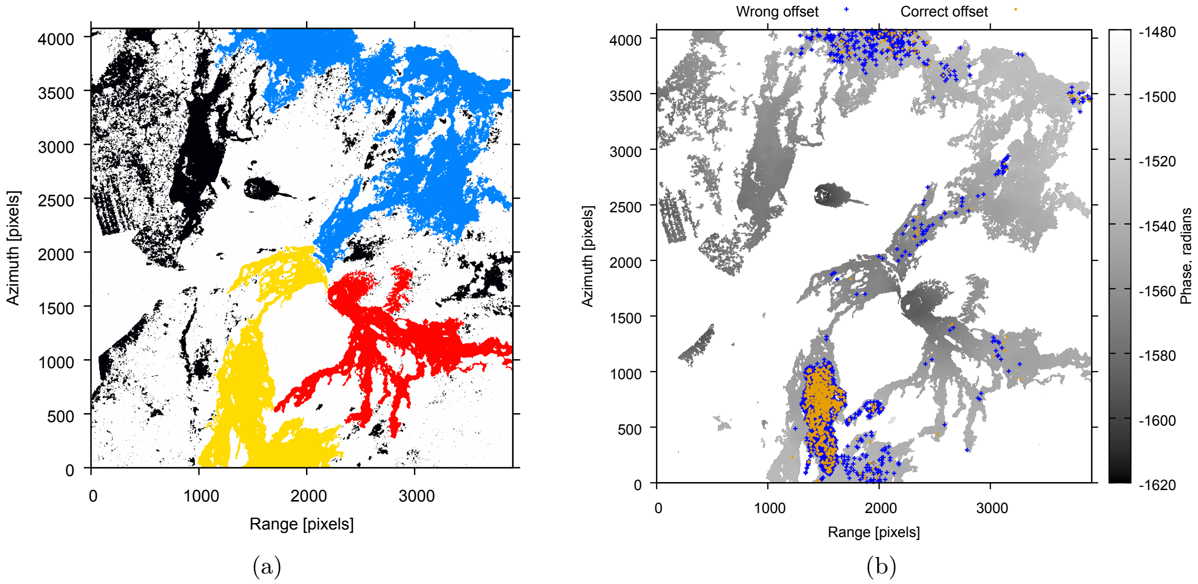

(a) (b)

Figure 2.46: Cosmo-SkyMed, February 10th, 2016 - February 18th, 2016. Map of the artificially disconnected regions. The yellow, red and blue regions are respectively regions 1, 2, and 3. Regions in black are the naturally disconnected areas, not considered for indirect validation. (b) Frequency-stable targets located over an image of the levelled phase after phase ambiguity correction. PS_f with the expected phase-offset are highlighted in orange, while the others are represented in blue.

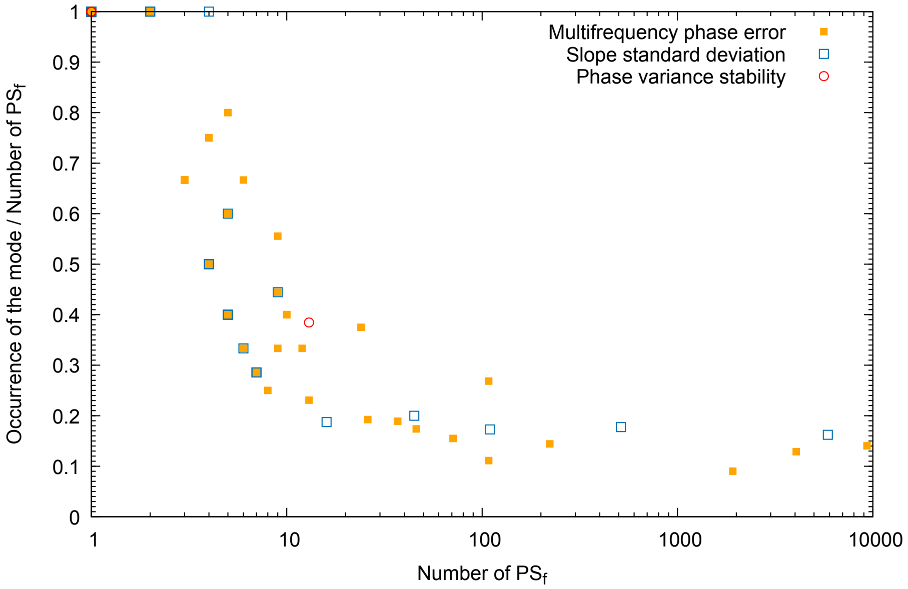

Figure 2.47: Cosmo-SkyMed, February 10th, 2016 - February 18th, 2016. Probability for a PS_f to correspond to the mode of the phase-offset distribution as a function of the PS_f population in a corrected region.

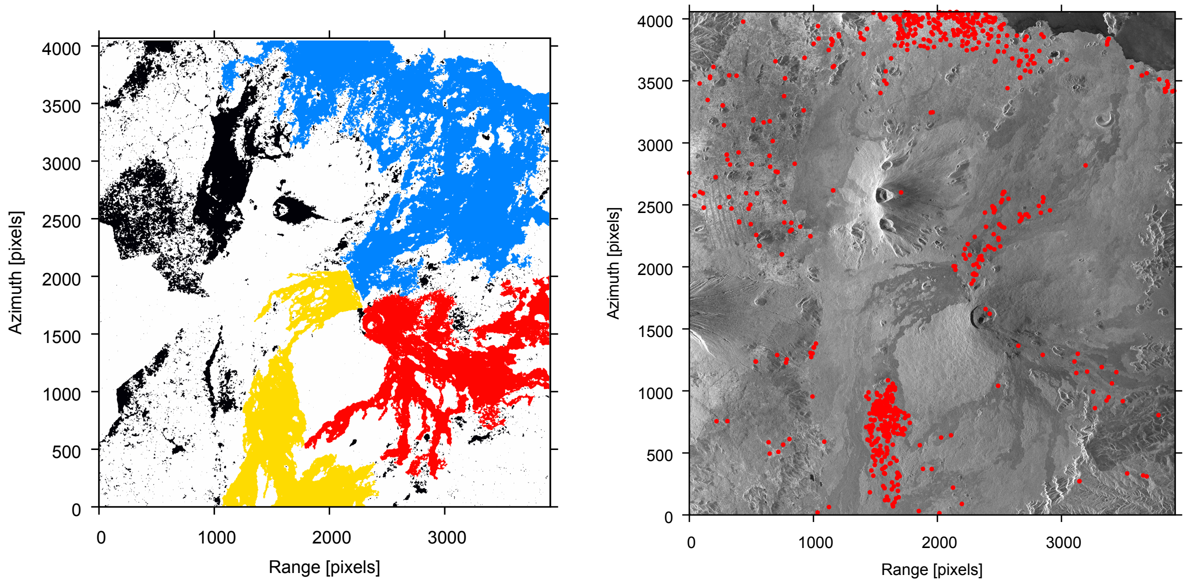

(a) (b)

Figure 2.48: Cosmo-SkyMed, February 26th, 2016 - March 5th, 2016. Map of the artificially disconnected regions. The yellow, red and blue regions are respectively regions 1, 2, and 3. Regions in black are the naturally disconnected areas, not considered for indirect validation. (b) Location of the detected $\mathrm{PS_f}$, highlighted in red.

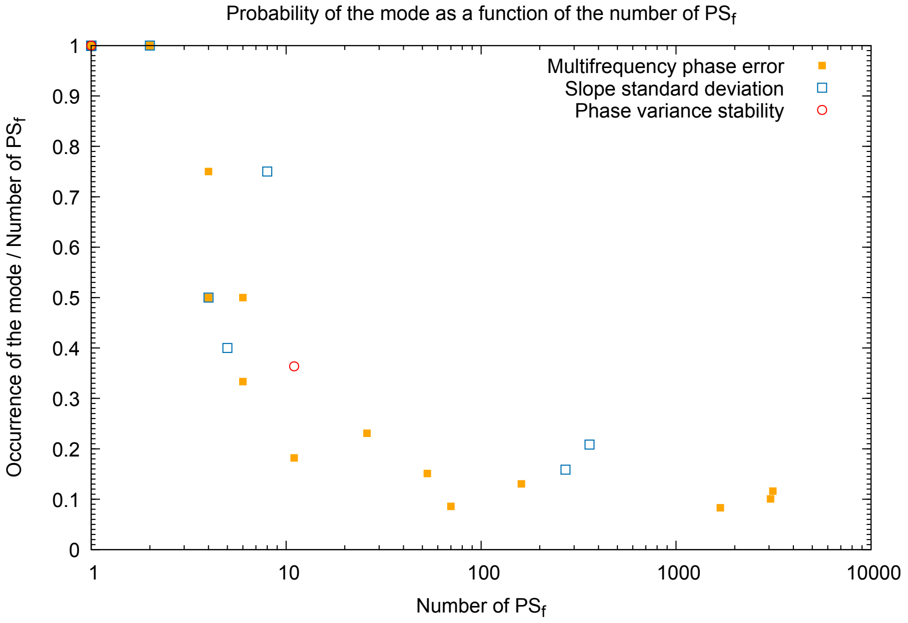

Figure 2.49: Cosmo-SkyMed, February 26th, 2016 - March 5th, 2016. Probability for a $\mathrm{PS_f}$ to correspond to the mode of the phase-offset distribution as a function of the $\mathrm{PS_f}$ population in a corrected region.

Phase-offset	**Cycles**
n_1	-235
n_2	-234
n_3	-234

(a)

Relative phase-offset	**Cycles**
$m_1 - m_2$	-1
$m_1 - m_3$	-1
$m_2 - m_3$	0

(b)

Table 2.14: Cosmo-SkyMed, February 10th, 2016 - February 18th, 2016. (a) Computed phase-offset corrections. (b) Relative phase-offsets.

Since this example is a bit more challenging than the Radarsat-2 ones, we choose to split the interferogram in three regions only, as represented in Figure 2.46a. In Table 2.14, we give the calculated phase ambiguities and the corresponding relative phase-offsets. All corrections are in agreement with the expected relative values.

In Figure 2.46b, we plot the frequency-stable targets for the artificially disconnected regions. We directly note that the 2011-2012 lava flow shows the highest density of $\mathrm{PS_f}$. Other places have a really scarce population of detected targets, which is nonetheless sufficient to obtain the phase ambiguity correction.

Similarly to the other test cases, we note a stable probability of the phase-offset mode for regions with more than 20 $\mathrm{PS_f}$ (Figure 2.47).

February 26th, 2016 - March 5th, 2016

The last example considered here is a pair of acquisitions on February 26th and March 5th, 2016. The pair has a temporal baseline of 8 days, a perpendicular baseline of 98 m and an incidence angle of 26.5°. Its CDR value equals 8.39, which is very close to the limit of detection determined in Section 2.7. Hence, we expect to have a very poor population of $\mathrm{PS_f}$ and no concluding results for SBInSAR.

Phase-offset	**Cycles**
n_1	-233
n_2	NC
n_3	-221

(a)

Relative phase-offset	**Cycles**
$m_1 - m_2$	1
$m_1 - m_3$	-1
$m_2 - m_3$	-2

(b)

Table 2.15: Cosmo-SkyMed, February 26th, 2016 - March 5th, 2016. (a) Computed phase-offset corrections. NC stands for "not corrected". (b) Relative phase-offsets.

We adopt disconnection pattern similar to the previous example and divide the interferogram into 3 parts (Figure 2.48a). The calculated corrections of the phase ambiguities and the relative phase-offsets are listed in Table 2.15. We have one region that is not corrected out of the three: region 2 (red) contains less than 20 $\mathrm{PS_f}$ and its distributions of the phase ambiguity estimates is multimodal. As a consequence, it is not possible to assess if the corrections applied to the other two regions are correct or not.

In Figure 2.48b, we locate the detected $\mathrm{PS_f}$. Even though we are close to the limit of detection, we observe a high density of $\mathrm{PS_f}$ at some locations. Actually, the limit of detection has been determined for the ground coverage in 2008, while we are studying a pair of 2016. In the meantime, ground has been reshaped and new lava flows have appeared. The highest density of $\mathrm{PS_f}$ is found over the recent 2011-2012 flow and population is scarce elsewhere. In particular, there is almost no $\mathrm{PS_f}$ over Nyiragongo.

Here again, we look at the probability of the phase-offset mode in Figure 2.49 and we observe a stable behaviour for populations larger than 10-20 PS_f. However, in this case, the amount of corrected regions is much lower than in the previous examples.

2.8.4 Conclusions

We have considered three types of sensors, both in X-band and C-band. Overall, we managed to perform SBInSAR-assisted phase unwrapping on all studied images. We observed in some cases errors of one cycle for the phase ambiguity correction, but this remains within the tolerance range fixed by the PS_f detection criterion. We checked for each example the behaviour of the probability for a PS_f to correspond to the phase-offset correction as a function of the PS_f content of the region and we observe that the probability becomes stable for regions of more than 20-30 PS_f. It seems that this is the minimum amount of targets to have a statistically significant population, as a smaller PS_f content leads to a very variable mode probability.

For the second Cosmo-SkyMed example, we were at the limit of detection determined from the temporal analysis. In this case, the population of stable targets was very scarce. One of the regions could not be levelled because of its multimodal distribution and phase ambiguity corrections remained quite uncertain.

For the C-band example, PS_f were detected on the Nyiragongo's rim and inside the crater. Given the density of targets present on the volcano, these data could be used for monitoring the platforms level via Split-Band Interferometry.

2.9 Summary and conclusions

In the introduction of this chapter, some questions were raised about SBInSAR. For example: when can we use Split-Band Interferometry? What are the sensitive parameters that must be taken into account? In some other words: when is the SBInSAR processing successfully applicable?

In a first step, after introducing the formalism of SBInSAR for a monostatic case, we undertook a theoretical study of the feasibility. We showed that performances are limited by two major and antagonistic effects: the first one is the limited SBInSAR phase accuracy, optimized when the ratio $\frac{\nu_0}{B}$ is low, and the other one is the geometrical decorrelation induced by the bandwidth reduction. This second effect is minimized for a large correlated-to-decorrelated ratio, which is a function that depends on acquisition parameters like the wavelength, the partial bandwidth, the incidence angle, the range distance and the perpendicular baseline. For the particular case of the Virunga Volcanic Province, we derived a limit of detection of about 8.6 for the CDR. This value is not restrictive, it is only a global indication for choosing adequate data.

Besides, we studied the influence of the split parameters on the SBInSAR phase error, both in theory and in practice. It was established that non overlapping subbands should be preferred for spectral decomposition, along with a weighted linear regression for the multichromatic analysis part of the processing. In practice, splitting the bandwidth into 5 non overlapping subbands proved to be a satisfactory choice.

Another question was: how to turn SBInSAR operational? For this purpose, we relaxed requirements on the SBInSAR phase to a one-cycle accuracy and, instead of using Split-Band Interferometry for direct absolute phase measurements, we proposed to exploit it to simply correct phase ambiguities of separately unwrapped regions. We presented an indirect way to validate the corrections in the case of a branch-cut algorithm and we defined an aspect ratio to assess the quality of the results. The approach was validated for a TerraSAR-X Spotlight pair of acquisitions over the Copahue volcano. It was then extended to TerraSAR-X, Radarsat-2 and Cosmo-SkyMed data over the Virunga with bandwidth between 100 and 150 MHz and it performed satisfactorily as long as the limit on the CDR was obeyed.

Despite its very simple approach, SBInSAR-assisted phase unwrapping relies on the need for reliable detection of frequency-stable targets, i.e. targets with a precise enough SBInSAR phase. We showed that the error of the SBInSAR phase is driven by the error on the slope of the linear regression, and that this can be exploited to select frequency-stable targets. In addition, considering an assumption of symmetrical split and another of phase variance stability, we demonstrated that the SBInSAR phase error is limited by the subband with the largest phase variance. This is used to define the phase variance stability criterion of detection. We tested these two criteria along with other ones, separated into phase quality estimators and goodness-of-fit estimators. In the scope of the phase ambiguity correction, goodness-of-fit estimators have been dismissed for their lack of efficiency in removing outlier pixels. The phase variance stability proved to be efficient to minimize the erroneous detections, but this criterion is restrictive and usually leads to sparse detections of stable targets. Based on both the phase ambiguity distribution and the detection problem stated in terms of probabilities, we finally determined that the slope standard deviation is a good trade-off between the precision of the SBInSAR phase and the detection rate. It outperforms the usual multifrequency phase error estimator, that was mainly used in previous studies.

Even though Split-Band Interferometry relies on their presence within the scene, frequency-stable targets, also called frequency-persistent scatterers, are still poorly understood. For this reason, we raised additional questions about their nature: what are their characteristic features? Are they stable in time? Do they correspond to some other well-known mechanisms like those of permanent scatterers? It was not possible to completely answer these questions and we still do not know exactly what a frequency-persistent scatterer is. However, we do know what it is *not*: a target stable in the frequency domain is not necessarily stable over time. It does not have to be a permanent scatterer to show spectral stability. Moreover, stability of the spectral signal is not stationary by definition. Let us stress that frequency-stable targets are characterized by a high coherence.

Despite these considerations, there is still a minor population of frequency-stable targets that persists over time. These are of interest for a potential continuous monitoring. We attempted to classify them according to their brightness and their spectral coherence, and it occurred that, in the Kivu region, they cannot be associated to a particular scattering mechanism: they can either be associated to single point targets and double bounce mechanisms, or to diffuse scattering over coherent lava flows. The fact that they could be transient in time and they can correspond to distributions of scatterers makes the name *"frequency-persistent scatterers"* inadequate. A more appropriate name would be *frequency-stable pixels*.

Indeed, classification of frequency-stable targets over time did not allow to characterize them fully. However, it showed that they could be bright structures stable in time, like buildings. This is investigated in more details in Chapter 4 through transponders and corner reflectors, as it could allow to define stable and reliable seed points and open a perspective of monitoring using Split-Band Interferometry.

List of symbols for Chapter 2

α	Apodization coefficient
B	Range bandwidth
B_s	Subband range bandwidth
$B_\perp$	Perpendicular baseline
c	Speed of light
χ^2_ν	Reduced chi-square
δ	Fraction of detected $\mathrm{PS_f}$
Δf	Subband frequency shift
Δr	Range coregistration offset
Δx	Range pixel size
$\Delta\varphi$	SBInSAR phase
$\Delta\phi$	InSAR unwrapped phase
$\Delta\phi_c$	Fully connected version of the InSAR unwrapped phase
$\Delta\phi_d$	Artificially disconnected version of the InSAR unwrapped phase
$\Delta\phi_{e_c}$	Misregistration phase
$\Delta\phi_{reg}$	Coregistration phase
e_c	Coregistration error
e_p	Coregistration error expressed in pixel units
γ	Lower incomplete gamma function
γ_s^{ij}	Spectral coherence of i-th and j-th subbands
$\langle\gamma_s\rangle$	Spectral coherence averaged for all combinations of subbands
γ_ν	SBInSAR coherence
Γ	Gamma function
λ	Wavelength
m	Relative phase ambiguity, relative phase-offset
n	Phase ambiguity, phase shift, phase-offset
N	Number of subbands
N_{DOF}	Number of degrees of freedom
ν_0	Radar carrier frequency

ν_i	Frequency of i-th subband
$p(\nu)$	Linear fitting function
Q	Plausibility of the fit
ϕ_i	Subband phase samples
r^2	Linear correlation coefficient
r_m	Range distance in the master image
r_s	Range distance in the slave image
S_m^i	Point target response in the i-th partial master image
S_s^i	Point target response in the i-th partial slave image
σ^0	Sigma-nought, backscattering coefficient estimate
σ_s	Slope standard deviation
$\sigma_{\Delta\varphi}$	SBInSAR phase standard deviation
σ_ν	Multifrequency phase error
$\sigma_{\phi_i}^2$	Phase variance of i-th partial interferogram
$\sigma_{\phi,max}^2$	Upper bound of partial phase variance
θ	Incidence angle
x_i	Subband index in symmetrical numbering

Chapter 3

Multidimensional Small Baseline Subset

For many years, differential SAR Interferometry (DInSAR) has been a unique tool to study ground deformations and the related geophysical processes [6]. However, classical DInSAR only captures the deformation pattern between two dates. Even though successful when applied to a single-episode phenomenon, like a fault rupture [18], the potential of classical DInSAR for spatio-temporal analysis is limited. For this reason, it has been a major concern for the InSAR users to integrate the phase information from multiple differential interferograms and reconstruct the history of ground deformations. Indeed, adding the time dimension eases the understanding of geophysical processes, enables monitoring and gives the possibility of detecting precursory signals of geohazard events.

In this context, many multitemporal DInSAR techniques have been developed for the past two decades. They are usually arranged in two categories: the *Permanent Scattererer Interferometry* (PSI) [10, 12, 62] and the *Small Baseline Interferometry* [11, 63, 64]. As its name indicates, the first category focuses on permanent scatterers, i.e. point-like targets stable over time; the second category studies ground deformation of distributed targets. These techniques are based on different algorithms, taking into account the peculiarities of each type of target (e.g. size, geometry, coherence). Besides, some techniques, like StaMPS [65], have been developed to consider both types of targets.

Conversely to PSI, a Small Baseline approach constrains the spatial and temporal baselines to preserve coherence through its whole interferogram sequence. Moreover, the used interferograms do not have a common master image and the generated displacement maps have a spatially dense coverage. A popular approach among the Small Baseline techniques is the *Small Baseline Subset* (SBAS) [11, 66]. This algorithm is meant to estimate the line-of-sight displacement over time from an interferogram sequence of independant subsets, i.e. spatially separated subsets of small baseline pairs. This technique has been widely applied to the study of volcanism [67, 68], landslides [69, 70], and urban or coastal subsidence [71–74]. Nevertheless, with this approach, the knowledge is restricted to the movement away or towards the satellite while, in general, a multidimensional estimate of the displacement constrains geophysical models better. The possibility of mapping 3-D deformations has been discussed in Reference [75].

The Multidimensional-SBAS (MSBAS) goes one step further and produces 2-D ground deformation time series (vertical and west-east) by integrating at once ascending and descending data from different sensors, with various geometries and acquisition parameters (e.g. wavelength, resolution, polarization, incidence angle, etc.) [14]. In addition to providing projected measurements, it presents the interest of merging together large data sets overlapping in space and time, which results in an increased temporal sampling rate and an uninterrupted monitoring. MSBAS has proven to be efficient to map ground deformation due to volcanic activity [14], mining [76], pingo growth [77] or water withdrawal [78].

Since MSBAS is particularly well designed to monitor small and continuous deformations, we focus in the present work on its capacity for monitoring geohazards in the Kivu region. We present the MSBAS mass processing chain developed in the scope of the RESIST project for interfacing the CSL InSAR Suite with the MSBAS software developed by Sergey Samsonov, and we test options meant to speed up mass processing chain and improve MSBAS results.

In the first part of this chapter, we present the rationale of the MSBAS. The problem is formulated in two steps: we first describe the SBAS problem; we then present a projected formulation of the SBAS and introduce the MSBAS problem. In the second part of the chapter, we briefly present the InSAR mass processing chain developed in order to finally obtain an end-to-end operational MSBAS processing chain. After presenting the developed tools, we investigate two ways for improving the MSBAS performance. First, we consider the spatial coverage. On the one hand, we propose a simple interpolation strategy in order to obtain a denser spatial coverage. On the other hand, we propose to mask decorrelating regions in order to gain computing time and we search for the best estimator to generate such a mask. For this purpose, we focus on the landslide-prone city of Bukavu and we present results of an MSBAS processing for the 2016-2017 period. Finally, we model the temporal coherence and attempt to determine an appropriate decorrelation time over the Virunga region. This decorrelation time can be further applied as a temporal baseline threshold to define an MSBAS interferogram sequence.

Software

MSBAS is a software of advanced InSAR post-processing developed by Sergey Samsonov. It is freely available on the following website: `www.insar.ca`. An implementation of the SBAS algorithm is also found at this address [66].

3.1 Rationale

Multidimensional Small Baseline Subset is a technique that is aimed at retrieving ground deformation time series in two dimensions and that especially focuses on distributed targets. It relies on the same basis as the one-dimensional Small Baseline Subset, but integrates data sets of images with various geometries and acquisition parameters to map 2-D displacements. Let us stress that MSBAS achieves only 2-D displacements due to the near polar orbits of spaceborne SAR sensors. If there existed SAR satellites on subpolar orbits, then 3-D displacements could be handled by the MSBAS software.

In this section, we introduce the mathematical description of MSBAS. In order to ease the understanding of the reader, we first introduce the SBAS problem and use it to derive the MSBAS formulation.

3.1.1 Small Baseline Subset

In this section, we review shortly the formalism of the Small Baseline Subset (SBAS) problem and point out the key elements. The uninitiated reader is provided with a simplified formalism to familiarize with the technique and introduce basic notions used in MSBAS. For readers interested in a deeper understanding, a more detailed formulation of the algorithm can be found in Reference [11].

Interferogram formation

Many methods have been proposed to generate InSAR time series [79]. In order to be effective, they must properly relate the phase information of one pair to the information content of the other pairs of the data set. The main difference between Small Baseline approaches and Permanent Scatterers Interferometry lies in the way they generate an appropriate sequence of interferograms.

In the case of the SBAS algorithm, pairs of images should be acquired from relatively close tracks to mitigate spatial decorrelation and residual topographic errors. Moreover, in order to prevent changes in the observed scene and limit temporal decorrelation, they should span a restricted time lapse. In practice, highly coherent interferograms are obtained by imposing maximum values on the spatial and temporal baselines. Besides, contrary to PSI, the sequence of interferograms is not focused on a single global master: each image can be the master of an interferogram, as long as the master and slave acquisitions remain ordered in time.

Let us consider a data set of $N+1$ SAR images observing the studied region and acquired at ascending times $(t_0, t_1, \ldots, t_N)$. The data set is made of images that are all acquired with the same sensor and with similar acquisition parameters (resolution, incidence angle, polarization, etc.). From these $N+1$ acquisitions, we determine an interferogram sequence following the above strategy and we form M differential unwrapped interferograms. Small Baseline Subset is based on the use of interferograms corrected from the topography, unwrapped and resampled on a common grid. Moreover, it assumes that the phase signal is calibrated with respect to a point or a region of known deformation. Ideally, this reference is a highly coherent pixel in a nondeforming zone.

Interferogram signal description

Let us take the image acquired at time t_0 as the reference scene and denote by d_j the cumulative deformation along the line-of-sight at time t_j with respect to the initial instant t_0. Given that t_0 is the temporal reference, we have $d_0 = 0$. In this case, the phase associated to the deformation at time t_j for a point of azimuth-range coordinates (x, r) is given, $\forall j = 1, \ldots, N$, by

$$\phi_j(x,r) \;=\; \frac{4\pi}{\lambda}\, d_j(x,r), \tag{3.1}$$

where λ is the wavelength. Therefore, if we neglect the noise and the atmospheric contribution and if we consider that the topographic component has been correctly removed, the signal in the i-th differential interferogram computed from acquisitions at times t_{m_i} and t_{s_i} is modelled by

$$\begin{aligned} \Delta\phi_i(x,r) \;&=\; \phi_{m_i}(x,r) \;-\; \phi_{s_i}(x,r) \\ &=\; \frac{4\pi}{\lambda}\left(d_{m_i}(x,r) \;-\; d_{s_i}(x,r)\right), \end{aligned} \tag{3.2}$$

where m_i and s_i are the time indices associated to the master and slave acquisitions of the i-th interferogram, $\forall i = 1, \ldots, M$. Let us stress that SBAS relies on a pixel-by-pixel analysis, but we will not explicitly state the dependency on the pixel coordinates (x, r) in the following.

Problem formulation

In matrix representation, Equation (3.2) can be written as

$$\mathbf{B}\boldsymbol{\phi} \;=\; \boldsymbol{\Delta\phi}, \tag{3.3}$$

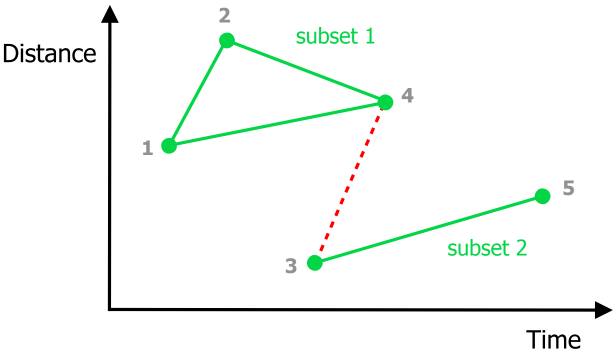

Figure 3.1: Simplified representation of a data set leading to an underdetermined SBAS system. This is a temporal baselines versus spatial baselines plot, where the $N + 1$ images of the data set are represented by green dots and are numbered by ascending time. The green segments represents the M interferograms, each one corresponding to a phase difference between two images. If we consider subset 1, the combination of the pairs 1-2 and 2-4 is equivalent to the pair 1-4: $\phi_4 - \phi_1 = (\phi_4 - \phi_2) + (\phi_2 - \phi_1)$. The corresponding equations are linearly dependent. When all images are connected, as it is the case with the dotted red line, then we have as much images as linearly independent equations. However, when images 3 and 4 are not connected and the subsets are independent, then the number of linearly independent equations is reduced by one unit and the system becomes underdetermined.

where $\boldsymbol{\Delta\phi}$ is the M-dimensional vector of the pointwise phase observations, $\boldsymbol{\phi}$ is the N-dimensional vector of the unknown phases associated to the cumulative deformations and $\mathbf{B}$ is a $M \times N$ matrix whose elements are defined, $\forall i = 1, \dots, M$, by

$$B_{ij} = \begin{cases} -1 & \text{if} \quad j = s_i \neq 0 \\ +1 & \text{if} \quad j = m_i \\ 0 & \text{otherwise.} \end{cases}$$

In order to retrieve the deformations we are looking for, the system must be inverted to isolate $\boldsymbol{\phi}$. However, the problem is usually underdetermined. This can be easily understood: if we assume the ideal case for which no error has been introduced by the processing in the differential phase, combinations of pairs covering the same time span will always correspond to linearly dependent equations in the system. Consequently, only a fully connected system can have as much unknowns as equations. If the data set is split into subsets, the system will lose one linearly independent equation per subset and the system will become underdetermined. This is sketched for a simple data set of 5 images in Figure 3.1. In the underdetermined case, the system cannot be solved directly, because it has an infinity of solutions. It is therefore inverted using the *Singular Value Decomposition* (SVD) method [80,81], which provides a minimum norm solution for the phase. A brief explanation of this method is provided in the next section.

However, the minimum norm constraint introduces non-physical discontinuities in the computed phase values. For this reason, it is preferable to reformulate the problem and solve it from the deformation rate point of view. The linear phase velocity between adjacent times t_{i-1} and t_i is given by

$$v_i = \frac{\phi_i - \phi_{i-1}}{t_i - t_{i-1}} \tag{3.4}$$

and the differential interferogram phase signal expressed by Equation (3.2) can be reformulated as

$$\Delta\phi_i = \sum_{k=s_i+1}^{m_i} (t_k - t_{k-1})\, v_k. \tag{3.5}$$

This finally leads to the following matrix representation:

$$\mathbf{A}\mathbf{v} \;=\; \boldsymbol{\Delta\phi}, \tag{3.6}$$

where $\boldsymbol{\Delta\phi}$ is still the M-dimensional vector of the pointwise phase observations, $\mathbf{v}$ is the M-dimensional vector of the unknown phase velocities and $\mathbf{A}$ is a $M \times N$ matrix whose elements are defined, $\forall i = 1, \ldots, M$, by

$$A_{ik} \;=\; \begin{cases} t_{k+1} - t_k & \text{if} \quad s_i + 1 \le k \le m_i \\ 0 \quad \text{otherwise.} \end{cases}$$

Using the SVD method to solve for the phase velocities, a solution with no large discontinuities can be obtained. Finally, an additional integration step must be performed to retrieved the phase associated to the deformation signal at time t_i:

$$\phi_i \;=\; \phi_{i-1} \,+\, v_i\,(t_i \,-\, t_{i-1})\,. \tag{3.7}$$

Even though we neglected the atmospheric contribution and the error in topography removal in the presented mathematical description, there are usually handled in practice. Moreover, we have assumed a linear rate of deformation between two instants. If another time-model of the deformation is available, the system can be reformulated to take it into account.

Singular Value Decomposition

Let us shortly explain how the underdetermined system can be solved using the Singular Value Decomposition method. The SVD of the matrix $\mathbf{A}$ is given by

$$\mathbf{A} \;=\; \mathbf{U}\mathbf{S}\mathbf{V}^{\mathbf{T}}, \tag{3.8}$$

where $\mathbf{U}$ is the $M \times M$ orthogonal matrix whose columns are the eigenvectors of $\mathbf{A}\mathbf{A}^T$, $\mathbf{V}$ is the $N \times N$ orthogonal matrix whose columns are the eigenvectors of $\mathbf{A}^T\mathbf{A}$ and $\mathbf{S}$ is the $M \times N$ matrix whose diagonal entries are the singular values σ_i of $\mathbf{A}$, which correspond to the square roots of the eigenvalues of the matrix $\mathbf{A}\mathbf{A}^T$. If $\mathbf{A}$ has a rank equal to R, such that $R \le N$, then $\mathbf{S}$ has the form

$$\mathbf{S} \;=\; \mathrm{diag}(\sigma_1, \ldots, \sigma_R, 0, \ldots, 0), \tag{3.9}$$

with the σ_i's ordered by descending values: $\sigma_1 > \ldots > \sigma_R$. A minimum norm solution of the phase velocities vector can finally be calculated using a pseudo-inversion of the decomposed matrix:

$$\mathbf{v} \;=\; \mathbf{V}\,\mathrm{diag}(1/\sigma_1, \ldots, 1/\sigma_R, 0, \ldots, 0)\,\mathbf{U}^{\mathbf{T}}\,\boldsymbol{\Delta\phi}. \tag{3.10}$$

3.1.2 Multidimensional Small Baseline Subset

With time, many SAR satellites have been launched in space and some regions of the Earth can today be observed simultaneously by several sensors. For monitoring purposes, it is highly desirable to exploit all SAR data available over a given region at once. This is achieved by the Multidimensional Small Baseline Subset technique which integrates spatially and temporally overlapping data sets to compute the 2-D evolution of ground deformations [14, 76].

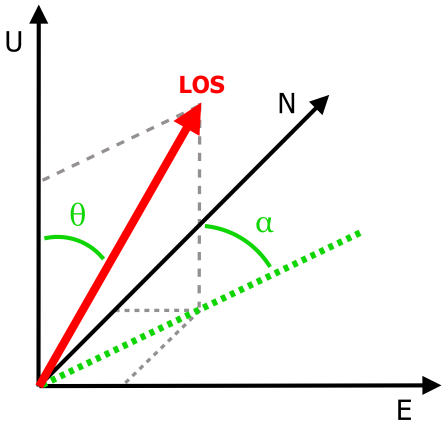

Figure 3.2: Representation of the MSBAS decomposition basis, whose axes are defined by the south-north (N), west-east (E) and down-up (U) directions. The orientation of the line-of-sight unit vector (**LOS**) can be described by the incidence angle θ and the azimuth angle α.

The formulation of this problem is similar to the one of SBAS, but we have to process images with various acquisition parameters: data sets are made of ascending and descending images from different sensors, with different incidence angles, wavelengths, resolutions, etc. Thanks to the variety in viewing geometries, it is possible reconstruct two-dimensional (vertical down-up and horizontal west-east) time series of ground deformations. Moreover, integration of numerous data sets improves the temporal resolution of the time series and secures a continuous monitoring in time.

In this section, we derive the formulation of the MSBAS problem and we explain the main key points of the processing. Expressions of the matrices and control parameters used by the MSBAS software are detailed in Reference [78].

Data sets and interferogram formation

Let us consider L data sets of SAR images acquired over a given region by sensors with different orbital parameters. The l-th data set is made of $N^l + 1$ images constituting M^l interferograms. A data set is defined by its sensor and its orbital parameters (azimuth and incidence angles). From each data set, an interferogram sequence is generated following the same strategy of small baselines as for the SBAS. Nevertheless, the user must take care: data sets should represent diverse viewing geometries of the studied area and they must overlap in time, such that no time gap appears in the data. In addition, ascending and descending data sets must be considered together to obtain reliable 2-D estimates of the deformations.

Like in the SBAS approach, the technique relies on unwrapped interferograms, corrected from the topography. All interferograms from the various data sets must be resampled on a common grid. For SBAS, this could be achieved by a simple coregistration on a global master. In the case of MSBAS, it is preferable to geocode all interferograms on a common grid. Calibration of the phase signal is handled by the MSBAS software, that can be provided with one or several reference regions.

Moreover, the MSBAS software can also be provided with deformation maps, obtained by the conversion of phase maps into metric units. Then the deformation products in output will be given in the corresponding units, i.e. metric deformation rates. Let us stress that, if using phase maps in input, then they must be scaled by a wavelength factor for the case of data sets acquired at different frequencies.

Problem formulation

Let us start by reformulating the SBAS formulation in order to obtain a projected version of it: if we consider a basis whose axes are respectively defined by the south-north (N), west-east (E) and up-down (D) directions, the line-of-sight unit vector $\vec{S}$ can be described by its incidence angle θ and its azimuth angle α: $\vec{S} = (S_E,\, S_N,\, S_U) = (\sin\alpha\sin\theta,\, \cos\alpha\sin\theta,\, \cos\theta)$ (Figure 3.2). We can then express the phase velocity norm v_i in terms of its north, east and up components as

$$v_i \;=\; \vec{v_i}\cdot\vec{S} \;=\; v_{iE}\,S_E \,+\, v_{iN}\,S_N \,+\, v_{iU}\,S_U \tag{3.11}$$

and Equation (3.5) can be reformulated as

$$\begin{aligned}\Delta\phi_i \;=\; & \sum_{k=s_i+1}^{m_i} (t_k \,-\, t_{k-1})\; S_E\, v_{kE} \\ & + \sum_{k=s_i+1}^{m_i} (t_k \,-\, t_{k-1})\; S_N\, v_{kN} \\ & + \sum_{k=s_i+1}^{m_i} (t_k \,-\, t_{k-1})\; S_U\, v_{kU}.\end{aligned} \tag{3.12}$$

It can be finally written in matrix representation as

$$\underbrace{\begin{pmatrix}\mathbf{A_E} & \mathbf{A_N} & \mathbf{A_U}\end{pmatrix}}_{\mathbf{A}_p}\underbrace{\begin{pmatrix}\mathbf{V_E}\\ \mathbf{V_N}\\ \mathbf{V_U}\end{pmatrix}}_{\mathbf{V}_{los}} = \boldsymbol{\Delta\phi}, \tag{3.13}$$

where $\boldsymbol{\Delta\phi}$ is the M-dimensional vector of pointwise phase values known from the unwrapped interferograms; $\mathbf{A_E} = S_E\mathbf{A}$, $\mathbf{A_N} = S_N\mathbf{A}$ and $\mathbf{A_U} = S_U\mathbf{A}$, with $\mathbf{A}$ being the same matrix as in (3.6), are the $M \times N$ matrices that constitute the $M \times 3N$ matrix $\mathbf{A}_p$ of the projected time delays; $\mathbf{V_E}$, $\mathbf{V_N}$, $\mathbf{V_U}$ are respectively N-dimensional vectors of the north, east and up components of the phase velocities that make up the $3N$-dimensional vector $\mathbf{V}_{los}$ of the projected velocities. As a consequence, if we know the azimuth and incidence angles of the l-th data set, its projected SBAS representation can be formulated, $\forall\, l = 1, 2, \ldots, L$, as

$$\mathbf{A}_p^l\mathbf{V}_{los}^l \;=\; \boldsymbol{\Delta\phi}^l. \tag{3.14}$$

Let us now consider the whole L data sets. The formulation of the projected SBAS given by Equation (3.14) can be generalized to process all the L independent data sets together. This multidimensional SBAS (MSBAS) is expressed under the following form:

$$\begin{pmatrix}\hat{\mathbf{A}}_p^1\\ \hat{\mathbf{A}}_p^2\\ \vdots\\ \hat{\mathbf{A}}_p^L\end{pmatrix}\begin{pmatrix}\mathbf{V}_{los}^1\\ \mathbf{V}_{los}^2\\ \vdots\\ \mathbf{V}_{los}^L\end{pmatrix} = \begin{pmatrix}\boldsymbol{\Delta\phi}^1\\ \boldsymbol{\Delta\phi}^2\\ \vdots\\ \boldsymbol{\Delta\phi}^L\end{pmatrix} \qquad \Leftrightarrow \qquad \hat{\mathbf{A}}_p\hat{\mathbf{V}}_{los} \;=\; \boldsymbol{\Delta\hat{\phi}}. \tag{3.15}$$

In this expression, we have that $\mathbf{\Delta}\hat{\boldsymbol{\phi}}$ is the observations vector of dimensions $\sum_{l=1}^{L} M^l \times 1$, $\hat{\mathbf{V}}_{los}$ is the projected phase velocitiy vector of dimensions $\sum_{l=1}^{L} 3N^l \times 1$, and $\hat{\mathbf{A}}_p$ is a $\sum_{l=1}^{L} M^l \times \sum_{l=1}^{L} 3N^l$ matrix of the projected time delays. This matrix is constituted by submatrices $\hat{\mathbf{A}}_p^l$ similar to the matrix $\mathbf{A}_p$ of the projected SBAS formulation, but stretched with additional zeros.

Similarly to SBAS, the system must be inverted to determine the unknown phase velocities components along the north, east and up directions. This time again, the system is underdetermined and we have to use a pseudo-inversion method. As it is explained below, the Tikhonov regularization is preferred to the SVD decomposition to solve the system.

2-D deformations

In order to determine the projected components of the phase velocities with sufficient accuracy, the diversity in viewing geometries is crucial, as explained in Reference [75]. Current spaceborne SAR sensors have antennas looking on a single side, on both ascending and descending passes. For some of them, they have several beam modes, acquiring data from different incidence angles. However, all the current and past SAR satellites orbit the Earth in a near-polar orbit that makes them poorly sensitive to the north component of a ground motion. This leads to very important errors in the estimates along this direction.

In practice, the north component is neglected and removed from the matrix system of Equation (3.15), reducing the number of unknowns down to $\sum_{l=1}^{L} 2N^l$. This assumption is reasonable as long as the magnitude of the south-north component of the motion is of the same order as the west-east and vertical components. MSBAS hence maps 2-D ground deformations, on the horizontal west-east and vertical up-down directions [14, 75].

Tikhonov regularization

Since we are handling several independent data sets of potentially disconnected interferogram subsets, we are necessarily facing an underdetermined system of equations. Even though it could be solved by a pseudo-inversion using the SVD approach, as for the SBAS problem, Tikhonov regularization of zero, first or second order is preferred by the MSBAS software.

Let us consider the solution obtained with the SVD approach for SBAS given by Equation (3.10): in this expression, the observed phase values are multiplied by a factor $1/\sigma_i$. If one or several σ_i have a very small value, this has the undesirable effect of amplifying the noise present in the observed phase values and it leads to highly incorrect estimates of the phase velocities. This phenomenon is estimated by the dimensionless ratio σ_1/σ_R. When this ratio is large, small errors in the data are significantly amplified and the problem is said to be *ill-conditioned* [82].

In practice, ill-conditioned systems are common. An alternative to the SVD approach is the *regularization*. The main idea of regularization is to replace the original problem by a slightly different formulation whose solution has a low bias with respect to the original solution and that is less sensitive to the noise in the data. While the SVD approach can be expressed as a least square problem minimizing the norm $\|\hat{\mathbf{A}}_p\hat{\mathbf{V}}_{los} - \mathbf{\Delta}\hat{\boldsymbol{\phi}}\|$, Tikhonov regularization will rather minimize the functional

$$\| \underbrace{\hat{\mathbf{A}}_p\hat{\mathbf{V}}_{los} - \mathbf{\Delta}\hat{\boldsymbol{\phi}}}_{\text{Residual}} \|^2 \; + \; \lambda^2 \, \| \underbrace{\mathbf{\Delta}\hat{\boldsymbol{\phi}}}_{\text{Sol.}} \|^2, \tag{3.16}$$

where λ is the regularization parameter. Thanks to the parameter λ, a trade-off can be achieved between the residual norm and the size of the solution vector. The regularized solution is similar to Equation (3.10), but the amplifying factors $1/\sigma_i$ become $\sigma_i/(\sigma_i^2 + \lambda^2)$. For singular values $\sigma_i \gg \lambda$, the contribution to the sum is almost left unchanged; for singular values $\sigma_i \ll \lambda$, the amplifying factor is close to 0 and the contribution is damped, preventing the noise from

being magnified. Regularization consists thus in damping the noise contribution, while keeping a solution of reasonable size [83].
Eventually, the regularized MSBAS problem will be synthetized for the different order of regularization by the following matrix representation:

$$\begin{pmatrix} \hat{\mathbf{A}}_p \\ \lambda \mathbf{L} \end{pmatrix} \hat{\mathbf{V}}_{los} = \begin{pmatrix} \boldsymbol{\Delta} \hat{\phi} \\ \mathbf{0} \end{pmatrix}, \tag{3.17}$$

where λ is the regularization parameter and $\mathbf{L}$ is a zero, first or second order difference operator. For the zero-order regularization, $\mathbf{L}$ is an identity matrix. Explicit expressions of the operator $\mathbf{L}$ and explanations about the choice of the regularization order can be found in Reference [78].

L-Curve

As explained in the previous section, Tikhonov regularization consists in finding a trade-off between the size of the solution and how well the solution fits the data. This trade-off is defined by the choice of the regularization parameter λ. The value of λ is of prime importance to solve the problem: if too much regularization is applied, the noise contribution is damped and the solution is smooth, but it does not fit the data correctly, giving a large residual norm. On the contrary, if not enough regularization is applied, then the noise contribution is too important and the size of the solution is too large.
The L-curve is the appropriate tool to determine the optimum regularization parameter. As shown in Figure 3.3, it is a logarithmic plot of the regularized solution norm as a function of the residual norm, parametrized by the regularization parameter λ. It is an L-shaped curve as its name indicates. The steep part of the curve is dominated by noise errors while the flat part of the curve is dominated by regularization errors. The best trade-off between the size of the solution and the residual norm is achieved by the parameter value that corresponds to the corner of the L-curve [83], i.e. the point of maximum curvature. In practice, the System (3.17) must be solved for several values of λ in order to draw the curve and determine the point at the corner.

3.2 InSAR mass processing chain

MSBAS software is a post-processing software that is fed by a huge amount of unwrapped differential phase maps, or the corresponding deformation maps. Indeed, large data sets of interferograms are required for monitoring long periods of time, for improving the time resolution of the time series and for mitigating the error on the deformation components. However, the MSBAS software does not deal with the interferometric processing, while these interferograms must be generated somehow.
For reasons of time and efficiency, it is clearly not possible to generate manually each interferogram of a data set. This is why we decided to develop an automatized mass processing chain within the scope of the RESIST project. This tool is meant to ease the processing of the very large data sets of SAR images available over the Kivu region and the associated ground deformation monitoring. Interferometric processing is handled by CIS software and a systematic procedure is achieved through shell scripts. The mass processing chain is thought to minimize the processing steps, and to save time and memory. In order to adapt CIS to the automatization strategy, it was necessary to make some modifications to the software. In the following, the main improvements and options of CIS are reviewed and the mass processing approach is explained shortly.

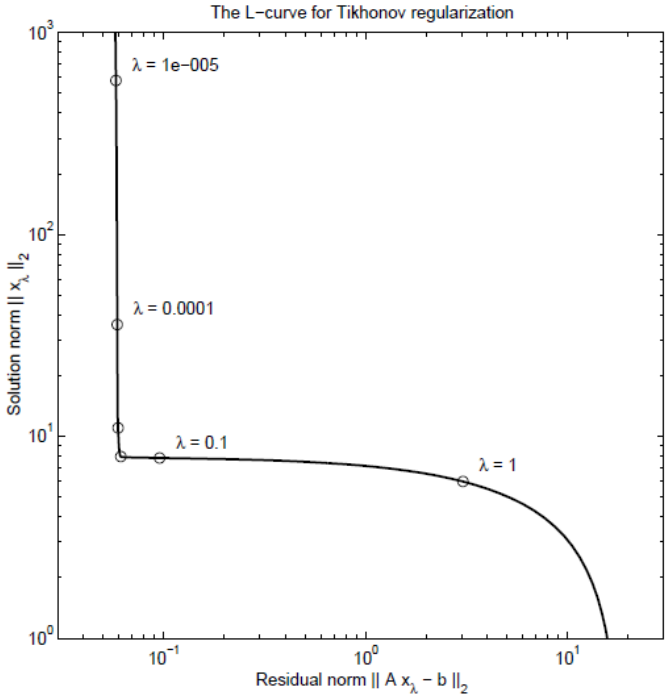

Figure 3.3: Example of L-curve for Tikhonov regularization, from Reference [83].

Shell scripts of the mass processing chain were developed by the European Center for Geodynamics and Seismology while changes to CIS were handled by Centre Spatial de Liège.

3.2.1 Current status of CIS software

CSL InSAR Suite is a software of SAR interferometry processing developed by CSL. It is coded in C language and its different processing modules are executed by command lines in a console. Shell scripts are thus a natural way to automatize the InSAR processing.

Except for Sentinel-1, the InSAR processing follows a step-by-step classical workflow: images are first converted in CIS format and InSAR processing is initiated for a given interferometric pair. Then, uncalibrated amplitude images are generated with a possible spatial averaging. The bilinear transformation of coordinates between the slave and master images is computed through the coarse (amplitude correlation) and fine (coherence correlation) coregistrations [84]. This transformation is applied and the slave image is interpolated to fit the master image geometry using a Chirp-Z Transform algorithm [85]. The interferogram is eventually generated, along with the coherence. At this stage, if a DEM is available, the topographic component can be removed from the interferogram, to leave the residual phase only. Filtering can also be performed on the wrapped phase. The phase can then be unwrapped using the coherence-guided branch-cut algorithm [41] implemented in CIS. Finally, products can be geocoded on a geodesic system, usually WGS84, and projected in a coordinate system. Both latitude-longitude coordinates and UTM coordinates are supported by CIS. Further details about the implementation of the basic steps can be found in Reference [86].

CIS supports data from various spaceborne sensors: ERS, Envisat, Radarsat, TerraSAR-X, TanDEM-X, Cosmo-SkyMed, KOMPSAT, ALOS-1 and ALOS-2. Sentinel-1 interferometry is also managed by the software. It follows a specific coregistration procedure proper to TOPSAR acquisitions [87], but all subsequent InSAR steps remain the same as for the other sensors.

For the purpose of the RESIST project, several options have been integrated to the tool. Let us cite a few ones: an adaptive filtering based on a Goldstein-modified filter is now proposed [88,89], an interface with SNAPHU [56–58] has been set for phase unwrapping and a geocoded mask can be given in input to suppress regions of low coherence.

3.2.2 Mass processing chain

The developed InSAR mass processing chain was developed to handle each data set separately. It follows a three-step sequence: in a first step, the interferometric pairs to process are selected, along with a super master. In a second step, all images of the data set are coregistered onto the super master. In the final step, the interferometric processing is run and the deformation maps are projected on a common georeferenced grid.

Selection of interferometric pairs

Obviously, it is crucial to provide the processing chain with the information of which pairs to process. Even though the mass processing chain can be used to generate any kind of interferogram sequence depending on the list of pairs provided, we developed a pair selection module specific to MSBAS. As explained in Section 3.1.2, the appropriate sequence of interferograms for MSBAS is achieved by imposing an upper threshold on the temporal and spatial baselines. These thresholds can of course be adapted from one data set to another, since each data set will be constrained by its own orbital tube and revisit time. In our developed module, we added the possibility to impose a lower threshold, in the event that the user wants to enlarge the data set with pairs of larger baselines.

Besides, a super master can be selected. When considering this option, the super master is chosen as the image that minimizes the average baseline: for each image, we consider the baseline formed with all the other images of the data set and we calculate the average value. The image with the smallest average baseline is chosen as super master, since it mitigates the spatial decorrelation in global. This choice ensures a better resampling of each image on the super master.

Coregistration on the super master

Coregistration of all pairs of the data set onto a common super master is not absolutely necessary, since the common grid is already obtained by the projection on a common georeferenced grid at the end of the process. However, this approach is adopted for the mass processing in order to mitigate the errors due to multiple transformations: interferometric products of a given data set are all generated for a common geometry, and then projected on a common grid.

In practice, this step considers the couples made by the super master with each image of the data set and computes the bilinear transformations used to coregister each each image onto the super master in the following step.

Interferometric processing and projection

The interferometric mass processing considers one pair at the time and follows a classical InSAR procedure. The automatization is thought so as to avoid the reprocessing of already existing products in order to gain time and memory. The CIS software is not particularly adequate for parallelization, but if the user wants to accelerate the mass processing by using multiple processors, it can be done by splitting the list of pairs that must be processed into several sequences.

Several options can be considered: we can choose the filtering and phase unwrapping methods; we can decide to crop the images to process a particular area, or keep the entire footprint; a geocoded mask can be provided to dismiss decorrelating areas and speed up the processing; products can be interpolated or not, and residual trends can be subtracted. Moreover, the mass processing scripts deal with interferometry of Sentinel-1 data sets.

Eventually, interferometric products are generated for the selected pairs of the data set and projected on a common georeferenced grid, in UTM coordinates. The projection grid is defined by its sampling along the x and y directions, its dimensions and the coordinates of its lower left corner. The final products generated by the mass processing chain for each pair are the differential unwrapped phase, the associated deformation map in meters, the interpolated deformation map and the deformation map corrected from a residual plane. Of course, other products like amplitude images and coherence are also provided. Besides, the mass processing scripts also provide the interface between the CIS software and the MSBAS software.

3.3 Optimizing spatial coverage

Spatial coverage is a main concern of the MSBAS processing. Indeed, in order to model geophysical processes using the deformation time series, the user wants an homogeneous information over the whole studied area and therefore a maximized spatial coverage. However, even though denser than for PSI, the spatial coverage provided by MSBAS is restricted by two factors. The first is the decorrelation, inherent to every interferometric processing: in a single interferogram, the phase information is not reliable in places where the coherence is low; these areas are usually masked out by a coherence threshold. The second factor is that the MSBAS software processes

Figure 3.4: Google Earth$^{\mathrm{TM}}$ view of the Bukavu city and its surroundings. The red line indicates the scarp of the Funu landslide.

only the footprint that is common to all interferograms in the data set: it checks if each pixel is defined in all deformation maps; if it is not, then the pixel is discarded for the MSBAS processing. Therefore, if a pixel is lost for one deformation map, it is lost for the whole processing.

Given the potentially limited common footprint, the user may want to improve the coverage by retrieving the phase information of pixels defined in almost all interferograms. In the first part of this section, we propose a spatial interpolation approach that can be applied either on a single image, or on a whole stack of images.

Besides, it is useful to avoid processing pixels that do not remain coherent in all pair. It takes time to handle phase unwrapping over these regions, while they are not be considered by MSBAS anyway. For this reason, we propose to discard them using a mask. The generation of this mask and the corresponding MSBAS study case are the object of the second part of this section.

Throughout this section, we focus on the city of Bukavu and its neighbourhood. This urban area is prone to landslides and surrounded by vegetation. In Figure 3.4, a view of Bukavu is provided and the scarp of the Funu landslide is highlighted by a red line. As we will see, it is problematic to obtain a satisfying coverage on this area. Results presented in this section are all obtained from Cosmo-SkyMed acquisitions in Stripmap HIMAGE mode.

3.3.1 Spatial interpolation

As explained above, it is usual to encounter pixels with no value in an interferometric product. They are often masked out by a coherence threshold, and it can be of interest to estimate their value in order to improve the spatial coverage. These undefined pixels can present different configurations: they can be located in the middle or on the border of a coherent patch, or they can also be located on the border of the image. For this reason, our interpolation strategy must take into account these different configurations.

Single image interpolation

For a single image, we propose a very simple interpolation strategy that is illustrated in Figure 3.5. For each undefined pixel of the image, our method first attempts to apply a bilinear interpolation using the first, i.e. direct, neighbouring pixels. This configuration is met when the undefined pixel is lost within a coherent region. If the first neighbours are not all defined, we attempt a bilinear interpolation on the second neighbours, which are located at the corners of the undefined pixel. If they are not defined either, we finally opt for a linear interpolation between the nearest neighbours along the vertical or horizontal dimension. This configuration can especially happen for pixels located on the border of the image, or along a concave border of a coherent region. If none of these three configurations is met, then the pixel is not interpolated and remains undefined. Let us stress that, when the first nearest neighbours are consider, the bilinear and linear interpolations reduce to a mean of the neighbours values. Of course, the implemented interpolation is not especially dedicated to InSAR products and can be performed on any kind of image.

Example An example of single image interpolation is presented in Figure 3.6. We apply our interpolation strategy to a deformation map obtained over Bukavu from Cosmo-SkyMed ascending images acquired on August 25th and September 30th, 2016. After interpolation, we observe a more homogeneous coverage of the city. In Figure 3.7, we highlight the different configurations of interpolation: the bilinear interpolation of direct neighbours, the bilinear interpolation of second neighbours and the linear interpolation of first neighbours.

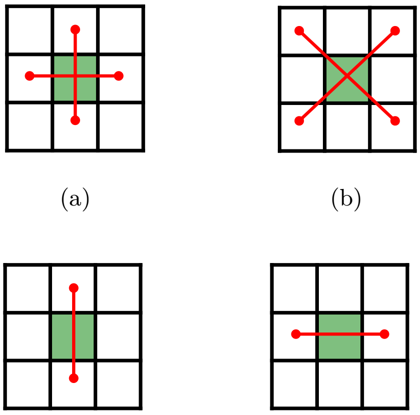

(a) (b)

(c)

Figure 3.5: Schematic representation of the interpolation strategy. The green box represents the pixel considered for interpolation and the red dots are the pixels used for the interpolation. (a) If all the direct neighbours of the central pixel are defined, then their values are interpolated to determine the value of the pixel. (b) If at least one of the nearest neighbours is not defined, then we look for the second neighbours. If they are all defined, then they are used to interpolate the value of the central pixel. (c) Finally, if neither the first, nor the second neighbours are completely defined, we look for the direct neighbours along the horizontal or vertical direction and we opt for a one-dimensional linear interpolation along one of these axes.

Data set interpolation

Interpolation must always be performed with caution: even though we want to retrieve information at some places, we do not want to artificially create this information. When handling a stack of deformation maps, it is interesting to recover a pixel only if it is undefined for a minority of maps. On the contrary, if the pixel has been discarded in most of the maps, then interpolation will lead to a mostly artificial information that is not reliable. For this reason, we propose a stack approach for the interpolation: interpolation is performed on each image of the stack following the single image strategy, but the pixel is considered for interpolation only if it is defined in a given percentage of images in the stack. This percentage is set by the user. This approach enables an improvement of the spatial coverage without turning the interpolation into extrapolation.

Example In Figure 3.8, we show how the common footprint of a data set can be improved using our stack approach. We consider a data set of 39 deformation maps over Bukavu generated from Cosmo-SkyMed ascending images acquired between December 13th, 2015 and October 20th, 2016. The initial footprint over Bukavu city, given in Figure 3.8a, is sparse. However, when the interpolation is applied to pixels defined in at least 90% of the data set maps, the global coverage is much improved (Figure 3.8b): the footprint is more homogeneous and covers a larger part of the city. When the threshold is reduced to 75%, the coverage is not improved noticeably with respect to the 90% case (Figure 3.8c).

3.3.2 Definition of the MSBAS coverage using a mask

Even though one wishes to have a maximized spatial coverage, there is no interest in processing areas that are likely to decorrelate. If some regions are non coherent for a given interferometric pair, then phase unwrapping on these regions is long and tedious to finally provide a phase information that we cannot trust. Moreover, if these regions are decorrelated throughout the whole sequence of interferograms, then the time loss is multiplied consequently.

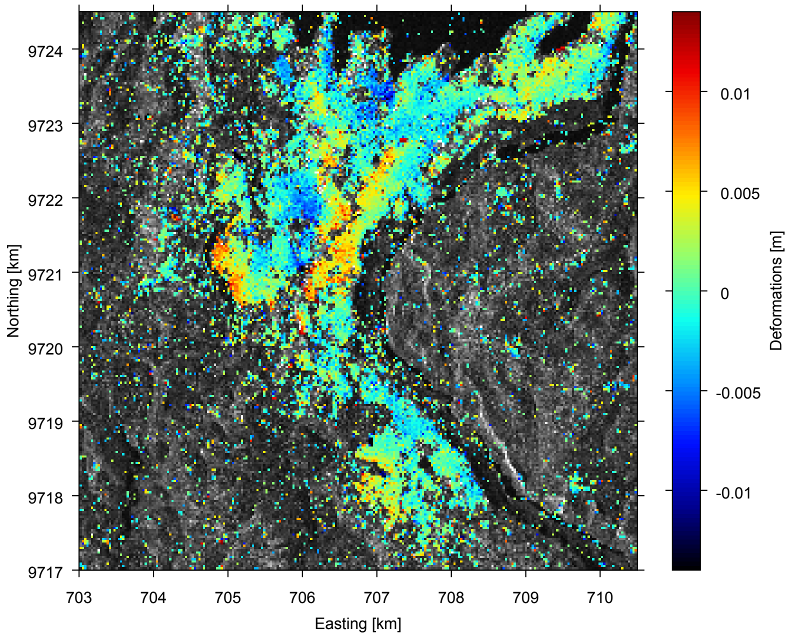

(a)

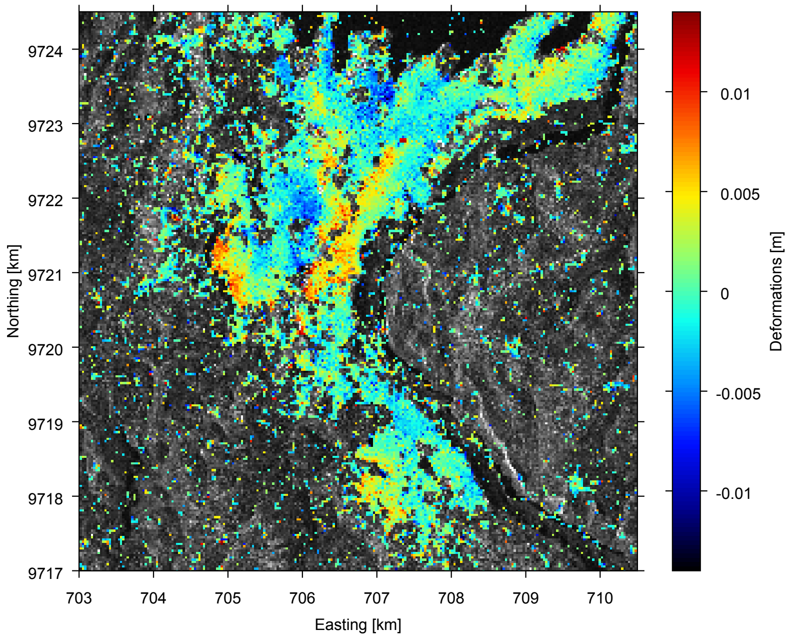

(b)

Figure 3.6: Interpolation of a deformation map. The deformation map is computed over Bukavu from the Cosmo-SkyMed pair of ascending images acquired on August 25th and September 30th, 2016 and overlaid on an amplitude image of the area. (a) Before interpolation. (b) After interpolation.

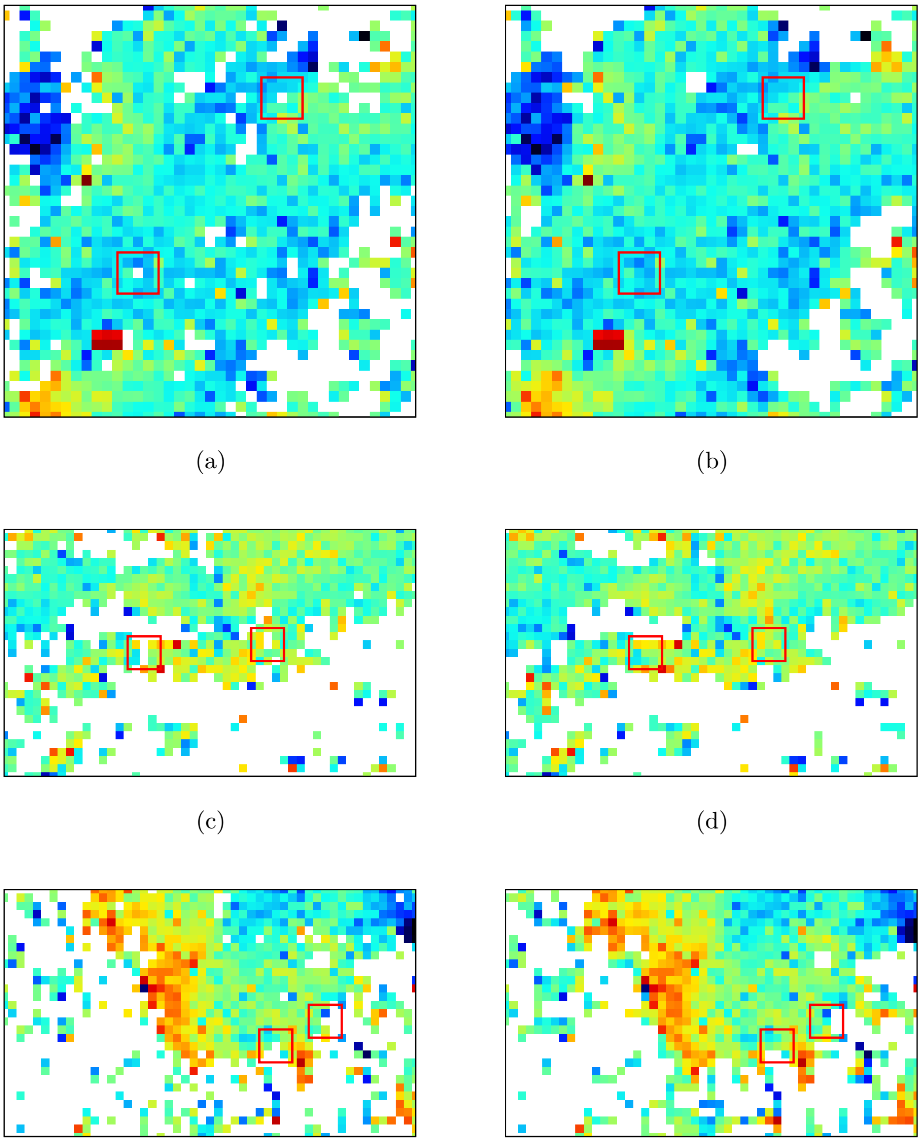

(a) (b)

(c) (d)

(e) (f)

Figure 3.7: Interpolation of a deformation map. The deformation map is computed over Bukavu from the Cosmo-SkyMed pair of ascending images acquired on August 25th and September 30th, 2016. Zooms on different configurations of undefined pixels are presented. The pixels of interest are highlighted by the red boxes. The left column gives the deformation map before interpolation. The right column gives the deformation map after interpolation. (a)-(b) Bilinear interpolation is performed using the first neighbours, which are all defined. (c)-(d) Bilinear interpolation is performed using the second neighbours. (e)-(f) Linear interpolation is performed along the vertical or horizontal direction.

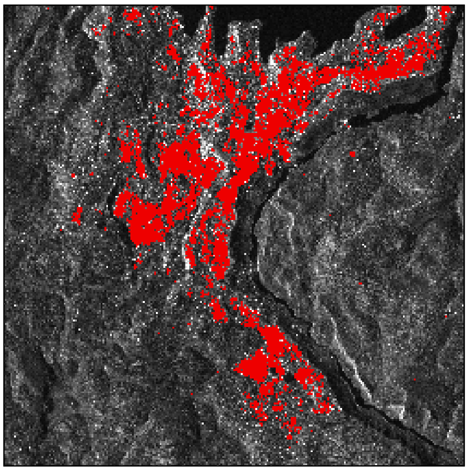

(a) Before interpolation

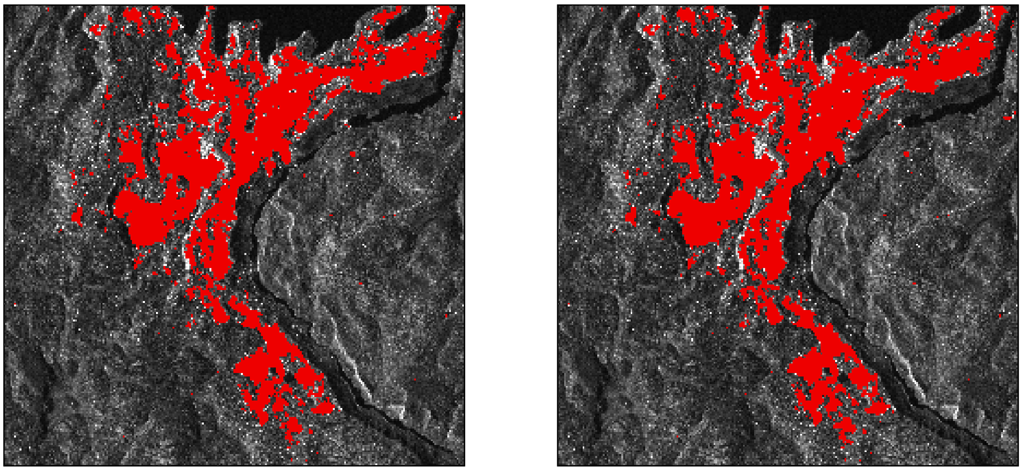

(b) Pixels defined in at least 90% of the stack

(c) Pixels defined in at least 75% of the stack

Figure 3.8: Interpolation of a stack of deformation maps. The stack is made of 39 deformation maps over Bukavu generated from Cosmo-SkyMed ascending images acquired between December 13th, 2015 and October 20th, 2016. (a) The common footprint of the stack before interpolation is shown in red and overlaid on an amplitude image of the area. (b) The common footprint of the stack after interpolation is shown in red. Pixels defined in more than 90% of the stack are the only ones that are interpolated. (c) The common footprint of the stack after interpolation is shown in red. Pixels defined in more than 75% of the stack are the only ones that are interpolated.

In order to solve this problem, we propose to exclude areas that are a priori known to be subject to decorrelation by using a mask. By applying a common mask to each interferometric pair of the mass processing, we have the same coverage for all deformation maps and it prevents from processing extra-regions outside the common footprint. In the first part of this section, we propose a procedure to generate such a mask. We investigate several estimators that are likely to discriminate between decorrelating and non decorrelating regions, and we compare the resulting masks. In the second part of this section, we present the results obtained with MSBAS over the Bukavu city when the selected mask is applied.

Sensor	Mode	Heading	Time span	Number of pairs
Cosmo-SkyMed	HIMAGE	Ascending	March 24th, 2015 - September 21st, 2017	31
Cosmo-SkyMed	HIMAGE	Descending	March 21st, 2015 - September 18th, 2017	32

Table 3.1: Data sets used for generating a mask over Bukavu.

Mask generation

The natural estimator to compute a mask is the coherence. In the present work, we propose several coherence-based estimators to compute the mask. Some of them are build to take into account the time variability in addition to the coherence. Since our mask must be generated on the basis of the coherence, we use coherence-optimized pairs of acquisitions to compute it, i.e. pairs with small spatial and temporal baselines. Indeed, it is reasonable to assume that decorrelated areas in such pairs remain non coherent in less favourable cases.

Data set and processing Over the city of Bukavu, we have at our disposal two data sets of Cosmo-SkyMed images, the first acquired along an ascending orbit and the other along a descending one (Table 3.1). A Google Earth$^{\mathrm{TM}}$ view of the area is presented in Figure 3.4. Both data sets span the period from March, 2015 to September, 2017 and are acquired in Stripmap HIMAGE mode. In both cases, we select the interferometric pairs with a perpendicular baseline smaller than 150 m and a time span of less than 20 days. These small baselines ensure a good coherence in global. Eventually, 31 pairs are selected for the ascending data sets, and 32 pairs for the descending data set.

Since we are mainly interested in the city, images are cropped to be processed over this area and its surroundings only, so that we speed up the interferometric process. The selected pairs are processed with a spatial averaging of 10×10 pixels to reduce the speckle and yield a stack of coherence maps. These maps are projected on the WGS84/UTM coordinate system using a $20\ \mathrm{m} \times 20\ \mathrm{m}$ sampling grid. A high resolution is not necessary to generate a mask with a smooth aspect. Finally, using the geocoded coherence maps, we compute the images of the pointwise mean coherence and the normalized variance-mean coherence ratio, described below.

On the other hand, SBInSAR is also applied to the selected pairs. The range bandwidth is of 96 MHz for the images in both data sets and we apply a spectral decomposition into 5 subbands of 18 MHz. A stack of geocoded SBInSAR coherence maps is finally generated. As done for the conventional coherence, we compute the image of the mean SBInSAR coherence of the stack.

Estimators Here, we propose three different estimators for the generation of the mask. Each one captures different features of the coherence:

- The mean coherence $\bar{\gamma}$
- The normalized variance-mean coherence ratio $\frac{1-\sigma_{\gamma}}{1-\bar{\gamma}}$
- The mean SBInSAR coherence $\bar{\gamma}_{\nu}$

The mean coherence $\bar{\gamma}$ is a classical estimator for discriminating between decorrelating and non decorrelating regions. In this case, we get rid of regions with a low mean coherence. Since we mitigate the spatial and temporal decorrelations by working with small baselines, we expect that areas that are decorrelated on average also decorrelate in the interferometric pairs of lower quality.

Although the conventional coherence is a good estimator of the phase quality, it is interesting to take into account the variability of the coherence through the data set. Indeed, MSBAS focuses

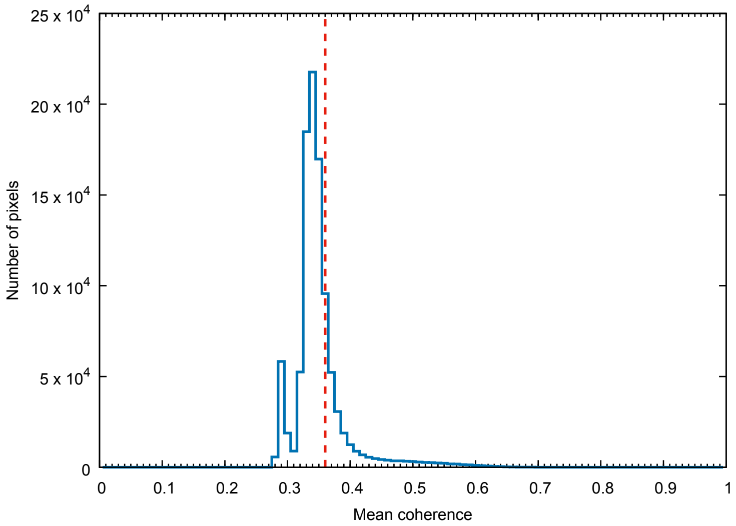

Figure 3.9: Mask generation. Histogram of the mean coherence value for the Cosmo-SkyMed ascending data set.

on coherent distributions of scatterers stable over time. The processed regions must remain coherent through the whole data set. Such regions are characterized by a high value of the mean coherence $\bar{\gamma}$ and a limited standard deviation of the coherence σ_γ. These two conditions are summarized by a large ratio $\frac{1-\sigma_\gamma}{1-\bar{\gamma}}$. In practice, it is easier to work with a ratio ranging between 0 and 1, the upper value corresponding to the best situation. This range of values is achieved by normalizing the $\frac{1-\sigma_\gamma}{1-\bar{\gamma}}$ image by its maximum value.
Finally, we also consider the mean SBInSAR coherence $\bar{\gamma}_\nu$. We have been concerned with Split-Band Interferometry in the previous chapter and we know that spectral stability can provide an additional information. It accounts for other scattering mechanisms than the conventional coherence or the time stability. It also selects frequency-stable pixels, whose SBInSAR phase could be used as benchmark. For this reason, we decide to test this estimator in the context of mask generation.

Generic procedure For each estimator presented above, the mask is obtained by setting a threshold on the estimator. This threshold is chosen based on the histogram of the estimator values, in order to get a good balance between unmasked and masked pixels. An example of mean coherence histogram is given for the Cosmo-SkyMed ascending data set in Figure 3.9: we observe that the mean coherence peaks around 0.34. By setting a slightly higher value of 0.36 for the threshold, low coherence pixels are efficiently discriminated from the highly coherent pixels. The chosen thresholds are listed in Table 3.2.

Estimator	Data set	Threshold
$\bar{\gamma}$	Cosmo-SkyMed Ascending	0.36
$\bar{\gamma}$	Cosmo-SkyMed Descending	0.36
$\frac{1-\sigma_\gamma}{1-\bar{\gamma}}$	Cosmo-SkyMed Ascending	0.35
$\frac{1-\sigma_\gamma}{1-\bar{\gamma}}$	Cosmo-SkyMed Descending	0.25
$\bar{\gamma}_\nu$	Cosmo-SkyMed Ascending	0.77
$\bar{\gamma}_\nu$	Cosmo-SkyMed Descending	0.77

Table 3.2: Thresholds used on the different estimators and data sets for the mask generation.

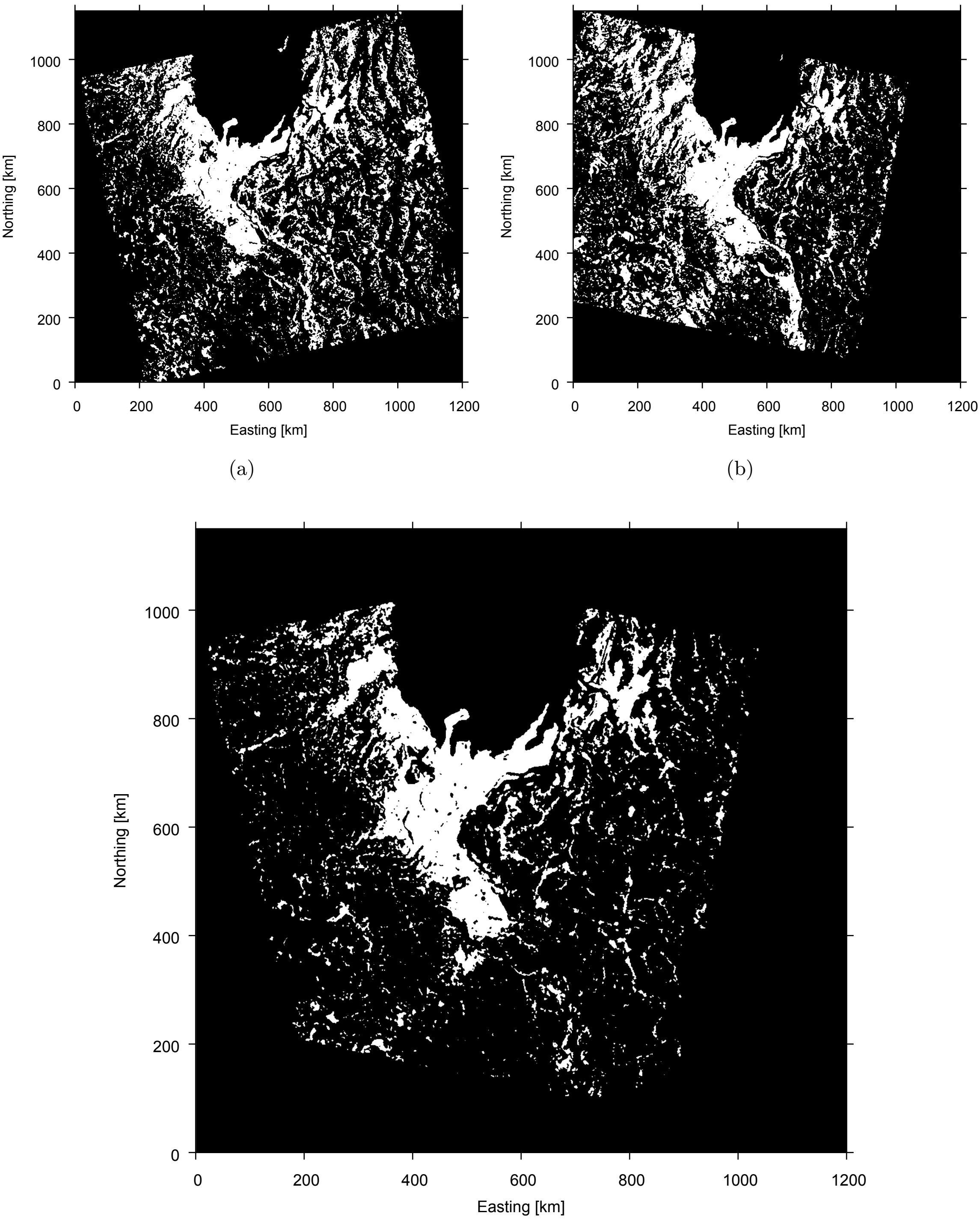

(a)

(b)

(c)

Figure 3.10: Mask generation. Mask over Bukavu generated using the mean coherence estimator. (a) Mask generated from the Cosmo-SkyMed ascending data set. (b) Mask generated from the Cosmo-SkyMed descending data set. (c) Mask generated when merging both Cosmo-SkyMed ascending and descending data sets. Black represents the masked pixels and white represents the unmasked ones.

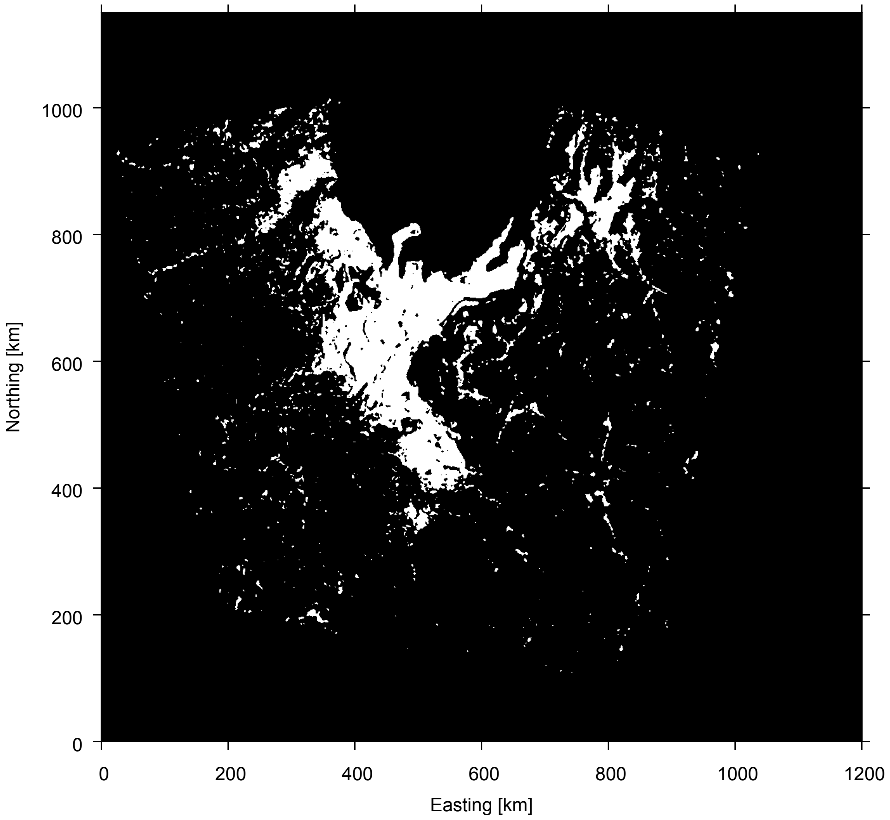

Figure 3.11: Mask generation. Mask over Bukavu generated using the ratio variance-mean coherence. The mask is obtained from both Cosmo-SkyMed ascending and descending data sets. Black represents the masked pixels and white represents the unmasked ones.

Some additional considerations are also handled during the computation. Let us first note that the values of the estimators can sharply vary from one pixel to another. A median filtering is therefore applied to the estimator image before applying the threshold, in order to obtain a smooth mask: median filtering makes the estimator pattern more homogeneous and removes outlier values. Moreover, we remove isolated pixels: the unwrapped phase of a lonely pixel with no neighbour do not provide useful information. Finally, since MSBAS deals with several viewing geometries, it is of interest to merge the footprints of the masks generated from the ascending and descending data sets.

Results

In Figure 3.10 , we present the masks obtained with the mean coherence estimator. Let us first consider the masks computed separately from the ascending data set (Figure 3.10a) and from the descending data set (Figure 3.10b): we observe that the coverage of the city is good and includes the areas of Cyangugu and Kabare. The landslide of Funu is almost entirely covered, except for the steep slope of the landslide in the ascending data set. Small isolated groups of pixels remain unmasked in the vegetated area around Bukavu. However, when both data sets are merged together (Figure 3.10c), patches lost in the vegetated areas are more efficiently removed.

The mask obtained with the ratio $\frac{1-\sigma_\gamma}{1-\bar{\gamma}}$ is given in Figure 3.11. Compared to the mean coherence mask, this estimator is more restrictive. It is more efficient in removing the vegetated parts of the region and keeps a good coverage of the urban area. The overall aspect of the mask is more

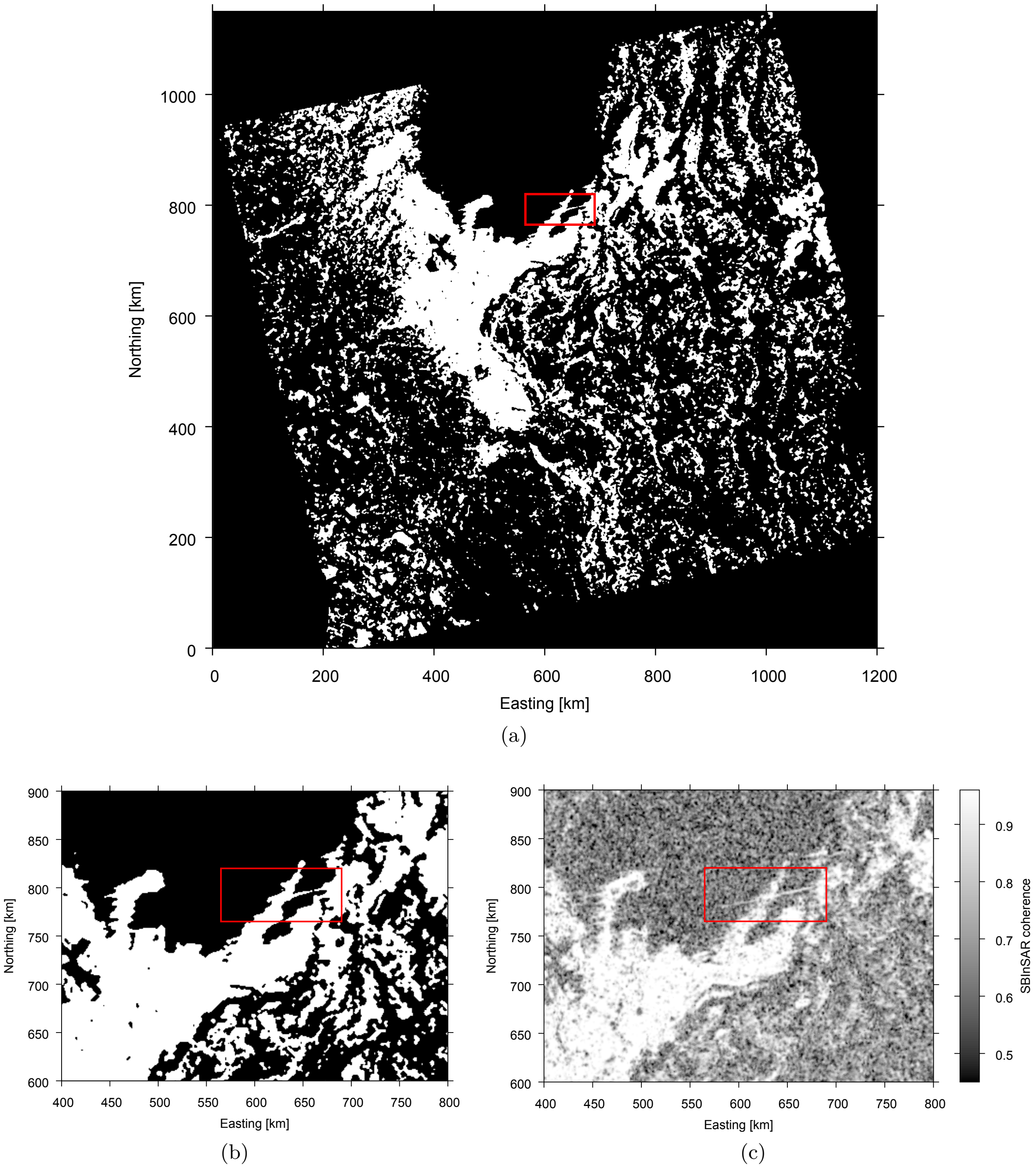

(a)

(b)

(c)

Figure 3.12: Mask generation. Mask over Bukavu generated using the mean SBInSAR coherence estimator. (a) Mask generated from the Cosmo-SkyMed ascending data set. (b) Zoom on a blurred feature of the mask. Black represents the masked pixels and white represents the unmasked ones. (c) Zoom on the same blurred feature in a SBInSAR coherence image generated with images acquired on August 16th and September 1st, 2017.

Sensor	Mode	Heading	Time span	$N+1$	M
Cosmo-SkyMed	HIMAGE	Ascending	January 14th, 2016 - September 21st, 2017	92	165
Cosmo-SkyMed	HIMAGE	Descending	January 3rd, 2016 - September 18th, 2017	93	163

Table 3.3: MSBAS analysis over Bukavu. Data sets. $N+1$ is the number of images per data set and M is the number of interferograms per data set.

homogeneous and less noisy.

Finally, a mask is also generated using the SBInSAR coherence (Figure 3.12). When looking at the mask generated from the ascending data set, we directly note that spectral decomposition has an undesirable side-effect: due to the reduced resolution, the *sinc* response of a point target spreads over a larger number of pixels in the range direction and the amplitude of the sidelobes of the response is not correctly compensated by the processor. This effect is present in amplitude images, but also in SBInSAR coherence maps where it results in unwanted blurred features. This is observed over land strips around the lake (see the red boxes in Figure 3.12), where buildings with strong backscattering responses are present. Given this phenomenon, this estimator is not usable to generate a mask over an urban area and we put it aside.

In conclusion, although mean coherence gives satisfactory results, we choose to adopt the mask generated from the variance-mean coherence ratio for the following MSBAS study. It is more efficient to eliminate vegetated areas where we do not expect to find any relevant and useful information.

3.3.3 MSBAS study case: Bukavu

This section is meant to test both the mask generated with the variance-mean coherence ratio and the processing chain developed for MSBAS on a practical case. We study ground deformations occurring in the area of Bukavu for the period 2016-2017 by means of the MSBAS technique. The coverage of this MSBAS processing is defined by the selected mask.

Test site

The city of Bukavu is located on the south coast of lake Kivu, on the Congolese side of the border between DRC and Rwanda. The city developed on the East African Rift (EAR), an area of active tectonics leading to frequent earthquakes [90, 91]. Moreover, rainfalls are abundant in this region, making it subject to landslides [92]. In such a urban environment, landslides can result in fatalities and damage to infrastructures (e.g. buildings, roads, houses). The threat is particularly important for the city of Bukavu, which hosts about 800 000 inhabitants and undergoes an uncontrolled growth of population [1]. The growing demographic pressure of this city forces newcomers to settle on unstable areas, like landslide slopes, and increases the chance of landslide triggering or reactivation.

In this work, we focus on the largest landslide of the Bukavu city, located in the neighbourhood of Funu (highlighted in red in Figure 3.4). This slow moving landslide stands in the south-west part of the city and is known to be particularly active. Its west-east global motion makes it well-oriented for the MSBAS processing. Kinematics of this landslide were already studied using the StaMPS-SBAS technique by Nobile et al. for a one-year period spanning March 2015 to April 2016, in Reference [70].

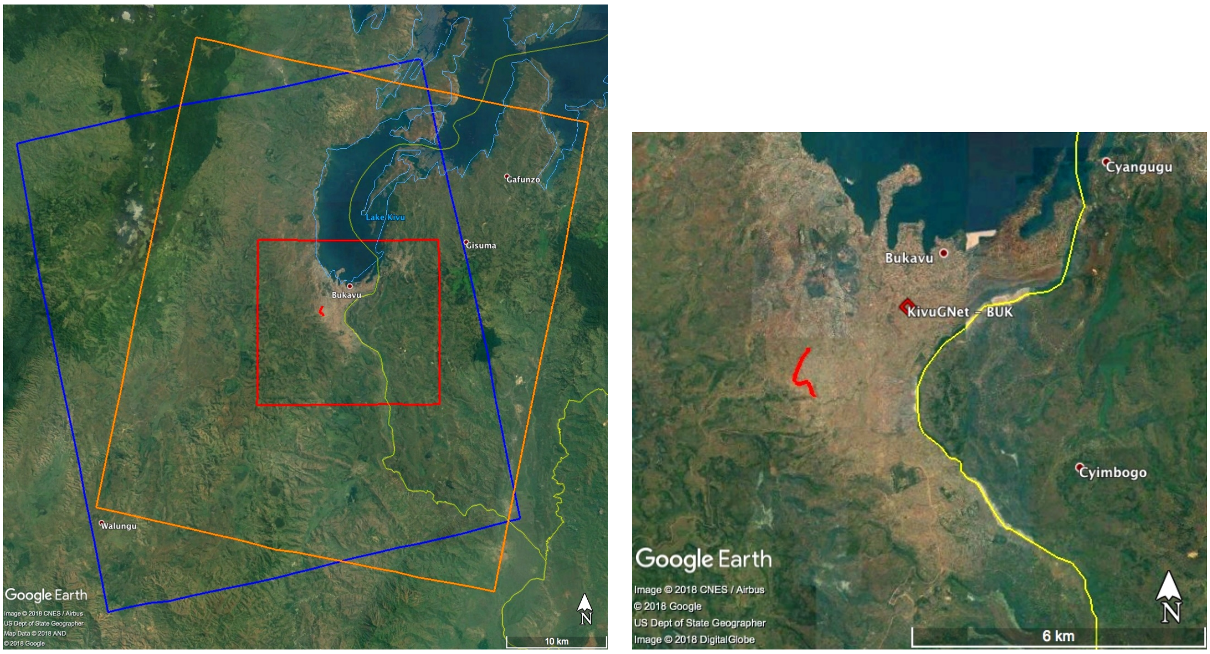

(a) (b)

Figure 3.13: MSBAS analysis over Bukavu. Google Earth$^{\text{TM}}$ views of Bukavu. (a) Footprints of the ascending (blue frame) and descending (orange frame) data sets. The red frame represents the cropped area considered for the processing. (b) Zoom on the city. The red curve indicates the scarp of the Funu landslide. The red diamond indicates the location of the BUK GNSS station (KivuGNet [93]).

Data set and processing

For this MSBAS analysis of the area of Bukavu, we consider the Cosmo-SkyMed ascending and descending data sets already used for the mask generation. However, we restrict ourselves to the period from 2016 to 2017, as the period 2015-2016 has already been studied by Reference [70]. Given that footprints of the acquisitions are much larger than the area of interest, we also restrict the processed frame to Bukavu and its surroundings (see Figure 3.13).

Acquisitions of both data sets are HH-polarized. Ascending and descending acquisitions have respectively an incidence angle of about 42° and 49.5°. As indicated in Table 3.3, the ascending data set is made of 92 acquisitions while the descending data set counts 93 acquisitions. For both data sets, we select couples of acquisitions with a perpendicular baseline smaller than 300 m and a time span smaller than 50 days. Some larger baselines pairs are integrated to obtain a fully connected sequence of interferograms for both data sets (Figure 3.14). Let us note that the atmospheric effects can be considered as mitigated thanks to the dense aspect of the interferoram sequences: we tried as much as possible to used each image in multiple pairs, sometimes as master and sometimes as slave. Therefore, the atmospheric contribution of each image is positive in some interferograms and negative in some other, leading to an atmospheric component null on average.

Interferometric processing is carried out on the selected pairs using the InSAR mass processing chain. Super master acquisitions are selected as follows: the acquisition of September 5th, 2017 is chosen for the ascending data set; the acquisition of July 24th, 2017 is chosen for the descending data set. During the interferometric processing, a spatial averaging of 5 × 5 pixels is applied, which leads to a spatial sampling of about 10 m in azimuth and ground range. The topographic component is removed using the 30m-resolution SRTM DEM. Of course, masking is performed on the interferometric products using the variance-mean coherence mask. The phase is filtered

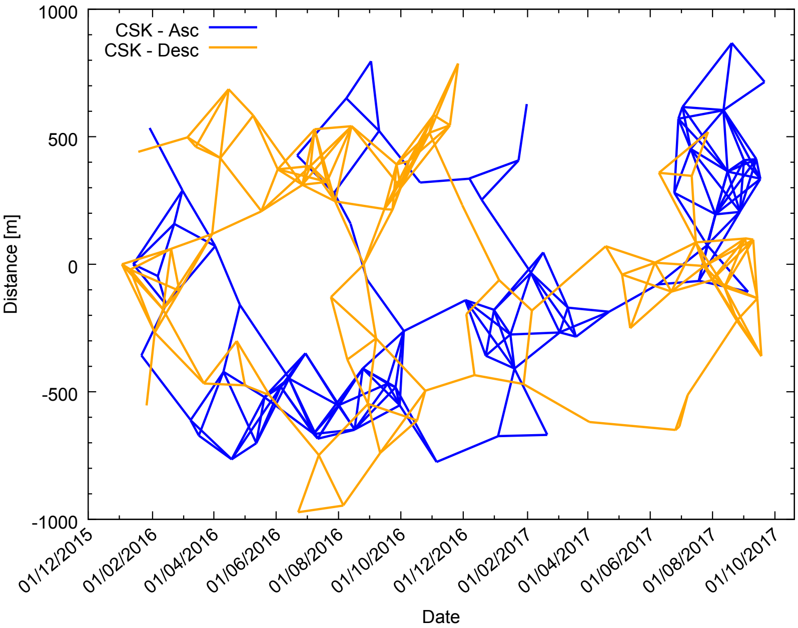

Figure 3.14: MSBAS analysis over Bukavu. Interferogram sequence presented as a perpendicular baselines versus temporal baselines plot. The blue sequence represents the Cosmo-SkyMed ascending data set; the orange sequence represents the Cosmo-SkyMed descending data set.

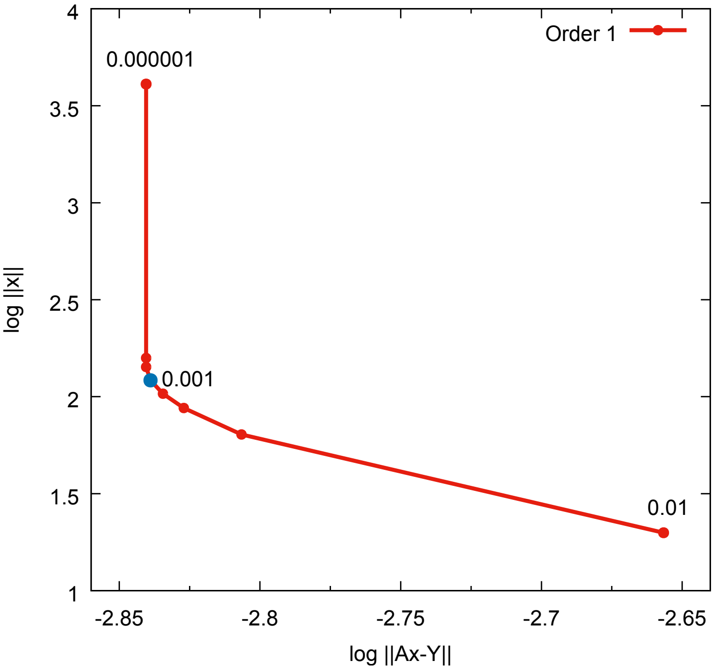

Figure 3.15: MSBAS analysis over Bukavu. L-curve for first order regularization. Values of the regularization parameter λ are labelled on the data points. The blue dot indicates the point at the corner of the curve, which corresponds to the best balance between the size of the solution and the norm of the residual.

using an adaptive filter and phase unwrapping is performed using SNAPHU. The unwrapped phase is converted to deformation in metric units and resampled on a 20 m × 20 m grid projected in UTM coordinates.

Once the deformation maps are generated, we perform MSBAS processing. Because it has been established in Reference [70] that this zone is stable, we choose the area around the BUK GNSS station (KivuGNet [93]) as reference for calibration. Several values are tested for the regularization parameter and the corresponding L-curve is reconstructed (Figure 3.15). We determine an optimum value of 0.001 for the regularization parameter, which corresponds to the corner of the curve.

Results

Once the optimum value of the regularization parameter is determined, MSBAS is run to reconstruct the history of the displacements. The computed maps of eastward and upward deformation rates are presented in Figure 3.16. In these maps, we observe several zones of active ground deformation. Let us analyze the ones indicated by the red boxes in more details. We provide a focus of the displacement rates on these regions in Figure 3.17.

Let us first focus on the Funu area, in the south-west part of Bukavu. We first note a discontinuity at the location of the grey box, particularly visible in the east-west deformation map. This unexpected discontinuity can be explained by phase unwrapping errors observed at the exact same place in some unwrapped differential interferograms. Actually, this area is located on the scarp of the Funu landslide. On the scarp, deformations are faster than in other places and the phase unwrapping can fail. However, despite our multiple attempts to correct this problem, we were not able to avoid these errors. We are therefore not very confident regarding the measurement quality on the scarp of the landslide.

The global movement of the landslide is directed towards east, combined to an overall subsidence. However, we clearly distinguish zones of different eastward deformation rates (see Figures 3.17a 3.17b), ranging between 1 cm/yr and 8 cm/yr. We point out the two areas of fastest displacement and select a point in each of the areas, for which the time series are calculated. These points are respectively labelled A and B, and the corresponding time series are shown in Figures 3.18a and 3.18b. The displacement curves have an almost linear trend corresponding to a steady rate of deformation for both east and up directions. Even though the subsidence rate is similar for both points, the movement towards east is slightly faster for point A.

We now focus on the area north of Ruzizi river, where subsidence can be observed. Indeed, the subsidence rate reaches more than 6 cm/yr while the eastward movement is negligible (Figures 3.17c and 3.17d). The origin of this subsidence is not clearly established, but Reference [70] proposed the urbanization and the water pumping in the area as an explanation. Two phases seems to exist in the history of the displacements of point C, given in Figure 3.18c: during the year 2016, we observe subsidence at a rate smaller than 5 cm/yr with an almost null component of the horizontal displacement. However, starting from 2017, the subsidence exhibits a higher rate and we also observe a correlated movement towards west.

Finally, we also observe a zone of active deformation in the north-west part of the city. As observed in Figures 3.17e and 3.17f, the most active parts of this zone show an uplift movement towards east.

Let us stress that the behaviour observed for the analyzed areas was already observed with similar deformation rates by the SBAS study of 2015-2016 performed by Reference [70]. Even though we do not have data for validation, the consistency between measurements of 2015-2016 and 2016-2017 gives us confidence in the quality of the results.

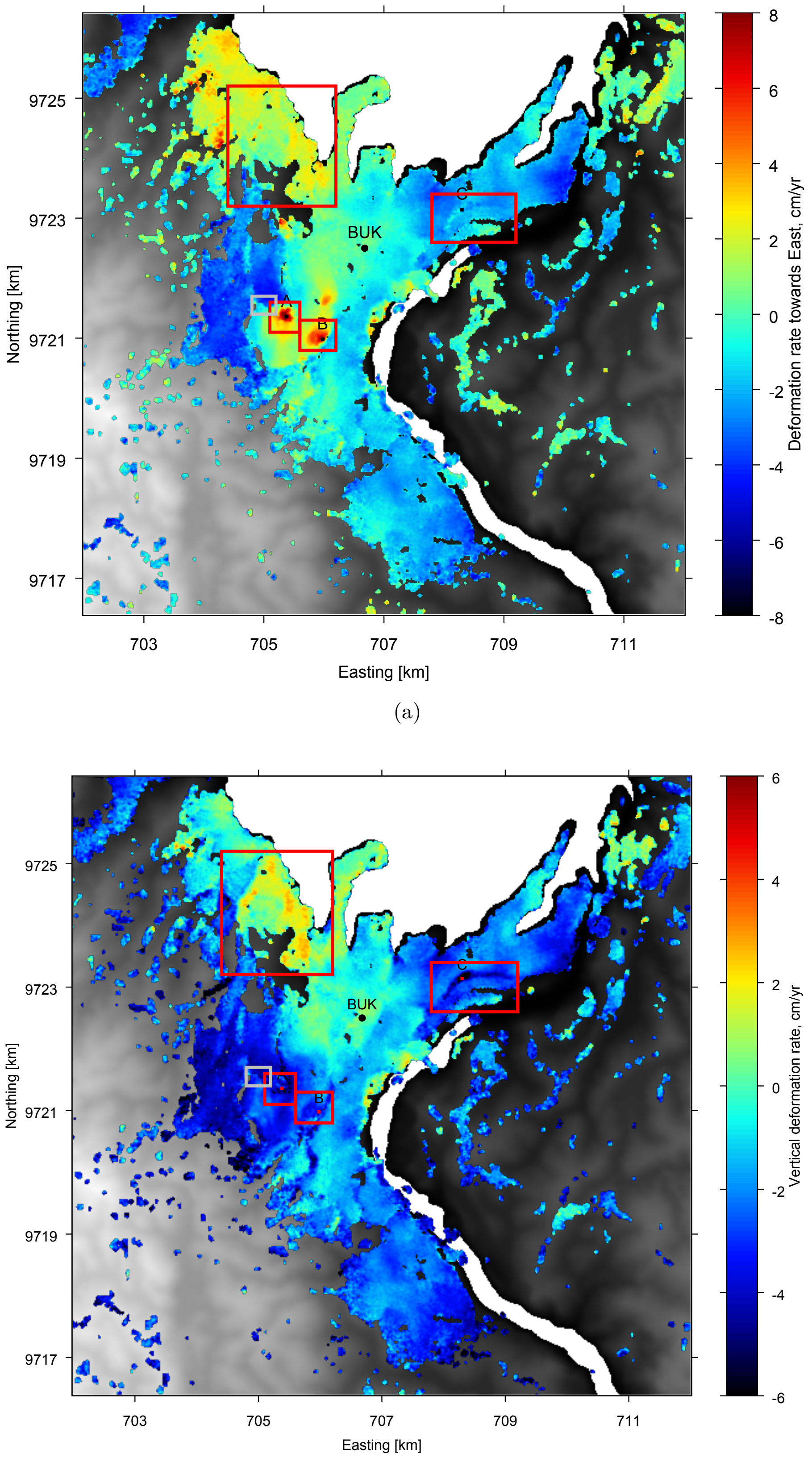

(a)

(b)

Figure 3.16: MSBAS analysis over Bukavu. Calculated displacement rates in cm/yr overlaid on the DEM. (a) Eastward displacement rate. Positive values correspond to a movement towards east. (b) Upward displacement rate. Positive values correspond to an uplift. Red boxes correspond to areas of interest and labels A, B and C are the points for which times series are extracted. The BUK dot indicates the location of the BUK GNSS station (KivuGNet). The grey box highlights errors due to incorrect phase unwrapping.

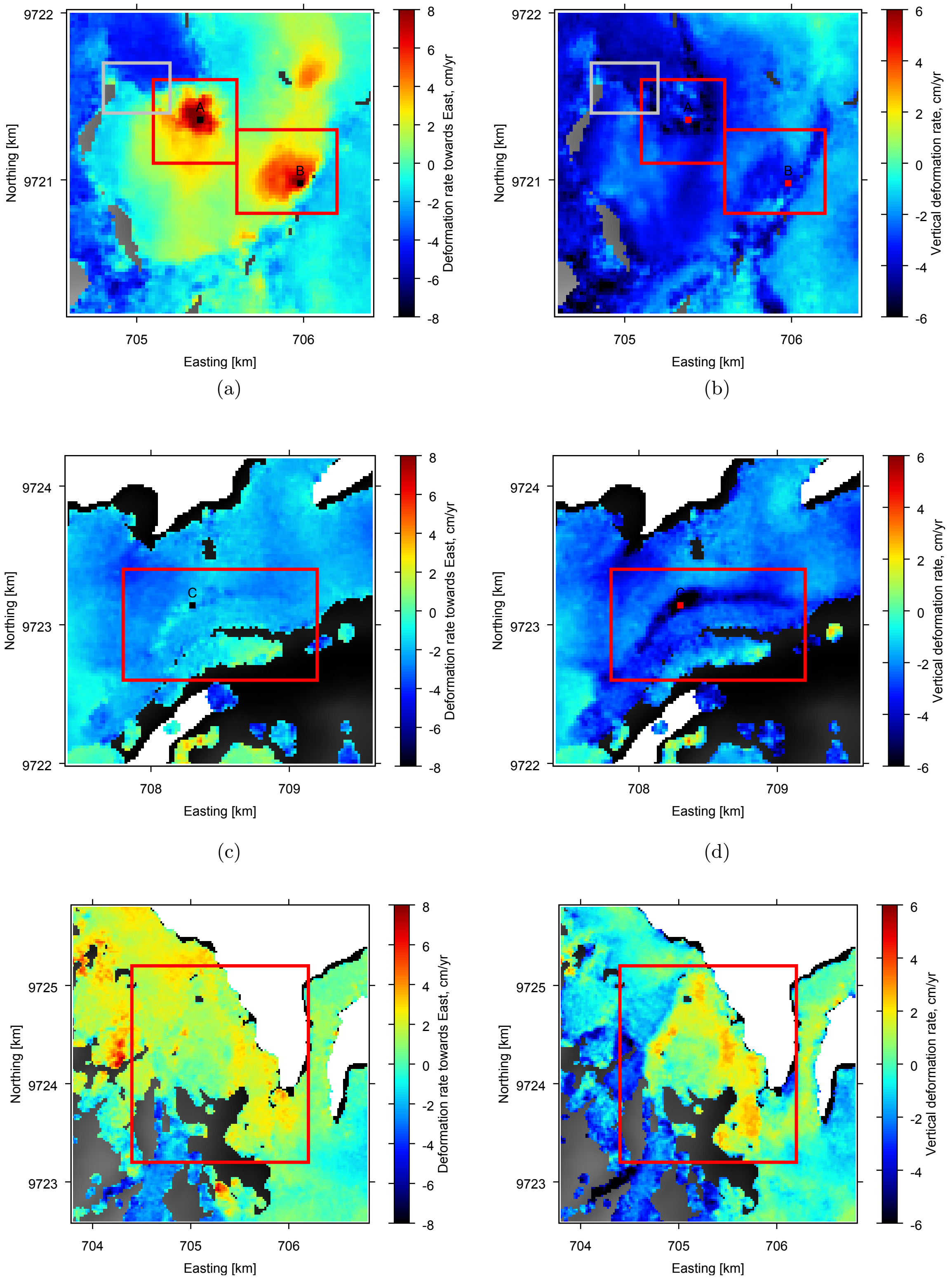

(a) (b)

(c) (d)

(e) (f)

Figure 3.17: MSBAS analysis over Bukavu. Calculated displacement rates in cm/yr overlaid on the DEM. Left column corresponds to the eastward displacement rate. Right column corresponds to the upward displacement rate. (a)-(b) Zoom on the displacements rates in the region of the Funu landslide. (c)-(d) Zoom on the displacement rates along Ruzizi river. (e)-(f) Zoom on the displacement rates in the north-west part of Bukavu.

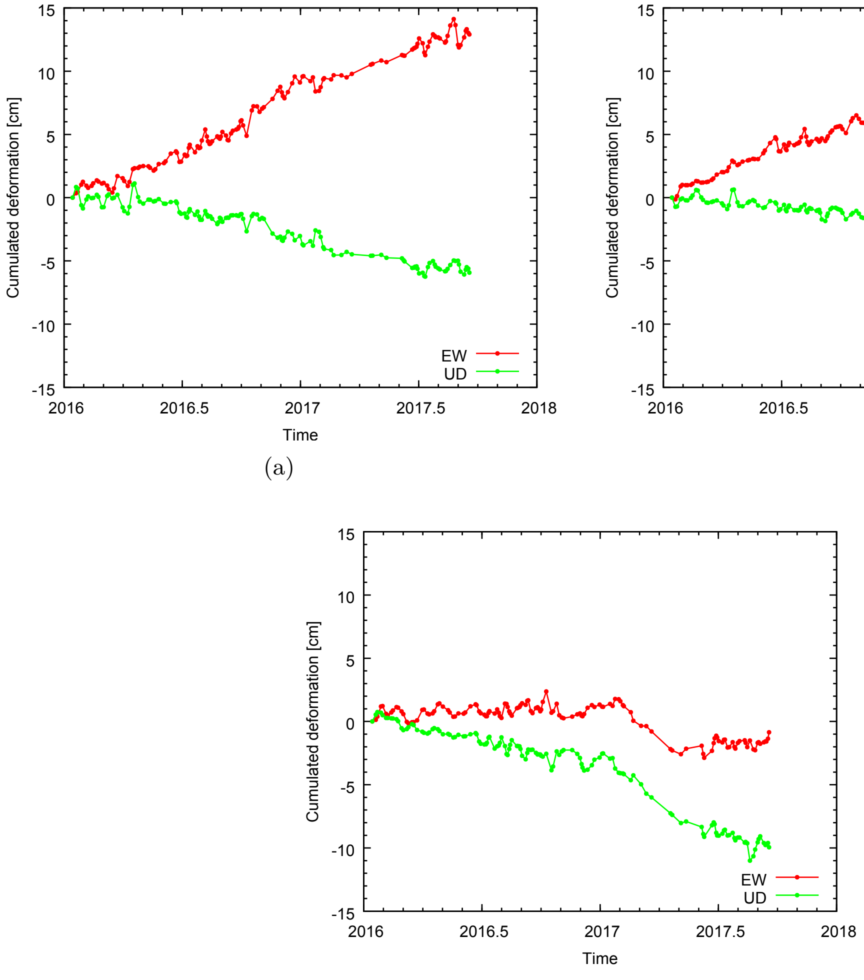

(a) (b) (c)

Figure 3.18: MSBAS analysis over Bukavu. Times series of the cumulated displacements in the eastward (red) and upward (green) directions at points A, B and C indicated on the maps in Figure 3.16. (a) Displacement at point A located on the Funu landslide. (b) Displacement at point B located on the Funu landslide.(c) Displacement at point C located over Ruzizi river.

Discussion and conclusions

An MSBAS analysis was performed over the city of Bukavu, for which the spatial coverage was defined by a mask generated using an estimator of the variance-mean coherence ratio. We studied the period from January 2016 to September 2017, which overlaps a recent InSAR study of deformations over the area. We focused on some active zones and in particular the landslide of Funu. The movement of the active zones and the calculated deformation rates correspond to the ones obtained by the previous work on the area.

Moreover, we observed discontinuities in the maps of displacement rate, in particular on the scarp of the Funu landslide. These discontinuities are errors due to phase unwrapping that failed to retrieve the correct unwrapped phase in the fast-moving areas. We conclude that our mask is not optimized for the scarp of the landslide, where phase unwrapping is challenging. This area could be further discriminated by setting a more stringent threshold on the estimator used for mask generation. In addition, let us note that we would not expect the path-following branch-cut algorithm to perform better than the SNAPHU method for unwrapping this area. Indeed, this method relies on a phase continuity assumption, that is not observed by the local fast displacements of the landslide.

3.4 Optimizing temporal coherence

The usual estimator of the interferometric phase quality is the coherence γ. It is used to assess the reliability of the computed phase. The coherence level results from several multiplicative sources of decorrelation, each of them quantified by its own correlation terms. It is expressed as [24]

$$\gamma = \gamma_{\mathrm{s}} \times \gamma_{\mathrm{t}} \times \gamma_{\mathrm{vol}} \times \gamma_{\mathrm{proc}} \times \gamma_{\mathrm{other}}, \tag{3.18}$$

where γ_{s} is the correlation term arising from the baseline or geometrical decorrelation, γ_{t} from temporal decorrelation, γ_{vol} from volume decorrelation, γ_{proc} from processing-induced decorrelation (coregistration, interpolation) and γ_{other} stands for other sources of decorrelation. Among these sources, let us focus on the temporal decorrelation: it is caused by changes of the ground cover and consitutes a major limitation of the interferometric repeat-pass measurement. Temporal decorrelation is particularly challenging: this effect is hard to model physically because the parameters of the model must be considered on a case-by-case basis [27]. This is probably why very few studies have undertook to estimate it. In order to overcome this difficulty, some studies have proposed to model empirically the temporal decorrelation effect rather than based on physical assumptions [94, 95]. Another successful approach was adopted by Rocca in Reference [96], who assumed that targets behave according to a Markov model and established a decreasing exponential model for the temporal coherence.

On the other hand, temporal decorrelation is a critical aspect of multitemporal InSAR methods like MSBAS. These methods make use of hundreds of interferograms, that are time consuming and memory expensive to produce. These two resources are highly valuable and it is therefore profitable to avoid processing useless interferometric pairs. For this reason, it is interesting to be able to assess a priori if the phase information of a given interferogram can be trusted or not. We know that decorrelation is mitigated by limiting the spatial and temporal baselines in the MSBAS approach. Nevertheless, the choice of the maximum time delay between two acquisitions is not subject to any other argument than the user's experience of the studied area and his knowledge of the data set.

In this section, we study the dynamics of the temporal decorrelation over the Virunga Volcanic Province and we rationalize the choice of the maximum temporal baseline. We adopt the empirical point of view and model the coherence as a function of the time delay between the acquisitions. Since coherence is terrain-dependent, we consider several areas that show different coherence dynamics and we derive the parameters of the best model for each area. It enables the determination of a typical decorrelation time for each type of terrain. Although such an analysis is not provided in this work, the decorrelation times that are determined by the modelling can be used in practice to build an interferogram sequence for an MSBAS study over the VVP.

3.4.1 Empirical modelling of temporal decorrelation

In order to model the behaviour of the coherence with respect to time, we consider sets of SAR images spanning long time periods. As we wish to model temporal decorrelation, we decide to mitigate the other sources of decorrelation as much as possible and we choose to only consider interferometric pairs with small spatial baselines. Besides, no restriction on the temporal baseline is imposed so that we have an important number of samples with the largest variety of possible time delays.

The selected pairs are processed using the developed mass processing chain to generate coherence maps and these maps are all resampled on a common grid. During the processing, spatial decorrelation is further mitigated by correcting coherence from the baseline decorrelation effect. This correction is done by simply dividing the coherence value by the well-known baseline correlation contribution, given by Equation (1.20) in Chapter 1, on a pointwise basis [5, 27]. If the other decorrelation sources are assumed to be negligible, then we finally obtain an estimate of the temporal correlation contribution γ_{temp}. At the end of the process, we have a stack of resampled coherence maps, each map corresponding to a given time span.

However, dynamics of the temporal decorrelation is not expected to be the same on the city and the lava flows, for example. Indeed, decorrelation is intrinsically linked to the type of terrain. For this reason we consider different areas of interest: the lava flows, the Goma city or the Nyiragongo crater. Temporal decorrelation is studied separately for each area. For this purpose, we use a mask for each region and we average the coherence of each coherence map over the mask. Therefore, for each region, a sample point corresponds to the coherence of a given interferometric couple averaged over the area of interest and corrected from the baseline decorrelation. Each sample point is associated to the time delay between acquisitions. As there are several pairs with the same time span, a given time delay can be associated to several sample points.

Empirical models

In Reference [96], Rocca established that a Markov assumption is efficient to model the coherence behaviour. This assumption corresponds to a distribution of scatterers whose reflectivity changes randomly without any influence from their previous states (memoryless system) [97]. In this case, the coherence is modelled by the function

$$\gamma(t) \;=\; \gamma_0 \, e^{-t/\tau}, \tag{3.19}$$

where γ_0 is the initial coherence and the parameter τ is a time constant to be determined. Considering this model, the coherence decreases exponentially with the time span t between two acquisitions. However, the memoryless assumption is not guaranteed for all configurations and it could be violated in some cases. Other functions could then better fit the coherence behaviour. We therefore test the decreasing exponential model, but also other models for the sake of completeness.

Of course, it is not possible to pick a model randomly and hope it will fit the coherence correctly. In order to determine candidate models, we highlight some features of the coherence that help to constrain its temporal behaviour. First, theory tells us that coherence is normalized and ranges between 0 and 1. Besides, the coherence usually becomes lower and lower as the temporal delay increases. The model function must therefore decrease with the time. For very large time delays, we would expect coherence to completely disappear. For a null time lapse, radar echoes should be perfectly correlated and the unit value should be reached. Given the coherence function $\gamma(t)$ of the positive time delay t between acquisitions, we can express these conditions as follows:

1. $0 \leqslant \gamma(t) \leqslant 1 \quad \forall t,$
2. $\frac{d\gamma}{dt} \leqslant 0 \quad \forall t,$
3. $\lim_{t\to+\infty} \gamma(t) \;=\; 0,$
4. $\gamma(0) \;=\; 1.$

Based on these conditions, we select the following modelling functions $g_i(t)$ of the temporal coherence:

1. **Simple decreasing exponential model**: $g_1(t) = e^{-b_1 t}$

   For this single parameter model, the decay rate of the coherence is defined by $\frac{dg_1}{dt} = -b_1 e^{-b_1 t}$. The decay rate is therefore directly proportional to the decay constant b_1. With this model, the coherence decrease is fast for small values of the time delay t and the decay rate reduces for longer time spans, to finally tend to zero for very large values of t.

2. **Decreasing exponential with quadratic time-dependence model**: $g_2(t) = e^{-b_2 t^2}$

   This second model has a quadratic dependence on the time span. In this case, the decay rate of the coherence is more important for the intermediate values of the time delay.

3. **Linear model**: $g_3(t) = 1 - m_3 t$

   In this simple linear model, the coherence decreases with a constant rate m_3. Even though it does not necessarily observe the third condition, the linear decrease is a simple model that is worth testing.

4. **Scaled and shifted decreasing exponential model**: $g_4(t) = a_4 e^{-b_4 t} + c_4$

   This model is similar to the simple decreasing exponential, but with more degrees of freedom due to its three parameters. Therefore, it does not necessarily fit the last two conditions. However, in practice, coherence is estimated rather than calculated and its estimator is biased, especially for low coherence [98]. For this reason, it is not expected to drop to zero for large values of t, but rather to the bias value. Moreover, normalization of the estimator is performed based on the Zebker model that assumes a random distribution of surface scatterers and does not take volume effects into account [27]. For this reason, the fourth condition might not be observed either. This model, with the shift and the scaling of the decay curve, takes these effects into account. Let us stress that in this case, the function starts from an initial value $c_4 + a_4$ and drops to the bias value c_4. The decay rate is given by $\frac{dg_4}{dt} = -b_4 a_4 e^{-b_4 t}$, which is commensurate with both parameters b_4 and a_4.

3.4.2 Data set and processing

The temporal behaviour of the coherence can only be studied on the basis of data sets spanning long periods of time. In our archives, we have several data sets spanning periods of at least one year. We decide to work first with Radarsat-2 C-band data that have a very long time coverage, and then extend the approach to Cosmo-SkyMed X-band acquisitions in order to analyze the change of dynamics from one frequency to the other.

For each data set, we only consider interferograms with small spatial baselines in order to mitigate the spatial decorrelation as much as possible. No threshold is set on the temporal baseline, so that we consider every possible time span between images. As explained above, we generate coherence maps projected on a common grid and we average the coherence over a given region, in order to associate a mean coherence to a time delay.

C-band

For C-band acquisitions, we have at our disposal two data sets of Radarsat-2 acquisitions spanning more than 4 years (see Table 3.4). This very long time coverage makes these data sets perfect for studying decorrelation on the long term, although Radarsat-2 has only 24 days revisit time. Fortunately, temporal decorrelation in C-band is slower than in X-band, and the length of each data set compensates for the poor revisit time.

Sensor	**Mode**	**Heading**	**Time span**	$N+1$	M
Radarsat-2 (1)	Fine	Descending	March 28th, 2010 - October 4th, 2015	37	379
Radarsat-2 (2)	Fine	Descending	December 15th, 2009 - April 17th, 2014	41	412
Cosmo-SkyMed	HIMAGE	Descending	July 9th, 2015 - March 9th, 2016	34	110

Table 3.4: Data sets used for temporal coherence modelling. $N+1$ is the number of images per data set and M is the number of interferograms per data set.

The two Radarsat-2 data sets are acquired in Fine mode over descending passes but with slightly shifted observation frames. The first data set has an incidence angle around 41° and an horizontal co-polarization (HH). Its footprint includes the city of Goma and the Nyiragongo, but only the southern part of the Nyamuragira lava field. The second data set has an incidence angle of about 35° and also an horizontal co-polarization (HH). It covers the whole Nyamuragira lava field and Nyiragongo volcano, but only a part of Goma.
For both data sets, an upper threshold of 200 m is imposed to the spatial baseline, resulting in 791 coherence maps produced out of 78 acquisitions. During the processing, a spatial averaging of 5×5 pixels is applied. In the case of the first data set, it leads to pixels of about 27.5 m×23.5 m in azimuth and slant range. In the case of the second data set, pixels have dimensions of about 25 m × 23.5 m.

X-band

For X-band acquisitions, no data set with comparable time coverage is available, neither regarding the length of the period, nor the considered time window. However, we have a one-year data set from Cosmo-SkyMed that overlaps slightly the first Radarsat-2 data set in time (Table 3.4). Though spanning a shorter time period, this data set has a higher revisit frequency and, consequently, we have a number of acquisitions comparable to the other data sets.
The Cosmo-SkyMed images are acquired in Stripmap HIMAGE mode, with an incidence angle of about 26° at mid-range and an horizontal co-polarization (HH). They cover the whole Virunga region, including the Nyamuragira lava field, the Nyiragongo volcano and the city of Goma. We set a threshold of 250 m on the perpendicular baseline, that gives 110 coherence maps. Indeed, with its larger orbital tube, Cosmo-SkyMed limits the number of small baseline pairs.
Regarding the processing, a spatial averaging of 10×10 pixels is applied this time. It results in a spatial sampling of about 22 m × 21 m.

3.4.3 Results

When the coherence maps are generated, we can fit the different empirical models to the data and determine the best model. Results are presented below for each region separately.

Nyamuragira lava flow of 2004

Let us first consider the results in C-band. Since the 2004 lava flow of the Nyamuragira volcano is present within the frames of both Radarsat-2 data sets, we merge data from both data sets together to increase the number of sample points. The fitted models and the corresponding residuals are represented in Figures 3.19a and 3.19b respectively. We can first observe that there is a large dispersion in the coherence data: a given time span can correspond to several and very different values of the mean coherence. It is therefore difficult to observe a clear trend. However, if we look at the fitted curves, the last model (red curve) seems to fit the coherence

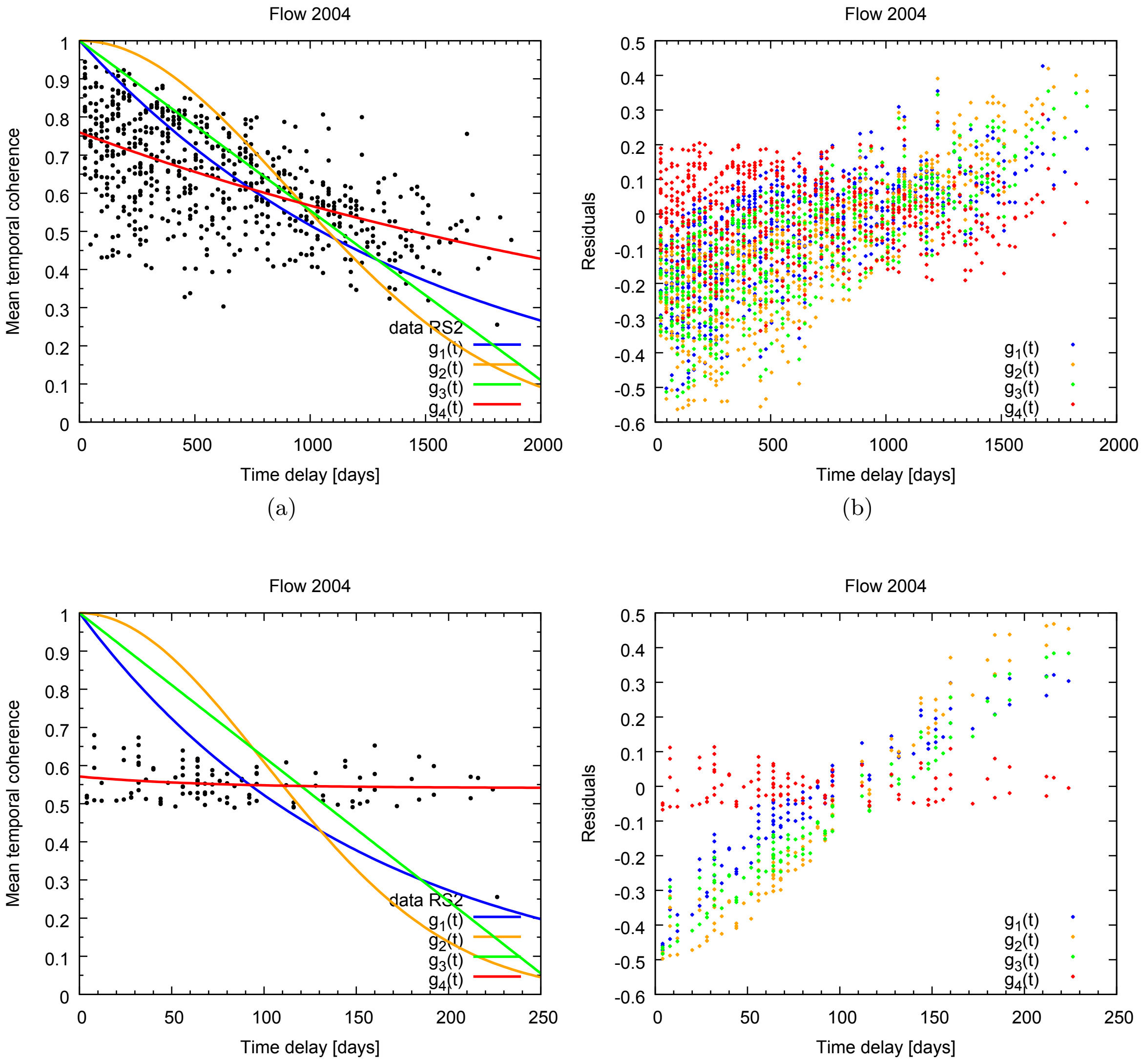

(a) (b)

(c) (d)

Figure 3.19: Empirical modelling of temporal decorrelation. Results over the Nyamuragira 2004 lava flow. Left column gives the temporal coherence samples and the fitted functions, while right column gives the corresponding residuals. Residuals are defined here as the difference between the data and the model. (a)-(b) Results for both Radarsat-2 data sets merged together. The four candidate models are considered. (c)-(d) Results for Cosmo-SkyMed data set. The four candidate models are considered.

data better than other three. Even though dispersion is important in the residuals in general, those corresponding to the scaled and shifted exponential (red points) are contained within a constant range of values centered on 0. This is not the case for the other models, that show a residual and almost linear trend. This residual trend is symptomatic of a model diverging from the observed values.

Let us now consider the X-band data set from Cosmo-SkyMed. The fitted curves and the corresponding residuals are represented in Figures 3.19c and 3.19d. We observe less dispersion in the coherence samples than in the C-band case. Besides, similarly to C-band data, the scaled and shifted exponential model is the one that fits the data best. Looking at the residuals, we observe an even clearer residual trend for the other models than in C-band.

Finally, let us compare directly the C-band and X-band dynamics using the best model (Figures

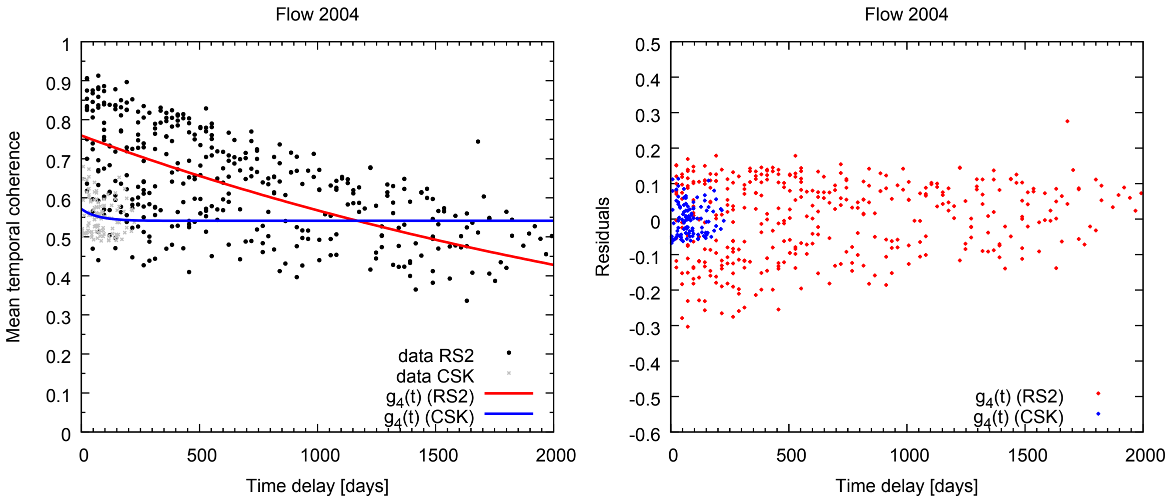

(e) (f)

Figure 3.19: Continued. (e)-(f) Comparison of Radarsat-2 (black and red) and Cosmo-SkyMed (grey and blue) results, showing only the scaled and shifted exponential model.

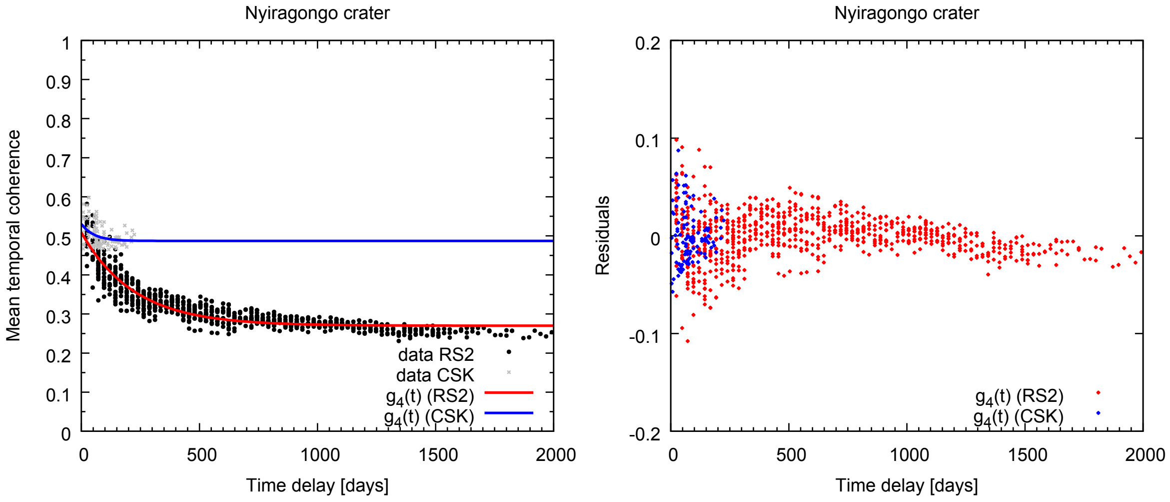

(a) (b)

Figure 3.20: Empirical modelling of temporal decorrelation. Results over the Nyiragongo crater. Comparison of Radarsat-2 (black and red) and Cosmo-SkyMed (grey and blue) results, showing only the scaled and shifted exponential model. For Radarsat-2 data, both data sets are merged. (a) Coherence data samples and the fitted scaled and shifted exponential model. (b) Corresponding residuals. Red corresponds to Radarsat-2 data and blue corresponds to Cosmo-SkyMed data.

3.19e and 3.19f). They are obviously extremely different, though it is no surprise. We can first note that coherence in X-band starts from a lower level than in C-band and the coherence samples show less dispersion for the X-band. Although both cases have different sample lengths, we observe clearly that the decrease is gradual with Radarsat-2 data while the drop is very fast with Cosmo-SkyMed data; the bias value is quickly reached and is much higher than for C-band (see value of c_4 in Table 3.5). We focus here on a single lava flow, but similar results were obtained for other lava flows.

The faster drop of coherence in X-band was expected: the shorter wavelength makes the radar signal more sensitive to small changes of position of the scatterers within the resolution cell and it easily decorrelates. However, it is of interest to note that in C-band, coherence of the lava flows can be kept over a very long period of time.

Nyiragongo crater

Let us first consider C-band results. This time again, both Radarsat-2 data were merged together to increase the number of sample points. For this second case, the dispersion of coherence values in C-band is far less important than over the lava flow (Figure 3.20). Actually, the radar signal is reflected on the bottom and the walls of the crater back towards the sensor, giving a more consistent return than in the case of diffuse scattering over the lava flows. A clear trend is observed in the coherence data, that fits extremely well the three-parameter exponential model. Data behaviour is so clear that the fit of the other models is not worth showing. Their divergence from the coherence samples is very large. The scaled and shifted exponential decay is once again established as the best model. The associated bias has a value of 0.27 and the decay constant b_4 is one order of magnitude larger than in the lava flow case (Table 3.5). Nevertheless, the overall level of coherence is smaller than in the lava flow case (< 0.6).
Let us now consider X-band data. Similarly to C-band data, we only fit the fourth model. The coherence level is larger than for C-band coherence, and similar to the lava flow case. Moreover, the decay constant has the same order of magnitude than for the previous region, with a slightly lower bias value.

Goma city

Let us consider the last area of interest, the city of Goma. Since the city is not entirely included within the footprint of the second Radarsat-2 data set, we consider only the first data set for C-band samples. The results are very similar to the Nyiragongo crater example for both C-band and X-band (Figure 3.21). For both frequency bands, the dispersion is even lower than for the Nyiragongo crater and the three-parameter exponential model is the one that fits the data best. Like in the Nyiragongo case, the low dispersion can be explained by the stable double-bounce backscattering mechanism over the city. Moreover, we only consider one data set, instead of two, and the lower number of samples probably helps reducing the dispersion. The model parameters in X-band have a magnitude similar to the two previous examples, from the bias value and the decay constant points of view (see Table 3.5).

3.4.4 Decorrelation time

It has been established in the previous section that the scaled and shifted decreasing exponential model was the one that fits the temporal coherence behaviour best. Its parameters have been determined for the different test areas and they can be used to determine typical decorrelation time. We propose two types of decorrelation time: the half-life time and the mean lifetime. Both are usually associated to radioactive decay which also follows an exponential law, and we decide to transpose their definition to our temporal coherence study. Their expressions are derived from the best model of temporal coherence. Of course, even though we do not explore this option, the user can also define the decorrelation time as the delay corresponding to a given coherence threshold.

Half-life time

For the radioactive decay, the half-life is defined as the time after which the population of elements has decreased by half its initial value. However, we face a slightly different type of

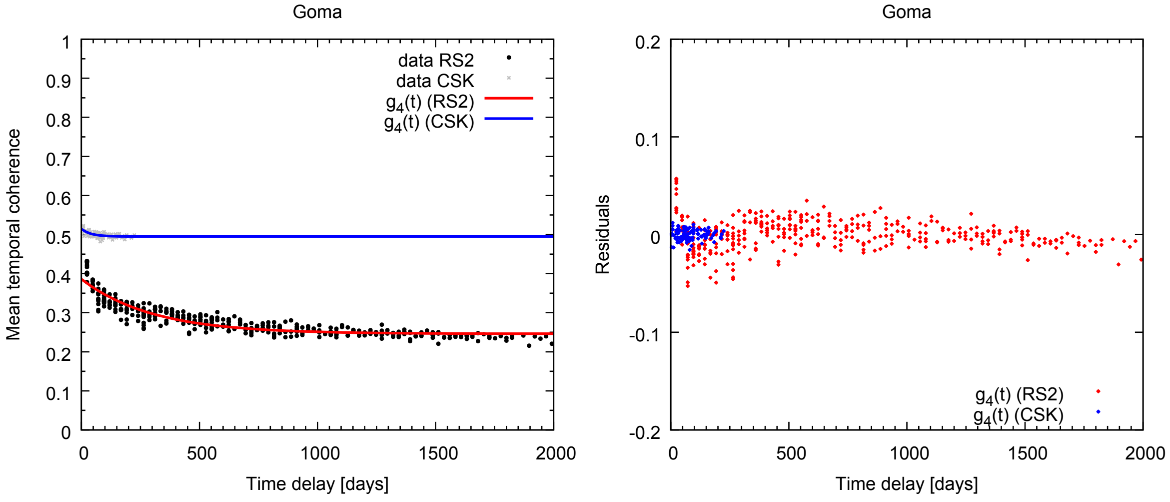

(a) (b)

Figure 3.21: Empirical modelling of temporal decorrelation. Results over the Goma city. Comparison of Radarsat-2 (black and red) and Cosmo-SkyMed (grey and blue) results, showing only the scaled and shifted exponential model. For Radarsat-2 data, only the first data set is considered. (a) Coherence data samples and the fitted scaled and shifted exponential model. (b) Corresponding residuals. Red corresponds to Radarsat-2 data and blue corresponds to Cosmo-SkyMed data.

exponential in the case of coherence: for the scaled and shifted exponential model, coherence decreases from $a_4 + c_4$ to c_4, not to zero. It is then necessary to modify the definition to take into account the coherence bias. Finally, the half-life time is defined as the time lapse after which the coherence drops to the median value $\frac{a_4}{2} + c_4$. Considering this, the expression of the half-life time is given by

$$t_{1/2} = \frac{\ln(2)}{b_4}. \tag{3.20}$$

Mean lifetime

For the radioactive decay of elements, mean lifetime is a scaling time that is defined as the inverse of the decay constant and after which the initial population is decreased by a factor $1/e$. However, for radioactive decay, the decay law does not deal with an additive bias. We thus have to adapt a bit the interpretation for our model. We define the mean lifetime τ has the inverse of the decay constant b_4 :

$$\tau = \frac{1}{b_4}. \tag{3.21}$$

It corresponds to the typical scale of decorrelation time. After a time τ, the coherence will have decreased from $(a_4 + c_4)$ to $(\frac{a_4}{e} + c_4)$.

Discussion

The values of both times are given in Table 3.5 for the different areas, in the C-band and X-band cases. We observe that typical decorrelation times over the lava are excessively large ($>$ 2000 days) and thus unusable in practice. This is due to the dispersion of the coherence values and the overall slow decrease of the coherence over time. For the other cases, both the half-life time

Region	**Band**	a_4	b_4	c_4	$t_{1/2}$	τ
Nyamuragira lava flow 2004	C-band	0.707	3.16×10^{-4} days^{-1}	0.052	2191 days	3160 days
Nyamuragira lava flow 2004	X-band	0.030	1.43×10^{-2} days^{-1}	0.541	49 days	70 days
Nyiragongo crater	C-band	0.238	4.46×10^{-3} days^{-1}	0.270	155 days	224 days
Nyiragongo crater	X-band	0.043	1.87×10^{-2} days^{-1}	0.487	37 days	54 days
Goma	C-band	0.140	3.33×10^{-3} days^{-1}	0.246	208 days	300 days
Goma	X-band	0.019	2.50×10^{-2} days^{-1}	0.495	28 days	40 days

Table 3.5: Empirical modelling of temporal decorrelation. Parameters a_4, b_4 and c_4 of the scaled and shifted exponential model for the different regions and the different frequency bands. The associated half-life time $t_{1/2}$ and mean lifetime τ are also provided.

and the mean lifetime have the same order of magnitude, but the mean lifetime is always slightly larger.

In X-band, the mean lifetimes and the half-lifetimes are always smaller than 100 days. Since the half-lifetime is smaller than the mean lifetime, it leads to very restrictive time delays. In practice, for the determination of an X-band interferogram sequence, the mean lifetime should be preferred in order to obtain an easily connected and consistent set of interferograms.

In C-band, decorrelation times are larger: the smallest mean lifetime reaches 224 days in the case of the Nyiragongo crater. This value is important and such a threshold would probably lead to a very dense sequence of interferograms, that is expensive to generate. In the C-band case, we should prefer the half-life time value to set a threshold on the time separation between acquisitions.

3.4.5 Summary

In this section, we modelled empirically the loss of coherence over time. Several modelling functions were selected and tested on the basis of their agreement with the main characteristics of the coherence. The three-parameter decreasing exponential model happens to be the one that suits the coherence behaviour best. Based on this model, we propose two typical decorrelation times: the mean lifetime and the half-life time.

We observe a difference of dynamics for the coherence in C-band and in X-band: for the X-band data set, the coherence behaviour over time remains the same whatever the region, with a quick loss of coherence, a decay constant ranging around 0.02 days^{-1}, and a bias value close to 0.5. In C-band, we note a different behaviour whether we are considering lava flows or more stable structures, like the urban area of Goma or the Nyiragongo crater. Lava flows show more dispersion of the coherence values, but a slower overall decrease of the coherence.

In the end, we derived decorrelation times based on the best model. Even though we do not test it in practice, these decorrelation times could be used as thresholds for the temporal baseline in order to generate interferogram sequences for MSBAS analysis over the VVP. Unfortunately, although values are realistic for X-band, typical decorrelation times derived for the lava flow in C-band are excessively large and unusable in practice.

3.5 Summary and conclusions

This chapter focused on the MSBAS part of the present work. As for the Split-Band Interferometry, the goal was to develop an operational tool of MSBAS processing, applicable to the Kivu region and to the peculiarities of geohazards in this region. We presented the developed tool and the proposed improvements. We validated the mass processing chain by testing it on the practical of the landslide-prone city of Bukavu.

First, we provided a mathematical description of SBAS and MSBAS, and we explained critical aspects of the MSBAS processing. Once we informed the reader with the studied technique, we briefly presented how the CIS InSAR processing was automatized to obtain an end-to-end MSBAS processing chain. The whole processing chain includes the selection of the pairs to process, the InSAR processing of these pairs and an interface with the MSBAS software.

The second step consisted in looking for improvements of the MSBAS preprocessing. From the spatial coverage point of view, we first proposed a fast and simple interpolation approach that avoids an exaggerated creation of information and that can be applied to any kind of images stack. Besides, we attempted to optimize the balance between spatial coverage and processing time by using a mask to define the common footprint considered for MSBAS processing. Several estimators were investigated and we finally selected the ratio of the variance-mean coherence for the mask generation, because it takes into account the time variability in addition to the coherence level. The mask and the mass processing chain were then applied to the test site of Bukavu, that shows multiple regions of active deformations. We retrieved the expected displacement patterns and rates, but we also observed phase unwrapping errors in unmasked places leading to incorrect estimates of the displacements by MSBAS.

Finally, we considered the problem of temporal coherence and its optimization. We tried to determine the maximum time delay between two acquisitions to preserve a satisfying coherence, depending on the frequency band and the terrain type. We modelled the temporal behaviour of coherence on an empirical basis and we determined that the scaled and shifted exponential model was the most representative of the coherence loss with time. We defined two time scales of decorrelation: the half-life and the mean lifetime. It was shown that decorrelation has very different time scales in X-band and C-band: over the Nyiragongo crater, the half-life reached 155 days in C-band while it was only about 37 days in X-band. The derived decorrelation times could be applied in practice to determine interferogam sequences and perform MSBAS analysis over the VVP.

List of symbols for Chapter 3

$\mathbf{A}$	Representation matrix of the SBAS problem
$\hat{\mathbf{A}}_p$	Representation matrix of the MSBAS problem
α	Azimuth angle
d_j	Line-of-sight cumulative deformation at time t_j
$\boldsymbol{\Delta\phi}$	Vector of the observed differential phases $\Delta\phi_i$
$\Delta\phi_i$	Phase in the i-th differential interferogram
$g_i(t)$	Modelling functions of the coherence
γ	Coherence
$\bar{\gamma}$	Mean coherence
γ_{geom}	Correlation term originating from the geometrical decorrelation
γ_{proc}	Correlation term originating from the processing-induced decorrelation
γ_{temp}	Correlation term originating from the temporal decorrelation
γ_{vol}	Correlation term originating from volume decorrelation
$\bar{\gamma}_\nu$	Mean SBInSAR coherence
L	Number of data sets
λ	Regularization parameter
m_i	Master time index of the i-th interferogram
M	Number of interferograms in the data set
M^l	Number of interferograms in the l-th data set
$N+1$	Number of acquisitions in the data set
N^l+1	Number of acquisitions in the l-th data set
$\boldsymbol{\phi}$	Vector of the unknown phases ϕ_j
ϕ_j	Phase associated to the deformation at time t_j
r	Slant range coordinate of a pixel
s_i	Slave time index of the i-th interferogram
$\mathbf{S}$	Diagonal matrix of singular values
$\vec{S}$	Line-of-sight unit vector
σ_i	i-th singular value
σ_γ	Coherence standard deviation

t_j	Acquisition time
$t_{1/2}$	Half-life time
τ	Mean lifetime
θ	Incidence angle
$\mathbf{U}$	Matrix of eigenvectors for $\mathbf{A}\mathbf{A}^T$
$\mathbf{v}$	Vector of the unknown phase velocities in the SBAS problem
v_i	Linear phase velocity between times t_{i-1} and t_i
$\mathbf{V}$	Matrix of eigenvectors for $\mathbf{A}^T\mathbf{A}$
$\hat{\mathbf{V}}_{los}$	Vector of the unknown projected velocities in the MSBAS problem
x	Azimuth coordinate of a pixel

Chapter 4

Artificial Spectrally Stable Reflectors

At this stage of the present work, advances were made towards an operational use of SBInSAR: in Chapter 2, we established the optimum parameters for spectral decomposition and we determined the limiting factors of SBInSAR. Moreover, we investigated several criteria for spectrally stable pixel detection and determined that the slope standard deviation was the best compromise. We also attempted to better understand the physical nature of spectrally stable pixels. Finally, we showed that relaxing the requirements on SBInSAR phase to a one-cycle precision allows the correction of the phase ambiguities. We developed the SBInSAR-assisted phase unwrapping and we tested it for various sensors, modes and geometric parameters. Nevertheless, this approach is valid as long as there are $\mathrm{PS_f}$ present within the studied scene. The presence of $\mathrm{PS_f}$ is required for all approaches based on absolute ranging using SBInSAR, and this constrain is a strong limitation for operational monitoring with SBInSAR. Indeed, spectrally stable pixels are targets of opportunity, and this population can change from one interferometric couple to another. The user has no control on their location, or even on their existence within the scene of interest, while the continuous presence of reliable targets is necessary to monitor a region. Otherwise the temporal continuity of measurements cannot be secured. The inability to ensure the presence of $\mathrm{PS_f}$ at a specific location raises difficulties for operational monitoring, which are reinforced by our lack of knowledge on the physical nature of spectrally stable targets.

Similar problems of target density are encountered in Persistent Scatterers Interferometry [10]: the number of permanent scatterers often drops drastically in low coherence regions, i.e. non urbanized, vegetated areas. For decorrelating sites, the population of PS can become very sparse, and working only with opportunistic PS may not be sufficient anymore. A popular solution to elude this drawback is the use of *artificial reflectors*, e.g. *corner reflectors* [99,100] or *transponders* [101–103], to artificially create PS: these reflectors have a strong and stable radar response, both in amplitude and phase, which makes them resistant to decorrelation and good candidates for high quality InSAR measurements over long time periods [104,105]. In addition to their InSAR performances, artificial reflectors present the advantage of a controlled design and the possibility to be installed at a specific location. Therefore, once placed on the site of interest, they are used as highly coherent reference points on which interferometry can be performed. For instance, such setups have been widely employed for slowly moving landslides [106–108].

Given the similarities between the PS and $\mathrm{PS_f}$, the solution of artificial reflectors suggests a possible use of *artificial spectrally stable targets.* In Chapter 2, we investigated the physical nature of $\mathrm{PS_f}$ and we showed that some $\mathrm{PS_f}$ persistent over time correspond for instance to urban targets, i.e. targets that are bright, stable and characterized by a double bounce scattering mechanism. Since these features perfectly match corner reflectors, we believe that artificial reflectors could be used as artificial spectrally stable targets.

The central question of this chapter is whether artificial reflectors are spectrally stable targets or not. Could they be used as SBInSAR reference points? And if yes, under which conditions? In the first section, we review the theoretical considerations used to characterize artificial reflectors. Then, we describe the two types of artificial reflectors, as well as their advantages and disadvantages. The next section is dedicated to an experiment in Wassenaar, Netherlands. This data set is used to assess the potential of artificial reflectors regarding SBInSAR. Finally, these results are studied to derive the relationship between the signal-to-clutter ratio of a target and its detectability as $\mathrm{PS_f}$. Once this relationship established, a threshold on the SCR can be calculated, as well as the corresponding dimensions of a corner reflector.

4.1 Reflectivity of a target

A point target such as an artificial reflector is often characterized in terms of its reflectivity properties and its visibility with respect to the background noise. In this section, we review the basic variables used for the radiometric characterization of a target and we briefly present the method that is used to estimate these variables in practice.

4.1.1 Theoretical considerations

Let us consider the *radar cross section* (RCS) σ_T of an imaged point target, e.g. an artificial reflector. The RCS is a measure of the scattering strength of the object. It is measured in surface units and it is often expressed in dBm^2.

The RCS of a point target can be related to another conventional estimate of the reflectivity: the *sigma-nought.* The sigma-nought σ^0 is an estimate of the target backscattering coefficient and it is a dimensionless number usually expressed in dB. It is calculated as the radar cross section of the target normalized by the surface A of the resolution cell projected on the ground [60]:

$$\sigma^0 = \frac{\sigma_T}{A}. \tag{4.1}$$

The radiometric response of a point target is not only characterized by its RCS, but also by its *visibility* in an amplitude image. A target is visible if its backscattering strength is well above the background backscattering level, known as *clutter.* The signal-to-clutter ratio (SCR) is the usual estimator for a target visibility. It is expressed as

$$SCR = \frac{\sigma_T}{< \sigma_C >}. \tag{4.2}$$

In this equation, $< \sigma_C >$ is the ensemble average of clutter RCS near the point target. Let us stress that, in order to obtain a good visibility contrast, the clutter surrounding the target must have a low contribution. Minimizing the clutter level is a main concern when selecting the deployment area of artificial reflectors. Ideally, bare soils, cultivated terrains or flat areas with low vegetation are preferred.

4.1.2 Practical considerations

In the following, we have to assess the radiometric stability of artificial reflectors, and we estimate therefore their RCS and SCR. To do so, we apply the integral method described in Reference [109]. Let us shortly review the principle of this method.

The integral method estimates the radar cross section of a target, the level of its neighbouring clutter and the corresponding SCR starting from a sigma-nought image in slant-range geometry. First, a target window that encompasses the *sinc* response of the target is defined. Four clutter quadrants of the same size are cut out from this window. These clutter quadrants surround

Figure 4.1: Triangular trihedral corner reflector installed in Sart Tilman for the EOregion project.

the impulse response of the target, that is contained within a cross pattern. Then, the clutter level is estimated by integrating the sigma-nought values over the four quadrants, that are representative of the direct neighbourhood of the studied target. The target RCS is calculated by integrating its *sinc* response over the target window and then subtracting the rescaled clutter level from the integrated response. Finally, the RCS is obtained by multiplying the integrated point response by the area of a resolution cell. The corresponding SCR is also calculated.

4.2 Artificial reflectors

An artificial reflector is a man-made object that exhibits a large radar cross section, or at least a good signal-to-clutter ratio, as well as stability of phase and amplitude in time. It is used to artificially create reference points at known locations in radar images and allows interferometric measurements with a high signal-to-noise ratio [110]. Artificial reflectors were originally used for external calibration of SAR systems [100, 111–113]. Nevertheless, with the increasing popularity in the last years of Permanent Scatterers Interferometry [10], they were also exploited to create measurement points in low coherence areas (rural, non urban, vegetated areas) and then improve the density of permanent scatterers [102, 106–108]. Artificial reflectors are either passive, e.g. corner reflectors, or active, e.g. transponders. In this section, we describe these two types of artificial reflectors and evaluate their pros and cons.

4.2.1 Corner reflectors

A corner reflector is a metal object whose shape is designed to reflect the incident radar signal back towards the sensor. The preferred geometry is usually trihedral, with either triangular, rectangular or square plates [114]. A triangular trihedral corner reflector is pictured in Figure 4.1. The optimized RCS of corner reflectors is obtained by taking advantage of the double/triple bounce of the transmitted radar signal over the orthogonal plates to maximize the intensity of the signal reflected back to the sensor. To achieve good performance, the corner reflector must be oriented to match the line-of-sight of the targeted SAR sensor. Details about the dimensions and design of a corner reflector depending on the sensor frequency can be found in Reference [109].

Corner reflectors are passive, they do not require any power supply, and their cost is moderate. However, they are large, cumbersome and difficult to manipulate. On the long term, they can be disturbed by external factors like wind, rain and snow accumulation, or human action. The design of a corner reflector can be modified in order to decrease the impact of these factors, e.g. by cutting holes in the plates to reduce the wind stress and drain the precipitations. However, these modifications are usually done at the expense of the radar cross section.

Moreover, a corner reflector is dedicated to a single geometry: its orientation is determined for a given incidence angle, either for an ascending or a descending orbit. Nevertheless, specific shapes, e.g. dihedral design, can be used in order to get high RCS reflectors that are visible by two sensors with different looking angles, but these require a very precise pointing [110].

4.2.2 Transponders

A radar transponder is an active device meant to amplify the incident radar signal, increasing thus the backscattering response at the corresponding location. In practice, the signal sent by the SAR sensor is received by the transponder, and an amplified and filtered version of it is directly retransmitted towards the satellite [102]. The transponder can be programmed according to the flight schedule of SAR satellites, so that it switches on during the satellite overflight and remains in sleep mode the rest of the time. Transponders are limited to a single frequency band, but a single setup can be active for both ascending and descending geometries, as well as for various sensors.

Transponders are active devices, requiring a power supply and therefore a minimum maintenance. Being electronical devices, their components can face aging or failure. On the other hand, they are small, compact and less subject to external factors, like weather events, than corner reflectors. These devices are described in details in Reference [102]. This study also assesses their long term phase stability.

4.3 Wassenaar experiment

It is now time to investigate the possibility for an artificial reflector to correspond to an artificial PS_f, in which case it could be used in Split-Band Interferometry the same way it is done for PSI, i.e. to ensure continuous monitoring over a given area. In other words, we want to determine if a large radar cross section is a sufficient condition for an object to be a reliable spectrally stable target. Then, if yes, installation of an artificial reflector would secure the presence of a stable SBInSAR reference point of known location in the area of interest, making monitoring feasible.

In this section, we examine the behaviour of artificial reflectors regarding Split-Band Interferometry and look for their correspondence with PS_f. However, no experiment involving artificial reflectors was carried out in our region of interest, making such an investigation impossible over this area. For this reason, the following study was performed using a Sentinel-1 data set kindly shared by the Geoscience and Remote Sensing team of the TU Delft, which is currently conducting a field experiment in Wassenaar (the Netherlands) to test C-band transponders for InSAR geodesy. The setup of this experiment is described in details in Reference [103].

4.3.1 Test site

The artificial reflectors of the TU Delft team are settled in a meadow located in the neighbourhood of Wassenaar, north of the Hague (the Netherlands) (Figure 4.2a). Since August 2017, three C-band transponders, manufactured by MetaSensing and referred to as *Electronic Corner Reflectors* (ECR), have been active for various orbits of Sentinel-1 in VV-polarization. Their

(a) (b)

Figure 4.2: Google Earth$^{\text{TM}}$ views of the Wassenaar test site. (a) Location of the test site indicated by the yellow pin. (b) Locations of the artificial reflectors. The green, red and blue pins indicate respectively the locations of the ascending corner reflector (CR-ASC), the transponder No. 2 (ECR2) and the transponder No. 3 (ECR3).

radar cross section was a priori estimated to be around 32 dB. Two square based triangular corner reflectors with a long edge length of 1.425 m are also installed on the test site, one oriented for ascending orbits and the other one aimed for descending orbits. Their C-band radar cross section was estimated from numerical simulations at 40.65 dB by TU Delft team. Let us note that two additional transponders were initially present on the terrain, but they were removed on September 4th, 2017.

4.3.2 Data set and processing

The Wassenaar setup is dedicated to Sentinel-1 satellites. However, Sentinel-1 is a medium resolution sensor, whose bandwidth is not particularly suited for Split-Band Interferometry. In Interferometric Wide (IW) mode, the range bandwidth reduces from the near to the far range, with a maximum value of 56.5 MHz in the first swath. In order to work with the maximum available bandwidth, we select the ascending relative orbit 88, for which the test site is located within the first swath. For this orbit, the transponders No. 2 and 3 were active during the targeted period from August 26th, 2017 to November 24th, 2017. The ascending corner reflector was also correctly oriented for this orbit. In the following, the studied targets are these two transponders and this corner reflector, and they are respectively referred to as ECR2, ECR3 and CR-ASC. Their precise locations are pictured in Figure 4.2b.

For the studied period, there were 16 images acquired with a 6-day revisit time on the relative orbit 88 by both Sentinel-1A and 1B. However, the acquisition of September 7th, 2017 is rejected because ECR2 was not active. Our data set is therefore made of 15 images acquired in an ascending geometry. The incidence angle at the location of the test site is of approximately 34°. Considering this data set, we select the acquisition of August 26th as the common master image, and we form 14 interferometric pairs using the other images as slaves. This common master ensures a temporal and geometrical reference. Interferometric processing is carried out on the selected couples of images. In order to spare computing resources, we focus on our area of interest and only process the two bursts of the first swath corresponding to our area of interest. A spatial averaging of 4×1 pixels is applied in range and azimuth respectively, leading to an approximate ground range-azimuth resolution of 20 m × 20 m. This moderate size of the averaging window is chosen to avoid merging signals from the neighbouring reflectors, which are only separated

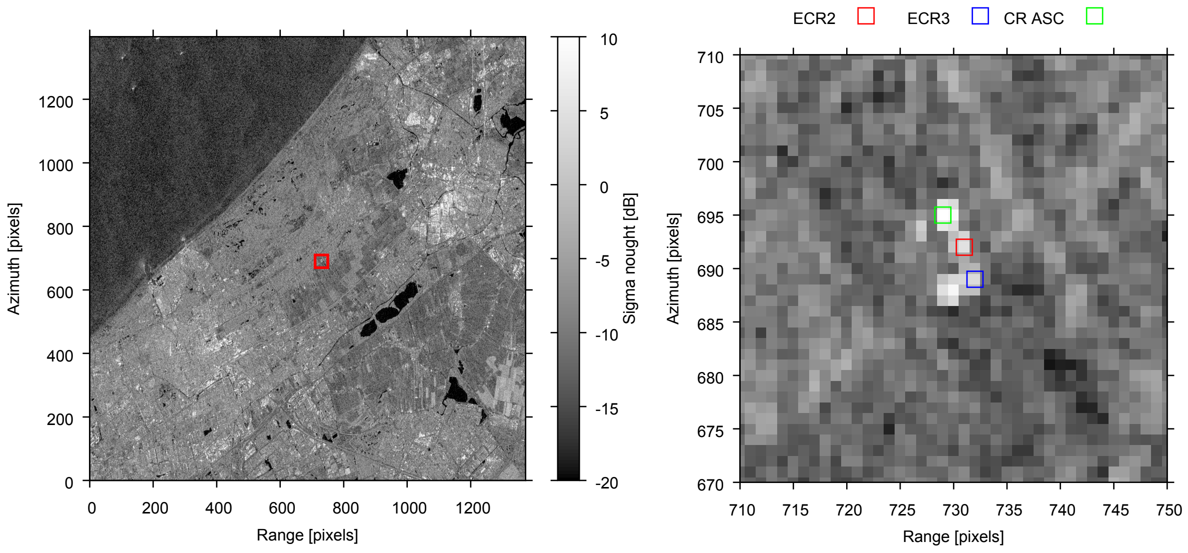

(a)

(b)

Figure 4.3: Wassenaar test site. Sigma-nought image of November 24th, 2017. (a) Large view of the area, with the test site highlighted by the red box. (b) Zoom on the red box area and identification the artificial reflector response. The green, red and blue squares correspond respectively to the locations of ECR2, ECR3 and CR-ASC. Another signal is detected in the sigma-nought image, which corresponds to a double backflip corner reflector not considered in this work.

by a few tens of meters, while still mitigating speckle in the image. Although the area is quite flat, the topographic component is subtracted using the SRTM 1 arcsec DEM provided by the U.S. Geological Survey. Interferograms are filtered using a Goldstein-modified adaptive filter and SNAPHU is used for phase unwrapping. Moreover, the intensity of each acquisition of the data set is calibrated to yield the corresponding sigma-nought images.

Split-Band interferometric processing is also applied to the selected pairs. Given the reduced range bandwidth of 56.5 MHz, the spectral decomposition is limited to 5 subbands of only 11.3 MHz, and a weighted linear regression is adopted.

4.3.3 Stability of the artificial reflectors

Their stable nature and their strong radar response make artificial reflectors good candidates for artificial spectrally stable targets. In this step, we check the stability of the reflectors response from the radiometric and interferometric points of view.

Radiometric stability

In order to assess the radiometric stability of the studied artificial reflectors, we estimated the RCS and SNR of each artificial reflector throughout the data set using the integral method presented in Section 4.1.2. In practice, all sigma-nought images are coregistered onto a common master and artificial reflectors are therefore located at the same pixel coordinates in each image. Thanks to that, we can adopt a repetitive procedure that uses the same target window throughout the stack of images to estimate the RCS and the SNR of a given artificial reflector. In Figure 4.3a, we present an image calibrated in intensity where the test site is highlighted. In Figure 4.3b, we zoom on the test site and we locate the artificial reflectors in the azimuth-slant range coordinate system based on their radiometric response. The devices are only separated by some tens of meters, making their respective signals spread on very close pixels, given the

Reflector	**RCS** [dBm^2]	**SCR** [dB]	**Coherence**	σ_ν [rad/GHz]
CR-ASC	38.60 ± 1.14	23.34 ± 1.03	0.97 ± 0.02	1.49 ± 0.39
ECR2	33.46 ± 1.73	18.29 ± 1.78	0.86 ± 0.06	4.45 ± 4.14
ECR3	31.52 ± 1.41	15.20 ± 1.18	0.94 ± 0.03	3.51 ± 1.33

Table 4.1: Wassenaar study case. Mean values of the RCS, SCR, coherence and slope standard deviation of the artificial reflectors through the data set. Standard deviations from the mean values are also given.

pixel resolution of 20 m × 20 m.

In Figures 4.4a and 4.4b, the estimated values of the RCS and the SCR are shown for each artificial reflector and each acquisition of the data set. Moreover, mean values of these parameters are provided in Table 4.1. We first observe that, as expected, the corner reflector has larger cross section than the transponders, and therefore a better SCR since they all approximately share the same clutter. Our estimates of the corner reflector RCS are in average slightly under the simulated value of 40.65 dB. Radar cross sections of the transponders match the rough estimation of 32 dB. The sigma-nought average clutter level ranges between -7 and -9 dB, which is a bit larger than expected for this kind of terrain. Indeed, the backscatter level of low vegetation or flat cultivated terrains is likely to range between -14 and -10 dB in C-band [109]. Let us note that, even though the integration windows were chosen to minimize the signal overlap, the proximity of the reflectors may lead to an overestimation of the clutter level by the integral method, and therefore a slight underestimation of the target RCS. This overestimation is probably even larger for acquisitions before September 7th, because two additional reflectors were present on the site. Nevertheless, in the worst case of dispersion corresponding to ECR2, the SCR varies of less than 10% with respect to the mean value. Given these considerations, the radiometric response of all devices is in global more or less stable over time.

Interferometric stability

In order to perform interferometry on artificial reflectors, there is not only their amplitude response that must be stable, but also their phase response. As it is well known, coherence is the usual way to evaluate the quality of an interferometric measurement. For this reason, we assess the stability of the studied artificial reflectors by looking at their coherence value.

The evolution of coherence at the devices locations is presented in Figure 4.4c. The common master image secures a temporal reference, and the coherence is plotted with respect to the date of the slave acquisition. The average coherence of the clutter is also estimated in the neighbourhood of the reflectors. We observe that the artificial reflectors have a much larger coherence level than the clutter. We also note that, although ECR2 has a better SCR than ECR3, its coherence level is lower. Moreover, its coherence values show more dispersion. Nevertheless, the corner reflector has a very high and stable coherence level. This is also the case of ECR3.

4.3.4 SBInSAR performances

After assessing the stability of artificial reflectors, it is now time to estimate their performances regarding SBInSAR. Are artificial reflectors detected as spectrally stable targets? Can we compute the absolute phase of these pixels? We now attempt to answer these questions.

Detectability as PS$_\mathrm{f}$

Let us first investigate the detectability of artificial reflectors as spectrally stable targets. The slope standard deviation being the reference criterion for PS$_\mathrm{f}$ detection, we use it to assess the

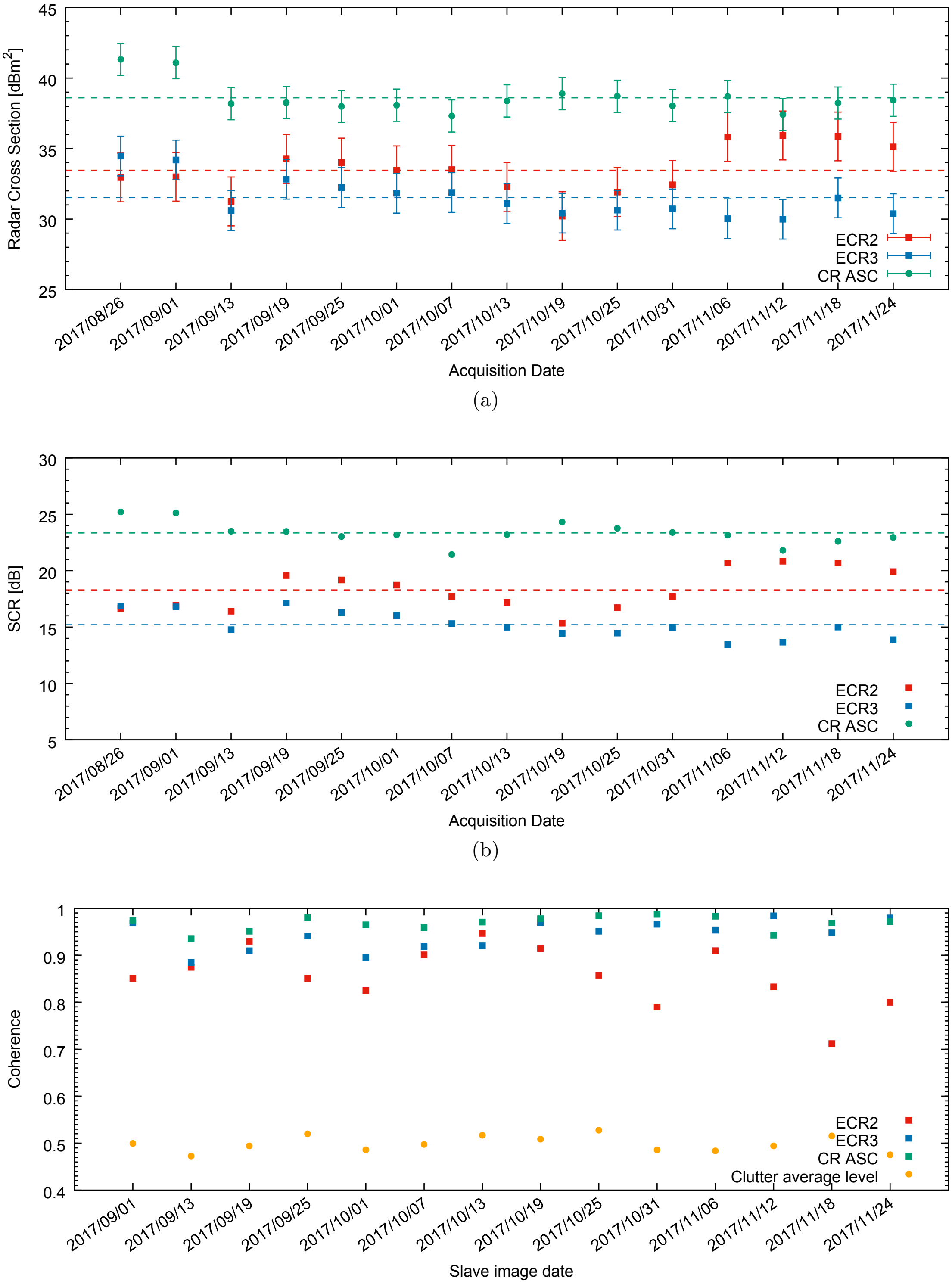

(a)

(b)

(c)

Figure 4.4: Wassenaar study case. (a) Radar cross sections of ECR2 (red), ECR3 (blue) and CR-ASC (green) calculated for all acquisitions of the data set. The x-axis gives the acquisition date. (b) Signal-to-clutter ratio of ECR2 (red), ECR3 (blue) and CR-ASC (green) estimated for all acquisitions of the data set. The x-axis gives the acquisition date. (c) Coherence of ECR2 (red), ECR3 (blue) and CR-ASC (green) estimated for the selected interferometric pairs. The mean level of the clutter is represented in orange. The common master image is the acquisition of August 26th and the x-axis gives the date of the slave acquisition.

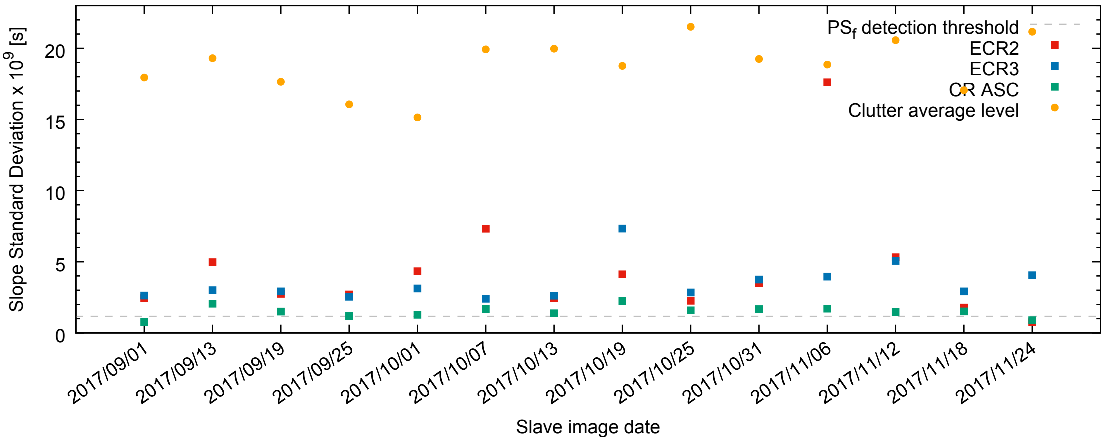

Figure 4.5: Wassenaar study case. Values of the slope standard devation for ECR2 (red), ECR3 (blue) and CR-ASC (green) in the selected interferometric pairs. The mean level of the clutter is represented in orange. The dotted grey line indicates the detection limit of PS_f. The common master image is the acquisition of August 26th and the x-axis gives the date of the slave acquisition.

quality of artificial reflectors regarding SBInSAR. In Figure 4.5, the slope standard deviation values of the artificial reflectors are plotted as a function of the slave acquistion date. The dotted grey line indicates the PS_f detection threshold, which is 1.16 rad/GHz in C-band.

We first observe that the ascending corner reflector, which has the largest RCS and the best SCR, is also the reflector with the lowest, and therefore the best, values of the slope standard deviation. The mean value of the slope standard deviation is provided for each reflector in Table 4.1, along with the corresponding standard deviation. In global, transponders have larger values of the slope standard deviation and show more variability. In particular, ECR2 has a higher dispersion than ECR3, partially due to an outlier value on November 6th. Besides, we also average the slope standard deviation values on a window corresponding to the clutter. The mean values estimated for the clutter are given in orange in Figure 4.5. The observed level is located around 20 rad/GHz, which is noticeably larger than the level of the artificial reflectors. From these data, it becomes clear that artificial reflectors have a better potential for spectral stability than a random scatterer from the clutter. We tend to conclude that the better the SCR of a target, the better its detectability of as a spectrally stable pixel. This idea is further exploited in the next section. Let us stress that the variable of interest is indeed the signal-to-clutter ratio, not the radar cross section: a large RCS is of no use when the target is drowned into an important clutter contribution.

In agreement with this conclusion, the ascending corner reflector is the target with the best potential of detection. However, even though it proved to be stable both from the radiometric and the interferometric points of view, and though it has high RCS and a good SCR, the slope standard deviation of CR-ASC meets the PS_f detection limit for two images only. We suspect that this limited performance originates from the Sentinel-1 acquisitions that are suboptimal for good SBInSAR results. Nevertheless, we are confident that artificial reflectors of such quality (with high RCS, good SCR, radiometric and interferometric stability) would be recognized as spectrally stable targets if acquisitions from wideband sensors and higher resolution modes were considered, for instance Radarsat-2 in Ultra-Fine mode.

Quality of SBInSAR phase

In Reference [103], it was shown that InSAR measurements at the location of the transponders have a steady behaviour over time. If artificial reflectors have an SBInSAR phase of high quality,

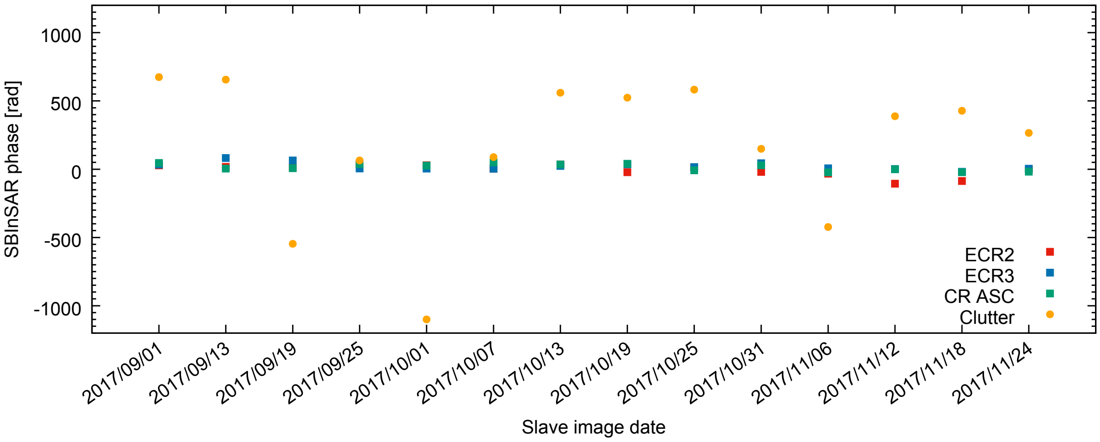

Figure 4.6: Wassenaar study case. Values of the SBInSAR phase for ECR2 (red), ECR3 (blue) and CR-ASC (green) through the stack of selected interferometric pairs. SBInSAR phase of a random clutter pixel is also pictured in orange. The common master image is the acquisition of August 26th and the x-axis gives the date of the slave acquisition.

we therefore do not expect much variability of the measurements over time.

In Figure 4.6, we present the evolution of the SBInSAR phase through the stack of selected interferometric pairs, each pair having the same master image. The SBInSAR phase is also pictured for a random pixel of the neighbouring clutter. With respect to the clutter pixel, the artificial reflectors show a steady behaviour: the SBInSAR phase is located around zero for all interferometric couples. If the SBInSAR-assisted phase unwrapping was applied, the artificial reflectors would not always give rise to the same phase ambiguity estimate, but their error would be much smaller than the one of the clutter contribution.

4.4 Practical recommendations

In the previous section, we highlighted the potential of artificial reflectors for spectral stability. We observed that the target with the larger SCR was the one with the best $\mathrm{PS_f}$ detection potential, and we deduced that the quality of the SBInSAR phase associated to artificial reflectors probably improves as the SCR of the targets increases. Here, we actually demonstrate this correlation and establish an estimation of the SCR required for $\mathrm{PS_f}$ detection. Thanks to this estimation, we can prescribe dimensions for a triangular trihedral corner reflector if the clutter level is known.

4.4.1 Correlation between SCR and $\mathrm{PS_f}$ detectability

For the Wassenaar experiment, we noticed the probable existence of a relationship between SCR and slope standard deviation values. We observed that, a priori, a large SCR corresponds to a good $\mathrm{PS_f}$ detectability, i.e. a low value of the slope standard deviation. In order to assess the correlation between the SCR and the slope standard deviation values, let us draw the correlation plot of the two parameters for the reflectors of the Wassenaar experiment and calculate their linear correlation coefficient. The linear correlation coefficient is computed as the covariance of the two variables normalized by the product of their respective standard deviations [48].

In practice, we consider the values of the slope standard deviation calculated for each artificial reflector and each interferometric couple of the Wassenaar data set, and we associate them to the SCR values calculated for the acquisition corresponding to the slave date. The correlation plot of

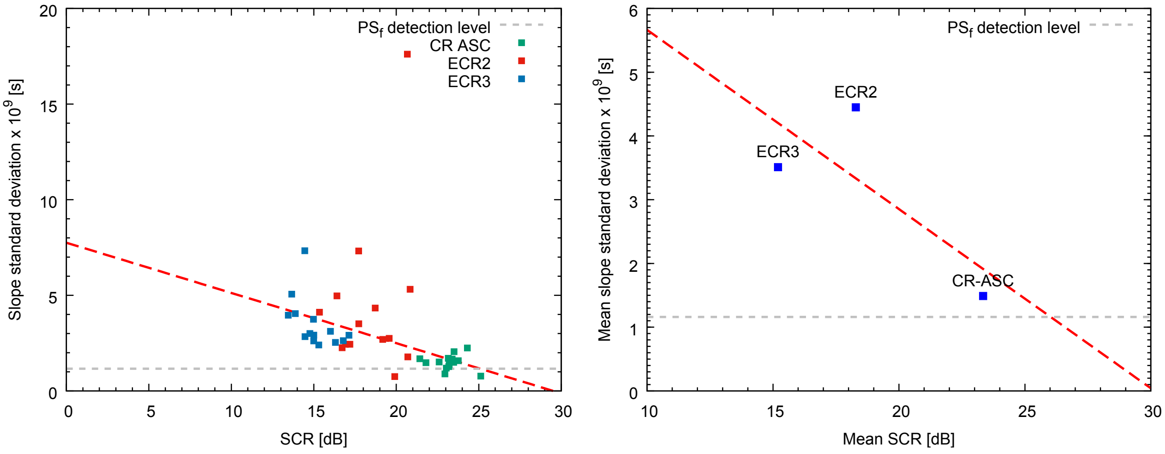

(a) (b)

Figure 4.7: Wassenaar study case. Correlation between the SCR and the slope standard deviation values of the artificial reflectors. (a) Correlation plot for which each sample point corresponds to a given artificial reflector and a given slave date. Sample points corresponding to CR-ASC, ECR2, and ECR3 are drawn respectively in green, red and blue. (b) Correlation plot for which sample points corresponds to the mean values of each reflector. For both figures, the dotted grey line represents the threshold of PS$_f$ detection for the slope standard deviation, and the dotted red line represents the linear regression on the sample points. The SCR threshold for PS$_f$ detection is found at the intersection between the dotted lines.

the slope standard deviation values against the SCR values for all artificial reflectors is presented in Figure 4.7a. Considering the sample point of each reflector separately, no clear correlation can be noticed. However, when the sample points of the three reflectors are gathered, a larger range of SCR values is explored and a linear correlation coefficient of -0.6 is obtained. This non negligible negative correlation translates our expectations, as it means that, in global, when the SCR increases, the slope standard deviation decreases. Let us note that in the correlation plot, there is a clear outlier value corresponding to the ECR2 measurement on November 6th, which was not taken into account when calculating the correlation coefficient. The linear trend between the variables is pictured by the fitted linear regression (dotted red line).

4.4.2 SCR threshold for PS$_f$ detection

Since the SCR seems to be related to the PS$_f$ detectability, it is of practical interest to determine the SCR threshold corresponding to a detectable spectrally stable target. This minimum SCR can be derived by using the correlation plot between the SCR and the slope standard deviation values, and extrapolating the calculated linear trend until it intersects the PS$_f$ detection threshold of the slope standard deviation (dotted grey line in Figure 4.7). By doing so, we estimate the SCR threshold for PS$_f$ detection to be around 25 dB in C-band.

A similar correlation plot can be obtained by considering the mean values of the slope standard deviation and the SCR, instead of all the sample points (Figure 4.7b). When considering the mean values, the estimation of the SCR threshold is slightly higher and reaches 26 dB. Let us stress that, if new data sets of artificial reflectors experiment become available in the future, this mean value approach offers the possibility to complete the correlation plot with new measurement points without facing weighting issues. Such an eventuality would allow a refined estimation of the C-band SCR threshold for PS$_f$ detection.

4.4.3 InSAR accuracy corresponding to the SCR threshold

When applying interferometry on point targets, the signal-to-clutter ratio can also be used to estimate the phase error of an interferometric measurement. Indeed, the interferometric phase error σ_ϕ is expressed in function of the SCR as [115]

$$\sigma_\phi = \frac{1}{\sqrt{2 \cdot SCR}}. \tag{4.3}$$

It is then straightforward to derive the line-of-sight displacement error σ_d from the phase error, dividing it by the wavenumber scaling factor:

$$\sigma_d = \frac{\lambda}{4\pi}\,\sigma_\phi. \tag{4.4}$$

Based on these expressions, we estimate that a SCR threshold of 26 dB corresponds to an error on the interferometric phase of 0.035 rad, equivalent to a submillimeter precision of the line-of-sight deformation ($\sim$ 0.15 mm). These results prove once again that very high accuracy is required to perform SBInSAR measurements.

4.4.4 Recommended dimensions for corner reflectors

Let us consider a practical situation for which the clutter level of the studied region is known. Then, it is of course possible to determine the minimum RCS corresponding the SCR threshold. Once the required RCS is known, the dimensions of a triangular trihedral corner reflector of such RCS can be calculated. Indeed, there exists an analytical expression of the maximum radar cross section σ_{TCR} of a triangular trihedral corner reflector, given by [99]

$$\sigma_{\text{TCR}} = \frac{4\pi l^4}{3\lambda^2}, \tag{4.5}$$

where l is the long-edge dimension of the triangular plates and λ is the sensor wavelength. We now apply this reasoning to the practical case of Sentinel-1 acquisitions over the Virunga Volcanic Province and assess a rough estimation of the corner reflector size needed for SBInSAR monitoring in this area. Let us note that analytical expressions of the RCS also exist for rectangular and square trihedral corner reflectors, and similar calculations could also be performed for these designs.

Example of the Virunga Volcanic Province

In order to illustrate our reasoning and provide the reader with an actual numerical estimation, we apply this approach to a practical example over our region of interest. We investigate three different potential locations for an artificial reflector: the Nyiragongo crater, and the Nyamuragira SE and NE flanks.

Let us consider the Sentinel-1 acquisition of August 14th, 2017 over the Virunga Volcanic Province. The calibrated sigma-nought image of this acquisition is generated to estimate the clutter in different places. Let us note that a spatial averaging of 8×2 pixels was applied in range and azimuth respectively. For each location, the local clutter mean RCS is calculated on an integration window. The studied locations are shown in Figure 4.8 along with the corresponding integration windows.

The average clutter level, given by the mean sigma-nought value per pixel, is similar for the three studied spots. It reaches approximately -8.5 dB. Given the size of a resolution cell and the spatial averaging applied, this corresponds to a mean clutter RCS of about 21 dBm^2. Therefore,

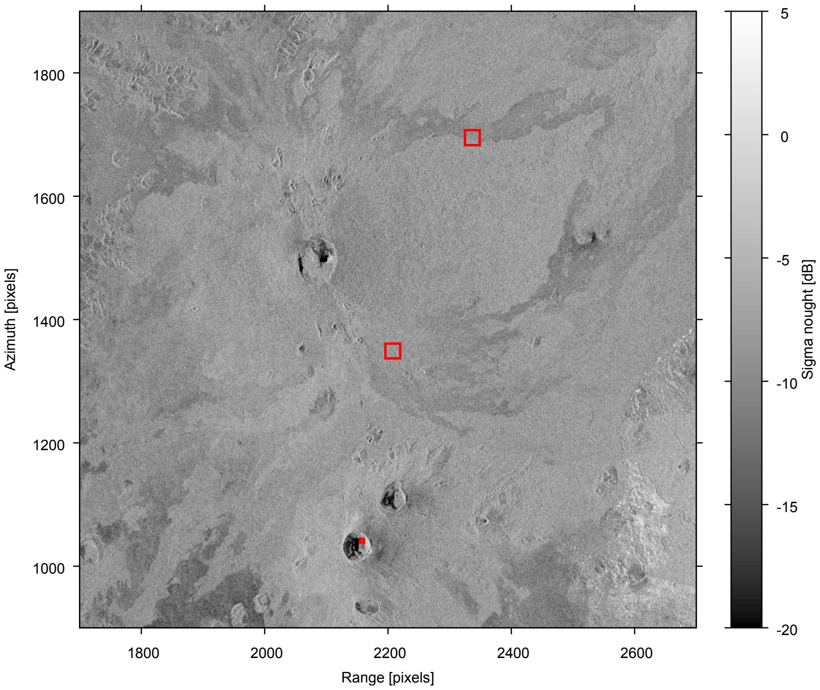

Figure 4.8: Sigma-nought image of the VVP from the Sentinel-1 acquisition of August 14th, 2017. Clutter is estimated for three places in the image: the Nyiragongo crater, and the Nyamuragira SE and NE flanks. Windows used for clutter estimation are represented by the red boxes. The window corresponding to the Nyiragongo crater has been reduced to fit the scale of the area of interest.

the RCS of the trihedral corner reflector should be of at least 47 dBm^2, which corresponds to a long edge dimension of the triangular plates of 2.45 m.

Let us stress that this value is a quick and rough estimate: it is purely indicative and simply illustrates our reasoning. Indeed, the clutter has been evaluated here from a single acquisition at a given time, while a robust evaluation for a further feasibility study should estimate the clutter through a large data set of images acquired at different seasons and, in particular, for different humidity conditions. Indeed, in this tropical region, the humidity parameter, which is known to impact the reflectivity, can drastically change along time.

4.5 Summary and conclusions

The central question of this chapter was to determine whether or not artificial reflectors could be used as high-quality SBInSAR reference points and therefore solve the $\mathrm{PS_f}$ density issue preventing operational monitoring with Split-Band Interferometry. In order to solve this question, we have been interested in the detectability of artificial reflectors as $\mathrm{PS_f}$.

In the absence of an adequate data set over our region of interest, we had the opportunity to work with a Sentinel-1 data set over Wassenaar, where the Geoscience and Remote Sensing team of the TU Delft had a setup of transponders and corner reflectors installed during the period from August 2017 to December 2017. We estimated the RCS and SCR of the artificial reflectors over the studied period and assessed their temporal stability. As expected, the corner reflector was the reflector with the highest RCS and the best SCR. It was also the target that showed the best stability trough time.

Once the stability of the reflectors was assessed, we looked whether thy were detectable as $\mathrm{PS_f}$. For this purpose, we used the preferred $\mathrm{PS_f}$ detection criterion, i.e. the slope standard deviation.

It appeared that artificial reflectors had much better values of the slope standard deviation than the clutter, and that the corner reflector, which had the largest RCS and the best SCR, was also the artificial reflector with the lowest standard deviation values and the least variability from one interferometric couple to another. From this observation, we assumed a probable correlation between the SCR of a target and its SBInSAR phase precision. However, Sentinel-1 acquisitions being ill-fitted to SBInSAR, the corner reflector did not even reach the $\mathrm{PS_f}$ detection limit for all pairs. We believe that such a target with such a good RCS and SCR should be detected as a $\mathrm{PS_f}$ in more SBInSAR-adequate acquisitions, like Radarsat-2 acquisitions in Ultra-Fine mode.
In the next step, we calculated a linear correlation coefficient of -0.6 between the SCR and the slope standard deviation, meaning that a large SCR corresponds to a low standard deviation value, and therefore to a reliable $\mathrm{PS_f}$ and a good SBInSAR precision. By extrapolating the linear behaviour between the variables, we determined that a SCR of approximately 26 dB was recommended to obtain an artificial spectrally stable reflector detectable in C-band. Based on this estimation, we showed that an artificial spectrally stable reflector would allow submillimeter precision of InSAR measurement. Moreover, with a rough estimation of the clutter contribution, we estimated that a corner reflector size of more than 2 m was necessary to monitor the VVP region (with Sentinel-1 acquisitions, or another medium resolution sensor), if the chosen design is a triangular trihedral corner reflector.

List of symbols for Chapter 4

A	Ground range area of a resolution cell
l	Long edge length of a triangular trihedral corner reflector
λ	Wavelength
SCR	Signal-to-clutter ratio
σ^0	Sigma-nought, backscattering coefficient estimate
$< \sigma_C >$	Average clutter radar cross section
σ_d	Error on the line-of-sight displacement
σ_T	Radar cross section of a target
σ_{TCR}	Radar cross section of a triangular trihedral corner reflector
σ_ϕ	Interferometric phase error

Chapter 5

Split-Band Interferometry for Ionospheric Phase Compensation

It is well known that, because it is not a neutral medium, the ionosphere impacts the propagation of radio waves. Radiocommunications have taken advantage of this peculiar behaviour, using the reflection of radio waves on the ionosphere for long distance communications. However, in SAR interferometry, ionosphere is no longer an advantage, but rather a limiting factor. Indeed, radar signals propagating through the ionosphere suffer from a phase advance that depends on their frequency and the population of free electrons along the propagation path. In particular, variations of the ionospheric *total electron content* (TEC) are a major source of error in low frequency interferograms. This variability can introduce *azimuth streaks*, that create coregistration issues, as well as an *ionospheric phase screen*, that masks the geophysical signal contained in SAR interferograms. When looking for ground displacements, it is thus necessary to estimate and correct the ionospheric phase contribution in order to retrieve an uncorrupted ground deformation signal.

Fortunately, the ionospheric phase component is dispersive, i.e. it has a behaviour that depends on the signal frequency, and it is therefore possible to exploit the spectral diversity of the SAR signal to calculate and correct the ionospheric phase contribution. This is what is done by the *Range Split-Spectrum* technique, which splits the range bandwidth of SAR images for generating chromatic views at low and high frequencies, performs interferometry to get low and high frequency phases, and then combines these phases in order to isolate the dispersive phase component induced by the ionosphere [116, 117]. This technique is already well developed and has proven to be efficient for discriminating between ionospheric and geophysical signals [38,40]. Estimates of the ionospheric phase have also been used to study the spatial structure of the ionospheric layers [39].

The Range Split-Spectrum technique, that uses at the same time the spectral content of SAR images and the interferometry, is another approach of Split-Band Interferometry that was already used in Chapter 2 for absolute ranging and for correcting phase ambiguities. Compared to SBInSAR for absolute ranging, the split-spectrum technique requires some slight modifications of the spectral decomposition and a different processing flow, but the basis of the SBInSAR tool is common. Starting from this common basis, these modifications enable the development of an additional application and the extension of the SBInSAR scope.

Although not mandatory over the Kivu Region since this region is located near the equator, ionospheric corrections are needed for polar and high-latitude regions. Moreover, with the advent of future L-band missions like e.g. TanDEM-L [118], SAOCOM [119] or NISAR [120], it becomes more and more necessary to correct interferometric measurements from these effects. For this reason, it is of interest for us to have at our disposal a tool for the ionospheric compensation, like e.g. the split-spectrum technique.

In this chapter, we present the integration of the Range Split-Spectrum method into the CIS software. This integration is not yet completed, the only missing step being the accurate coregistration. Nevertheless, preliminary results could be obtained even so. In the first section, we shortly explain the origin of the ionospheric contribution to the InSAR phase. In the second section, we review the rationale of the technique, the processing flow and the key points of the processing. In the third section, we present the modifications introduced in CIS in order to manage ionospheric corrections. We then test the processor in its current state on ALOS-2 data over Siberia and we present the results. Finally, in the last section, we present our conclusions and discuss the work left to be done with the implementation of the range split-spectrum technique.

5.1 Ionospheric distortions in SAR interferograms

The ionosphere is a region of the upper atmosphere that extends from about 50 km to more than 1000 km. This region is populated with free electrons and ions produced by ionization of the atmospheric gases by the solar radiation. The density of charged particles varies with the altitude, with a peak between 300 and 400 km. For SAR modelling purposes, the ionosphere is usually approximated by a thin layer with an effective height around these altitudes.

Given that the ionosphere is made of charged particles, it is a plasma and the propagation of a radio wave in this medium is thus described by the Appleton-Hartree equation [121]. The expression of this equation of dispersion depends on the ionization of the plasma, i.e. its density of free electrons, and the frequency of the electromagnetic signal. It can be shown, as done in Reference [30], that the phase velocity of a SAR signal propagating through the ionosphere is smaller than the speed of light, leading to a refractive index of the ionospheric plasma smaller than 1. Consequently, SAR signals undergo a phase advance proportional to the density of free electrons and inversely proportional to the carrier frequency with respect to an ionosphere-free propagation. This ionospheric phase advance, calculated along the two-way path of the SAR signal, is given by

$$\phi_{\text{iono}}(\nu) \;=\; -2\,\frac{2\pi}{\lambda}\frac{K}{\nu^2}\int n_e(z)\,dz \;=\; -\frac{4\pi K}{c\nu}\,\text{TEC}, \tag{5.1}$$

where c is the speed of light, n_e is the density of free electrons, $K = 40.28\,\text{m}^3/\text{s}^2$ and TEC is the slant total electron content. The TEC is defined as the number of electrons contained within a tube of one square meter cross section along the propagation path of the signal. The TEC is thus computed by integrating the electron density along the signal path and it is usually measured in TEC units (TECUs), one TECU being defined as 10^{16} electrons/m^2. The slant TEC can be converted into vertical TEC using a mapping function that is one over the cosine of the zenith angle [122].

From Equation (5.1), it is clear that the ionosphere is a dispersive medium and that waves of different frequencies undergo different phase advances, the low frequency signals being more advanced than the high frequency ones. Moreover, the ionospheric phase contribution is dependent on the TEC, which is variable both in space and time. This variability strongly affects SAR and InSAR measurements, and introduces ionospheric distortions of two types: the first is the presence of azimuth streaks in SAR images [123], which cause coregistration errors and local loss of coherence when performing interferometry; the second is the existence of an ionospheric phase screen, superimposed on the ground signal in the InSAR phase, which is a major source of errors when measuring ground displacements.

Let us first consider distortions along the azimuth. If the TEC varies linearly along the flight path of the satellite on a scale comparable to the azimuth resolution, this causes an azimuthal phase gradient. This phase gradient is equivalent to Doppler shifts and corrupts the phase history of the imaged pixels on the length of the synthetic aperture, resulting in offsets between the azimuth position of the actual pixels and the imaged pixels [30, 123, 124]. In addition, the state of the ionosphere varying with time, these offsets are different for images acquired at distinct moments. When dealing with interferometric processing, conventional coregistration methods based on a global low order polynomial transformation are not able to take these offsets into account. Some regions of the scene may thus be ill-coregistered, which appears as local losses of coherence and blurred streaks in the corresponding interferogram. Azimuth streaks can be corrected using an accurate coregistration method, as proposed by Chen and Zebker in Reference [30]. This method is briefly explained in the next section. If TEC variations are of higher order than an approximately linear gradient, i.e. if they are not smooth, this can cause a defocusing of the image that is not corrected by the accurate coregistration.

Let us now consider the second ionospheric distortion, which is the ionospheric phase screen that contaminates InSAR phase measurements. It is well known that the InSAR phase is a superposition of several components from different origins. We can group together the topographic phase $\Delta\phi_{\text{topo}}$, the differential phase delay $\Delta\phi_{\text{defo}}$ that is due to ground deformations and the tropospheric phase delay $\Delta\phi_{\text{tropo}}$, defining the non dispersive component $\Delta\phi_{\text{non-disp}}$ of the phase. The dispersive component $\Delta\phi_{\text{iono}}$ related to the ionospheric phase advance must be added to this non dispersive contribution, and the InSAR phase is written as

$$\Delta\phi = \underbrace{\Delta\phi_{\text{topo}} + \Delta\phi_{\text{defo}} + \Delta\phi_{\text{tropo}}}_{\Delta\phi_{\text{non-disp}}} \underbrace{- \frac{4\pi K}{c\nu_0}\Delta\text{TEC}}_{\Delta\phi_{\text{iono}}}, \tag{5.2}$$

where ν_0 is the carrier frequency of the SAR signal, ΔTEC is the differential TEC, i.e. the variation of TEC between the two acquisitions, and the minus sign indicates that an increase of TEC corresponds to a phase advance. This equation shows that the InSAR phase is contaminated by the ionospheric contribution, which constitutes a major source of error when measuring the signal related to the ground. The ionospheric delay must be estimated and corrected from the InSAR phase in order to retrieve highly accurate ground displacements. This is achieved by the Range Split-Spectrum technique presented below [116, 117].

Let us note that, due to its dependency on the signal frequency, the ionospheric phase screen is larger for low frequency signals. For instance, a TEC variation of 1 TECU produces an ionospheric phase advance of more than 2 cycles in L-band, while the corresponding phase advance in C-band is of only half a cycle. In X-band, it corresponds to one-fifth of a cycle.

Moreover, the ionospheric phase screen appears only when the TEC distribution changes between the two acquisitions, i.e. when there is an anomaly in the TEC. There exist several sources for TEC variability: the diurnal variations, the seasonal variations or the 11-year solar cycle. In particular, solar flares, auroral activity and magnetic storms can induce anomalies in the density of electrons [125], and these events are more frequent at the maximum of the solar cycle. However, in order to have detectable effects, these phenomena should induces inhomogeneities in the distribution of thr TEC on spatial scales smaller than the size of the SAR image ($\sim$ few tens of kilometers). Small-scale travelling ionospheric disturbances, created by e.g. gravity waves, can also be a source of such disturbances: these are wavelike phenomena propagating from polar regions to lower latitudes, producing fluctuations in the spatial distribution of the TEC [122]. Let us stress that variations of TEC and their effects on SAR images are mainly relevant for polar and high latitude regions.

5.2 Ionospheric phase compensation

It has been explained above that the ionosphere can introduce a phase advance in the interferometric phase when there exists a variation of TEC and that this is a source of error in the estimation of ground displacements from the SAR differential phase, especially for low-frequency acquisitions. It is thus necessary to correct the InSAR contribution of the ionosphere, in particular when observing high latitudes regions with acquisitions at low-frequency, i.e. P-band and L-band, sometimes also C-band acquisitions.

The ionospheric contribution can be estimated by using the dispersive nature of the medium. This is achieved by the Range Split-Spectrum method [116,117] presented below. In this section, we briefly present the rationale of the method, the associated workflow and we provide some additional remarks on the processing. Let us note that this method and the corresponding processing are described in details by Gomba et al. in Reference [38].

5.2.1 Range Split-Spectrum method

The interferometric phase, described by Equation (5.2), is the sum of two contributions, one dispersive and the other one non dispersive. Taking advantage of the dispersive nature of the ionosphere, its phase contribution can be retrieved when the interferometric phase is calculated simultaneously at different frequencies. Fortunately, acquisitions from recent sensors have large range bandwidth and, thanks to this spectral diversity of SAR signals, InSAR phase can be estimated at different frequencies by applying a spectral decomposition and performing interferometry on the subbands centered at different frequencies, similarly to Split-Band Interferometry.

Let us have an interferometric couple of SLC acquisitions. Both the master and the slave images are then spectrally decomposed into two non overlapping subbands, one centered on the lower frequency ν_L and the other centered on the higher frequency ν_H. In practice, subbands of one third of the original bandwidth are recommended to optimize the accuracy of the ionospheric phase [126]. The slave subband images are resampled onto the master subband images, and the interferograms at low and high frequencies are computed, yielding respectively the phases $\Delta\phi_L$ and $\Delta\phi_H$. Starting from Equation (5.2), these phases can be expressed as functions of the ionospheric and dispersive phases under the form

$$\Delta\phi_L = \frac{\nu_L}{\nu_0}\,\Delta\phi_{\text{non-disp}} + \frac{\nu_0}{\nu_L}\,\Delta\phi_{\text{iono}}, \tag{5.3}$$

$$\Delta\phi_H = \frac{\nu_H}{\nu_0}\,\Delta\phi_{\text{non-disp}} + \frac{\nu_0}{\nu_H}\,\Delta\phi_{\text{iono}}. \tag{5.4}$$

Inverting these equations, it is straightforward to isolate the dispersive and non dispersive phase components. They are estimated with the expressions

$$\Delta\hat{\phi}_{\text{iono}} = \frac{\nu_L\,\nu_H}{\nu_0^2\left(\nu_H^2 - \nu_L^2\right)}\,\left(\nu_H\,\Delta\phi_L - \nu_L\,\Delta\phi_H\right), \tag{5.5}$$

$$\Delta\hat{\phi}_{\text{non-disp}} = \frac{\nu_0}{\left(\nu_H^2 - \nu_L^2\right)}\,\left(\nu_H\,\Delta\phi_H - \nu_L\,\Delta\phi_L\right). \tag{5.6}$$

Knowing the ionospheric phase, the differential TEC can be derived as

$$\Delta\text{TEC} = \frac{c\nu_0}{4\pi K}\,\Delta\phi_{\text{iono}}. \tag{5.7}$$

Assuming that the coherence is the same in the low and high interferograms, the ionospheric phase accuracy can be approximated by [38]

$$\sigma_{\Delta\hat{\phi}_{\text{iono}}} \approx \frac{3\nu_0}{4B}\sqrt{\frac{3}{N}}\,\frac{\sqrt{1-\gamma^2}}{\gamma}, \tag{5.8}$$

where N is the number of looks applied for the spatial averaging and γ is the coherence. In this expression, the number of looks has been divided by three to take into account the spectral decomposition into subbands of one third of the original bandwidth . Converted in TEC contribution, this leads to

$$\sigma_{\Delta\mathrm{TEC}} = \frac{3c\nu_0^2}{16\pi B}\sqrt{\frac{3}{N}}\frac{\sqrt{1-\gamma^2}}{\gamma}. \tag{5.9}$$

Let us stress that, although simple in its mathematical formulation, the Range Split-Spectrum method requires special attention to some key details of the processing. This is explained in the following section.

5.2.2 Processing flow

We now present the general flow of the split-spectrum processing and provide additional comments on some specific steps. As the implementation is still under development, we also recapitulate the operational steps and the ones left to implement.

As illustrated in Figure 5.1, the Range Split-Spectrum processing starts from an SLC master image and an SLC slave image. First, the coregistration shifts are computed based on the full bandwidth images. Then, the low and high frequency subbands are generated for each images by applying spectral decomposition. This spectral decomposition is basically executed the same way as it is done for SBInSAR absolute ranging, but we have to take into account an additional demodulation term, as explained in the next section. After generating the subbands, the low and high subband slave images are respectively resampled onto the low and high subband master images, using the coregistration shifts computed in the first step. Let us note that this step requires an accurate coregistration method, as explained in Reference [30].

Once the subband images are coregistered and resampled, the low and high frequency interferograms are generated. During the interferogram formation, a multilooking is applied and the topographic phase component is removed using an external DEM, leaving the differential phase only. The low and high differential interferograms are then unwrapped, yielding the low and high frequency phases $\Delta\phi_L$ and $\Delta\phi_H$. Using these phases, the ionospheric and non dispersive phase components can be directly calculated from Equations (5.5) and (5.6).

Finally, some additional steps, proposed in Reference [38], can be considered to improve these phase estimates. These steps are non mandatory but they are strongly recommended, as they are meant to improve the ionospheric phase accuracy. They consist in a correction of the phase unwrapping errors, that estimates the common and differential phase ambiguities of the low and high phases; an outlier detection based on median filtering and checking for the gaussian behaviour of the pixels [40]; and a gaussian filtering used to smooth the ionospheric phase.

Most of the tools needed for this processing, such as the phase unwrapping and the generation of interferometric products, are similar to a conventional InSAR processing and are already available in CIS. The implementation of this processing flow requires a new module for the interferometric phase estimation. In addition to estimate the ionospheric phase, the dispersive phase, the differential TEC and the errors on these products, this module includes the filtering of the phase, the outliers removal and the corrections of phase unwrapping errors. However, this processing also relies on the accurate coregistration method, which is still under development because it requires a new resampling method. Except for the accurate coregistration, which is the missing step of the processing, all the other modules that are necessary for ionospheric phase compensation are implemented and functional in CIS.

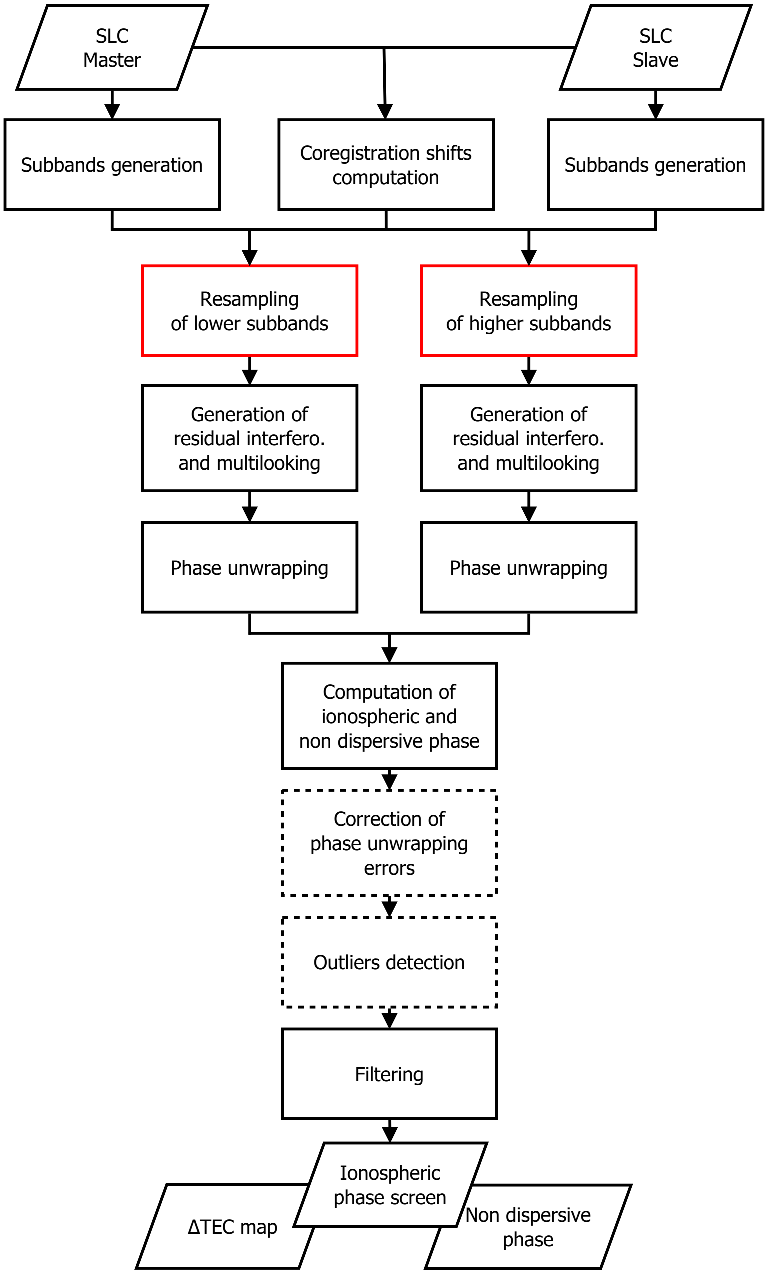

Figure 5.1: Flow chart of the Range Split-Spectrum technique. The red boxes indicate the steps for which implementation is not yet finished.

Accurate coregistration

The accurate coregistration, described in Reference [30], is meant to correct the azimuth streaks. The conventional coregistration methods use a global affine transformation, which is usually a low order polynomial of the azimuth and range offsets. Instead of using a global transformation, the accurate coregistration works with local offsets.

The first step of the algorithm consists in measuring the coregistration offsets on a grid whose resolution is defined by the user. It can be sparse to medium resolution, depending on the allocated computing time. The offsets are calculated using either amplitude cross-correlation or complex cross-correlation, i.e. coherence maximization. The grid of offsets can be furthered filtered and outliers can also be removed. Then the grid is interpolated using bilinear interpolation to match the initial resolution of the images and get the offsets corresponding to each pixels. Finally, the calculated offsets are used for resampling to slave image onto the master image.

At this stage, though the grid of offsets can be calculated, the resampling method used by CIS must be modified to take into account the pointwise offsets. This is not implemented yet and therefore limits the quality of the results presented hereafter.

Multilooking and filtering

The amount of multilooking, i.e. spatial averaging, performed during the interferogram generation can be partially replaced by an increased a posteriori filtering of the ionospheric phase. Nevertheless, as explained in Reference [127], a certain amount of multilooking must be performed initially to obtain an efficient estimate of the phase. In practice, we cannot retrieve a satisfying smooth ionospheric phase estimate for ALOS-2 images of 24.9 MHz bandwidth with an averaging window as large as 20×50 pixels in range and azimuth respectively despite a strong a posteriori filtering. When increasing the averaging window to a size of 50×80 pixels, the ionospheric signal is retrieved. Of course, the needed multilooking depends on the sensor resolution.

Remarks

It is important to make some additional remarks regarding the processing and the products generated. First, it is important to stress that the estimated phase screen is a low resolution version of the true ionospheric contribution. Indeed, the resolution of the ionospheric phase is limited in range by the image resolution and the applied multilooking, and in azimuth by the synthetic aperture length projected at the ionosphere altitude [38].

Second, we have to underline that the split-spectrum technique is easily applied to standard acquisition modes, like Stripmap. However, some modifications must be made to the basic formulation of the technique for squinted geometries of acquisitions, like e.g. TOPSAR mode of Sentinel-1. Indeed, with these modes, some portions of the ionosphere are not scanned and discontinuities of the ionosphere are present in the measured phase due to the sudden changes in the line-of-sight direction. The ionospheric phase compensation must therefore take this phase jump into account, as explained in Reference [128].

5.3 Modification of the SBInSAR processor

In order to generate the low and high frequency chromatic views of the master and slave images, we use the SBInSAR processor already implemented in CIS for absolute ranging. However, though both techniques are exploiting interferometry throughout the spectral band, the absolute ranging and the ionospheric corrections require some slightly different types of spectral decompositions. First, the Range Split-Spectrum method applies spectral decomposition to non coregistered images, while SBInSAR for absolute ranging starts from already coregistered images. Moreover, compared to SBInSAR for absolute ranging, the split-spectrum method is not based on the existence of a coregistration error. Finally, the dependency on the original carrier frequency ν_0 must disappear in the subband signal for the ionospheric correction, as we are looking for the InSAR phase at low and high frequencies. As a consequence, some modifications must be brought to the spectral decomposition applied by the SBInSAR processor in order to have the adequate signal for ionospheric compensation. These changes are described below.

In Chapter 2, we showed that, once the master acquisition is split into subbands, the point scatterer signal in the i-th master chromatic view is described by

$$S_i^m(r) \;\propto\; e^{-2\pi i \nu_0 \frac{2}{c} r_m}\, e^{2\pi i (\nu_i - \nu_0) \frac{2}{c}(r - r_m)}\, \text{sinc}\left(\pi B_s \frac{2}{c}\,(r - r_m)\right), \tag{5.10}$$

where r_m is the sensor-target distance in the master image, ν_0 is the initial carrier frequency, ν_i is the central frequency of the subband and B_s is the bandwidth of the subband. Here, the subband index i can either correspond to the lower (L) or the higher (H) frequency subband. The signal described by this equation is the one computed by the SBInSAR processor of CIS when performing absolute ranging. For ionospheric corrections, some adjustments are necessary. At this stage, since we work with SLC images, demodulation has been applied. However, demodulation has been handled with respect to the initial carrier frequency ν_0. In the split image, this should be compensated for by applying the inverse demodulation factor, and then demodulation should be performed with respect to the subband central frequency. This corresponds to multiplying the signal described by Equation (5.10) by a factor $e^{-2\pi i (\nu_i - \nu_0) \frac{2}{c} r}$. The point signal in the master subband image is then given by

$$S_i^m(r) \;\propto\; e^{-2\pi i \nu_i \frac{2}{c} r_m}\, \text{sinc}\left(\pi B_s \frac{2}{c}\,(r - r_m)\right). \tag{5.11}$$

For ionospheric corrections, spectral decomposition is applied before coregistration, in contrast with absolute ranging. Therefore, the expression of the signal in the master and slave subband scenes will only differ by the sensor-target distance, meaning that the master index m of the range distance must simply be replaced by the slave index s. Then, interferometric phase computed for the i-th subband is found to be

$$\Delta\phi_i \;=\; \frac{4\pi\nu_i}{c}\,(r_s \,-\, r_m)\,, \tag{5.12}$$

which corresponds to the InSAR phase relative to the frequency ν_i, either low or high depending on the index i, as expected for the split-spectrum technique. This InSAR phase is the one used for computing the ionospheric and non dispersive phase with Equations (5.5) and (5.6).
In practice, the additional demodulation has been introduced into the SBInSAR processor as an option, so that the user can choose to use the processor either for absolute ranging or for ionospheric phase compensation. In the case of ionospheric phase compensation, the SBInSAR processor provides the subband scenes for the master and slave images, and the conventional interferometric processing must then be carried out on the chromatic views before estimating the ionospheric phase screen.

5.4 Test case: Siberia

As the only missing step in our implementation of the ionospheric phase compensation is the accurate coregistration, it is already worth testing our split-sprectrum processing. At this stage, preliminary results were already obtained. The ionospheric effects being limited over the Kivu Region, we prefer a region located at a higher latitude in this case. This section presents the correction estimated for ALOS-2 acquisitions over the Yamal peninsula, Siberia. These data were shared by the team of the Earth and Planetary Sciences Department of Hokkaido University (Sapporo, Japan), which already processed these data for ionospheric corrections using the Gamma software and adding the modulation term described hereabove. Their results were presented in Reference [129] and are a good reference to assess the performance of our processing.

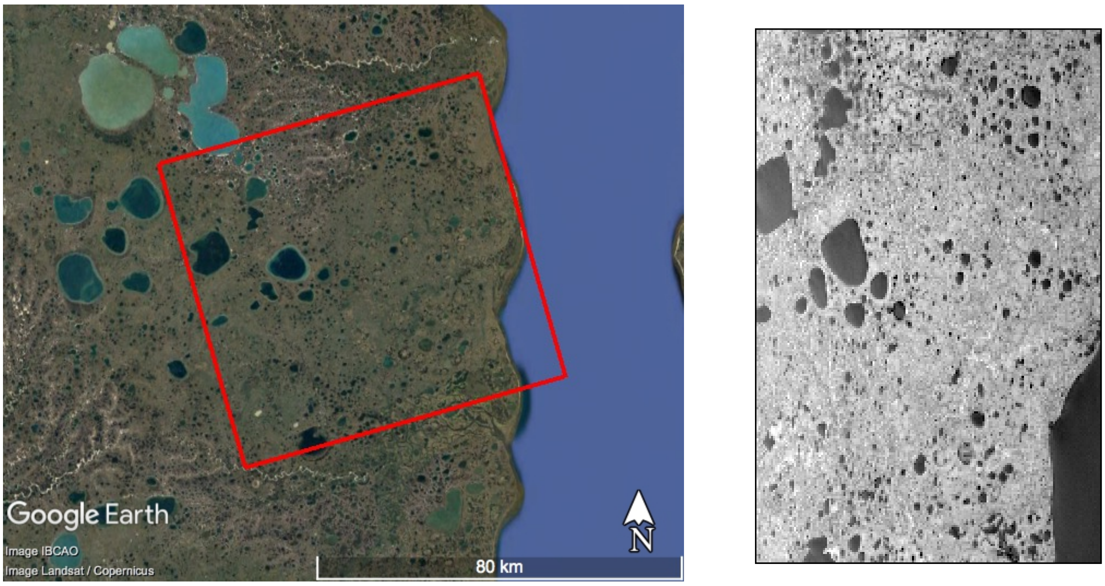

(a) (b)

Figure 5.2: Yamal peninsula, Siberia. (a) Google Earth$^{\text{TM}}$ view of the test site. The red frame indicates the footprint of the acquisitions. (b) Amplitude image of the test area acquired on August 17th, 2015.

Test site

The test area is located in the Yamal peninsula, in north-west part of Siberia, Russia. Yamal peninsula is a huge strip of land of more than 120 000 km^2 extending over the Arctic Ocean (see Figure 5.2) and densely covered by thermokarst lakes created by the melt of the permafrost [130–132]. The terrain is mostly flat in this region and no large deformation is expected at the studied period. In addition, we know that this area is prone to ionospheric effects, since it is located at more than 69°N of latitude.

Data set and processing

We have at our disposal two ALOS-2 images acquired over the test area on August 17th and September 14th, 2015. These images are acquired in L-band, i.e. with a wavelength of 24.2 cm, over an ascending orbit and they have an horizontal co-polarization (HH). They have a range bandwidth of 24.9 MHz, an incidence angle of about 31.5° and they form a perpendicular baseline of approximately 103 m.

These images are spectrally decomposed into subbands of one third of the original bandwidth, which corresponds to 8.3 MHz. Therefore, the lower and higher subband scenes are centered on frequencies equal to 1.2365 ± 0.0083 GHz. During the interferometric processing, a spatial averaging of 50×80 pixels is applied in the range and azimuth directions respectively. This spatial averaging leads to pixel range-azimuth dimensions of about 215 m × 270 m. This coarse resolution is furthered reduced for the ionospheric phase when the filtering step is applied. Moreover, though the terrain is mostly flat in the area, the topographic component is subtracted from the interferogram using the GETASSE 30 arcseconds DEM. SNAPHU is used for the phase unwrapping. Regarding the coregistration, in the absence of accurate coregistration, we use the bilinear transformation approach. We compute the transformation used for the slave resampling from the full bandwidth images and we apply this transformation to the lower and higher subband scenes, after spectral decomposition and before generating the InSAR products. Of course, we are aware that this coregistration approach is likely to introduce errors in the InSAR

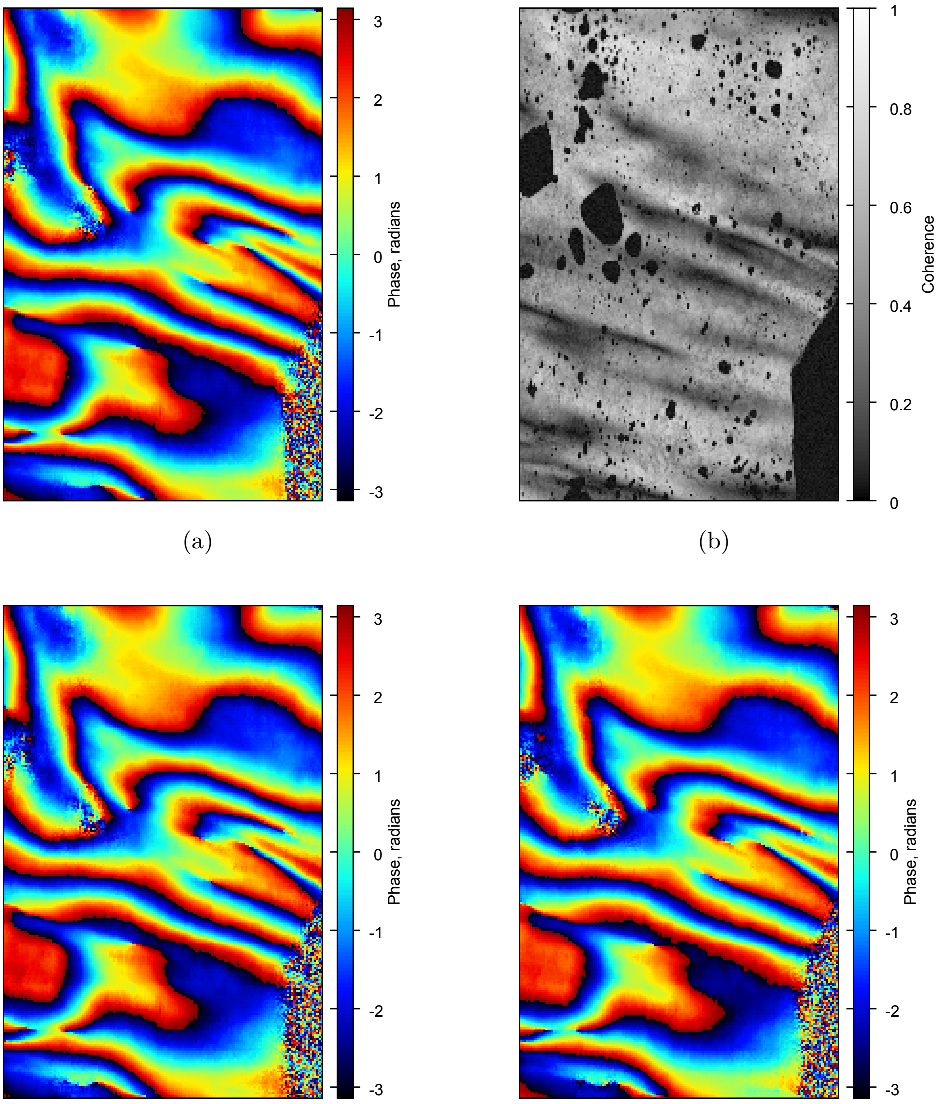

(a) (b)

(c) (d)

Figure 5.3: Siberia test case. Interferometric products obtained with ALOS-2 images acquired on August 17th and September 14th, 2015. (a) Interferogram computed from the original full bandwith acquisitions. (b) Coherence of the original acquisitions. Local losses of coherence under the form of strips correspond to azimuth streaks caused by a gradient in TEC. (c) Lower frequency interferogram. (d) Higher frequency interferogram. The width and the height of the images correspond respectively to the range and azimuth directions.

phase and the products generated by the Range Split-Spectrum technique.

5.4.1 Results

As already stated in the test site description, the region is flat in global and does not suffer from long scale deformations. However, a large scale signal is observed in the original full bandwidth interferogram, given in Figure 5.3a. This is symptomatic of a strong ionospheric contribution and makes this pair a good candidate to test the split-spectrum processing. Besides, in the original coherence image (Figure 5.3b), azimuth streaks are observed. They appear as strips of coherence loss and induce errors in the interferometric processing (noise, discontinuities). As explained in Section 5.1, these azimuth streaks can be corrected using the accurate coregistration

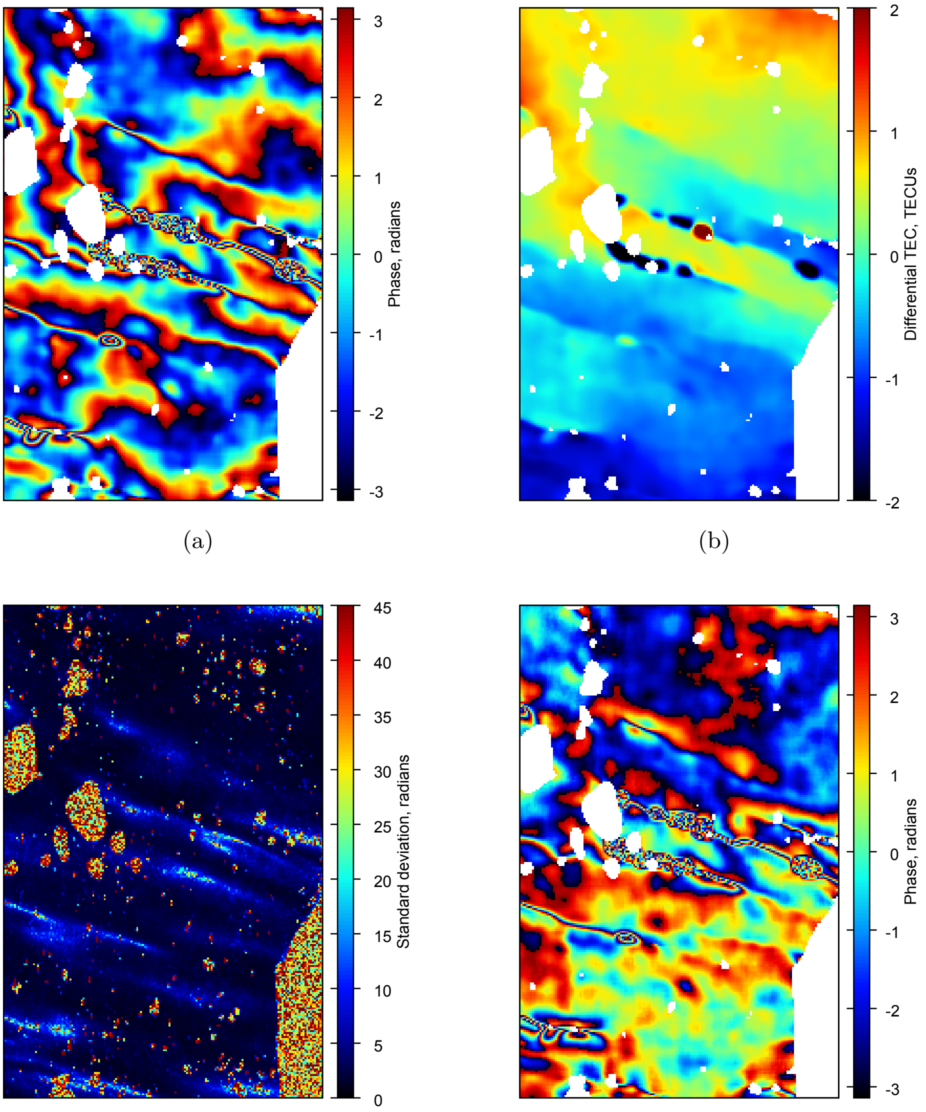

(a) (b) (c) (d)

Figure 5.4: Siberia test case. Ionospheric products computed using the Range Split-Spectrum technique. (a) Estimated ionospheric phase screen. Ionospheric phase has been filtered and corrected from outliers. It has also been wrapped, in order to easily observe the phase gradient and the errors. (b) Corresponding differential TEC. (c) Standard deviation of the raw ionospheric phase. (d) Original full bandwidth phase corrected from the estimated ionospheric contribution and wrapped. This corresponds to a low resolution estimate of the non dispersive phase contribution. The width and the height of the images correspond respectively to the range and azimuth directions.

method. Let us note that the numerous thermokarst lakes and the other water bodies are also a source of local decorrelation and we mask them in most of the subsequent products.

Figures 5.3c and 5.3d illustrate respectively the low and high frequency interferograms, obtained after the spectral decomposition and the interferometric processing on the subband scenes. Though their signals look very similar to the original interferogram, they are not exactly the same and slight differences can be noted. From these low and high frequency interferograms, the ionospheric contribution can be estimated using Equation (5.5). The raw estimate of the ionospheric phase is then corrected from outliers and filtered. Let us note that we also attempt to apply phase unwrapping corrections, as recommended by Gomba et al. in Reference [38], but

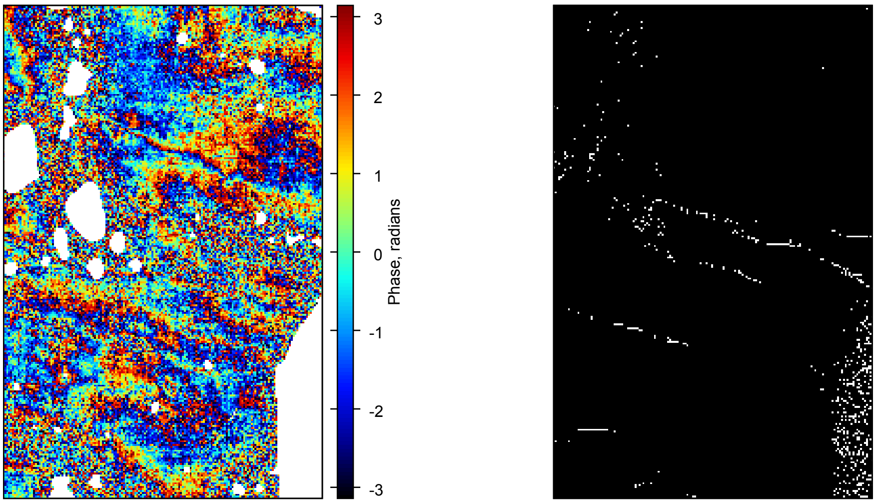

(a) (b)

Figure 5.5: Siberia test case. Products from the Range Split-Spectrum processing. (a) Wrapped estimate of the ionospheric phase screen, before filtering and outliers correction. (b) Map of the residual outliers, shown in white in the image. The width and the height of the images correspond respectively to the range and azimuth directions.

no error is detected using this procedure, although an erroneous unwrapping is obvious in some places. Nevertheless, this correction method depends highly on the accuracy of the ionospheric and non dispersive phases, and it is not robust. We thus suspect that the lack of accurate coregistration limits the efficiency of the phase unwrapping corrections.

The outlier-corrected and filtered ionospheric phase estimate is presented in Figure 5.4a in its wrapped version. Except for the influence of the azimuth streaks and the phase unwrapping errors they introduced in the phase, this signal looks very similar to the results obtained by Furuya et al. in Reference [129]. The corresponding TEC variation between the two acquisition times is given in Figure 5.4b. If we neglect the discontinuities introduced by the streaks errors, we note an approximately linear gradient along the azimuth direction. Spatial variations of the differential TEC range between about -1.3 to 1.2 TECU from one end of the scene to the other, and larger values are found at the locations of the streaks, but these are not reliable. Indeed, in the standard deviation image of the raw ionospheric phase presented in Figure 5.4c, we observe larger inacurracies (up to 30 radians) at the streaks locations, making the phase estimate completely meaningless for these places. Moreover, as expected, ionospheric phase measurements are not reliable either over the water bodies due to decorrelation. Finally, the ionospheric phase component is subtracted from the original full bandwidth interferogram and the ionosphere-corrected interferogram is shown in Figure 5.4d. This non dispersive phase, which corresponds to the deformation and tropospheric contribution, is relatively smooth, though polluted by the discontinuities of the azimuth streaks once again. The fringe rate is rather low in this non dispersive interferogram and no strong local signal is present elsewhere than at the azimuth streaks location, meaning that there is probably no local deformation.

Let us now focus on the processing. On the one hand, we tested different dimensions of averaging windows. Smaller dimensions than the 50×80 pixels were tried, but no signal could be retrieved then, despite an important a posteriori filtering. We therefore had to apply such an important smoothing, leading to a very coarse resolution of the ionospheric phase estimate. On the other hand, we consider the corrections that are applied to the raw ionospheric phase. Before the outlier correction and filtering, the raw ionospheric phase has a very noisy aspect, as observed in Figure 5.5a. An additional filtering is thus obviously necessary in order to retrieve a smooth long scale signal, as expected from the ionosphere. The second correction that is applied is the outlier removal: pixels diverging from a gaussian distribution are detected using a median filter and replaced by interpolation of their neighbours. However, this can introduce new outliers if one of the neighbours does not follow a gaussian distribution, and therefore this approach is applied iteratively until the number of residual outliers does not evolve anymore with respect to the previous iteration. The residual outliers obtained for this test case are shown in white in Figure 5.5b. We see that they correspond mostly to water bodies and azimuth streaks, where errors are expected anyway.

5.5 Summary and conclusions

The goal of this chapter was to present the implementation of the Range Split-Spectrum technique for the ionospheric phase compensation, as well as the preliminary results obtained with this tool. Although the interest of ionospheric corrections is limited over the Kivu region, the possibility of managing ionospheric phase compensation with CIS may be useful for future projects studying polar or higher latitudes, especially with the L-band missions planned in the future years, e.g. TanDEM-L, SAOCOM or NISAR. In addition, ionospheric corrections could also appear necessary for C-band Sentinel-1 acquisitions. However, in this case, an additional adaptation should be made to the SBInSAR processor so that phase jumps due to the squinted geometry of acquisition are compensated for. The split-spectrum technique exploits the spectral diversity of SAR images. It is just another approach of Split-Band Interferometry and its implementation in CIS represents an added-value to the SBInSAR processor, as it opens a new range of applications.

In this chapter, we first explained the effects induced by the ionosphere on the InSAR phase. We showed that the ionosphere could be a major source of inacurracies and that it is necessary to estimate and correct it in order to obtain ionosphere-free measurements. We also showed that the ionospheric phase screen is inversely proportional to the frequency, so that low frequency acquisitions are more impacted by ionospheric effects. Besides, the ionosphere contribution is intrisically linked to the TEC variation, allowing to retrieve TEC maps from ionospheric phase measurements.

In a second step, we presented the Range Split-Spectrum technique used to estimate the ionospheric phase component. We provided the mathematical basis of the technique, and we described the corresponding work flow. In addition, we described some specific steps in more details, like the accurate coregistration and the spatial averaging.

Even though the Range Split-Spectrum is based on a spectral decomposition similar to the Split-Band Interferometry for absolute ranging, demodulation must be performed with respect to the subband frequency rather than with respect to the original carrier frequency. As a consequence, slight modifications were introduced in the SBInSAR processor to take this different demodulation term into account. The SBInSAR processor can now be used either for absolute ranging or for ionospheric phase compensation.

However, we stressed that the split-spectrum processing is not fully operational yet. Indeed, the accurate coregistration must still be included in CIS. This is the main limitation of the ionospheric phase measurement for the moment. Nevertheless, except for this coregistration step, the processing flow is completed and tools like outliers correction and filtering, that are also meant to improve the quality of ionospheric products, are already developed in the algorithm.

Finally, we tested the implemented split-spectrum processing in its current state on a pair of ALOS-2 acquisitions over Siberia, known to contain an ionospheric contribution. This test case was already studied by the team of Hokkaido University using the Gamma software and we were hence able to compare our results to theirs. The presence of azimuth streaks in the interferometric products, caused by the lack of accurate coregistration, induced coherence losses, phase unwrapping errors and discontinuities in the phase estimates. However, if neglecting these streaks, the calculated ionospheric phase screen was overall similar to the one obtained by the Japanese team. It was observed that most of the discontinuities, residuals outliers and noise are related to the azimuth streaks or the water bodies. These results are therefore encouraging and we are confident that, once the accurate coregistration will be added to the processing, the errors should disappear.

List of symbols for Chapter 5

B	Range bandwidth
B_s	Subband range bandwidth
c	Speed of light
$\Delta\phi_{\text{defo}}$	Ground deformation phase component
$\Delta\phi_H$	High frequency InSAR phase
$\Delta\phi_L$	Low frequency InSAR phase
$\Delta\phi_{\text{iono}}$	Ionospheric phase component
$\Delta\phi_{\text{non-disp}}$	Non-dispersive phase component
$\Delta\phi_{\text{topo}}$	Topographic phase component
$\Delta\phi_{\text{tropo}}$	Tropospheric phase component
ΔTEC	Differential total electron content
γ	Coherence
K	Constant term of the ionospheric advance
λ	Wavelength
N	Number of looks
n_e	Density of free electrons
ν_0	Carrier frequency
ν_L	Lower subband frequency
ν_H	Higher subband frequency
r_m	Range distance in the master image
r_s	Range distance in the slave image
S_m^i	Point target response in the i-th partial master image
$\sigma_{\Delta\hat{\phi}_{\text{iono}}}$	Ionospheric phase accuracy
$\sigma_{\Delta\text{TEC}}$	Differential TEC accuracy

Chapter 6

Towards Combining SBInSAR and MSBAS

At this point, Split-Band Interferometry and Multidimensional Small Baseline Subset have been extensively investigated and advances towards an operational use have been achieved for both techniques. Amongst the two techniques, Split-Band Interferometry turned out to be the most challenging, especially for managing the absolute phase measurements. Indeed, some previous studies had focused on this technique, but none obtained results satisfactory enough to consider an operational use [8,9,33]. In this work, we proposed a less stringent approach than the previous studies. This approach uses the absolute phase in complement to the InSAR phase. Instead of looking for precise pointwise phase measurements, it exploits the absolute phase information throughout a given region for correcting phase ambiguities. In complement to this SBInSAR-assisted phase unwrapping, we proposed a quality indicator based on the aspect ratio of the phase ambiguity distribution, as well as an indirect validation approach. We determined the limiting factors and the optimum spectral decomposition that should be applied in practice. We also tested different criteria for the detection of spectrally stable pixels and determined that the slope standard deviation constitutes the best compromise. The SBInSAR-assisted phase unwrapping has been tested on several sensors and modes, so that the extent of the technique could be appreciated. In global, although not tested yet on an actual geohazard event, this work enabled an almost operational use of the Split-Band Interferometry.

In addition, the nature of spectrally stable pixels was investigated. While the exact reason for spectral stability is not yet understood, we showed that most of the spectrally stable pixels do not persist over time. Nevertheless, some of them are still stable over time and this population is of interest for the continuous monitoring of a given region. As we determined that this persistent population could correspond to both distributed scatterers and single point targets, we suspected that, focusing on the second type, it could be possible to create spectrally stable targets with artificial reflectors, e.g. corner reflectors or transponders, and therefore get freed of the opportunistic nature of the $\mathrm{PS_f}$ population. We explored this lead by studying the behaviour of transponders and corner reflectors with respect to SBInSAR and we highlighted a probable correlation between the slope standard deviation, i.e. the detectability as a spectrally stable pixel, and the signal-to-clutter ratio. This relationship means that a point scatterer with a large enough SCR (> 25) has a satisfactory SBInSAR phase precision and can be detected as a spectrally stable target. Although this behaviour still needs to be validated with additional data, we assume it to be true in this chapter.

Although not relevant for the studied area, we also developed the correction of the ionospheric phase screen in SAR interferograms as an extra application of Split-Band Interferometry. Ionospheric corrections are of interest for low frequency interferograms and in high latitude regions only, but they could reveal useful for future developments and represent an added-value to CIS. In order to manage these corrections, we worked on a new module that estimates the ionospheric phase and the associated differential TEC based on the Range Split-Spectrum technique. In addition to estimating the raw ionospheric phase, this module performs filtering, correction of phase unwrapping errors and detection of outliers. Though the accurate coregistration method necessary to obtain correct results is still under development, we were able to carry out preliminary tests that proved satisfactory.

Contrary to SBInSAR, Multidimensional Small Baseline Subset is an already well-developed technique, that showed its efficiency for numerous types of applications, e.g. monitoring of landslides, volcanoes, subsidence [14, 76, 133]. In the scope of RESIST, it was meant to develop an end-to-end processing chain, making the InSAR processing aumotatic for a great number of pairs and providing an interface with the MSBAS software. This way, the generation of deformation maps and the use of MSBAS is eased. This was achieved with the InSAR mass processing chain developed by the ECGS and CSL. Moreover, we attempted to optimize the spatial coverage and temporal coherence of the deformations maps in order to improve their quality and speed up the overall processing. For this purpose, we developed interpolation and masking procedures to increase the spatial information provided by the MSBAS results. We also established typical decorrelation times that can be used to determine MSBAS interferogram sequences.

Although these techniques could have been further developed, it has been demonstrated in practice that both SBInSAR and MSBAS are applicable in their current state. In this chapter, we conclude this work by presenting ideas to go one step further regarding both techniques. These ideas are either a work left to do due to the lack of time and data, or clues for a new research based on the results of this work. In the first section, we focus on the opportunities relative to SBInSAR and MSBAS separately. In the second section, as the end goal of this thesis was to achieve a combined use of SBInSAR and MSBAS, we propose leads to achieve such an ambitious objective.

6.1 One step further

At some point, a thesis must come to an end and it always leaves unexplored leads. Although we already made progress for making the Split-Band Interferometry and MSBAS tools operational, we still have ideas to go one step further regarding the knowledge and the practical use of these two techniques. Unfortunately, these ideas were not achievable in the absence of time, means or data. In this section, we propose clues for future work with both SBInSAR and MSBAS. We focus here on the work that could be done for each technique separately, as suggestions for combining both methods will be provided in the next section.

6.1.1 Split-Band Interferometry

Let us begin with the work left to do with Split-Band Interferometry. We start with the ionospheric phase compensation. As already explained in Chapter 5, though we can use Split-Band Interferometry to estimate the ionospheric phase contribution to the InSAR phase, the accurate coregistration must still be implemented to obtain a correct compensation. The implementation of this new coregistration method is necessary to obtain a functional tool.

In this work, absolute ranging was the main objective of Split-Band Interferometry, and we would like to suggest some potential studies for improving our understanding of this approach in the future. In particular, it would be a great achievement for SBInSAR-assisted phase unwrapping to be tested on an actual geohazard case, so that it could prove useful for practical applications.

However, this would require targeting an adequate deformation event, as well as being provided with wideband acquisitions of this specific event. Ideally, these acquisitions should also form a small perpendicular baseline. It has been considered to carry out such a study in the scope of this thesis and our idea was directed towards a seismic event, or a volcanic eruption, as both would both most probably give rise to large deformations. Unfortunately, we were not able to collect data fulfilling these conditions and this practical proof of applicability must still be provided.

Besides, our work on artificial spectrally stable reflectors also leaves questions to be answered. It would be interesting in the future to plan a terrain experiment with corner reflectors or transponders dedicated to a satellite more suited to SBInSAR than Sentinel-1, e.g. Radarsat-2, TanDEM-X or Cosmo-SkyMed. Such an experiment would allow to confirm the relationship between values of the SCR and the spectral stability, and to complete the corresponding graph in order to determine more accurately the SCR threshold for $\mathrm{PS_f}$ detectability and see if this value is sensor-dependent (see Chapter 4). Moreover, an experiment dedicated to an X-band sensor would enable to study the difference of $\mathrm{PS_f}$ behaviour from one frequency to another.

Finally, topographic measurements, i.e. DEM generation or validation, could also be carried out with Split-Band Interferometry, especially if applied to bistatic pairs of acquisitions. However, SBInSAR formalism has been developed for a monostatic case and it should therefore be adapted. Moreover, if using bistatic data from e.g. TanDEM-X, there could exist other issues due to the method used by DLR for data focusing and the fact that these images are provided already coregistered.

6.1.2 Multidimensional Small Baseline Subset

From the MSBAS point of view, tools are operational. However, some improvements could still be made. For example, we pointed out in Chapter 3 that a major limitation to MSBAS is that it is restricted to pixels consistently coherent throughout the data set. This may cause the loss of pixels that are coherent at a given moment, but not for the entire studied period (e.g. due to changes in land cover, soil moisture or weather conditions) so that the global coverage of the deformation measurements is restricted. An interesting improvement of MSBAS would be to overcome this restriction and improve the spatial distribution of time series measurements by implementing *intermittent* MSBAS, following the same approach as the one proposed for intermittent SBAS in Reference [134]. This consists in modifying the MSBAS algorithm to take into account not only pixels that are coherent throughout the whole data set, but also *intermittently coherent pixels*, i.e. pixels defined in a number of interferograms larger than a given threshold.

We also studied the behaviour of temporal decorrelation for several types of terrain. Though we already compared this behaviour for C-band and X-band data, it could be investigated into more details, e.g. by studying the influence of the resolution and the spatial averaging factor.

6.2 How to combine SBInSAR and MSBAS ?

The ultimate goal of this work was to combine SBInSAR and MSBAS together. However, the essences of these techniques are radically different, not to say opposite, and combining the two approaches is no easy task, even now that we have worked on making them both operational.

Despite our efforts to relax the accuracy requirements on the SBInSAR phase, some restrictions on the data parameters cannot be avoided. In order to achieve good results with this technique, wideband high-resolution acquisitions are necessary, as well as small spatial baseline interferometric pairs. On the other hand, contrary to SBInSAR, MSBAS can work with any kind of InSAR data, would they have a low or high resolution. In the end, the resolution of the deformation maps must be downgraded due to the integration of various data sets and the resampling on a common grid. Besides, the spatial coverage of MSBAS is more or less continuous while SBInSAR provides reliable measurements only on a pointwise basis. In addition, MSBAS is a post-processing technique that does not directly deal with the generation of interferometric products, unlike SBInSAR.

Although combining both techniques is not straightforward because of all these fundamentals differences, some options can be explored. In this section, we provide the reader with several suggestions to achieve this goal. Let us stress that the combined use of both techniques requires an intensive computational effort anyway. In addition, some suggestions are also demanding regarding the SBInSAR accuracy and therefore rely on the assumption that artificial reflectors are indeed spectrally stable targets of extremely good quality. Unfortunately, due to either our lack of SBInSAR-adequate data set including artificial reflectors or due to the computing effort required by these suggestions, they were not tested in practice and remain theoretical.

6.2.1 Ionospheric corrections

The first suggestion, which is also the most obvious one, is not based on the absolute phase measurement with SBInSAR, but rather on the compensation of the ionospheric phase contribution. We showed in Chapter 5 that, though the approach is not fully operational yet, the SBInSAR processor can be used to calculate and correct the dispersive phase contribution of the ionosphere in order to isolate the phase signal of ground deformation, as done by the Range Split-Spectrum technique.

In practice, once the accurate coregistration implemented, the correction of the ionospheric phase component could be made automatic and could be introduced in the chain of mass processing, therefore improving the deformation maps used as input products of MSBAS. Let us note that, when implementing an unsupervised procedure, a quality check of the results is always necessary before moving to the next step of the processing. For the Range Split-Spectrum technique, such a quality control is managed by the outlier detection and the correction of the phase unwrapping errors proposed by Gomba et al. in Reference [38].

Even though our region of interest is located near the equator and thus does not suffer much from ionospheric disturbances, ionospheric corrections are of particular interest for data sets over regions of higher latitudes and acquisitions at low frequency, e.g. for the future TanDEM-L or SAOCOM missions. Integrating ionospheric corrections would allow an extended use of the tools developed for InSAR processing and MSBAS, and would therefore constitutes a real added-value.

6.2.2 SBInSAR-assisted phase unwrapping for phase levelling

Similarly to the first suggestion, we propose this time again to use SBInSAR for improving the quality of the MSBAS input products. Our second suggestion consists in integrating the SBInSAR-assisted phase unwrapping to the InSAR mass processing chain in order to correct the phase ambiguities and level the phase of the differential interferograms, thus connecting the information from separated regions in the computed deformation maps. SBInSAR-assisted phase unwrapping is less demanding than exploiting the pointwise information of the SBInSAR phase, which makes it easier to use from the operational point of view.

Of course, the levelling approach is of interest when facing situations of disconnected areas and its usefulness therefore depends on the studied geophysical phenomenon. Indeed, when working on urban subsidence, levelling might not be necessary because of the probable high coherence and continuous coverage. However, it could reveal useful when studying decorrelating areas of

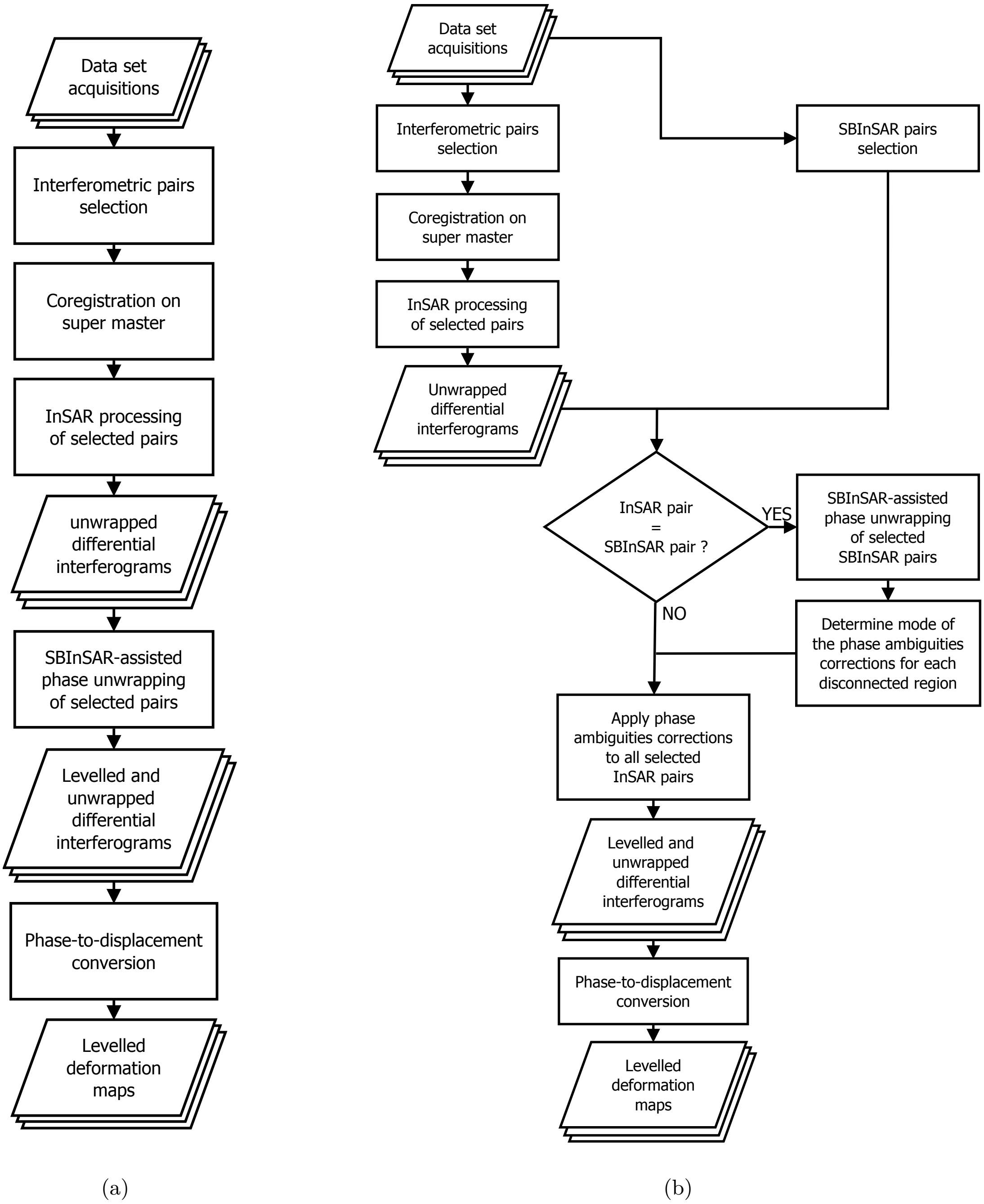

Figure 6.1: Workflows suggesting how to integrate SBInSAR-assisted phase unwrapping to the InSAR mass processing chain for phase levelling. (a) SBInSAR-assisted phase unwrapping is applied to all selected pairs. (b) SBInSAR-assisted phase unwrapping is run on the adequate pairs only, assuming the phase ambiguities are the same for all pairs. The phase ambiguity corrections are determined as the mode value occuring for these pairs and are then applied to the whole data set.

steep topography, as it is the case in the Virunga Volcanic Province, or for geophysical events of large and fast displacements, like a fault rupture for instance.

Ideally, levelling should be applied to the entirety of the deformation maps used for MSBAS, so that no discrepancy is introduced in the data. However, SBInSAR cannot be applied to any interferometric couple: we know that it performs better on wideband acquisitions and interferometric pairs with small perpendicular baselines, which translates into a large enough CDR of the interferometric couples (> 8.5). In practice, it is unlikely for the user to have at his disposal several wideband data sets with different geometries and spanning the same time period, so that they can be used to perform MSBAS. It is more probable have a single short-term data set particularly suited to SBInSAR. If this is the case, levelling would be easier to handle throughout this single data set and SBAS could be performed instead of MSBAS.

In practice, SBInSAR-assisted phase unwrapping could easily be integrated by adding some lines of code to the shell scripts. However, the actual difficulty would be to establish an automatic quality control procedure. Indeed, for the moment, the population of spectrally stable pixels and the phase ambiguity corrections are manually checked by the user, and we lack objective criteria for assessing the reliability of the results. Let us note that, if SBInSAR-assisted phase unwrapping was part of the InSAR mass processing chain, the criteria for interferometric pair selection should be slightly modified to consider a CDR threshold in addition to the small baseline conditions.

We know that a main limiting factor of SBInSAR in general, and SBInSAR-assisted phase unwrapping in particular, is the presence of spectrally stable pixels in the studied region. In that regard, installing an artificial reflector at the location of interest would secure the controlled presence of a spectrally stable pixel within the scene. Moreover, if such a target was present, then the levelling approach could be applied in combination with the suggestion of Section 6.2.3, that proposes to use SBInSAR phase as a reference for phase calibration.

Finally, we would also like to propose an alternate solution for phase levelling using SBInSAR, applicable when disconnected regions are consistent throughout all interferometric couples of the data set, i.e. when a common mask is used to compute interferometric products. This solution is based on the assumption that a given disconnected region has same phase ambiguity whatever the interferometric pair. If this assumption is indeed true, then there is no need to apply SBInSAR-assisted phase unwrapping to the whole data set, or even to restrict our data set to interferometric couples with large CDR. It is sufficient to apply SBInSAR-assisted phase unwrapping to a single pair, therefore calculating the phase ambiguity correction that must be applied to the whole data set. This phase ambiguity correction could also be calculated based on statistics on several pairs. This alternate solution is less expensive from the computational point of view. In Figure 6.1b, we present a schematic workflow of the InSAR mass processing integrating this approach for phase levelling. This workflow can be compared to the one calculating the phase ambiguities for each interferometric couple of the data, presented in Figure 6.1a.

6.2.3 SBInSAR phase as calibration data

As a third suggestion, we propose to exploit the absolute nature of the SBInSAR phase in order to reconstruct the deformation history of a spectrally stable pixel, to assess if this pixel is located in a non deforming zone, and use this point as a calibration reference for MSBAS. In the envisioned situation, we would work with the pointwise phase information of SBInSAR rather than using the distribution of a population of pixels. Therefore, high accuracy of the SBInSAR phase is required and the point considered for calibration should probably correspond to an artificial reflector, assuming that artificial reflectors correspond to spectrally stable pixels of good quality. Although this would require installing an additional equipment in the studied area, the SBInSAR phase of a single reflector is sufficient to reconstruct its displacement evolution over time, while a GNSS station, for example, must be part of a larger network.

6.2.4 SBInSAR phase as validation data

This last suggestion is probably the most demanding in terms of SBInSAR accuracy. It consists in using the SBInSAR phase of a reference point as a validation data, like it is done with DGPS for instance. As for the suggestion to use spectrally stable pixels as an MSBAS calibration reference, this suggestion relies on the SBInSAR phase quality of artificial reflectors.

However, SBInSAR provides line-of-sight deformations while DGPS data, which are typically used for validation, present the advantage of providing 3-D measurements, which is more adequate for MSBAS. Moreover, it is most likely that DGPS data have a higher accuracy than SBInSAR phase measurements. Nevertheless, if SBAS is considered instead of MSBAS, then SBInSAR would provide a validation information directly comparable to the SBAS deformation measurements.

Let us note that a major drawback of this suggestion is the use of the same data for both measurement and validation, simply processing them in different ways. This means that if there exist errors introduced by the studied data, e.g. atmospheric effects, these could not be detected by this validation approach. Nevertheless, in comparison, DGPS data can also suffer from atmospheric errors, and validation with SBInSAR presents the advantage of a potentially similar time resolution for the validation data and the time series measurements.

6.3 Summary and conclusions

Even though the investigation fields of SBInSAR and MSBAS remain vast and mostly unexplored, this work contributed to great progress regarding their operational development. As highlighted in the previous sections, there exist multiple ways to keep on enhancing our understanding of these two techniques and maybe to combine one with to other. Added to the results obtained in this work, these leads open perspectives for future work.

In its current state, Split-Band Interferometry should improve the potential for phase unwrapping and monitoring of sharp and large deformation events. Applied to artificial reflectors, SBInSAR may be a valuable source of information, as it should give access to the absolute phase knowledge of these targets. In addition to deformation measurements, calibration or validation of interferometric measurements, this information could be used as a geodesic reference. By combining SBInSAR with the MSBAS processing chain, the quality of the ground displacement time series should be upgraded. The monitoring capabilities should increase and allow a better characterization of landslides and volcanoes, which was the primary goal of the RESIST project.

Beyond the scope of the RESIST project, the developed MSBAS mass processing chain and its potential add-ons could be used to monitor any site provided with an important amount of SAR data. In particular, it is well known that remote tropical regions with difficult access to the field and an almost permanent cloud coverage are great candidates to apply InSAR and such regions would greatly benefit from the MSBAS processing chain. The integration of the SBInSAR-assisted phase unwrapping to the mass processing chain would enhance the performance over regions with a large range of cover types or dissected landscape, that are candidates to decorrelation.

Moreover, with the numerous low frequency missions planned in the years to come, managing the ionospheric effects is a main asset. Their integration in the InSAR processing chain would be appreciated for studying places other than the Kivu region and insuring continuous measurements by making the connection between actual and future SAR missions.

Conclusion

This thesis was intended to develop operational tools from Split-Band Interferometry and Multidimensional Small Baseline Subset, so as to improve ground deformation measurements in the Kivu region. Despite that both techniques are relevant in rather different cases, the spectral diversity exploited by SBInSAR constitutes an additional channel of information that could be used as a complement to the temporal information provided by MSBAS time series. In addition to turn the techniques operational, a further goal of this work was to ensure that the techniques meet at some point, so that the spectral information provided by one method could be used in combination with the temporal information from the other.

On the one hand, at the beginning of this work, there existed no study encouraging a practical use of Split-Band Interferometry for measuring ground deformations. As a consequence, there were major questions to be asked: what are the conditions for SBInSAR to perform efficiently? How can it be applied in practice and for what use? These basic questions raised several others, like e.g. what is exactly a spectrally stable pixel and how could it be detected? On the other hand, MSBAS was an already well established technique in the investigation field on InSAR time series. As an effective implementation of the method itself was already available, making MSBAS operational consisted on working on the preprocessing steps and the generation of deformation maps. We wondered how to speed up the process of generation maps and how to ensure their quality.

In Chapter 1, we introduced the basic concepts of SAR imaging and SAR interferometry. We also reviewed the concepts of coherence, interferometric processing and phase unwrapping.

In Chapter 2, we first carried out a feasibility study in order to gain some insights regarding the dependency of the SBInSAR phase precision on the processing parameters. We determined that the efficiency of SBInSAR processing is limited by two parameters: the first is the frequency-bandwidth ratio, which is a measure of the spectral diversity and should be as low as possible; the second is the geometrical decorrelation, which is increased by the degradation of the bandwidth. We estimated the impact of geometrical decorrelation through the CDR, which is expected to be high for good performances of SBInSAR. By studying the number of detected spectrally stable pixels as a function of the CDR, we derived an approximate critical value of 8.6 below which no more $\mathrm{PS_f}$ should be detected. This value is used as an indication for the choosing the adequate interferometric pairs for SBInSAR. Moreover, it was shown in practice that the chosen spectral decomposition had an influence on the quality of the results, the best ones being obtained with non overlapping subbands and a weighted linear regression. Regarding the operational aspect of SBInSAR, it was achieved by using the technique as a complement to conventional InSAR for correcting the phase ambiguities in the unwrapped interferograms. As this requires less stringent conditions on the SBInSAR phase precision, it can be applied to a larger range of data. We developed in addition a validation approach, proposed an indicator of quality and demonstrated the validity of the approach on a test case over the Copahue volcano. This approach was then tested on images over the Virunga Volcanic Province from different sensors and modes, with an overall success for bandwidths as low as 100 MHz, and both C-band

and X-band. As the key point of the SBInSAR processing is the identification of spectrally stable pixels, several criteria were investigated for their detection and we determined that the best trade-off between detections and false alarms was obtained for the slope standard deviation. Regarding the physical nature of spectrally stable pixels, we established that only a minor part of $\mathrm{PS_f}$ persisted over time. This population was not characterized by a particular type of targets, as it was made of distributed scatterers and single point targets at the same time.

In Chapter 3, we presented the InSAR mass processing chain developed in collaboration with the ECGS for the MSBAS preprocessing. We then considered two ways of improving the quality of deformation maps, by either focusing on the spatial coverage or the temporal coherence. For the spatial coverage, we developed an interpolation approach that can be applied to a single image or a whole stack. We also tested different estimators for generating a global mask applied during the mass processing in order to save computing time. A mask generated from the normalized variance-mean coherence ratio was used for a mass processing of Cosmo-SkyMed data over Buvavu spanning the 2016-2017 period, and MSBAS time series were calculated from this mass processing. The final results were in agreement with a previous study of landslides in this area. Regarding the temporal coherence, we modelled the empirical behaviour of decorrelation over time. We determined that the best model was a decreasing exponential with a bias with respect to zero and modulated by an amplitude factor. From this model, we derived typical decorrelation times for different types of terrain. These decorrelation times can be used as temporal baselines to define interferogram sequences for an MSBAS processing over the Virunga Volcanic Province.

In Chapter 4, we investigated the possibility for artificial reflectors to be spectrally stable targets. As there exists no experiment involving corner reflectors over the Kivu region, we worked on the area of Wassenaar, with a Sentinel-1 experiment of the TU Delft team. Even though Sentinel-1 data are not especially suited to SBInSAR, we observed strong evidences of a correlation between the SCR of a target and its detectability as a $\mathrm{PS_f}$. From these observations, we inferred that a SCR of about 25 corresponds to a detectable $\mathrm{PS_f}$, i.e. a target that has an SBInSAR phase precision better than a cycle. Given a quick estimation of the clutter level in the Kivu region, it was determined that a triangular trihedral corner reflector with a plate length of 2.45 m could achieved this SCR. Although the relation between SCR and $\mathrm{PS_f}$ is not confirmed, its probable existence would potentially allow the use of artificial reflectors as SBInSAR reference points and therefore ensure monitoring capabilities of SBInSAR.

In Chapter 5, we developed the Range Split-Spectrum technique for the correction of the ionospheric phase contribution in low frequency interferograms. Although not of interest for studying the Kivu region, we still investigated this technique because it is an extra application of the Split-Band Interferometry. Except for the accurate coregistration, the technique was fully developed, including the filtering, the correction of phase unwrapping errors and the outlier removal. It was tested on L-band acquisitions over the Yamal peninsula and, when neglecting the effect of the azimuth streaks, the results were in agreement with those obtained by the team of Hokkaido University.

Finally, in Chapter 6, we proposed perspectives for the work achieved in this thesis. In addition to providing clues for a further investigation of SBInSAR and MSBAS techniques, we presented suggestions for merging the information provided by both approaches. It was proposed to integrate the SBInSAR-assisted phase unwrapping and Range Split-Spectrum approaches to the MSBAS preprocessing. Moreover, assuming that artificial reflectors are indeed high quality spectrally stable targets, the use of the SBInSAR phase for calibration and validation of the MSBAS times series could be envisioned as well.

Bibliography

[1] C. Michellier, P. Pigeon, F. Kervyn, and E. Wolff, "Contextualizing vulnerability assessment: a support to geo-risk management in central Africa," *Natural Hazards*, vol. 82, no. 1, pp. 27–42, 2016.

[2] B. Smets, C. Wauthier, and N. d'Oreye, "A new map of the lava flow field of Nyamulagira (D.R. Congo) from satellite imagery," *Journal of African Earth Sciences*, vol. 58, no. 5, pp. 778–786, 2010.

[3] L. C. Graham, "Synthetic interferometer radar for topographic mapping," *Proceedings of the IEEE*, vol. 62, no. 6, pp. 763–768, 1974.

[4] H. A. Zebker and R. M. Goldstein, "Topographic mapping from interferometric synthetic aperture radar observations," *Journal of Geophys. Res.: Solid Earth*, vol. 91, no. B5, pp. 4993–4999, 1986.

[5] F. K. Li and R. M. Goldstein, "Studies of multibaseline spaceborne interferometric synthetic aperture radars," *IEEE Trans. Geosci. Remote Sens.*, vol. 28, no. 1, pp. 88–97, 1990.

[6] A. K. Gabriel, R. M. Goldstein, and H. A. Zebker, "Mapping small elevation changes over large areas: Differential radar interferometry," *J. Geophys. Res.*, vol. 94, no. B7, pp. 9183–9191, 1989.

[7] H. A. Zebker, P. A. Rosen, R. M. Goldstein, A. Gabriel, and C. L. Werner, "On the derivation of coseismic displacement fields using differential radar interferometry: The Landers earthquake," *Journal of Geophys. Res. : Solid Earth*, vol. 99, no. B10, pp. 19617–19634, 1994.

[8] N. Veneziani, F. Bovenga, and A. Refice, "A Wide-Band Approach to the Absolute Phase Retrieval in SAR Interferometry," *Multidimensional Systems and Signal Processing*, vol. 14, pp. 183–205, 2003.

[9] F. Bovenga, F. M. Rana, A. Refice, and N. Veneziani, "Multichromatic Analysis of Satellite Wideband SAR Data," *IEEE Geosci. Remote Sens. Lett.*, vol. 11, no. 10, pp. 1767–1771, 2014.

[10] A. Ferretti, C. Prati, and F. Rocca, "Permanent Scatterers in SAR Interferometry," *IEEE Trans. Geosci. Remote Sens.*, vol. 39, pp. 8–20, 2001.

[11] P. Berardino, G. Fornaro, R. Lanari, and E. Sansosti, "A New Algorithm for Surface Deformation Monitoring Based on Small Baseline Differential SAR Interferograms," *IEEE Trans. Geosci. Remote Sens.*, vol. 40, no. 11, pp. 2375–2383, 2002.

[12] A. Hooper, H. Zebker, P. Segall, and B. Kampes, "A new method for measuring deformation on volcanoes and other natural terrains using InSAR persistent scatterers," *Geophys. Res. Letters*, vol. 31, no. 23, 2004.

[13] A. Ferretti, A. Fumagalli, F. Novali, C. Prati, F. Rocca, and A. Rucci, "A New Algorithm for Processing Interferometric Data-Stacks: SqueeSAR," *IEEE Trans. Geosci. Remote Sens.*, vol. 49, no. 9, pp. 3460–3470, 2011.

[14] S. V. Samsonov and N. d'Oreye, "Multidimensional time-series analysis of ground deformation from multiple InSAR data sets applied to Virunga Volcanic Province," *Geophysical Journal International*, vol. 191, no. 3, pp. 1095–1108, 2012.

[15] P. Matgen, R. Hostache, G. Schumann, L. Pfister, L. Hoffmann, and H. H. G. Savenije, "Towards an automated SAR-based flood monitoring system: Lessons learned from two case studies," *Physics and Chemistry of the Earth, Parts A/B/C*, vol. 36, no. 7, pp. 241 – 252, 2011.

[16] H. McNairn and B. Brisco, "The application of C-band polarimetric SAR for agriculture: a review," *Canadian Journal of Remote Sensing*, vol. 30, no. 3, pp. 525–542, 2004.

[17] Jiancheng Shi, J. Wang, A. Y. Hsu, P. E. O'Neill, and E. T. Engman, "Estimation of bare surface soil moisture and surface roughness parameter using L-band SAR image data," *IEEE Trans. Geosci. Remote Sens.*, vol. 35, no. 5, pp. 1254–1266, 1997.

[18] D. Massonnet, M. Rossi, C. Carmona, F. Adragna, G. Peltzer, K. Feigl, and T. Rabaute, "The displacement field of the Landers earthquake mapped by radar interferometry," *Nature*, vol. 364, no. 6433, pp. 138–142, 1993.

[19] D. Massonnet, P. Briole, and A. Arnaud, "Deflation of Mount Etna monitored by spaceborne radar interferometry," *Nature*, vol. 375, pp. 567–570, 1995.

[20] E. Rignot, K. C. Jezek, and H. G. Sohn, "Ice flow dynamics of the Greenland Ice Sheet from SAR interferometry," *Geophys. Res. Letters*, vol. 22, no. 5, pp. 575–578, 1995.

[21] F. Amelung, D. L. Galloway, J. W. Bell, H. A. Zebker, and R. J. Laczniak, "Sensing the ups and downs of Las Vegas: InSAR reveals structural control of land subsidence and aquifer-system deformation," *Geology*, vol. 27, no. 6, pp. 483, 1999.

[22] J. C. Curlander and R. N. McDonough, *Synthetic Aperture Radar*, John Wiley and Sons, 1991.

[23] G. Franceschetti and R. Lanari, *Synthetic Aperture Radar Processing*, CRC Press, 1999.

[24] R. Hanssen, *Radar Interferometry: Data Interpretation and Error Analysis* , Kluwer Academic Publishers, 2001.

[25] D. L. Evans, J. Apel, R. Arvidson, R. Bindschadler, F. Carsey, J. Dozier, K. Jezek, E. Kasischke, F. Li, and J. Melack, "Spaceborne Synthetic Aperture Radar: Current status and future directions," 1995, NASA Technical report NASA-TM-4679, NAS 1.15:4679.

[26] A. Pepe and F. Calò, "A Review of Interferometric Synthetic Aperture RADAR (InSAR) Multi-Track Approaches for the Retrieval of Earth's Surface Displacements," *Applied Sciences*, vol. 7, no. 12, 2017.

[27] H. A. Zebker and J Villasenor, “Decorrelation in interferometric radar echoes,” *IEEE Trans. Geosci. Remote Sens.*, vol. 30, no. 5, pp. 950–959, 1992.

[28] D. C. Ghiglia and M. D. Pritt, *Two-dimensional Phase Unwrapping: Theory, Algorithms, and Software*, John Wiley and Sons, Inc, 1998.

[29] R. M. Goldstein, H. A. Zebker, and C. L. Werner, “Satellite radar interferometry: Two-dimensional phase unwrapping,” *Radio Science*, vol. 23, no. 4, pp. 713–720, 1988.

[30] A. C. Chen and H. A. Zebker, “Reducing Ionospheric Effects in InSAR Data Using Accurate Coregistration,” *IEEE Trans. Geosci. Remote Sens.*, vol. 52, no. 1, pp. 60–70, 2014.

[31] F. Bovenga, V. M. Giacovazzo, A. Refice, N. Veneziani, and R. Vitulli, “Multi-Chromatic Analysis of InSAR Data: Validation and Potential,” in *Proceedings of Fringe 2009*, Frascati, Italy, 30 November - 4 December 2009.

[32] F. Bovenga, V. M. Giacovazzo, A. Refice, and N. Veneziani, “Multichromatic Analysis of Insar Data,” *IEEE Trans. Geosci. Remote Sens.*, vol. 51, no. 9, pp. 4790–4799, 2013.

[33] F. Bovenga, D. Derauw, F. M. Rana, C. Barbier, A. Refice, N. Veneziani, and R. Vitulli, “Multi-Chromatic Analysis of SAR Images for Coherent Target Detection,” *Remote Sens.*, vol. 6, pp. 8822–8843, 2014.

[34] F. Bovenga, F. Rana, A. Refice, D. O. Nitti, and N. V. Veneziani, “Interferometric multi-chromatic analysis of Cosmo-SkyMed data for height retrieval,” in *Proceedings of IGARSS 2012*, Munich, Germany, 22-27 July 2012.

[35] D. De Rauw, F. Kervyn, N. d’Oreye, F. Albino, and C. Barbier, “Split-Band Interferometric SAR Processing Using TanDEM-X Data,” in *Proceedings of FRINGE’15: Advances in the Science and Applications of SAR Interferometry and Sentinel-1 InSAR Workshop*, Frascati, Italy, 23-27 March 2015.

[36] H. Jiang, G. Feng, T. Wang, and R. Burgmann, “Toward full exploitation of coherent and incoherent information in Sentinel-1 TOPS data for retrieving surface displacement: Application to the 2016 Kumamoto (Japan) earthquake,” *Geophys. Res. Lett.*, vol. 44, pp. 1758–1767, 2017.

[37] L. Libert, D. Derauw, N. d’Oreye, C. Barbier, and A. Orban, “Split-Band Interferometry-Assisted Phase Unwrapping for the Phase Ambiguities Correction,” *Remote Sens.*, vol. 9, no. 9, 2017.

[38] G. Gomba, A. Parizzi, F. De Zan, M. Eineder, and R. Bamler, “Toward Operational Compensation of Ionospheric Effects in SAR Interferograms: The Split-Spectrum Method,” *IEEE Trans. Geosci. Remote Sens.*, vol. 54, no. 3, pp. 1446–1461, 2016.

[39] M. Furuya, T. Suzuki, J. Maeda, and K. Heki, “Midlatitude sporadic-E episodes viewed by L-band split-spectrum InSAR,” *Earth, Planets and Space*, vol. 69, no. 1, 2017.

[40] H. Liao, F. J. Meyer, B. Scheuchl, J. Mouginot, I. Joughin, and E. Rignot, “Ionospheric correction of InSAR data for accurate ice velocity measurement at polar regions,” *Remote Sens. Env.*, vol. 209, pp. 166–180, 2018.

[41] D. Derauw, “Phase unwrapping using coherence measurements,” in *Synthetic Aperture Radar and Passive Microwave Sensing, SPIE Proceedings*, Paris, France, 21 November 1995, vol. 2584.

[42] R. Schreiber and A. Moreira, “Coregistration of Interferometric SAR Images Using Spectral Diversity,” *IEEE Trans. Geosci. Remote Sens.*, vol. 38, no. 5, pp. 2179–2191, 2000.

[43] F. Bovenga, N. Veneziani, M. Giacovazzo, A. Refice, D. Derauw, F. Minati, and F. Malvarosa, “WiMCA : Wide-Band Multi-Chromatic Assessment,” Project final report, 16 July 2010, ESA contract 21319/07/NL/HE.

[44] F. Kervyn, F. Albino, D. Derauw, N. d’Oreye, and B. Smets, “Vi-X: Study and monitoring of Virunga volcanoes using TanDEM-X,” Final activity report, August 2014, BELSPO contract SR/00/150.

[45] K. Itoh, “Analysis of the phase unwrapping algorithm,” *Appl. Opt.*, vol. 21, no. 14, pp. 2470–2470, 1982.

[46] W. H. Press, S. A. Teukolsky, W. T. Vetterling, and B. P. Flannery, *Numerical Recipes in C: The Art of Scientific Computing*, pp. 517–528, Cambridge University Press, 1st edition, 1988.

[47] F. Bovenga, V. M. Giacovazzo, A. Refice, D. O. Nitti, and N. V. Veneziani, “Interferometric Multi-Chromatic Analysis of High Resolution X-Band Data,” in *Proceedings of Fringe 2011 Workshop*, Frascati, Italy, 19-23 September 2011.

[48] P. R. Bevington and D. K. Robinson, *Data Reduction and Error Analysis for the Physical Sciences*, pp. 194–204, Mc Graw Hill, 3rd edition, 2003.

[49] F. de Coulon, *Traité d’Electricité VI: Théorie et Traitement des Signaux*, pp. 441–453, Presses Polytechniques et Universitaires Romandes, 4th edition, 1998.

[50] C. Tison, F. Tupin, and H. Maître, “Retrieval of building shapes from shadows in high resolution SAR interferometric images,” in *Proceedings of IGARSS 2004*, Anchorage, Alaska, USA, 20-24 September 2004, vol. 3, pp. 1788–1791.

[51] N. d’Oreye, D. Derauw, H. Geirsson, B. Smets, S. Samsonov, J. Barrière, A. Oth, N. Theys, C. Kassereka, L. Libert, A. Nobile, and F. Kervyn, “Recent activity in Nyiragongo active crater, Democratic Republic of Congo – remote sensing and in-situ measurements,” Poster, IAVCEI Scientific Assembly 2017, 14-18 August 2017.

[52] J. A. Naranjo and E. Polanco, “The 2000 AD eruption of Copahue Volcano, Southern Andes,” *Rev. geol. Chile*, vol. 31, pp. 279 – 292, 2004.

[53] G. Tamburello, M. Agusto, A. Caselli, F. Tassi, O. Vaselli, S. Calabrese, D. Rouwet, B. Capaccioni, R. Di Napoli, C. Cardellini, G. Chiodini, M. Bitetto, L. Brusca, S. Bellomo, and A. Aiuppa, “Intense magmatic degassing through the lake of Copahue volcano, 2013–2014,” *Journal of Geophysical Research: Solid Earth*, vol. 120, no. 9, pp. 6071–6084, 2015.

[54] T. J. Fournier, M. E. Pritchard, and S. N. Riddick, “Duration, magnitude, and frequency of subaerial volcano deformation events: New results from Latin America using InSAR and a global synthesis,” *Geochemistry, Geophysics, Geosystems*, vol. 11, no. 1, 2010.

[55] M. L. Velez, P. Euillades, A. Caselli, M. Blanco, and J. M. Díaz, “Deformation of Copahue volcano: Inversion of InSAR data using a genetic algorithm,” *Journal of Volcanology and Geothermal Research*, vol. 202, no. 1, pp. 117 – 126, 2011.

[56] C. W. Chen and H. A. Zebker, “Network approaches to two-dimensional phase unwrapping: intractability and two new algorithms,” *Journal of the Optical Society of America A*, vol. 17, pp. 401–414, 2000.

[57] C. W. Chen and H. A. Zebker, “Two-dimensional phase unwrapping with use of statistical models for cost functions in nonlinear optimization,” *Journal of the Optical Society of America A*, vol. 18, pp. 338–351, 2001.

[58] C. W. Chen and H. A. Zebker, “Phase unwrapping for large SAR interferograms: Statistical segmentation and generalized network models,” *IEEE Trans. Geosci. Remote Sens.*, vol. 40, pp. 1709–1719, 2002.

[59] F. Bovenga, F. Rana, A. Refice, D. O. Nitti, and N. V. Veneziani, “Frequency coherent vs. temporally coherent targets,” in *Proceedings of IGARSS 2013*, Melbourne, Australia, 21-26 July 2013.

[60] F. M. Henderson and A. J. Lewis, *Manual of Remote Sensing, Volume 2: Principles and Applications of Imaging Radar*, pp. 32–34, John Wiley and Sons, 3rd edition, 1998.

[61] D. Derauw, A. Orban, and C. Barbier, “Wide Band SAR Sub-Band Splitting and Inter-Band Coherence Measurements,” *Remote Sens. Lett.*, vol. 1, no. 3, pp. 133–140, 2010.

[62] B. Kampes, *Radar Interferometry: Persistent Scatterer Technique*, vol. 12, Springer, 1st edition, 2006.

[63] M. P. Doin, S. Guillaso, R. Jolivet, C. Lasserre, F. Lodge, and G. Ducret, “Presentation of the small baseline NSBAS processing chain on a case example: The Etna deformation monitoring from 2003 to 2010 using Envisat data,” in *Proceedings of FRINGE 2011*, Frascati, Italy, 19-23 September 2011.

[64] E. A. Hetland, P. Muse, M. Simons, Y. N Lin, P.S Agram, and C. J. Di Caprio, “Multiscale InSAR Time Series (MInTS) analysis of surface deformation,” *J. Geophys. Res. Solid Earth*, vol. 117, 2012.

[65] A. Hooper, “A multi-temporal InSAR method incorporating both persistent scatterer and small baseline approaches,” *Geophys. Res. Letters*, vol. 35, no. 16, 2008.

[66] S. V. Samsonov, M. van der Kooij, and K. Tiampo, “A simultaneous inversion for deformation rates and topographic errors of DInSAR data utilizing linear least square inversion technique,” *Computers and Geosciences*, vol. 37, no. 8, pp. 1083 – 1091, 2011.

[67] P. Lundgren, F. Casu, M. Manzo, A. Pepe, P. Berardino, E. Sansosti, and R. Lanari, “Gravity and magma induced spreading of Mount Etna volcano revealed by satellite radar interferometry,” *Geophys. Res. Letters*, vol. 31, no. 4, 2004.

[68] E. Trasatti, F. Casu, C. Giunchi, S. Pepe, G. Solaro, S. Tagliaventi, P. Berardino, M. Manzo, A. Pepe, G.P. Ricciardi, E. Sansosti, P. Tizzani, G. Zeni, and R. Lanari, “The 2004–2006 uplift episode at Campi Flegrei caldera (Italy): Constraints from SBAS-DInSAR ENVISAT data and Bayesian source inference,” *Geophys. Res. Letters*, vol. 35, no. 7, 2008.

[69] C. Zhao, L. Zhong, Z. Qin, and J. de la Fuente, "Large-area landslide detection and monitoring with ALOS/PALSAR imagery data over Northern California and Southern Oregon, USA," *Remote Sens. Env.*, vol. 124, pp. 348 – 359, 2012.

[70] A. Nobile, A. Dille, E. Monsieurs, J. Basimike, T. M. Bibentyo, N. d'Oreye, F. Kervyn, and O. Dewitte, "Multi-temporal dinsar to characterise landslide ground deformations in a tropical urban environment: Focus on bukavu (dr congo)," *Remote Sens.*, vol. 10, no. 4, 2018.

[71] S. Dong, S. Samsonov, H. Yin, S. Ye, and Y. Cao, "Time-series analysis of subsidence associated with rapid urbanization in Shanghai, China measured with SBAS InSAR method," *Environmental Earth Sciences*, vol. 72, no. 3, pp. 677–691, 2014.

[72] B. Xu, G. Feng, Z. Li, Q. Wang, C. Wang, and R. Xie, "Coastal Subsidence Monitoring Associated with Land Reclamation Using the Point Target Based SBAS-InSAR Method: A Case Study of Shenzhen, China," *Remote Sens.*, vol. 8, no. 8, 2016.

[73] L. Zhou, J. Guo, J. Hu, J. Li, Y. Xu, Y. Pan, and M. Shi, "Wuhan Surface Subsidence Analysis in 2015–2016 Based on Sentinel-1A Data by SBAS-InSAR," *Remote Sens.*, vol. 9, no. 10, 2017.

[74] J.-W. Kim, L. Zhong, J. Yuanyuan, and C. K. Shum, "Ground subsidence in Tucson, Arizona, monitored by time-series analysis using multi-sensor InSAR datasets from 1993 to 2011," *ISPRS Journal of Photogrammetry and Remote Sensing*, vol. 107, pp. 126–141, 2015.

[75] T. J. Wright, B. E. Parsons, and Z. Lu, "Toward mapping surface deformation in three dimensions using InSAR," *Geophys. Res. Letters*, vol. 31, no. 1, 2004.

[76] S. V. Samsonov, N. d'Oreye, and B. Smets, "Ground deformation associated with post-mining activity at the French–German border revealed by novel InSAR time series method," *International Journal of Applied Earth Observation and Geoinformation*, vol. 23, pp. 142–154, 2013.

[77] S. Samsonov, T. Lantz, S. Kokelj, and Y. Zhang, "Growth of a young pingo in the Canadian Arctic observed by RADARSAT-2 interferometric satellite radar," *The Cryosphere*, vol. 10, no. 2, pp. 799–810, 2016.

[78] S. V. Samsonov and N. d'Oreye, "Multidimensional Small Baseline Subset (MSBAS) for Two-Dimensional Deformation Analysis: Case Study Mexico City," *Canadian Journal of Remote Sensing*, vol. 43, no. 4, pp. 318–329, 2017.

[79] W. Gong, A. Thiele, S. Hinz, F. J. Meyer, A. Hooper, and P. S. Agram, "Comparison of Small Baseline Interferometric SAR Processors for Estimating Ground Deformation," *Remote Sens.*, vol. 8, 2016.

[80] G. H. Golub and C. F. Van Loan, *Matrix Computations*, pp. 69–75, The John Hopkins University Press, 3rd edition, 1996.

[81] G. Strang, *Linear Algebra and Its Applications*, pp. 331–338, Thomson Brooks/Cole, 4th edition, 2006.

[82] A. E. Yagle, "Regularized matrix computations," unpublished, 2005.

[83] P. C. Hansen, “The L-Curve and its Use in the Numerical Treatment of Inverse Problems,” in *Computational Inverse Problems in Electrocardiology*, Advances in Computational Bioengineering, pp. 119–142. WIT Press, 2001.

[84] A. K. Gabriel and R. M. Goldstein, “Crossed orbit interferometry: theory and experimental results from SIR-B,” *International Journal of Remote Sensing*, vol. 9, no. 5, pp. 857–872, 1988.

[85] S. Roose, B. Brichau, and E. W. Stijns, “An efficient interpolation algorithm for Fourier and diffractive optics,” *Optics Communications*, vol. 97, pp. 312–318, 1993.

[86] D. Derauw, *Phasimétrie par Radar à Synthèse d’Ouverture; théorie et applications*, Ph.D. thesis, Université de Liège, 1998.

[87] N. Yagüe-Martínez, P. Prats-Iraola, F. Rodríguez González, R. Brcic, R. Shau, D. Geudtner, M. Eineder, and R. Bamler, “Interferometric Processing of Sentinel-1 TOPS Data,” *IEEE Trans. Geosci. Remote Sens.*, vol. 54, no. 4, pp. 2220–2234, 2016.

[88] R. M. Goldstein and C. L. Werner, “Radar interferogram filtering for geophysical applications,” *Geophys. Res. Letters*, vol. 25, no. 21, pp. 4035–4038, 1998.

[89] I. Baran, M. P. Stewart, B. M. Kampes, Z. Perski, and P. Lilly, “A modification to the Goldstein radar interferogram filter,” *IEEE Trans. Geosci. Remote Sens.*, vol. 41, no. 9, pp. 2114–2118, 2003.

[90] N. d’Oreye, P. J. González, A. Shuler, A. Oth, L. Bagalwa, G. Ekström, D. Kavotha, F. Kervyn, C. Lucas, F. Lukaya, E. Osodundu, C. Wauthier, and J. Fernández, “Source parameters of the 2008 Bukavu-Cyangugu earthquake estimated from InSAR and teleseismic data,” *Geophys. J. International*, vol. 184, no. 2, pp. 934–948, 2011.

[91] D. Delvaux, J.-L. Mulumba, Mwene Ntabwoba Stanislas Sebagenzi, S. F. Bondo, F. Kervyn, and H.-B. Havenith, “Seismic hazard assessment of the Kivu rift segment based on a new seismotectonic zonation model (western branch, East African Rift system),” *Journal of African Earth Sciences*, vol. 134, pp. 831–855, 2017.

[92] J. Moeyersons, P. Trefois, J. Lavreau, D. Alimasi, I. Badriyo, B. Mitima, M. Mundala, D. O. Munganga, and L. Nahimana, “A geomorphological assessment of landslide origin at Bukavu, Democratic Republic of the Congo,” *Engineering Geology*, vol. 72, no. 1, pp. 73 – 87, 2004.

[93] H. Geirsson, N. d’Oreye, N. Mashagiro, M. Syauswa, G. Celli, B. Kadufu, B. Smets, and F. Kervyn, “Volcano-tectonic deformation in the Kivu Region, Central Africa: Results from six years of continuous GNSS observations of the Kivu Geodetic Network (KivuGNet),” *Journal of African Earth Sciences*, vol. 134, pp. 809–823, 2017.

[94] F. Chaabane, F. Tupin, and H. Maitre, “An empirical model for interferometric coherence,” in *Proceedings of SPIE*, Bruges, Belgium, 12 October 2015, vol. 5980.

[95] M. Foumelis, Z. Mitraka, R. Cuccu, Y.-L. Desnos, and M. Engdahl, “Moving from Temporal Coherence to Decorrelation Time of Interferometric Measurements Exploiting ESA’s SAR Archive,” in *Proceedings of FRINGE 2015*, Frascati, Italy, 23-27 March 2015.

[96] F. Rocca, “Modeling Interferogram Stacks,” *IEEE Trans. Geosci. Remote Sens.*, vol. 45, no. 10, pp. 3289–3299, 2007.

[97] A. Papoulis, *Probability, Random Variables, and Stochastic Processes*, pp. 635–654, McGraw-Hill International Editions, 3rd edition, 1991.

[98] R. Touzi, A. Lopes, J. Bruniquel, and P. W. Vachon, “Coherence estimation for SAR imagery,” *IEEE Trans. Geosci. Remote Sens.*, vol. 37, no. 1, pp. 135–149, 1999.

[99] L. J. Cantafio, *Spacebased radar handbook*, pp. 349–372, Artech House, 1989.

[100] K. Sarabandi and T.-C. Chiu, “Optimum corner reflectors for calibration of imaging radars,” *IEEE Trans. Antennas Propag.*, vol. 44, no. 10, pp. 1348–1361, 1996.

[101] R. M. Jr Axline, G. R. Sloan, and R. E. Spalding, “Radar transponder apparatus and signal processing technique,” 1994, patent.

[102] P. S. Mahapatra, S. Samiei-Esfahany, H. van der Marel, and R. F. Hanssen, “On the Use of Transponders as Coherent Radar Targets for SAR Interferometry,” *IEEE Trans. Geosci. Remote Sens.*, vol. 52, no. 3, pp. 1869–1878, 2014.

[103] H. van der Marel, F. van Leijen, and R. F. Hanssen, “First analysis of C-band ECR transponder for InSAR geodesy,” in *Proceedings of IGARSS 2018*, Valencia, Spain, 22-27 July 2018.

[104] P. Marinkovic, V.B.H. Ketelaar, F. J. van Leijen, and R. F. Hanssen, “InSAR quality control : Analysis of five years of corner reflector time series,” in *Proceedings of Fringe 2007: Advances in SAR Interferometry from ENVISAT and ERS missions*, Frascati, Italy, 26-30 November 2007.

[105] G. Quin and P. Loreaux, “Submillimeter Accuracy of Multipass Corner Reflector Monitoring by PS Technique,” *IEEE Trans. Geosci. Remote Sens.*, vol. 51, no. 3, pp. 1775–1783, 2013.

[106] X. Ye, H. Kaufmann, and X. F. Guo, “Landslide Monitoring in the Three Gorges Area Using D-INSAR and Corner Reflectors,” *Photogramm. Eng. and Remote Sens.*, vol. 70, no. 10, pp. 1167–172, 2004.

[107] T. Strozzi, p. Teatini, L. Tosi, U. Wegmüller, and C. Werner, “Land subsidence of natural transitional environments by satellite radar interferometry on artificial reflectors,” *J. of Geophys. Res.: Earth Surface*, vol. 118, no. 2, pp. 1177–1191, 2013.

[108] F. Bovenga, G. Pasquariello, R. Pellicani, A. Refice, and G. Spilotro, “Landslide monitoring for risk mitigation by using corner reflector and satellite SAR interferometry: The large landslide of Carlantino (Italy),” *CATENA*, vol. 151, pp. 49–62, 2017.

[109] M. C. Garthwaite, “On the Design of Radar Corner Reflectors for Deformation Monitoring in Multi-Frequency InSAR,” *Remote Sens.*, vol. 9, no. 7, 2017.

[110] A. Ferretti, G. Savio, R. Barzaghi, A. Borghi, S. Musazzi, F. Novali, C. Prati, and F. Rocca, “Submillimeter Accuracy of InSAR Time Series: Experimental Validation,” *IEEE Trans. Geosci. Remote Sens.*, vol. 45, no. 5, pp. 1142–1153, 2007.

[111] A. L. Gray, P. W. Vachon, C. E. Livingstone, and T. I. Lukowski, “Synthetic aperture radar calibration using reference reflectors,” *IEEE Trans. Geosci. Remote Sens.*, vol. 28, no. 3, pp. 374–383, 1990.

[112] A. Freeman, “Sar calibration: an overview,” *IEEE Trans. Geosci. Remote Sens.*, vol. 30, no. 6, pp. 1107–1121, 1992.

[113] R. K. Hawkins, L. D. Teany, S. Srivastava, and S. Y. K. Tam, “Radarsat precision transponder,” *Advances in Space Research*, vol. 19, no. 9, pp. 1455–1465, 1997.

[114] C. Li, J. Yin, J. Zhao, G. Zhang, and X. Shan, “The selection of artificial corner reflectors based on RCS analysis,” *Acta Geophysica*, vol. 60, no. 1, pp. 43–58, 2012.

[115] V. B. H. Ketelaar, *Satellite Radar Interferometry: Subsidence Monitoring Techniques*, Springer Netherlands, 2009.

[116] R. Brcic, A. Parizzi, M. Eineder, R. Bamler, and F. Meyer, “Estimation and compensation of ionospheric delay for SAR interferometry,” in *Proceedings of IGARSS 2010*, Honolulu, HI, USA, 25-30 July 2010, pp. 2908–2911.

[117] P. A. Rosen, S. Hensley, and C. Chen, “Measurement and mitigation of the ionosphere in L-band Interferometric SAR data,” in *2010 IEEE Radar Conference*, Washington, DC, USA, 10-14 May 2010, pp. 1459–1463.

[118] A. Moreira, G. Krieger, I. Hajnsek, K. Papathanassiou, M. Younis, P. Lopez-Dekker, S. Huber, M. Villano, M. Pardini, M. Eineder, F. De Zan, and A. Parizzi, “Tandem-L: A Highly Innovative Bistatic SAR Mission for Global Observation of Dynamic Processes on the Earth’s Surface,” *Geosci. Remote Sens. Mag.*, vol. 3, no. 2, pp. 8–23, 2015.

[119] D. D’Aria, D. Giudici, A. M. Guarnieri, P. Rizzoli, and J. Medina, “A wide swath, full polarimetric, L band spaceborne SAR,” in *2008 IEEE Radar Conference*, Rome, Italy, 26-30 May 2008, pp. 1–4.

[120] P. Rosen, S. Hensley, S. Shaffer, W. Edelstein, Y. Kim, R. Kumar, T. Misra, R. Bhan, and R. Sagi, “The NASA-ISRO SAR (NISAR) mission dual-band radar instrument preliminary design,” in *Proceedings of IGARSS 2017*, Fort Worth, TX, USA, 23-28 July 2017, pp. 3832–3835.

[121] K. G. Budden, *Radio Waves in the Ionosphere*, Cambridge University Press, 2009.

[122] R. Hanssen, *Radar Interferometry: Data Interpretation and Error Analysis* , pp. 197–215, Kluwer Academic Publishers, 2001.

[123] A. L. Gray, K. E. Mattar, and G. Sofko, “Influence of Ionospheric Electron Density Fluctuations on Satellite Radar Interferometry,” *Geophys. Res. Letters*, vol. 27, no. 10, pp. 1451–1454, 2000.

[124] G. Gomba and F. De Zan, “Bayesian Data Combination for the Estimation of Ionospheric Effects in SAR Interferograms,” *IEEE Trans. Geosci. Remote Sens.*, vol. 55, no. 11, pp. 6582–6593, 2017.

[125] R. C. Whitten and I. G. Popoff, *Fundamentals of Aeronomy*, John Wiley and Sons, 1971.

[126] R. Bamler and M. Eineder, “Accuracy of differential shift estimation by correlation and split-bandwidth interferometry for wideband and delta-k SAR systems,” *IEEE Trans. Geosci. Remote Sens.*, vol. 2, no. 2, pp. 151–155, 2005.

[127] F. De Zan, P. Prats-Iraola, and M. Rodriguez-Cassola, “On the Dependence of Delta-k Efficiency on Multilooking,” *IEEE Geosci. Remote Sens. Lett.*, vol. 12, no. 8, pp. 1745–1749, 2015.

[128] G. Gomba, F. Rodríguez González, and F. De Zan, "Ionospheric Phase Screen Compensation for the Sentinel-1 TOPS and ALOS-2 ScanSAR Modes," *IEEE Trans. Geosci. Remote Sens.*, vol. 55, no. 1, pp. 223–235, 2017.

[129] M. Furuya, T. Suzuki, and D. Derauw, "A step-by-step recipe of band splitting technique for isolation of ionospheric signal in L-band InSAR data," in *Proceedings of AGU Fall Meeting*, San Francisco, CA, USA, 12-16 December 2016.

[130] S. Kirpotin, Yu. Polishchuk, E. Zakharova, L. Shirokova, O. Pokrovsky, M. Kolmakova, and B. Dupre, "One of the possible mechanisms of thermokarst lakes drainage in West-Siberian North," *International Journal of Environmental Studies*, vol. 65, no. 5, pp. 631–635, 2008.

[131] J. M. Karlsson, S. W. Lyon, and G. Destouni, "Thermokarst lake, hydrological flow and water balance indicators of permafrost change in Western Siberia," *Journal of Hydrology*, vol. 464-465, pp. 459–466, 2012.

[132] M. O. Leibman, A. I. Kizyakov, A. V. Plekhanov, and I. D. Streletskaya, "New permafrost feature - deep crater in central yamal (west siberia, russia) as a response to local climate fluctuations," *Geography, Environment and Sustainability*, vol. 7, no. 4, pp. 68–79, 2014.

[133] S. V. Samsonov, N d'Oreye, P. J. González, K. F. Tiampo, L. Ertolahti, and J. J. Clague, "Rapidly accelerating subsidence in the Greater Vancouver region from two decades of ERS-ENVISAT-RADARSAT-2 DInSAR measurements," *Remote Sens. Env.*, vol. 143, pp. 180–191, 2014.

[134] A. Sowter, L. Bateson, P. Strange, K. Ambrose, and M. F. Syafiudin, "DInSAR estimation of land motion using intermittent coherence with application to the South Derbyshire and Leicestershire coalfields," *Remote Sens. Letters*, vol. 4, no. 10, pp. 979–987, 2013.